HAL
open science

Structural and photophysical studies of coordination polymers of coinage metals thiolates

Oleksandra Veselska

To cite this version:

Oleksandra Veselska. Structural and photophysical studies of coordination polymers of coinage metals thiolates. Other. Université de Lyon, 2019. English. NNT : 2019LYSE1197 . tel-02444536

HAL Id: tel-02444536

https://theses.hal.science/tel-02444536

Submitted on 18 Jan 2020

HAL is a multi-disciplinary open access archive for the deposit and dissemination of scientific research documents, whether they are published or not. The documents may come from teaching and research institutions in France or abroad, or from public or private research centers.

L'archive ouverte pluridisciplinaire **HAL**, est destinée au dépôt et à la diffusion de documents scientifiques de niveau recherche, publiés ou non, émanant des établissements d'enseignement et de recherche français ou étrangers, des laboratoires publics ou privés.

N°d'ordre NNT :
2019LYSE1197

THESE de DOCTORAT DE L'UNIVERSITE DE LYON
opérée au sein de
l'Université Claude Bernard Lyon 1

Ecole Doctorale N° 206
Ecole Doctorale de Chimie de Lyon

Discipline : Chimie

Soutenue publiquement le 17/10/2019, par :
Oleksandra VESELSKA

Études Structurales et Photophysiques de Polymères de Coordination de Thiolates de Métaux Monétaires

---

Devant le jury composé de :

Pr. Dominique LUNEAU	Professeur	Université Lyon 1	Président du jury / Examinateur
Pr. Nicolas MERCIER	Professeur	Université d'Angers	Rapporteur
Dr. Sandrine PERRUCHAS	Chargée de Recherche CNRS	Université de Nantes	Rapporteur
Dr. Nathalie GUILLOU	Chargée de Recherche CNRS	Université de Versailles Saint-Quentin-en-Yvelines	Examinatrice
Dr. Aude DEMESSENCE	Chargée de Recherche CNRS	Université Lyon 1	Directrice de thèse
Dr. Pierre BORDET	Directeur de Recherche CNRS	Université Grenoble Alpes	Co-directeur de thèse
Dr. Gilles LEDOUX	Directeur de Recherche CNRS	Université Lyon 1	Co-directeur de thèse

UNIVERSITE CLAUDE BERNARD - LYON 1

Président de l'Université	M. le Professeur Frédéric FLEURY
Président du Conseil Académique	M. le Professeur Hamda BEN HADID
Vice-président du Conseil d'Administration	M. le Professeur Didier REVEL
Vice-président du Conseil Formation et Vie Universitaire	M. le Professeur Philippe CHEVALIER
Vice-président de la Commission Recherche	M. Fabrice VALLÉE
Directrice Générale des Services	Mme Dominique MARCHAND

COMPOSANTES SANTE

Faculté de Médecine Lyon Est – Claude Bernard	Directeur : M. le Professeur G.RODE
Faculté de Médecine et de Maïeutique Lyon Sud – Charles Mérieux	Directeur : Mme la Professeure C. BURILLON
Faculté d'Odontologie	Directeur : M. le Professeur D. SEUX
Institut des Sciences Pharmaceutiques et Biologiques	Directeur : Mme la Professeure C. VINCIGUERRA
Institut des Sciences et Techniques de la Réadaptation	Directeur : M. X. PERROT
Département de Biologie Humaine	Directeur : Mme la Professeure A-M. SCHOTT

COMPOSANTES ET DEPARTEMENTS DE SCIENCES ET TECHNOLOGIE

Faculté des Sciences et Technologies	Directeur : M. F. DE MARCHI
Département Biologie	Directeur : M. le Professeur F. THEVENARD
Département Chimie Biochimie	Directeur : Mme C. FELIX
Département GEP	Directeur : M. F. DE MARCHI
Département Informatique	Directeur : M. le Professeur S. AKKOUCHE
Département Mathématiques	Directeur : M. le Professeur G. TOMANOV
Département Mécanique	Directeur : M. le Professeur H. BEN HADID
Département Physique	Directeur : M. le Professeur J-C PLENET
UFR STAPS	Directeur : M. P.FARGIER
Observatoire de Lyon	Directeur : M. B. GUIDERDONI
Polytech Lyon	Directeur : M. le Professeur E.PERRIN
Ecole Supérieure de Chimie Physique Electronique	Directeur : M. G. PIGNAULT
Institut Universitaire de Technologie de Lyon 1	Directeur : M. le Professeur C. VITON
Ecole Supérieure du Professorat et de l'Education	Directeur : M. le Professeur A. MOUGNIOTTE
Institut de Science Financière et d'Assurances	Directeur : M. N. LEBOISNE

Acknowledgments

My three and half years spent in Lyon are coming to the end. These years were great. This is indisputable. Even if I had some negative emotions, all the positive things that have happened to me exceed them by a good factor of ten! And while this was time of my Ph.D. project, it was so much more than just a scientific project. People I worked with, I communicated with, people which I met, you all contributed a lot not only to me as a scientist, You made me better, You made me know myself better. Let's try to remember everyone. Hopefully, no one will be forgotten here…

Aude, when I saw your internship proposal proposing to study 'structure-properties' relationship, I knew immediately that it was exactly what I wanted to do. It was clear to me back then, and I still keep the same opinion. Even if I had moments of demotivation or laziness, I am sure it was the best choice I could do. Therefore I want to thank you for accepting me as an internship student, for finding funding for a thesis project and accepting me again as a Ph.D. student. It is clear for me that you are quite a visionary and this project could be better if I listened to you more. I was not that much obedient, and instead of being more strict with me, you gave me freedom to choose in what direction to advance. Not every supervisor does that, but you did. You were always open, accessible and present for a talk or advice. And I am grateful for that.

'Structure team'. I want to express my deep gratitude to Nathalie Guillou and Pierre Bordet for allowing me to stay by their side and to learn how we can find out the structural arrangement of those powders! Without you, the study of 'structure-properties' relationship would not work! Thank you for a great patience and readiness to answer my sometimes stupid questions. The refinements did not always work, nevertheless, it was exciting. Few times I was lucky enough to have single crystals, therefore I have pleasure to thank Alexandra Fateeva, Guillaume Pilet, Erwann Jeaneau for structure determination of those. This list wouldn't be completed without Erik Elkaim (Cristal, Soleil) and Marco di Michiel (ID15, ESRF). We had a great luck having you helping us at synchrotrons. It was a great experience.

Now we come to 'properties team' – Gilles Ledoux and Darjan Podbevšek. I enjoyed time I spent in ILM, even though it often meant sitting alone in darkness. At the end you were there every time when I could not turn on something or align the optical fiber. And not only that, you were there to talk, to joke and to make me a good company. And while photophysics was easier than structure determination (at least success rate was higher), my questions and problems were sometimes even more absurd than those related to 'structure team'. And still I got answers (even with a smile). I need to thank also Miguel

Monge and Katerina Newell, who I have not met personally. Miguel Monge has performed DFT calculi, what gave us deeper understanding of the properties of our materials. Katerina Newell has performed quantum yield measurements, what confirmed us that some of our samples are really cool!

Of course I want to express my gratitude to Nicolas Mercier and Sandrine Perruchas to have kindly accepted to be my reporters and to have dedicate time to read and evaluate this manuscript. I would like to thank Nathalie Guillou and Dominique Luneau for accepting to participate in my defense as members of jury as well.

I want to thank Francoise Bosselet, Yoann Aizac and Bernadette Jouguet. Due to your work, I could be sure that my samples were pure. I thank also Chantal Lorentz for solid state NMR measurements.

I have to thank Satoshi Horike and all students of his team who kindly welcomed me during my stay in iCeMS (Japan). It was a pleasure to be there.

I thank also the institutions which have provided funding and supported this project: ARC6 – Communautés de Recherche Académique Auvergne-Rhône-Alpes, ANR and SCF.

And of course, people who have been creating a great atmosphere in lab every single day! Some of you I know better: Lucie, Shefali, Dolorès, Diane (girls first, so sexist!), Antonio, Miguel, Jonathan, Stéphane, Thibaut, ~~Toï Toï~~. All the discussions we had about the world we live in, politics and human rights, discussions so passionate and loud (when Spanish people were joining us). Some of you I encountered less: Zahraa, Natalia, Sarah, Alexandra, Lama, Bhagyesh, Kamila, Sweta… you are all nice and good people, I like you a lot, but unfortunately during these years I did not find enough time to know you better. Ah, and there are some internship students to remember, my favorite ones: Nicolas, Antonii, Firat, Antoine… All you (and people whom I maybe had shame to forget here) were bringing joy to the every day spent here. There will be always a special place for you in my heart and door of my home will be always opened for you no matter where I would be. I sincerely hope to stay in touch and that our lives will cross again and not once.

Last, but for sure not least… I express my deep appreciation and love to my big and now international family: to my Ukrainian family, *я дякую моїй любій сім'ї, мамі Вікторії, тату Ярославу, сестрі Наталці, а також Наташі, Льоні, Вікі, Валерії, Владу та бабусям Надіям, усім тим кого мені так хотілось би бачити частіше*; to my French family, Alain and Nicole, and Tunisian sister, Olfa, who took care of me during my master studies (if not them, I might not make it till here); and to my newly acquired Slovak family, this new part is numerous, so I will not list all of them, only you Miro, thank you for not leaving me, not giving up on me, helping me, thank you for showing the right way… and may the new page begin!

Introduction

The coordination polymers based on thiolates of coinage metals are widely known (i) for their applications in pharmaceuticals, (ii) as crucial intermediates in the synthesis of functionalized nanoparticles and (iii) for their attractive electronic, conductive and photophysical properties. Despite a number of potential applications, there is a huge lack of systematic structural studies of the neutral homoleptic coordination polymers of the formula $[M(SR)]_n$ (M = Cu(I), Ag(I), Au(I)). This is caused by the fast reactivity of the thiols with those metals, what prevents the formation of large single crystals and precluded their structural studies.

In this work a series of coordination polymers with thiophenolate ligand and its derivatives will be synthetized and crystallographically characterized in order to understand the role of different parameters such as: metal nature, presence and position of substituents, as well as weak interactions (hydrogen bonds and metalophilic interactions) in the self-assembly. Then, the photophysical studies will be carried out in order to establish the 'structure-properties' correlation. The development of new luminescent coordination polymers and the fine tuning of their structure to target precise photophysical behaviors would bring new potential applications.

Table of Contents

Introduction 1

State of the Art: Coordination Polymers of Coinage Metals Thiolates 11

I.1. Structures of CPs of Coinage Metal Thiolates: What Do We Already Know? 14

I.1.1. Compounds with 0D Inorganic Subnetwork 15

I.1.2. Compounds with 1D Inorganic Subnetwork 18

I.1.3. Compounds with 2D Inorganic Subnetwork 23

I.1.4. Other Structural Models 26

I.1.5. Structural Trends 28

I.1.6. Amorphous Coordination Polymers 33

I.2. Synthetic and Instrumental Approaches 33

I.2.1. Synthesis 33

I.2.2. Crystalline Structure Determination from Powder X-ray Diffraction Data 35

I.2.3. Total Scattering Methods and Pair Distribution Function (PDF) analysis 38

I.3. Basics of Luminescence 41

I.3.1. Important Characteristics. 43

I.3.2. Coordination Compounds and Charge Transfer 43

I.4. Goals of the Work 47

I.5 References 50

Chapter 1: $[M(SPh)]_n$ 55

1.1 Introduction 55

1.2 $[Cu(SPh)]_n$ Polymorphs 56

1.2.1 Synthesis and PXRD Characterization 56

1.2.2 Characterizations 59

1.2.3 Luminescent Properties 61

1.3 $[Ag(SPh)]_n$ Phases 67

1.3.1 Synthesis and Structural Investigation 67

1.3.2 Characterizations 72

1.3.3 Luminescent Properties 75

1.4 $[Au(SPh)]_n$ 80

1.4.1 Characterizations 80
1.4.2 Luminescent Properties 81
1.5 Potential Application: Lifetime Luminescence Thermometry 82
1.6 Conclusions 85
1.7 Experimental part 86
1.7.1 Synthesis 86
1.7.2 PXRD structural determination of $[Ag(SPh)]_n$ phase 1 87
1.8 References 90
Chapter 2: $[M(p\text{-}SPhCO_2R)]_n$, R = H, Me 93
2.1 Introduction 93
2.2 Structures 96
2.2.1 $[Cu(p\text{-}SPhCO_2H)]_n$ Structure 98
2.2.2 $[Cu(p\text{-}SPhCO_2Me)]_n$ Structure 99
2.2.3 $[Ag(p\text{-}SPhCO_2H)]_n$ and $[Ag(p\text{-}SPhCO_2Me)]_n$ Structures 100
2.2.4 $[Au(p\text{-}SPhCO_2H)]_n$ Structure 102
2.2.5 Conclusion 103
2.3 Characterization 104
2.4 Photophysical Properties 107
2.4.1 $[Cu(p\text{-}SPhCO_2H)]_n$ 107
2.4.2 $[Cu(p\text{-}SPhCO_2Me)]n$ 110
2.4.3 $[Ag(p\text{-}SPhCO_2H)]_n$ and $[Ag(p\text{-}SPhCO_2Me)]_n$ 113
2.4.4 $[Au(p\text{-}SPhCO_2H)]_n$ 116
2.4.5 Conclusion 118
2.5 Potential Application: Ratiometric Intensity Measurement Luminescence Thermometry 120
2.6 Conclusions 122
2.7 Note 123
2.8 Experimental Part 124
2.8.1 Synthesis 124
2.8.2 Single Crystal Structure Determination of $[Cu(p\text{-}SPhCO_2H)]_n$ and $[Cu(p\text{-}SPhCO_2Me)]_n$ 125

2.8.3 PXRD Structure Determination of [Ag(*p*-SPhCO$_2$H)]$_n$ and [Ag(*p*-SPhCO$_2$Me)]$_n$ 126
2.8.4 PXRD Structure Determination of [Au(*p*-SPhCO$_2$H)]$_n$ 128
2.8.5 CIE (Commision Internationale de l'Eclairage) Chromaticity Diagram 131
2.9 References 133
Chapter 3: [M(*m*-SPhCO$_2$H)]$_n$ 139
3.1 Introduction 139
3.2 Syntheses and Structures 141
3.2.1 Structure of [Cu(*m*-SPhCO$_2$H)]$_n$ 142
3.2.2 Structure of [Ag(*m*-SPhCO$_2$H)]$_n$ 144
3.2.3 Structure of [Au(*m*-SPhCO$_2$H)]$_n$ 144
3.3 Characterization 145
3.4 Photophysical Properties 147
3.4.1 [Cu(*m*-SPhCO$_2$H)]$_n$ 148
3.4.2 [Ag(*m*-SPhCO$_2$H)]$_n$ 152
3.4.3 [Au(*m*-SPhCO$_2$H)]$_n$ 155
3.5 Conclusions 160
3.6 Experimental Part 161
3.6.1 Synthesis 161
3.6.2 Single Crystal Structure Determination of [Cu(*m*-SPhCO$_2$H)]$_n$ 161
3.6.3 PXRD Structural Determination of [Au(*m*-SPhCO$_2$H)]$_n$ 162
3.7 References 165
Chapter 4: [M(*o*-SPhCO$_2$H)]$_n$ 169
4.1 Introduction 169
4.2 Syntheses and structures 173
4.2.1 [Cu(*o*-SPhCO$_2$H)]$_n$ Structure 174
4.2.2 [Ag(*o*-SPhCO$_2$H)]$_n$ Structure 176
4.2.3 [Au(*o*-SPhCO$_2$H)]$_n$ Structure 177
4.3 Characterization 180
4.4 Photophysical Properties 182
4.5 Conclusions 193
4.6 Experimental Part 194

4.6.1 Synthesis 194
4.6.2 PXRD and Total Scattering Measurements 194
4.6.3 PXRD Structure Determination of $[Cu(o\text{-}SPhCO_2H)]_n$ and $[Ag(o\text{-}SPhCO_2H)]_n$ 195
4.6.4 PDF Analysis of $[Au(o\text{-}SPhCO_2H)]_n$ Structure 197
4.7 References 200
Chapter 5: $\alpha[Au(SR)]_n$ 205
5.1 Introduction 205
5.2 Synthesis and Characterization 205
5.3 PDF Analysis of Crystalline and Amorphous $[Au(SPh)]_n$ 208
5.4 Comparison of PDFs of $\alpha[Au(SPh)]_n$, $\alpha[Au(SMePh)]_n$ and $\alpha[Au(SEtPh)]_n$ 214
5.5 Photophysical Properties 215
5.6 Conclusions 219
5.7 Experimental Part 220
5.7.1 Synthesis 220
5.7.2 Total Scattering Measurements 220
5.8 References 223
Conclusions 225
Appendix A. Experimental Part 229
A.1 Experimental Part 229
A.2 References 236
Appendix B. Photophysical Measurements 239
B.1 Photophysical Measurements 239
B.1.1 Chapter 1 235
B.1.2 Chapter 2 253
B.1.3 Chapter 3 259
B.1.4 Chapter 4 265
B.1.5 Chapter 5 271
B.2. References 274

List of studied CPs

Crystalline CPs

Thiophenol-based (HSPh)

Four polymorph phases of $[Cu(SPh)]_n$

Two polymorph phases of $[Ag(SPh)]_n$

$[Au(SPh)]_n$

para-mercaptobenzoic acid-based (*p*-$HSPhCO_2H$ or 4-MBA)

$[Cu(p\text{-}SPhCO_2H)]_n$

$[Ag(p\text{-}SPhCO_2H)]_n$

$[Au(p\text{-}SPhCO_2H)]_n$

para-methylmercaptobenzoic acid-based (*p*-$HSPhCO_2Me$)

$[Cu(p\text{-}SPhCO_2Me)]_n$

$[Ag(p\text{-}SPhCO_2Me)]_n$

$[Au(p\text{-}SPhCO_2Me)]_n$

meta-mercaptobenzoic acid-based (*m*-$HSPhCO_2H$ or 3-MBA)

$[Cu(m\text{-}SPhCO_2H)]_n$

$[Ag(m\text{-}SPhCO_2H)]_n$

$[Au(m\text{-}SPhCO_2H)]_n$

ortho-mercaptobenzoic acid-based (*o*-$HSPhCO_2H$ or 2-MBA)

$[Cu(o\text{-}SPhCO_2H)]_n$

$[Ag(o\text{-}SPhCO_2H)]_n$

$[Au(o\text{-}SPhCO_2H)]_n$

Amorpous CPs

Thiophenol-based (HSPh)

$\alpha[Au(SPh)]_n$

Phenylmethanethiol-based (HSMePh)

$\alpha[Au(SMePh)]_n$

Phenylethanethiol-based (HSEtPh)

$\alpha[Au(SEtPh)]_n$

List of abbreviations

CP(s)	Coordination Polymer(s)
*a*CP(s)	Amorphous Coordination Polymer(s)
Characterization techniques	
(P)XRD	(Powder) X-Ray Diffraction
TGA	Thermogravimetric analysis
(FT)IR	(Fourier-Transform) Infrared Spectroscopy
SEM	Scanning Electron Microscopy
PDF	Pair Distribution Function
Luminescence	
MO	Molecular Orbital
HOMO	Highest Occupied Molecular Orbital
LUMO	Lowest Unoccupied Molecular Orbital
CT	Charge Transfer
LMCT	Ligand-to-Metal Charge Transfer
MLCT	Metal-to-Ligand Charge Transfer
LMMCT	Ligand-to-Metal-Metal Charge Transfer
MC	Metal Centered
LC	Ligand Centered
IL	Intra-Ligand
(TD)DFT	(Time-Dependent) Density Functional Theory
HE	High Energy
LE	Low Energy
NIR	Near-Infrared
QY	Quantum Yield
Chemical compounds	
DMF	Dimethylformamide
THF	Tetrahydrofuran

Exercise in optimism, strong will, and faith[1]

A spark is a little thing, yet it may kindle the world.

Martin Farquhar Tupper

State of the Art:

Coordination Polymers of Coinage Metals Thiolates

Coordination polymers (CPs) are vast and diverse group of materials that bridges the gap between organic and inorganic chemistry. Along with the molecular coordination compounds, they form an object of investigation of the coordination chemistry. Coordination chemistry is not only a simple combination of organic and inorganic components with their individual properties, but much more than that. Many interesting properties result from the synergy of those components. It opens an unprecedented possibility to obtain unique properties in one material, which might have never been reached in its purely organic or inorganic phase. Not surprisingly, a large number of potential applications arises once we talk about coordination compounds.

One could name Metal-Organic Frameworks (MOFs) as the most iconic of CPs. They possess a high structural, and, therefore, functional tunability. It originates from the multitude of inorganic and organic building blocks that one can use, and results into an infinite number of formed CPs. Researchers are nowadays reaching beyond just a tunability of MOFs. An extensive research in the field has led to numerous practical and conceptual developments. Due to this, more and more scientists in the field talk about the *design* of MOFs with desired structure and properties. [2] Some of the authors question whether it is possible to design a material,[a,3] however, it is inarguable fact, that with a progressing research in the field the predictability of structures properties improves significantly.[1, 2, 4] Nevertheless, the methods are not yet ideal. [5,6]

On the conceptual level, the possibility to predict the expected MOF structure stems from the fact that MOF's network can be deconstructed into basic building units: the inorganic metal-based units (*e. g.*, the multi-nuclear metal–carboxylate units: $Zn_4O(CO_2)_8$, $Cu_2(CO_2)_4$ or

[a] Statement stems from the Concept of the Energy Landscape of Chemical Systems. The quote follows: The quintessence of these considerations with respect to the topic … "humans are the explorers, and not the creators of chemical worlds".

$Cr_3O(CO_2)_6$, etc.) or secondary building units (SBUs) and the organic linkers (*e. g.*, di- or tricarboxylic acids: terephthalic or trimesic acid, etc.). SBUs lock down the geometry around the metal ions thanks to its attributes, such as rigidity, directionality and type of coordination (connectivity). Furthermore, the number and type of coordination functions (carboxylate, azolate, phosphate…) and the geometry of the organic linkers allow to target a particular MOFs' topology (**Figure I. 1**)[b].[1] Such assembly of rigid molecular building blocks (SBUs and organic linkers) into predetermined ordered structures (networks), held together by strong coordination bonding, can be referred as reticular synthesis.[2] The use of rigidity and directionality of the building blocks is a fundamental principle of the metalloligand, pillar-layered, supramolecular building blocks and supramolecular layer building strategies.[7]

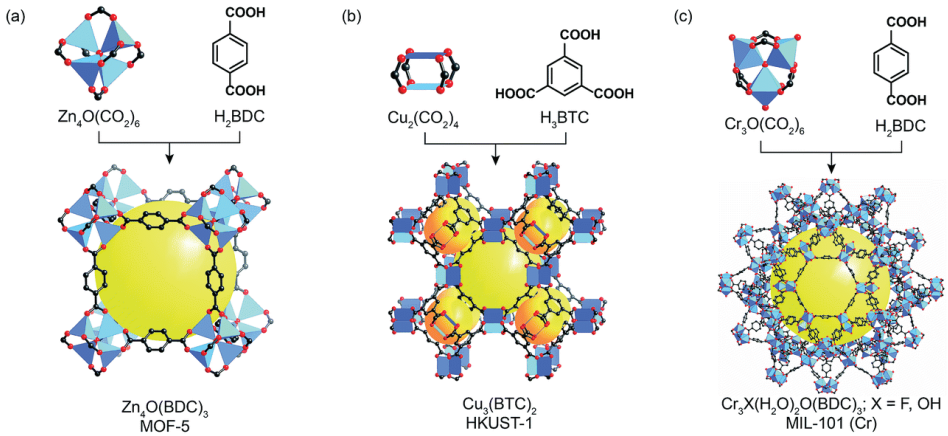

Figure I. 1 The combination of rigid and directional inorganic building blocks with charged organic linkers leads to the formation of MOFs. C, black; O, red; metals, blue polyhedra. Hydrogen atoms are omitted for clarity. Yellow and orange spheres represent the space in the framework. Adapted with permission from ref. [1]. Copyright 2017 Royal Society of Chemistry.

Aforementioned strategies are successful for the development of MOFs, however, not all the families of coordination polymers involve inorganic SBUs. In the case, when simple metal ions are used, it is difficult to predict a coordination network formed with a given ligand. This is due to the relative lack of directionality of the metal ion. It often implies a flexibility around the ion, resulting into multiplicity of possible structures and general lack of control over the resulting arrangement.[2] Metal coordination geometries are particularly unpredictable for those malleable metal ions which possess two or more common coordination geometries, such as Cu(I), Cu(II), Zn(II), Ag(I) or Cd(II).[6] A following discussion will be dedicated to the coordination

[b] Solvent, anion species in the reaction medium, temperature and pressure play their role as well. However, their influence won't be discussed herein.

polymers formed with the metal ion, precisely – *neutral thiolates of nd^{10} metals, such as Cu(I), Ag(I) and Au(I)* or *coinage metals*.

Except for the lack of directionality when the metal ions are used, there is yet another difficulty encountered when one is working with this type of coordination polymers. As the bond strength between the constituents of structures increases, the difficulty to synthetize single crystals increases dramatically, because of the fast reactivity.[1] The difficulty to form extended structures increases with the increase of the bond energy between molecular blocks.[8] Systematic comparison of the metal–thiolate bonds of noble metal monothiolates has shown that all the noble metal–SR bonds show a degree of covalency.[9] The thiolates of nd^{10} metals with N- and P-containing auxiliary ligands form small mono- or oligomeric species which are mainly soluble, and could be recrystallized.[10] Meanwhile, the neutral homoleptic thiolates of nd^{10} metals given by formula $[M(SR)]_n$ (M = Cu(I), Ag(I), Au(I)) are often formed rapidly in the reactional medium as quasi-insoluble precipitates of nonmolecular nature. This makes the synthesis of crystals large enough for single crystal X-ray diffraction structure determination rather challenging.

The aforementioned reasons explain why relatively few crystalline structures of neutral thiolates of nd^{10} metals were reported in the past. This is despite the fact that the first compounds of this class have been reported in the 80s and that they are known for their applications in pharmaceuticals, as crucial intermediates in the synthesis of functionalized nanoparticles and show attractive electronic, conductive and photophysical properties.[10]

Throughout the work, we will tackle the issue of lack of systematic structural studies and will perform accurate characterizations of their photophysical (luminescence) properties. We will attempt to understand correlation of the structure and the properties. It would be too naive to hope for ability to perform 'design' (like for MOFs), or to predict an expected structural patterns of the formed $[M(SR)]_n$ CPs. However, we hope to gain better understanding of the factors involved into the structure formation, and to investigate their potential for future applications. Last but not least, we aim to attract more attention to this category of CPs.

Before we dive into the "*fascinating chemistry or frustrating unpredictability*",[5] following questions have to be accounted for:

- *What structures have been already reported? What do we know about $[M(SR)]_n$ CPs?*
- *What are the amorphous CPs?*
- *What synthetic and instrumental approaches are we going to use?*
- *What are the basics of luminescence? What is its physical basis in nd^{10} metal thiolates?*
- *What are the hypotheses we want to examine?*

I.1. Structures of CPs of Coinage Metal Thiolates: What Do We Already Know?

In the following, we are discussing previously reported $[M(SR)]_n$ (M = Cu(I), Ag(I), Au(I)) CPs. Due to the strong structural resemblance, CPs of other chalcogenolates, such as selenoates and telluroates will be discussed as well.

The d^{10} coinage atoms are known to adapt linear, angular or trigonal planar, trigonal pyramidal geometries, while sulfur or chalcogen atoms of the organic group tend to adopt μ_2- or μ_3-bridging modes (**Figure I. 2**). It will be illustrated with examples further in the text.

The d^{10} coinage metals are also known to form weak attractive metallophilic interactions. If the distance between two metal atoms is smaller than a sum of the van der Waals radii, it can be considered to be a metallophilic interaction. The upper limit on distance depends on the nature of the metal. They are following: 2.8 Å for Cu-Cu distance, 3.44 Å for Ag-Ag distance and 3.32 Å for Au-Au distance.[11] The last years, however, Au–Au distances up to 3.5 Å are considered as metallophilic interactions. [12]

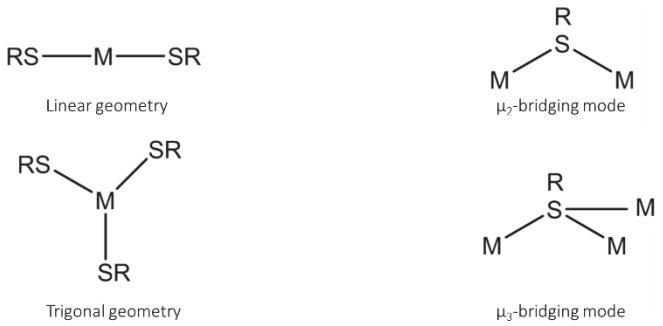

Figure I. 2 Typical coordination geometries of d^{10} coinage atoms and bridging modes of sulfur.

In this work, we are mainly interested in the luminescence properties of $[M(SR)]_n$ CPs. It is believed that their luminescence originates mainly from molecular orbitals centered on metal and sulfur atoms. Therefore, the dimensionality of an inorganic $[MS]_n$ backbone is chosen as their classification criterion (similarly to the MOFs dimensionality according to G. Férey (**Figure I. 3**)[13]). Thus, all known $[M(SR)]_n$ are divided into three groups:

- 0D (small oligomeric species $[M(SR)]_n$, with a small and defined value of n).
- 1D (mono-dimensional extended networks).
- 2D (two-dimensional extended networks).

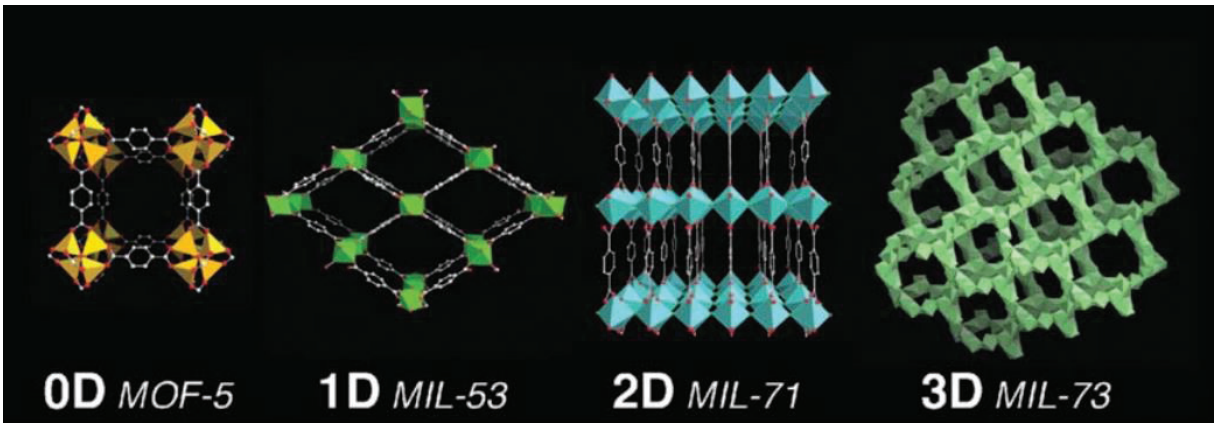

Figure I. 3 Examples of MOFs with various dimensionality of inorganic backbone. Reprinted with permission from ref. [13] Copyright 2008 Royal Society of Chemistry.

I.1.1. Compounds with 0D Inorganic Subnetwork

This category includes oligomeric species of formula $[M(SR)]_n$, where $3 \leq n \leq 12$.

$[M(SR)]_3$. The smallest reported species are composed of three units of repetition, forming six-membered non-planar cyclic structures with an alternating 2-coordinated metal and sulfur atoms. They are – $[Cu(SPh\text{-}2,6\text{-}(Mes)_2)]_3$, [14] $[Cu(SePh\text{-}2,6\text{-}(Mes)_2)]_3$, [14] $[Ag(SSi(OPh\text{-}2,6\text{-}iPr)_3]_3$ [15] and $[Ag(SC(SiPhMe_2)_3)]_3$.[16] The metal atoms show unusual angular geometry imposed by constraints of the small cycle (**Figure I. 4** (a)). $[Ag(SSi(OPh\text{-}2,6\text{-}iPr)_3]_3$ was shown to emit in green part of the spectrum at room temperature.[15]

$[M(SR)]_4$. The species composed of four units of repetition make up the majority of reported $[M(SR)]_n$ oligomers. There are eleven species: $[Cu(SSi(OtBu)_3)]_4$,[17] $[Cu(SPh\text{-}2,6\text{-}(SiMe_3)_2)]_4$,[18] $[Cu(SPh(iPr)_3)]_4$,[19] [Cu(S*m*-carborane-9)]$_4$,[20] $[Ag(SC(SiMe_3)_3)]_4$,[16] $[Ag(SeC(SiMe_3)_3)]_4$,[21] $\{[Ag(SCH(SiMe_3)_2)]_4\}_2$,[16] $\{[Ag(o\text{-}SPhSiMe_3)]_4\}_2$,[22] $[Au(SSi(OtBu)_3)]_4$,[23]

$[Au(SC(SiMe_3)_3)]_4$ [24] and $[Au(TeC(SiMe_3)_3)]_4$. [23] All of them are formed by $[MS]_4$ ring with an alternating 2-coordinated metal and sulfur atoms. While rings of the four structures ($[Cu(SPh(iPr)_3)]_4$, [Cu(S*m*-carborane-9)]$_4$, $\{[Ag(SCH(SiMe_3)_2)]_4\}_2$, $[Au(TeC(SiMe_3)_3)]_4$) are folded along S-S diagonal, giving a V-like shape, the rest of the species can be considered as planar or slightly distorted planar cycles (**Figure I. 4** (b), (c)). In all compounds, except for $\{[Ag(o\text{-}SPhSiMe_3)]_4\}_2$, two ligands are located on one side of the cycle, and two others point to the opposite direction.

Two of these compounds are forming dimers through the weak interactions: $\{[Ag(SCH(SiMe_3)_2)]_4\}_2$ and $\{[Ag(o\text{-}SPhSiMe_3)]_4\}_2$. In the case of $\{[Ag(o\text{-}SPhSiMe_3)]_4\}_2$, unlike the other cases, three ligands are located on one side of the cycle, creating a space allowing establishing metallophilic bonds (3.065(4) and 3.297(3) Å) with another cycle of the dimer (**Figure I. 4** (d)). In the $\{[Ag(SCH(SiMe_3)_2)]_4\}_2$, the thiolated ligand is the less sterically hindered comparing to all other cycles, thus secondary Ag-S interactions (3.166(6) Å) can be formed between units of the dimer (**Figure I. 4** (e)).

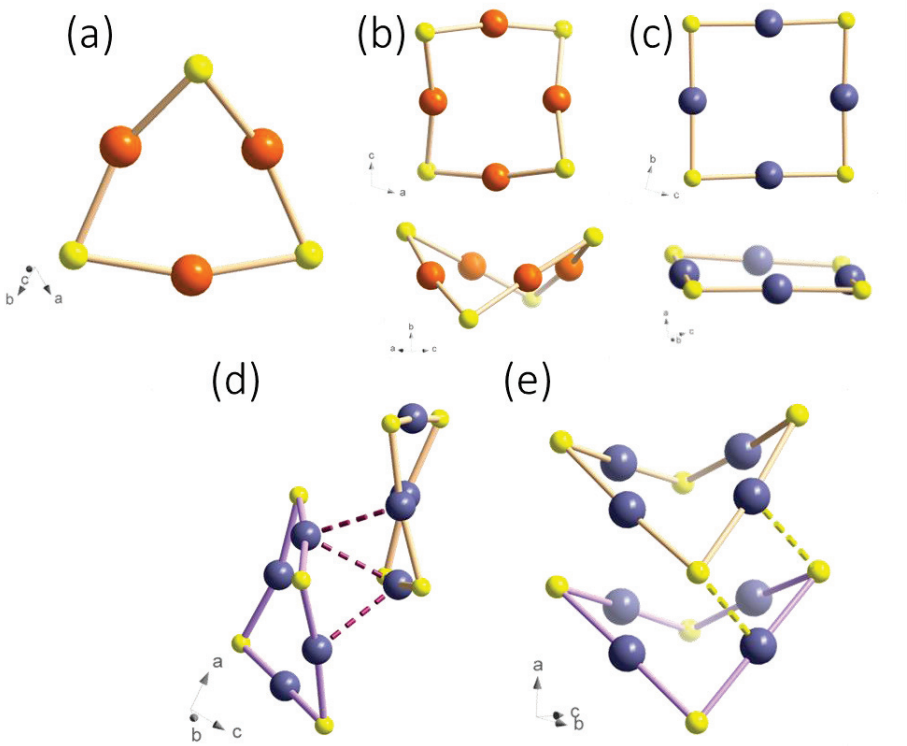

Figure I. 4 The representation of the inorganic subnetworks $[MS]_n$ of the small oligomeric species (n = 3, 4): (a) $[Cu(SPh\text{-}2,6\text{-}(Mes)_2)]_3$, [14] (b) $[Cu(SPh(iPr)_3)]_4$, [19] (c) $[Ag(SC(SiMe_3)_3)]_4$, [16] (d) $\{[Ag(o\text{-}SPhSiMe_3)]_4\}_2$ [22] and (e) $\{[Ag(SCH(SiMe_3)_2)]_4\}_2$. [16] Orange, Cu; blue, Ag; yellow, S. Violet dashed lines represent metallophilic interactions. Yellow dashed lines represent secondary M-S interactions. Organic ligands are omitted for clarity.

[M(SR)]$_n$, n = 6, 8, 10, 11 and 12. The complexity and diversity of the species, naturally, grow with the increasing number of units n.

Two compounds with n = 6 are known: [Cu(SePh-2,4,6-(*i*Pr)$_3$)]$_6$[25] and [Au(SPh-2,4,6-(*i*Pr)$_3$)]$_6$. [26] Both compounds are formed by the ligands with the same radical R and they have the same value of n, nevertheless, their structures are different. The structure of [Cu(SePh-2,4,6-(*i*Pr)$_3$)]$_6$ can be seen as distorted antiprism Se_6 and a distorted octahedron Cu_6 embedded into this antiprism. Selenium atoms exhibit both μ_2 and μ_3 bridging modes, as well as copper atoms having 2- and 3-coordinated geometry (**Figure I. 5** (a)). In the [Au(SPh-2,4,6-($_i$Pr)$_3$)]$_6$ all the gold atoms are in quasi-linear coordination and linked through the μ_2-sulfur atoms into 12-membered ring. This cycle forms a hexagon with a chair conformation (**Figure I. 5** (b)).

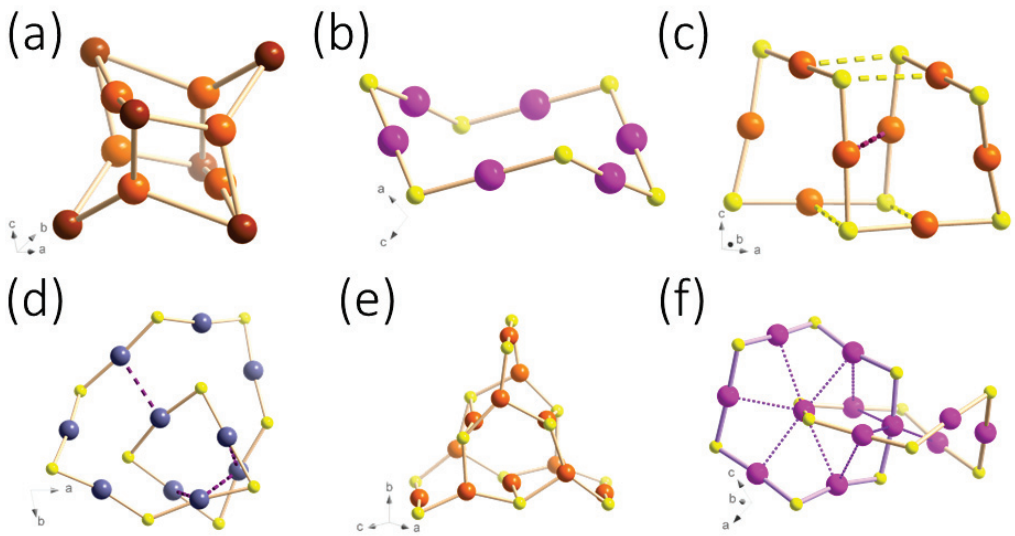

Figure I. 5 The representation of the inorganic subnetworks [MS]$_n$ of the small oligomeric species (n = 6, 8, 10, 12): (a) [Cu(SePh-2,4,6-(*i*Pr)$_3$)]$_6$, [25] (b) [Au(SPh-2,4,6-($_i$Pr)$_3$)]$_6$, [26] (c) [Cu(SPh-2,4,6-(*i*Pr)$_3$)]$_8$, [19] (d) [Ag(SPh-2,4,6-(*i*Pr)$_3$)]$_{10}$, [27] (e) [Cu(*o*-SPhSiMe$_3$)]$_{12}$ [22] and (f) [Au(*o*-SPh*t*Bu)]$_{12}$.[28] Orange, Cu; blue, Ag; yellow, S; brown, Se. Violet dashed lines represent metallophilic interactions. Yellow dashed lines represent secondary M-S interactions. Organic ligands are omitted for clarity.

Unlikely to the previous couple of compounds, the two compounds with n = 8 exhibit the same [MS/Se]$_8$ arrangement. These compounds are formed with the same ligands as the aforementioned compounds with n = 6: [Cu(SPh-2,4,6-(*i*Pr)$_3$)]$_8$,[19] [Ag(SePh-2,4,6-(*i*Pr)$_3$)]$_8$.[29] The [MS/Se]$_8$ core forms a 16-membered cycle of alternating metal and chalcogen atoms folded into U-like shape. It can be also described as a compressed distorted M_8 hexagonal bipyramid embedded into a distorted S/Se_8 rhombohedron (**Figure I. 5** (c)). This fold is held through the

metallophilic and secondary M-S/Se interactions. The optical limiting properties of silver-based compound $[Ag(SePh\text{-}2,4,6\text{-}(iPr)_3)]_8$ were studied. It exhibits a strong optical limiting effect with threshold of 0.2 $J{\cdot}cm^{-2}$, which is about 2.5 times lower than that of C_{60} in toluene under identical experimental conditions.[29]

The silver-based structure with n = 10 $[Ag(SPh\text{-}2,4,6\text{-}(iPr)_3)]_{10}$ [27] is a compactly folded ring held by metallophilic interactions (**Figure I. 5** (d)). Its optical limiting capability has also been evaluated but it was found to be weaker than that of $[Ag(SePh\text{-}2,4,6\text{-}(iPr)_3)]_8$.

The copper-based compound with n = 12, $[Cu(o\text{-}SPhSiMe_3)]_{12}$,[22] has an inorganic core formed by two parallel and staggered Cu_3S_3 rings with trigonal planar CuS_3 sites. The Cu_3S_3 rings are connected through three copper atoms bonded directly to the sulfur atoms of the Cu_3S_3 rings and through three S-Cu-S belts connected to the copper atoms of the Cu_3S_3 rings (**Figure I. 5** (e)).

The gold-based compounds with n = 10, 12 and 11, are known as well. All three, $[Au(p\text{-}SPhtBu)]_{10}$, [28] [Au(S2,3,4,6-tetra-O-acetylglucopyranose)]$_{11}$ [30] and $[Au(o\text{-}SPhtBu)]_{12}$ [28] (**Figure I. 5** (f)) are composed of two catenane rings with [5+5], [5+6] and [6+6] units, respectively. The [Au(S2,3,4,6-tetra-O-acetylglucopyranose)]$_{11}$ showed a weak luminescence in the red part of the spectra at room temperature. [30]

I.1.2. Compounds with 1D Inorganic Subnetwork

Compounds with different 1D inorganic subnetworks have been described. We can put them in few categories: chains and helices, ribbons and columns.

Chains and helices. Following CPs belong to the category: $[Cu(p\text{-}SPhNO_2)]_n$,[31] $[Ag(SPh\text{-}2,4,6\text{-}(iPr)_3)]_n$,[32] $[Ag(SAdamantane)]_n$,[20] $[Ag(SDiamantane)]_n$,[20] $[Ag(SCMeEt_2)]_n$,[33] $[Au_2(L)(LH)Na_2Cs]_n$ [34] (L = $[O_2C\text{-}CH_2\text{-}CH(S)\text{-}CO_2]^{3-}$) and $[Au(SPh)]_n$.[35]

The structure of $[Cu(p\text{-}SPhNO_2)]_n$ [31] is composed of packs of four parallel -Cu-S-Cu- chains, where copper atoms are in the angular geometry (S-Cu-S angle is 114.6(6)°) and sulfur atoms are in μ_2-bridging mode. The chains are held together by metallophilic interactions generating Cu_4 squares with sides of 2.649(4) Å (**Figure I. 6** (a)). In the crystal, these packs of chains are interacting with one another through the hydrogen bonds formed between hydrogen atoms of the benzyl ring and oxygen atoms of the nitro group (C-H⋯O-N) (**Figure I. 6** (f)).

The structure of the [Ag(SPh-2,4,6-(*i*Pr)$_3$)]$_n$ [32] comes also in form of chains. However, in this case, there are only two chains in each pack. The silver atoms are in the distorted linear coordination geometry (average S-Ag-S angle is 171.3(4)°) and sulfur atoms are in μ_2-bridging mode. The chains are connected through the metallophilic contacts (**Figure I. 6** (b)).

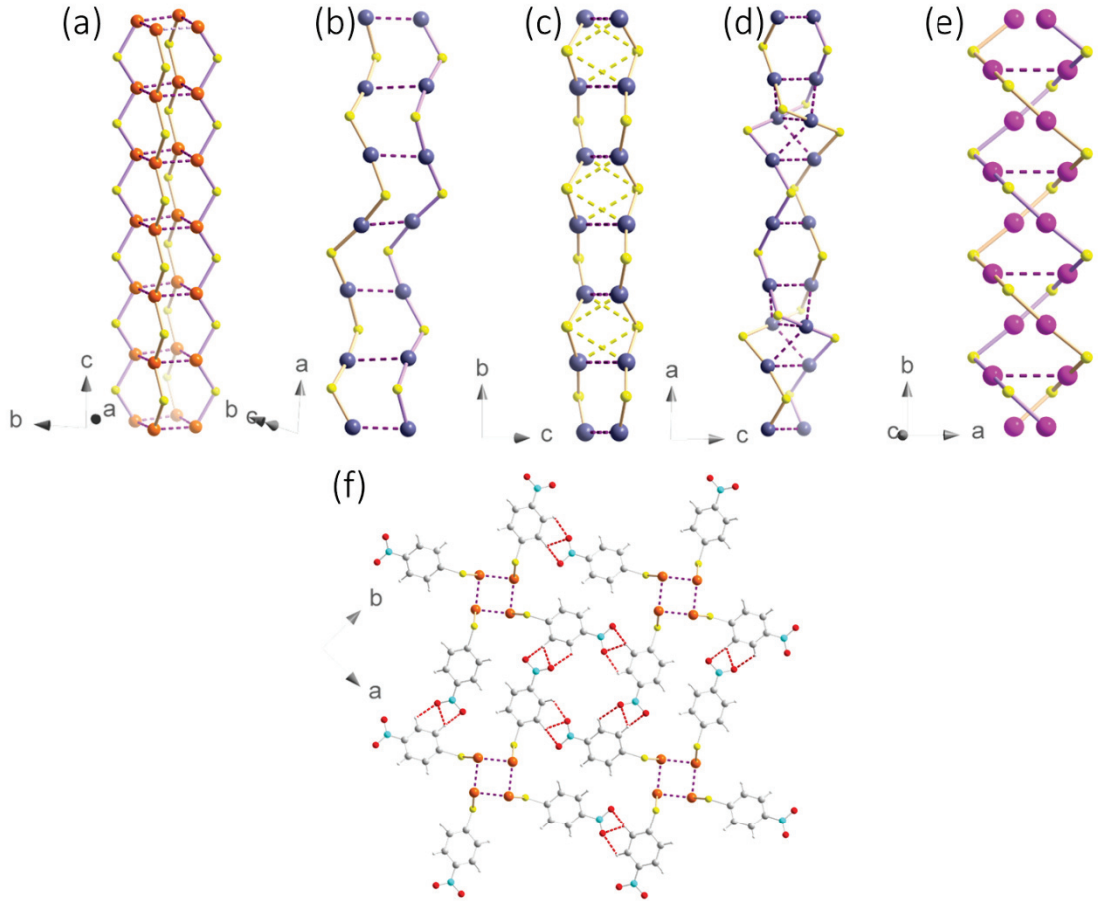

Figure I. 6 The representations of the 1D chain-like inorganic subnetworks [MS]$_n$: (a) [Cu(*p*-SPhNO$_2$)]$_n$, [31] (b) [Ag(SPh-2,4,6-(*i*Pr)$_3$)]$_n$, [32] (c) [Ag(SAdamantane)]$_n$, [20] (d) [Ag(SCMeEt$_2$)]$_n$ [33] and (e) [Au(SPh)]$_n$;[35] (f) the representation of the chains' crystalline package of [Cu(*p*-SPhNO$_2$)]$_n$ formed via hydrogen bonds. Orange, Cu; blue, Ag; pink, Au; yellow, S; red, O; gray, C, sky-blue, N, white, H. Violet and yellow dashed lines represent metallophilic and secondary M-S interactions. Red dashed lines represent hydrogen bonds. Organic ligands are omitted for clarity in the figures (a)-(d).

The structures of the two CPs with diamandoid ligands, [Ag(SAdamantane)]$_n$ and [Ag(SDiamantane)]$_n$, [20] are composed of two zig-zag chains. In the case of the first compound, the chains are held together via metallophilic and secondary Ag-S interactions, while in the case of the second one, they are held only by weak secondary Ag-S interactions (**Figure I. 6** (c)). In the [Ag(SDiamantane)]$_n$, organic groups are located on one side of the [AgS]$_n$ chain, in *cis* configuration, while, in the [Ag(SAdamantane)]$_n$, they are in *trans* configuration. One can

speculate that *trans* configuration 'locks up' two chains together, favoring stronger interactions between them.

The structure of $[Ag(SCMeEt_2)]_n$[33] has some similarities to the previous silver-based compounds. There are two chains formed by silver atoms in the distorted linear coordination geometry (S-Ag-S angles are in the range between 169 and 178°) and sulfur atoms in μ_2-bridging mode. Metallophilic interactions occur between these two chains. Chains are not parallel, but wind around each other form a double helix with a pitch of 8 units (**Figure I. 6** (d)).

The structures of both $[Au_2(L)(LH)Na_2Cs]_n$ [34] and $[Au(SPh)]_n$ [35] are formed by double interpenetrated helices as well. Similarly to the previous helical arrangement, gold atoms are in close-to-linear coordination geometry and sulfur atoms in μ_2-bridging mode. The helix has a pitch of 4 units. The chains are connected through the metallophilic bonds. The helices are slightly squeezed according to one axis perpendicular to the direction of the chain propagation. Thus, there are two types of Au-Au distances – one slightly shorter (and considered to be a metallophilic interaction), and another – slightly longer (not a metallophilic interactions) (**Figure I. 6** (e)). The structure of $[Au(SPh)]_n$ was determined from powder X-ray diffraction data.

The $[Au_2(L)(LH)Na_2Cs]_n$ structure determination was a crucial step towards understanding of the solid state structure of Myochrysine, an artiarthritic drug (the commercial Myochrysine is a mixture of the monosodium $[Au(LH)Na]_n$ and disodium $[Au(L)Na_2]_n$ salts).[36]

The compound $[Au(SPh)]_n$ was synthesized and had its structure solved in our team. [35] Interestingly, it is possible to synthesize it using two different synthetic procedures. The product can be obtained by direct synthesis under hydrothermal conditions. Furthermore, it can be obtained via temperature induced crystallization of an amorphous isomer. The crystalline phase possesses a red luminescence in the solid state at room temperature.[35]

Analogical double helix structure was proposed based on single point energy DFT calculations for $[Au(6\text{-thioguanosine})]_n$, a DNA-based CP. It forms a luminescent micrometer-long fibers, which can be transformed into a wire-like conducting form by oxidative doping and can be integrated into the framework of DNA materials. [37]

Ribbons. In this category we find only one CP – $[Cu(SDiamantane)]_n$.[38] Its structure is formed by copper atoms in both the linear and the trigonal coordination, as well as μ_2- and μ_3-bridging sulfur atoms. They are organized into alternating eight-membered Cu_4S_4 and four-

membered Cu_2S_2 rings (**Figure I. 7**). No metallophilic interaction is observed. The electron transport properties of this compound were studied. $[Cu(SDiamantane)]_n$ has band-like electronic properties and low effective carrier mass with a resistivity of ~300 Ω m. [38]

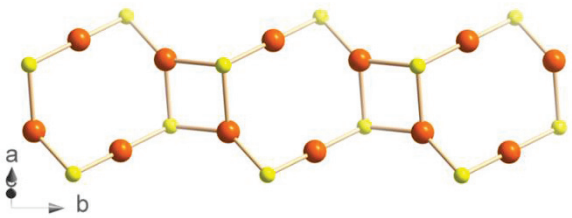

Figure I. 7 The representation of the 1D ribbon-like inorganic subnetwork $[MS]_n$ of $[Cu(SDiamantane)]_n$.[38] Orange, Cu; yellow, S. Organic ligands are omitted for clarity.

Columns. The category of CPs with column-like inorganic subnetworks is the biggest among 1D CPs: $[Cu(SMe)]_n$, [39] $[Cu(SeMe)]_n$, [40] $[Cu(SPh)]_n$, [31] $[Cu(SePh)]_n$, [40] $[Cu(p\text{-}SPhMe)]_n$, [31] $[Cu(p\text{-}SPhOMe)]_n$, [31] $[Cu(SAdamantane)]_n$ [38] and $[Ag(SCy)]_n$. [41]

The majority of the copper-based CPs in this category such as ($[Cu(SMe)]_n$, $[Cu(SeMe)]_n$, $[Cu(SPh)]_n$, $[Cu(SePh)]_n$, $[Cu(p\text{-}SPhMe)]_n$, $[Cu(p\text{-}SPhOMe)]_n$) possess very similar structures. [31,39,40] The inorganic subnetwork is composed of the fused-in six-membered Cu_3S/Se_3 rings forming a tubular column. The five atoms of the ring Cu_2S/Se_3 have a quasi-planar arrangement, whereas the sixth copper atom is pointing out of the plane. The copper atoms are tricoordinated, and sulfur/selenium atoms are in μ_3-bridging mode. While the inorganic subnetwork of $[Cu(SMe)]_n$, $[Cu(SeMe)]_n$, $[Cu(SPh)]_n$ and $[Cu(SePh)]_n$ possess an S_4 symmetry along the *c* axis (**Figure I. 8** (a)), the subnetworks of the substituted CPs, $[Cu(p\text{-}SPhMe)]_n$, $[Cu(p\text{-}SPhOMe)]_n$, are slightly squeezed (**Figure I. 8** (b)), probably due to the presence of the –Me and –OMe groups in the *para*- position. It is worth noting, that the inorganic core of these structures is also very similar to the one of $[Cu(p\text{-}SPhNO_2)]_n$. The difference might arise as a result of constraints imposed by the (C-H⋯O-N) hydrogen bonds. Note that the structures of these copper-based CPs were determined from powder X-ray diffraction data.

The CPs $[Cu(SPh)]_n$, $[Cu(p\text{-}SPhMe)]_n$ and $[Cu(p\text{-}SPhOMe)]_n$ were used for the fabrication of FETs (Field Effect Transistors) and exhibit a p-type charge mobility. Their charge mobility (μ) values range from 10^{-2} to 10^{-3} cm^2 V^{-1} s^{-1}, while for $[Cu(p\text{-}SPhNO_2)]_n$ the charge mobility was

rather low ($\mu < 10^{-6}$ cm^2 V^{-1} s^{-1}). This finding underlines importance of the inorganic core arrangement for the physical properties of the resulting CP. [31]

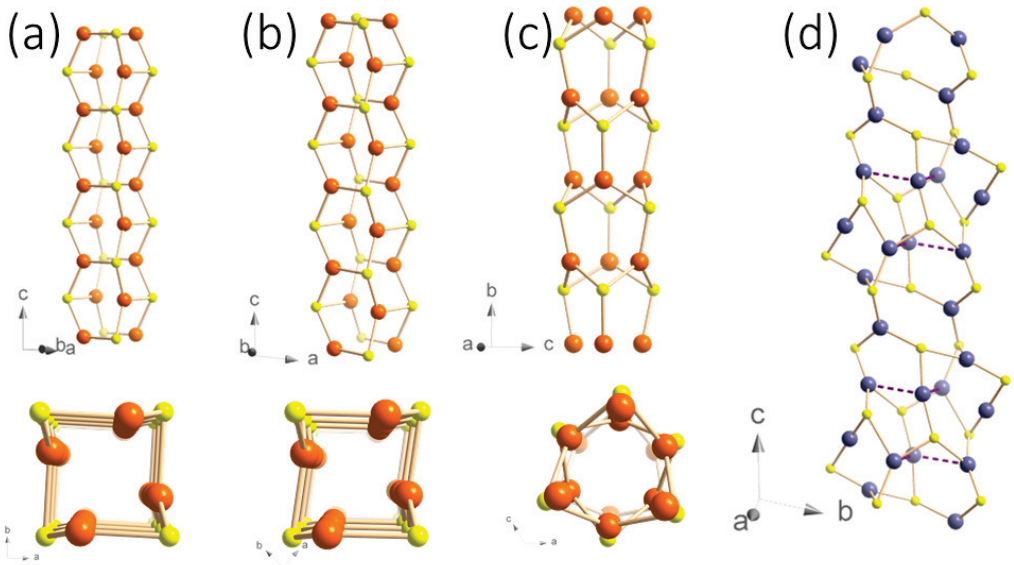

Figure I. 8 The representations of the 1D column-like inorganic subnetworks $[MS]_n$: (a) $[Cu(SMe)]_n$, [39] (b) $[Cu(p\text{-}SPhMe)]_n$, [31] (c) $[Cu(SAdamantane)]_n$ [38] and (d) $[Ag(SCy)]_n$. [41] Orange, Cu; blue, Ag; yellow, S. Violet dashed lines represent metallophilic interactions. Organic ligands are omitted for clarity.

The CP $[Cu(SePh)]_n$ has shown hole mobility of $4{\cdot}10^{-2}$ cm^2 V^{-1} s^{-1}. It is reported to possess a red luminescence at 77 K (similarly to its thiolate-based counterpart $[Cu(SPh)]_n$).[40]

For $[Cu(SMe)]_n$, an optimized, synthetic procedure was reported. The hole mobility of the material synthesized according to the new procedure was as high as 2 cm^2 V^{-1} s^{-1}. [42]

The inorganic $[CuS]_n$ core of $[Cu(SAdamantane)]_n$ [38] is composed of six-membered Cu_3S_3 rings. The sulfur atoms point out of the plane, while the other five atoms (Cu_3S_2) have a quasi-planar arrangement. The copper atoms are tricoordinated, and sulfur atoms are in μ_3-bridging mode. In this compound, Cu_3S_3 rings are fused together differently to previously mentioned similar CPs. The resulting column possesses an S_3 symmetry along the *b* axis (**Figure I. 8** (c)). This compound has band-like electronic properties and low effective carrier mass with a resistivity of ~100 Ω m. The Cu(II) doping of this compound was tested as well. It was reached through the oxidation of the CP with H_2O_2. It decreased the resistivity by three orders of magnitude. Enhanced electron conductivity originates from the created holes moving in the

monodimensional $[CuS]_n$ core. This shows a potential of copper-thiolate CPs as charge carriers.[38]

The inorganic core of $[Ag(SCy)]_n$ [41] is more complex. It is composed of the fused rings, where some silver atoms are in linear coordination geometry, and others – in trigonal. Metallophilic interactions are observed between certain silver atoms (**Figure I. 8** (d)).

I.1.3. Compounds with 2D Inorganic Subnetwork

While lamellar thiolate compounds were widely studied as solids for luminescent properties, [43 44] the crystallographic structures of 2D inorganic subnetworks are the most rarely represented in the literature. Indeed, it is more difficult to obtain highly crystalline powders of 2D compounds than of 1D, what prevents their successful structure determination. Only five structures of this type have been reported prior to this work: $[Cu(p\text{-}SPhOH)]_n$,[45] $[Cu(SC_2H_4OH)]_n$,[46] $[Cu(SC_2H_4OC_2H_4OH)]_n$, [46] $[Ag(SePh)]_n$ [47] and $[Au(p\text{-}SPhCO_2Me)]_n$.[48]

In the case of the copper-based CPs, all three of them, $[Cu(p\text{-}SPhOH)]_n$, $[Cu(SC_2H_4OH)]_n$ and $[Cu(SC_2H_4OC_2H_4OH)]_n$, possess quasi-identical $[CuS]_n$ network. The 2D network is formed by six-membered Cu_3S_3 rings (similar to Cu_3S_3 rings of $[Cu(SMe)]_n$ and other 1D copper-based columns-like CPs). The five atoms Cu_2S_3 of the ring have a quasi-planar arrangement, and the sixth copper atom is pointing out of the plane. These rings are fused into two-dimensional network. The organic groups are located above and below of the $[CuS]_n$ layer.

In the case of **$[Cu(p\text{-}SPhOH)]_n$**, the aromatic cycles interact through weak π-π interactions. The interlayer non-bond O-O distances point to presence of weak cooperative O-H-O hydrogen bonds. The catemer hydrogen bonds form a zig-zag array sewing together neighboring layers (**Figure I. 9** (a)-(c)). [45]

Both $[Cu(p\text{-}SPhOMe)]_n$ and $[Cu(p\text{-}SPhOH)]_n$ have their inorganic networks formed by Cu_3S_3 rings. Nevertheless, one has a 1D inorganic network and another – a 2D network. It underlines the importance of the weak interactions (hydrogen bonds, in this case) for the final structure assembly of CPs.

A four-point probe electrical conductivity measurement on a $[Cu(p\text{-}SPhOH)]_n$ pellet gave a value of a bulk electrical conductivity value of 120 $S{\cdot}cm^{-1}$. [45]

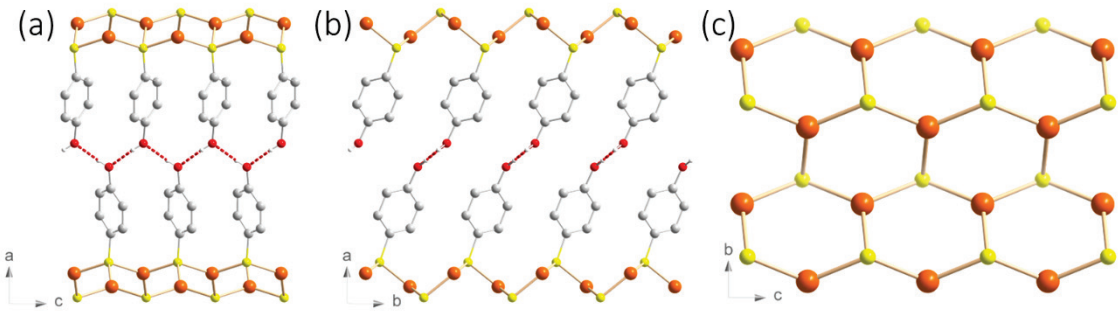

Figure I. 9 The representations of the 2D structure of $[Cu(p\text{-}SPhOH)]_n$,: [47] (a) projection on (*ac*) and (b) (*ab*) planes; (c) representation of the inorganic sheet on (*bc*) plane. Orange, Cu; yellow, S; red, O; gray, C; white, H. Red dashed lines represent hydrogen bonds. Non-acidic hydrogen atoms are omitted for clarity.

The structure of $[Cu(p\text{-}SPhOH)]_n$ was determined using powder X-ray diffraction data. The same article [45] reported yet another copper-based compound, $[Cu(p\text{-}SPhCO_2H)]_n$. Similarly to previous case, it was thought to form an infinite covalent $[CuS]_n$ 2D network. The significant preferred orientation of its X-ray diffraction pattern strongly suggested a layered structure. Unfortunately, a structural determination using powder XRD data was not successful. [45]

In the **$[Ag(SePh)]_n$** the layers are formed by silver atoms in distorted tetrahedral coordination connected through μ_4-selenium atoms. The Ag-Ag contacts between neighboring atoms form a hexagonal net. The organic groups are located above and below the $[AgS]_n$ layer without interpenetration (**Figure I. 10** (a), (b)). [47]

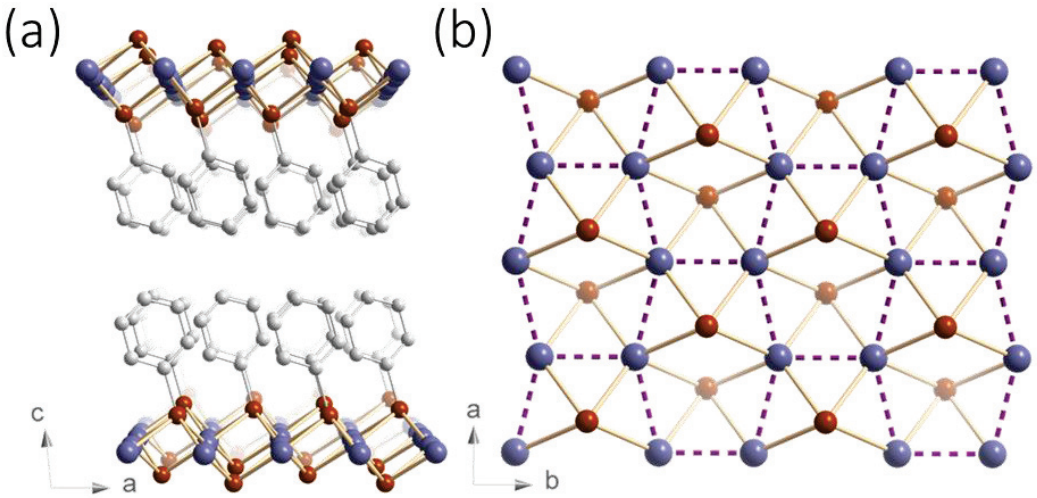

Figure I. 10 The representation of the 2D structure of $[Ag(SePh)]_n$: [47] (a) central projection on (*ac*) and (b) representation of the inorganic sheet on (*ab*) plane. Blue, Ag; brown, Se; gray, C. Violet dashed lines represent metallophilic interactions. Hydrogen atoms are omitted for clarity.

This compound emits blue light at the room temperature under UV-irradiation, with emission peak maximum at 467 nm. The morphology of the crystallites of this compound formed under different synthetic conditions, as well as original way of its synthesis (via tarnishing of silver metal in presence of benzene dichalcogenide), was studied by J. Nathan Hohman.[49,50]

The **[Au(*p*-SPhCO$_2$Me)]$_n$** [48] was synthesized, characterized and studied by our team. The structure was determined from powder X-ray diffraction data. It is formed by 1D -Au-S-Au- chains, where gold atoms are in quasilinear geometry and are connected through μ_2-sulfur atoms forming a zig-zag arrangement. The metallophilic interactions connect the neighboring chains into a planar 2D network (**Figure I. 11** (a), (b)). Despite the fact that the gold thiolate forms strictly 1D chain, this compound is classified in the 2D solids because it is characterized from PXRD as a layered compound. This compound is highly emissive at the room temperature with a quantum yield around 70 % (bright orange emission).

Similar structural model was proposed for pseudomorphic [Au(S(CH$_2$)$_2$CO$_2$H)]$_n$ phases (**Figure I. 11** (c)). [51]

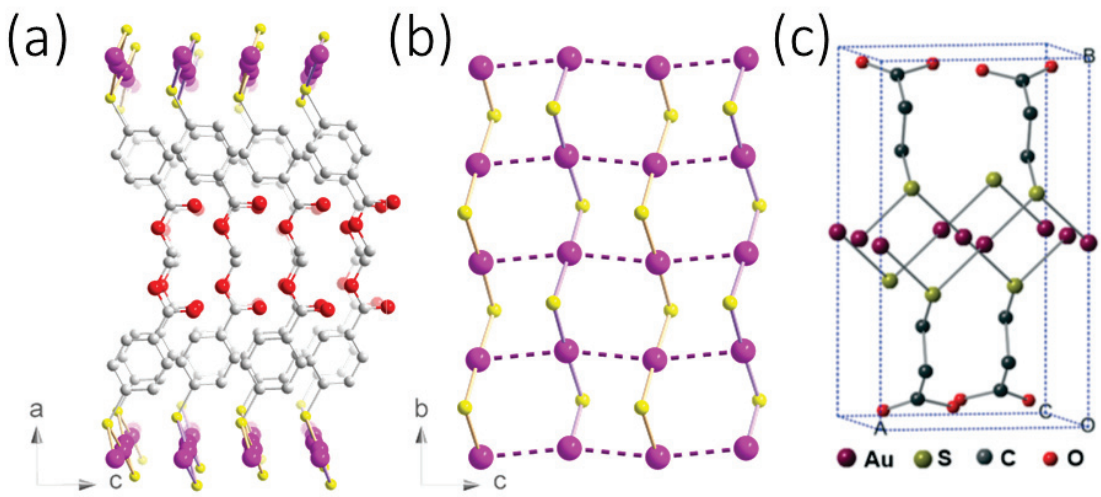

Figure I. 11 The representations of the 2D structure of [Au(*p*-SPhCO$_2$Me)]$_n$: [48] (a) central projection on (*ac*) and (b) representation of the inorganic sheet on (*bc*) plane. Pink, Au; yellow, S; red, O; gray, C. Violet dashed lines represent metallophilic interactions. Hydrogen atoms are omitted for clarity. (c) A schematic illustration of packing modes of the [Au(S(CH$_2$)$_2$CO$_2$H)]$_n$ prepared in water. [51] Adapted with permission from ref. [48,51] Copyright 2016 & 2018 Royal Society of Chemistry.

I.1.4. Other Structural Models

There is a great number of articles reporting $[M(SR)]_n$ CPs without complete structure elucidation. Probably, the most numerous of them are lamellar CPs such as silver alkanethiolates[52,53,54,55], mixed gold-silver alkanethiolates[56], gold alkanethiolates [43,44,57,58] and gold 3-mercaptopropinoates $[Au(S(CH_2)_2CO_2H)]_n$.[59,60] For the gold-based compounds luminescence properties are often reported.

A remarkable study was performed by **I. G. Dance** *et al*. on a family of layered $[Ag(SR)]_n$ CPs with primary alkane thiolates and arenethiolates being used as ligands. Despite the fact that, synthesis has not yielded crystals suitable for single crystal structure determination, the rigorous powder X-ray diffraction pattern analysis (without full structural resolution) revealed the main features of their two-dimensional structure. A following structural model has been proposed for **$[Ag(SPh)]_n$**. [61] $[Ag(SPh)]_n$ is formed with a quasi-hexagonal network with trigonal-planar coordination of silver bridged by three sulfur atoms, which in their turn are coordinated by three silver atoms. In this network, the silver atoms are in a central plane, the sulfur atoms – in the planes on either side, and the organic groups extend perpendicularly to the slab on both sides (**Figure I. 12** (a), (b)).[61]

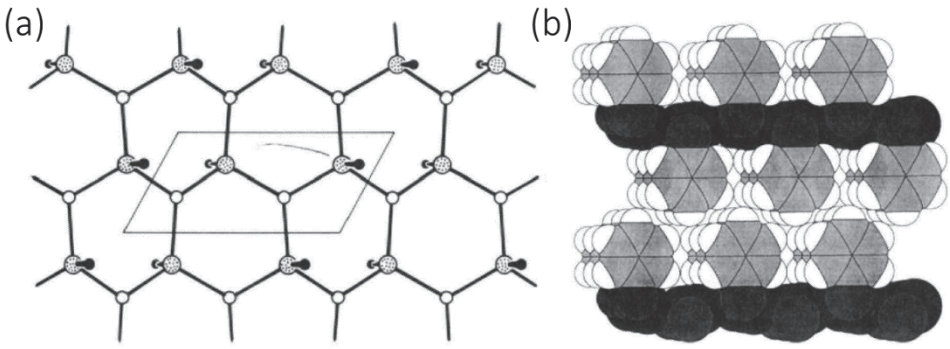

Figure I. 12 The representations of the 2D structure of $[Ag(SPh)]_n$. [61] (a) Quasi-hexagonal network proposed for the central slab of $[Ag(SPh)]_n$. White circles, Ag; dotted circles, S; filled circles, substituents. The view direction is off-normal. The two-dimensional unit cell is outlined. (b) Space-filling view normal to the layers of $[Ag(SPh)]_n$, showing the interpenetration of the rings from adjacent layers. Atom shading is increasing with atomic number. Reprinted with permission from [61]. Copyright 1991 American Chemical Society.

There are proposed models based on the theoretical investigations. For example, recently Massote and Mazzoni have applied first-principles calculations to investigate the electronic and structural properties of $[Ag(SPh)]_n$. [62] The study lead to the model similar to the one proposed

by I. G. Dance, with a small distinctions like inclination of the phenyl groups (24.2° from a vertical line, unlike the model of I. G. Dance where those are perpendicular to the $[AgS]_n$ layer) (**Figure I. 13** (a), (b)). The mono- and multilayers of $[Ag(SPh)]_n$ are expected to possess attractive properties from the point of view of applied physics, such as direct band gap in the range from 2.0 to 3.0 eV, thus the possible modulation and occurrence of a controlled semiconductor-metal transition.

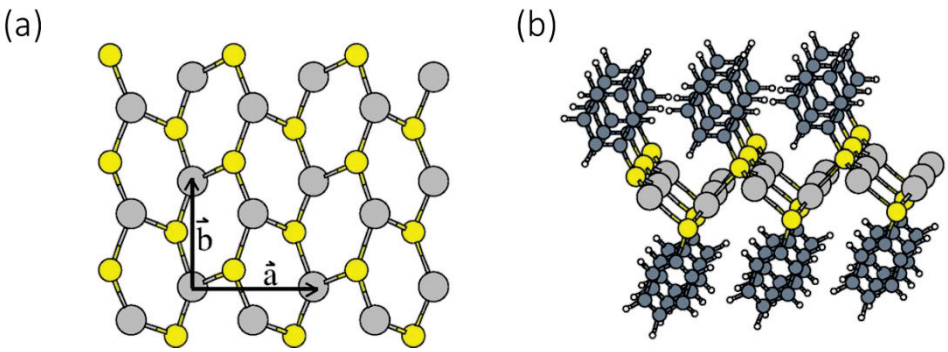

Figure I. 13 The representations of the 2D structure of $[Ag(SPh)]_n$: [62] (a) top (carbon and hydrogen atoms omitted for clarity) and (b) side views. Light gray, Ag; yellow, S; dark gray, C, white, H. Reprinted with permission from ref. [62] Copyright 2017 AIP Publishing.

Another interesting model was proposed for 1D copper-based CPs. [63] It is based on the results of molecular dynamic (MD) simulations and first-principle density functional theory (DFT). It was performed for $[Cu(p\text{-}SPhNH_2)]_n$ and $[Cu(3,5\text{-}SPhMe_2)]_n$ CPs. The MD simulations confirmed that low-energy core–shell nanowires readily form and are composed of copper–sulfur inorganic cores encapsulated within organic shells provided by ligand assembly (**Figure I. 14** (a)). The DFT-relaxed $[Cu(p\text{-}SPhNH_2)]_n$ nanowire structures revealed an atomically precise core–shell arrangement (**Figure I. 14** (b)). Within the inorganic core, five copper or sulfur atoms compose each cross section (**Figure I. 14** (c)). Each copper atom is connected to the three sulfur atoms, and each sulfur bonds to three copper atoms. Therefore, it is similar to the structure of $[Cu(SAdamantane)]_n$.[38] The proposed model is in agreement with the experimentally observed morphology from SEM, major PXRD features and atomically resolved TEM imaging. The solid nanowire cores were further found to be electrically conductive, with an estimated ∼120 Ω·m resistivity for aligned chains. It is more conductive than intrinsic silicon, even though, the nanowire cores are less than 6 Å in diameter. [63]

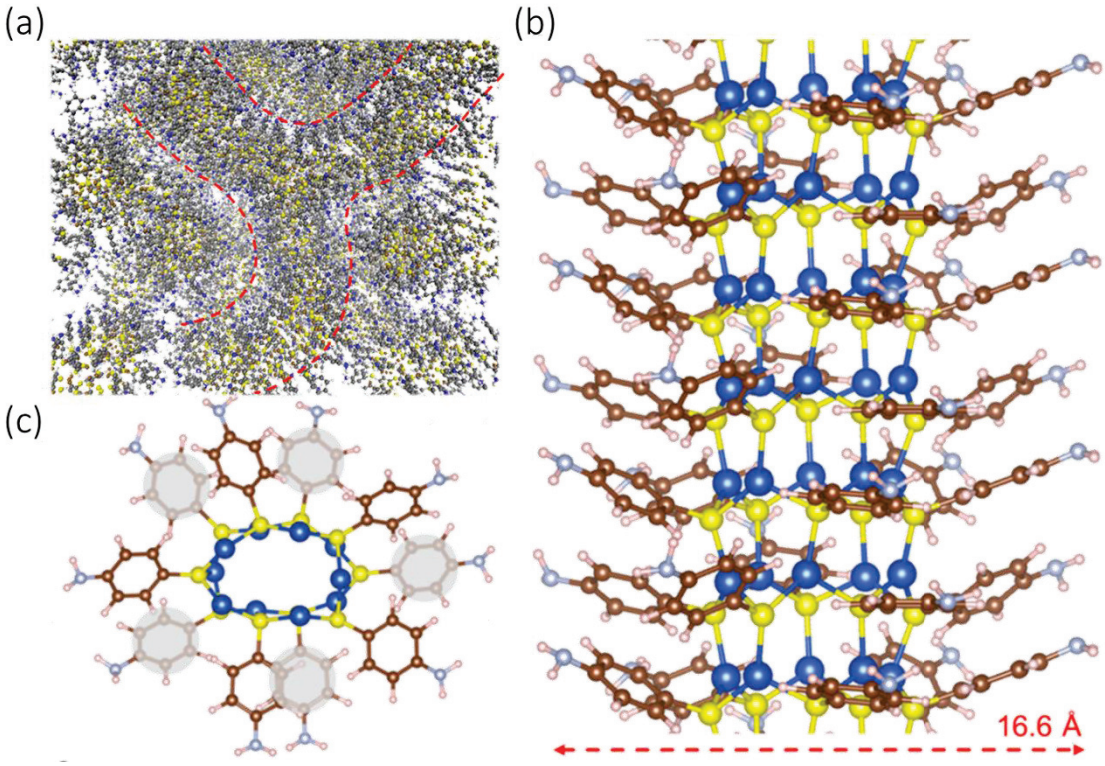

Figure I. 14 The representations of the 1D structure of $[Cu(p\text{-}SPhNH_2)]_n$.[63] (a) Metal–organic core–shell nanowires revealed by MD simulations. (b) Atomically precise core–shell nanowire structure elucidated by DFT computations and (c) its top-down view. Blue, Cu; yellow, S; brown, C; light blue, N; white: H. Adapted with permission from ref. [63] Copyright 2018 American Chemical Society.

I.1.5. Structural Trends

Despite the lack of systematic structural studies, more and more examples of CPs based on chalcogenolates of coinage metals are appearing in the literature. These materials start forming their own class and recently even gained a name, in analogy with MOFs, - Metal Organic Chalcogen[ides/olates][c,64, 65] for MOCHAs [49] or MOCs. [38]

Based on the discussed structures, we can draw some conclusions concerning the influence of different factors on resulting coordination compounds. Further in the thesis we will observe whether they are getting confirmed or not.

The **steric hindrance** is a factor having, probably, the most obvious influence. Its action is quite intuitive and has been observed before in other coordination compounds: [66] more

[c] While the term 'chalcogenides' was used in the article; it seems more reasonable to use the term 'chalcogenolates' in appliance with IUPAC recommendations.

sterically hindered the ligand is, the more difficult the formation of the condensed $[MS]_n$ arrangement is. The use of the sterically hindered ligands leads both to the decrease of the dimensionality of the network and decrease of the number of units, n, in oligomeric compounds (see **Table I. 1**).

There are two important facts to underline in the **Table I. 1**. Firstly, while the introduction of the substituent the *para*-position on the thiophenol usually leads to the decrease of the dimensionality from 1 to 0 in the case of $[Au(SPh)]_n$ and $[Au(p\text{-}SPh\mathit{t}Bu)]_{10}$, it is not always the case. For example, introduction of the substituent in *para*-position in the case of $[Cu(SPh)]_n$ does not decrease the dimensionality. $[Cu(SPh)]_n$, $[Cu(p\text{-}SPhMe)]_n$ and $[Cu(p\text{-}SPhOMe)]_n$ have similar 1D structures, however, they are lower in symmetry in substituted CPs. In the case of $[Cu(p\text{-}SPhOH)]_n$ dimensionality is increased to 2D. The formation of the 2D network is favored, probably, due to the presence of catemeric hydrogen bonds. Despite the absence of the hydrogen bonds, *para*-substituent in the $[Au(p\text{-}SPhCO_2Me)]_n$ favors 2D structure as well.

Table I. 1 Change of the dimensionality, D, and number of units, n, in coordination compounds upon the introduction of the steric hindrance.

Metal	Steric hindrance growth →			
Cu	$[Cu(SPh)]_n$ [31] 1D, n = ∞	$[Cu(o\text{-}SPhSiMe_3)]_{12}$ [22] 0D, n = 12	$[Cu(SPh\text{-}2,6\text{-}(SiMe_3)_2)]_4$ [18] 0D, n = 4	$[Cu(SPh\text{-}2,6\text{-}(Mes)_2)]_3$ [14] 0D, n = 3
Ag	[Ag(SPh)] [61] 2D, n = ∞	$[Ag(SCy)]_n$ [41] 1D, n = ∞	$\{[Ag(o\text{-}SPhSiMe_3)]_4\}_2$ [22] 0D, n = 4×2	
Au	$[Au(SPh)]_n$ [35] 1D, n = ∞	$[Au(o\text{-}SPh\mathit{t}Bu)]_{12}$ [28] 0D, n = 12 $[Au(p\text{-}SPh\mathit{t}Bu)]_{10}$ [28] 0D, n = 10		

Secondly, it is necessary to mention the comparison of $[Ag(SPh)]_n$ and $[Ag(SCy)]_n$. One could argue that bulkiness difference induced by the absence of aromaticity (loss of planarity of the cycle) is too small to induce the structural change. This is a reasonable argument. We can speculate that formation of the layered slabs is easier thanks to the π-π or C-H⋯ π interactions between thiophenol groups. This example points to another important structure formation factor – **weak interactions**.[67]

Another demonstration of importance of the weak interactions is a case of [Cu(*p*-SPhNO$_2$)]$_n$. The introduction of the substituents like –OMe or –Me does not change an inorganic backbone of [Cu(SPh)]$_n$ substantially. However, the –NO$_2$ group forms hydrogen bonds with hydrogen atoms of the benzyl cycle and causes a major change to the [CuS]$_n$ backbone from the column-like to the chain-like arrangement (**Figure I. 6** (a), (f)).

The question of the **nature of metal and chalcogen atom**s is an obscure one. When a number of compounds [M(ER)]$_n$ (M = Cu, Ag, Au; E = S, Se) formed with the same R = Ph-2,4,6-(*i*Pr)$_3$ are compared (**Table I. 2**), one can notice that every time the nature of the metal or chalcogen is changed, the [ME]$_n$ arrangement is changed as well. The only array that occurs more than once is U-like cycle for [Cu(SPh-2,4,6-(*i*Pr)$_3$)]$_8$ and [Ag(SePh-2,4,6-(*i*Pr)$_3$)]$_8$.

Table I. 2 Comparison of the influence of the nature of the metal and the chalcogen atoms on the formed structure, case of [M(EPh-2,4,6-(*i*Pr)$_3$)]$_n$ (M = Cu, Ag, Au, E = S, Se).

Metal	Ligand = (SPh-2,4,6-(*i*Pr)$_3$)	Ligand = (SePh-2,4,6-(*i*Pr)$_3$)
Cu	[Cu(SPh-2,4,6-(iPr)$_3$)]$_8$ [19] U-like cycle	[Cu(SePh-2,4,6-(iPr)$_3$)]$_6$ [25] Distorted Cu$_6$ octahedron embedded into Se$_6$ antiprism
Ag	[Ag(SPh-2,4,6-(iPr)$_3$)]$_{10}$ [27] Compactly folded ring hold by metallophilic interactions	[Ag(SePh-2,4,6-(iPr)$_3$)]$_8$ [29] U-like cycle
	[Ag(SPh-2,4,6-(iPr)$_3$)]$_n$ [32] Two chains interacting through the metallophilic contacts	
Au	[Au(SPh-2,4,6-(iPr)$_3$)]$_6$ [26] Cycle in a chair conformation	

Once the analysis is extended to the compounds with other ligands (**Table I. 3**), it is clear that the change of the nature of the metal or chalcogen does not always provoke a change of the [ME]$_n$ arrangement. Thus, it seems impossible to attribute the role of nature of the metal or chalcogen in the structure formation unambiguously. The empirical observations of the metal's impact rely mainly on the common coordination geometry adopted by metal atoms:

- Gold atoms adopt linear or angular planar trigonal coordination which result in chains (infinite or locked cycles) and helices; however, the coordination number of 3 has not been yet observed for pure gold thiolate compounds.
- Silver atoms adopt different coordination numbers – 2, 3 or even 4; therefore condensed arrays are possible, *e. g.*, columns, 2D layers.
- Copper atoms adopt coordination number 2 and 3; thus, similarly to silver, condensed arrays are possible, *e. g.*, columns, ribbons, 2D layers. Moreover, copper shows strong 'preference' to form Cu_3S/Se_3 hexagons; which were observed in 0D, 1D and 2D CPs and are encountered in the literature in heteroleptic thiolate coordination compounds. [68]

The examples of $[Ag(SPh\text{-}2,4,6\text{-}(iPr)_3)]_{10}$ [27] and $[Ag(SPh\text{-}2,4,6\text{-}(iPr)_3)]_n$,[32] amorphous and crystalline phase of $[Au(SPh)]_n$, [35] and studies of $[Au(S(CH_2)_2CO_2H)]_n$[51] show that polymorphism is possible depending on synthetic procedure.

Finally, the structure formation is a **result of complex interplay between the different driving forces** of assembly – metal-chalcogen coordination, metal-metal interactions, secondary metal-chalcogen interactions, hydrogen, C-H⋯π and π-π bonding, which govern the assembly according to the steric accessibility and synthetic procedure. [51]

For more in-depth discussion upon aforementioned structures, the following article shall be consulted:

O. Veselska, A. Demessence. d^{10} coinage metal organic chalcogenolates: From oligomers to coordination polymers. *Coord. Chem. Rev.* 2018, **355**, 240-270.

Table I. 3 Comparison of the influence of the nature of metal and chalcogen atoms on the formed structure.

	Same arrays	Different arrays
Metal's nature		**$[Cu(SAdamantane)]_n$[38] vs. $[Ag(SAdamantane)]_n$[20]** 1D-columns vs. 1D-chains **$[Cu(SDiamantane)]_n$[38] vs. $[Ag(SDiamantane)]_n$[20]** 1D-ribbons vs. 1D-chains **$[Cu(SPh)]_n$[31] vs. $[Ag(SPh)]_n$[61] vs. $[Au(SPh)]_n$[35]** 1D-columns vs. 2D-layers vs. 1D-helices **$[Cu(SePh)]_n$[40] vs.$[Ag(SePh)]_n$[47]** 1D-columns vs. 2D-layers
Chalcogen's nature	**$[Ag(SPh)]_n$,[61] and $[Ag(SePh)]_n$[47]** 2D-layers **$[Cu(SPh)]_n$[31] and $[Cu(SePh)]_n$[40]** 1D-columns **$[Cu(SMe)]_n$[39] and $[Cu(SeMe)]_n$[40]** 1D-columns **$[Ag(SC(SiMe_3)_3)]_4$[16] and $[Ag(SeC(SiMe_3)_3)]_4$[21]** Quasi-planar cycles **$[Cu(SPh\text{-}2,6\text{-}(Mes)_2)]_3$[14] and $[Cu(SePh\text{-}2,6\text{-}(Mes)_2)]_3$[14]** Distorted triangles	**$[Au(SC(SiMe_3)_3)]_4$[24] vs. $[Au(TeC(SiMe_3)_3)]_4$[23]** Quasi-planar cycles vs. V-like cycles

I.1.6. Amorphous Coordination Polymers

Working with compounds which are difficult to crystallize, one can encounter the extreme case of 'poor crystallinity' or amorphous phases.

Amorphous solid is a solid that lacks long-range order, in other words, it shows no lattice periodicity characteristic to a crystalline solid. Purely amorphous inorganic or organic solids are well known and widely used by human in daily life (*e. g.* glasses and plastics). Meanwhile, examples of amorphous CPs (*a*CPs) stay rather underreported and scarce. One of the factor limiting their study for a long time was a lack of means for structural characterization. However, the recent technical advancements and understanding of the fact that defects and amorphous state can expand the functionality of CPs [69] gave a rise to the interest towards disordered systems.

A number of amorphous MOFs, ZIFs (Zeolitic Imidazolate Frameworks) and nonporous CPs have been reported since the beginning of 2000s.[70] While their characterization still represents a challenge, the work of teams of T. D. Bennett and S. Horike is particularly notable and deserves attention due to their rigorous structural studies linked to their properties.

In this work we look to seize upon the assumed weakness of $[Au(SR)]_n$ CPs, such as the difficulty of crystallization process, and turn it into an advantage. It gives us access to the easy and direct synthesis of amorphous products. While amorphous $[Au(SR)]_n$ products have been reported before,[35,71] and even some structural studies were performed,[72] no systematic insight into 'structure-properties' correlation was gained.

I.2. Synthetic and Instrumental Approaches

I.2.1. Synthesis

There are some practical issues to be addressed considering the synthesis of $[M(SR)]_n$ CPs. While synthesis of oligomeric species with sterically hindered ligands allows obtaining soluble compounds that can be recrystallized, it is not the case for the CPs with 1D or 2D inorganic backbone.

As it has been demonstrated, synthesis of polymeric species (with sterically non-hindering ligands) at room temperature leads to the formation of copper- and silver-based products of worst crystallinity, and even of gold-based amorphous products. [71] Successful synthesis of highly crystalline samples and even single crystals of polymeric networks has been reported by C.-M. Che *et al*. (under reflux) [31,40,45] and H. Yan *et al.* (biphasic reactions at 80°C). [20,38] These reports, as well as the experience of our team (synthesis of highly crystalline $[Au(SR)]_n$ CPs under hydrothermal conditions [35]) have inclined us to choose a *solvo(hydro)thermal synthesis* as a default option in our work.

Hydro(solvo)thermal synthesis has proven to be one of the most efficient ways for production of various CPs. Initially, this method was developed for synthesis of zeolites, but then it was adapted to synthesis of MOFs and extended to other groups of CPs. [7,73]

It is important to adjust synthetic conditions, including the choice of reagents, temperature and pressure, concentration, time of reaction, pH, solubility, etc. The optimization of the synthetic conditions was done for every CP in this work.

In our work on $[Cu(SR)]_n$ – $Cu^{II}Cl_2$, $Cu^{II}(NO_3)_2$ and $Cu^{II}(CH_3CO_2)_2$ were used as precursors. Therefore, the net reaction includes two steps – redox reaction of thiol molecules and Cu^{II} atoms, followed by complexation of the thiol by Cu^{I} atoms:

Redox reaction: $2Cu^{II} + 2HSR \rightarrow 2Cu^{I} + (SR)_2 + 2H^+$

Coordination reaction: $Cu^{I} + HSR \rightarrow [Cu^{I}(SR)] + H^+$

Net reaction: $Cu^{II}X_2 + 2HSR \rightarrow [Cu^{I}(SR)]_n + \frac{1}{2}(SR)_2 + 2HX, \;\; X = Cl^-, NO_3^-, CH_3CO_2^-$

In the case of $[Ag(SR)]_n$, $Ag^{I}NO_3$ was used; thus only coordination reaction occurs:

$$Ag^{I}NO_3 + HSR \rightarrow [Ag^{I}(SR)]_n + HNO_3$$

In the case of $[Au(SR)]_n$, $HAuCl_4$ was used. Therefore, the net reaction includes two steps (similarly to the case of copper CPs):

Redox reaction: $Au^{III} + 2HSR \rightarrow Au^{I} + (SR)_2 + 2H^+$

Coordination reaction: $Au^{I} + HSR \rightarrow [Au^{I}(SR)] + H^+$

Net reaction: $HAu^{III}Cl_4 + 3HSR \rightarrow [Au^{I}(SR)]_n + (SR)_2 + 4HCl$

This approach was turned out to be very efficient in our work with Cu(I)-based compounds (some single crystals were obtained). In the case of Ag(I)- and Au(I)-CPs syntheses no single crystals were obtained, though, the powder samples of high crystallinity were isolated.

For the synthesis of amorphous phases two approaches have been reported. They include direct preparation and amorphization of the crystalline networks by pressure, ball milling, heating or electrical discharge. [70] In our work, we took advantage of the ability of $[Au(SR)]_n$ to rapidly precipitate and to form poorly crystalline solids – the direct synthesis was applied.

I.2.2. Crystalline Structure Determination from Powder X-ray Diffraction Data

The impossibility of synthesis of single crystals for some of the products precludes structural studies for many compounds. In such cases, the crystalline structure determination from powder X-ray diffraction data can help. [74,75]

A powder X-ray diffraction pattern is a collapsed projection of the Bragg reflections from 3D space into one dimension. Unit cell dimensions, space group and reflection intensities are less straightforward to determine due to the reflection overlap. Structural determination from powder X-ray diffraction data can be really complicated and might often require additional information provided by supplementary analysis, such as TGA, IR, elementary analysis and density measurements.

The following list represents the generalized plan of the structure determination procedure used for CPs studied in this work (**Figure I. 15**):

1. Acquisition of high-resolution data. With high resolution, problems arising from peak overlap can be alleviated to some extent. In order to achieve this, synchrotron radiation with its high flux, excellent vertical collimation and monochromaticity is helpful, particularly at the stage of the powder diffraction pattern indexing. In our work, with few exceptions, the data were collected at Soleil (CRISTAL beamline) or ESRF (ID15A beamline).
2. Accurate determination of peak positions and their intensities.
3. Indexing step, when an unknown unit cell is determined and the *hkl* indices of each reflection are assigned. For this, the Least Square Indexing (LSI) algorithm of

Topas software [76] was used. The credibility of searched cells can be evaluated with goodness-of-fit (Gof) parameter (the higher is value of Gof, the higher is the chance that correct cell was successfully found).

$$Gof = \frac{M_N}{N_{impurity}+1} \quad \text{(Eq. I.1)}$$

$$M_N = \frac{Q_N}{2\langle \Delta Q \rangle N_{poss}} \quad \text{(Eq. I.2)}$$

Where $N_{impurity}$ is a number of unexplained lines with a given cell, Q_N is a Q value ($1/d^2$) of Nth observed line (peak); N_{poss} is a number of theoretically possible lines until Nth observed line; $\langle \Delta Q \rangle$ is an average deviation between Q_{obs} and Q_{calc}.

4. Pattern matching – fit of the experimental diagram without structural hypothesis, using the crystallographic unit cell, space group and profile parameters only.
5. Charge Flipping (reciprocal space method). Once the cell is determined, the charge flipping method is used to position heaviest (metal) atoms. This method has proven itself to be an efficient way to place sulfur atoms as well. The positioning of lighter atoms of the organic molecule (carbon and oxygen) might be possible depending on the nature of metal of a given CP. It can work in the case of copper- or even silver-based CPs. However, in the presence of such a dominant scatterer as gold atom it was largely unsuccessful.
6. Simulated Annealing (direct space method). If the metal atoms were properly positioned at the previous stage, in this stage they are fixed. Organic moieties are added considered as rigid bodies. A ligand is randomly positioned, a trial structure is generated by variation of involved parameters (translation and orientation of the organic molecule). The diffraction pattern is calculated and compared to the measured one. The trial model is accepted or rejected, and then the loop is repeated until the moment the optimized parameters of the model are adjusted and agreement between the observed and calculated data is maximized.

In some cases, the precedent step (charge flipping) does not result in a satisfying solution. In such case, the simulated annealing is applied to both the metal atoms, and the organic fragment.

7. Rietveld refinement. Once the viable model was obtained, it goes through the so-called Rietveld refinement. At this step, the structural parameters (atomic coordinates, thermal parameters, bond angles and distances in rigid bodies, scale factor) and profile factors (cell parameters, zero error, profile function parameters, background) are subjected to a least-squares procedure in order to obtain the best fit based on point by point comparison between the experimental pattern and the pattern calculated from the trial structure. The most common criterion to assess quality of the refinement of the profile and of the structural model are R_{wp} and R_{Bragg}, respectively.

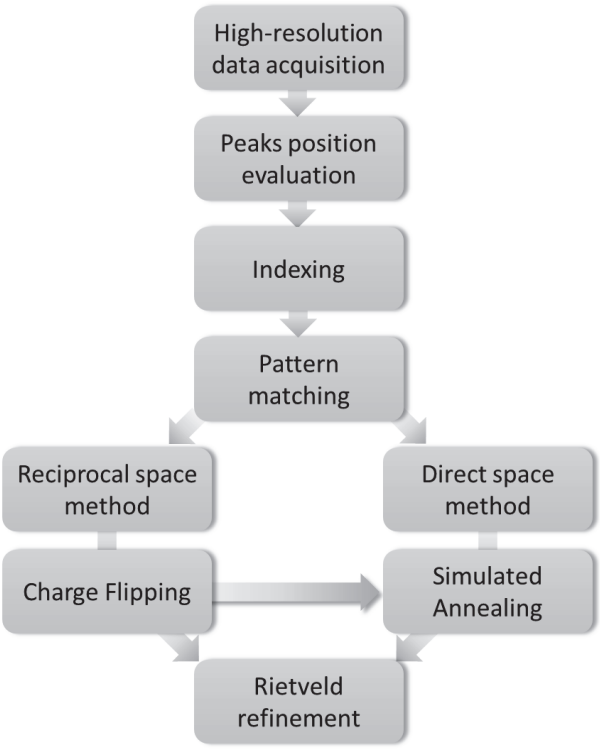

Figure I. 15 The generalized plan of the structure determination procedure used for CPs studied in this work.

There are few more challenges to overcome which are characteristic for studied $[M(SR)]_n$ CPs, e.g. strong preferred orientation (in the case of lamellar - 2D - compounds), presence of small cell parameters along with big ones and presence of a highly dominant scatterer (in the case of gold or silver based compounds).

A preferred orientation arises when the crystallites in the sample are oriented preferentially in a certain direction. It is caused by strong anisotropy of crystallites (the case of

the studied compounds). Such distribution of crystallites causes the difference between the measured relative peak intensities and the intrinsic relative diffraction intensities. It also leads to anisotropic line broadening effects, which are complicated to model.

Reflections associated with small cell parameters are expected at high diffraction angles, where peak overlap is stronger. Small cell parameters with their few reflections are prone to overlap with the numerous reflections generated from a large cell dimension (typical case for the lamellar compounds). It makes the indexing step even more challenging.

The presence of the dominant scatterers (gold and silver atoms) can simplify the task of their positioning. In the same time, it can mask information concerning the organic component, making the completion of the crystalline structure more difficult.

I.2.3. Total Scattering Methods and Pair Distribution Function (PDF) analysis [77, 78]

The traditional method of structural characterization such as X-ray or neutron diffraction cannot be applied to amorphous materials, as it relies on the assumption of lattice periodicity. The non-periodic atom arrangement results in the X-ray diffraction patterns which are dominated by broad variety of features caused by diffuse scattering.

EXAFS, solid state NMR or total scattering methods with pair distribution function (PDF) analyses are other examples of structural characterizations. The first two, EXAFS and solid state NMR, are probing the local structure. The dominant contribution to these probes comes from the structural correlations between the closest neighbors. It can provide useful information about the coordination environment with respect to a reference atom, but fewer information about correlations at longer distances. Even though, the NMR is a great source of complementary information that can greatly facilitate structure determination of CPs,[79] the full crystal structure determination via NMR is still challenging.

Total scattering methods coupled with PDF analysis are the methods playing a crucial role in the understanding of the structure-property correlation since the late 90s. The total scattering experiments give the total scattering function (*S(Q)*), which includes information about both the Bragg and the diffuse scattering. After the data treatment, the Fourier transform of *S(Q)* gives the PDF. PDF describes the distribution of distances between pairs of atoms and, the most importantly, it is not limited to the closest neighbors. It acts as a bridge

between the averaged structure (the one we see due to the X-ray diffraction) and local structure (from EXAFS or solid state NMR), giving the description of material at both the short and the long range distances. [78]

From an experimental point of view, the data have the same form as those obtained by regular powder diffraction experiment. The measured experimental intensity, *I(Q)*, is expressed as:

$$I(Q) = PA\,[N(I_{coh} + I_{inc} + I_{mul})] \quad \text{(Eq. I.3)}$$

where *P* is the polarization factor, *A* is the absorption coefficient, *N* is a normalization constant to the incident flux and I_{coh}, I_{inc} and I_{mul} are the coherent, incoherent and multiple scattering intensities, respectively. $I(Q)$ is a function of *Q*, the magnitude of the scattering vector defined as:

$$Q = \frac{4\pi sin\theta}{\lambda} \quad \text{(Eq. I.4)}$$

where θ is a half of scattering angle and λ is the wavelength. The total coherent scattering function, *S(Q)*, is obtained by division of *I(Q)* by the number of scatterers (atoms) so that *S(Q)* is expressed in absolute unit of scattering-per-atom. For an X-ray experiment, it is expressed as:

$$S(Q) = \frac{I_{coh} - \langle f^2 \rangle + \langle f \rangle^2}{\langle f \rangle^2} \quad \text{(Eq. I.5)}$$

where $\langle f \rangle^2$ and $\langle f^2 \rangle$ are the square of the mean and the mean square scattering factors of the sample, respectively. In order to obtain the *S(Q)*, the experimental *I(Q)*, is used after application of suitable corrections (correction for absorption, polarization factor, multiple and incoherent scattering, background) and proper normalization.

In the PDF analysis we are interested in reduced pair distribution function, *G(r)*, which is defined as:

$$G(r) = 4\pi r[\rho(r) - \rho_0] \quad \text{(Eq. I.6)}$$

where *ρ(r)* is the microscopic pair density and ρ_0 is the average number density. The sine Fourier transform of *F(Q)=Q.[S(Q)-1]* gives *G(r)*:

$$G(r) = \frac{2}{\pi}\int_0^\infty Q\,[S(Q) - 1]\sin(Qr)\,dQ \quad \text{(Eq. I.7)}$$

The *G(r)* can be also calculated from a structural model:

$$G_c(r) = \frac{1}{r}\sum_i \sum_j \left[\frac{f_i f_j}{\langle f \rangle^2}\delta\left(r - r_{ij}\right)\right] - 4\pi\rho_0 \quad \text{(Eq. I.8)}$$

where f_i and f_j are the scattering factors for atoms *i* and *j*. The sum runs over all atom pairs ij ($i \neq j$) with a given separation of r_{ij}. A peak of *G(r)* indicates a *r*-range where the probability of finding given inter-atomic vectors is greater than the one determined by the number density ($\rho(r) > \rho_0$).

The real-space resolution of the PDF is related to the range of *Q* used for measurement. In order to increase Q_{max} the λ used for measurements should be decreased (eq. I.2.). This can be reached by collecting X-ray diffraction data at high-energy synchrotron facilities using short wavelengths. In the laboratory conditions, it can be performed using silver X-ray tube (λ = 0.56 Å).

Additionally, the background measurements are performed in order to subtract unwanted effects such as the scattering from the air or from the capillary if one is used. The data for standard samples (LaB_6, CeO_2 and Ni) are collected, in order to characterize the instrumental resolution function (Q_{damp} and Q_{broad}, parameters that characterize a loss of amplitude and peak broadening of *G(r)* at high *r*). The reciprocal space data are converted to PDFs using the PDFgetX3 software. [80]

The PDF is an atom-pair correlation function, therefore, it provides some information directly. For example, the peak positions carry the information about the bond length / the distance between the pairs of atoms. The integrals (surface) of peak give information about the coordination number / number of neighboring atoms at a given distance. The peak width helps to estimate thermal or static disorder.

The most common modelling method is the real-space least-squares approach with the use of a full-profile fitting. It is analogous to the Rietveld method in which the fitted function is the PDF. Similarly to the Rietveld method, the refined structural parameters are cell parameters, atomic positions, thermal displacement parameters, scale factor, sharpening factor delta*1* (it accounts for the correlated motion of atoms at low *r*, which sharpens the corresponding peaks) and *sp diameter* (factor that accounts for the size of coherency range).

PDFgui is commonly used software capable to perform the method.[81] In this work, however, the MolPDF software[82] was employed for the data fitting. An important feature of the MolPDF software is a possibility to apply constraints on bond distances and angles, allowing the refinement of complex molecular structures. It reduces the number of refined parameters while maintaining the configuration of the molecules, especially in the presence of heavy atoms (*e. g.* metal atoms). This makes the software particularly attractive to use for CPs where both metal atoms and organic molecules are present.

I.3. Basics of Luminescence [83, 84]

Luminescence is a process of the light [photon] emission as a result of the deexcitation from the electronic excited state of a species.

Whenever the term "luminescence" is used throughout the thesis, photoluminescence is meant. Prefix *photo-* means that a species were excited through the absorption of a photon.

The luminescence processes can be well visualized and explained by Jablonski diagram (**Figure I. 16**). It represents singlet electronic states denoted S_0 (fundamental electronic state), S_1, S_2… and triplet electronic states, T_1, T_2… Vibrational levels are associated with each electronic state.

The first step that occurs during process of photoluminescence is *absorption*, $S_0 \rightarrow S_1$ or $S_0 \rightarrow S_2$. It happens quickly with respect to the other processes (~10^{-15} s). Once the species is excited, internal conversion and vibrational relaxation occur.

When a species is excited to an energy level higher than the lowest vibrational level of the first electronic state S_1, *vibrational relaxation* occurs. It brings the excited species to the 0 vibrational level of S_1 state. This process involves the dissipation of the energy from the species to its surroundings. If the singlet excited state is higher than S_1, an *internal conversion* occurs. Thus, internal conversion is defined as a non-radiative transition between two electronic states of the same spin multiplicity (*e. g.*, $S_2 \rightarrow S_1$).

A time-scale of vibrational relaxation and of internal conversion is in range of 10^{-12} – 10^{-10} and 10^{-11} – 10^{-9} s, respectively.

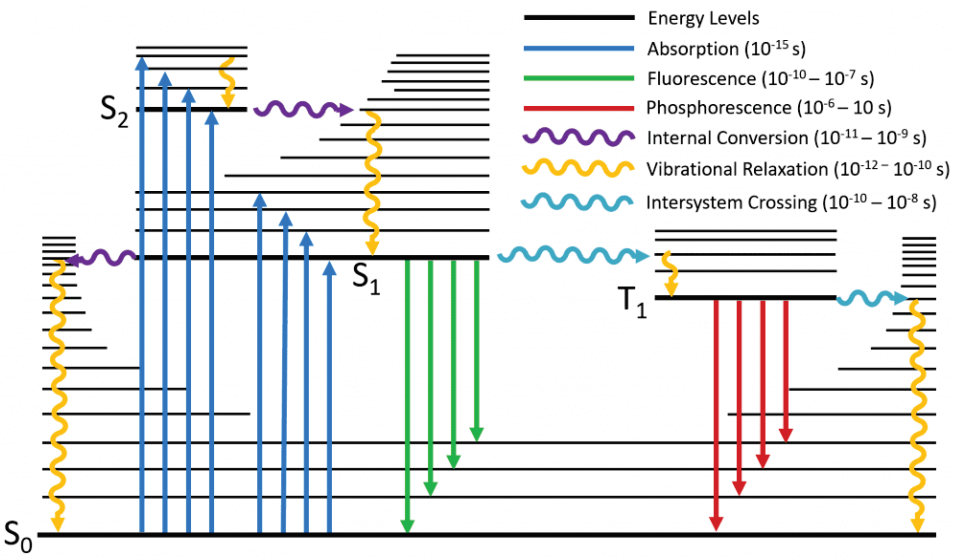

Figure I. 16 Jablonski diagram. The states are arranged vertically by energy and horizontally by spin multiplicity. The vibrational ground states of each electronic state are depicted as thick lines, while higher vibrational states – as thin lines. The processes that occur are shown as straight (radiative transitions) or squiggly (non-radiative transitions) arrows.[4] [85]

Once an excited species is at S_1 state, the following processes are possible: internal conversion from S_1 to S_0 (possible, but normally not efficient), deexcitation through photon emission and intersystem crossing to the triplet state.

A deexcitation $S_1 \rightarrow S_0$ accompanied by the emission of a photon is called *fluorescence*. With a few exceptions it occurs from S_1 state. The lifetime of the excited state S_1 is lying in the range of $\sim 10^{-10} - 10^{-7}$ s.

Intersystem crossing is a non-radiative transition between two vibrational levels of the same energy belonging to electronic states of different spin multiplicities. Crossing between states of different spin multiplicity is in principle forbidden, but spin–orbit coupling (*i.e.* coupling between the orbital magnetic moment and the spin magnetic moment) can be large enough to make it possible. The presence of heavy atoms increases spin–orbit coupling and thus favors intersystem crossing (*heavy atom effect*). A time-scale of intersystem crossing is in range of $10^{-10} - 10^{-8}$ s.

An intersystem crossing can be followed by *phosphorescence*. It is a spin-forbidden deexcitation $T_1 \rightarrow S_0$ accompanied by the emission of a photon. The lifetime of the excited

[4] A figure is taken from : https://www.edinst.com/blog/jablonski-diagram/

state T_1 is lying in the range of ~10^{-6} – 1 s. The phosphorescence spectrum is located at wavelengths higher than the fluorescence spectrum, because the energy of the lowest vibrational level of the triplet state T_1 is lower than that of the singlet state S_1.

I.3.1. Important Characteristics

Emission spectrum and excitation spectrum are the luminescence intensity as a function of the emission or the excitation wavelengths and are maybe the most important characteristics of luminescence. The gap between their maxima is called *Stokes shift*. This value provides information whether the process that occurs is fluo- or phosphorescence. Roughly speaking small Stokes shift implies fluorescent process while large Stokes shift implies phosphorescent process.

Another important parameter that can help distinguish between fluo- and phosphorescence is a lifetime of an *excited state*. Emission and absorption of a photon are both fast processes. Between these two acts, an excited species stays some time in S_1 state undergoing possible vibrational relaxation, internal conversion and maybe intersystem crossing followed by some time in T_1 state. Thus, after excitation of a population of species by a very short pulse of light, the luminescence intensity decreases exponentially with a characteristic time, reflecting the average lifetime of the species in a given excited state. The short lifetime is characteristic for a fluorescent process, while long lifetime corresponds to a phosphorescent process.

Another important value that provides information about efficiency of the studied emitter is a *quantum yield*. It is the ratio of the number of photons emitted to the number of photons absorbed by sample. [86]

These are the main important characteristics that will be used in the discussion of the photophysical properties of the studied CPs.

I.3.2. Coordination Compounds and Charge Transfer [87]

In coordination compounds, the metal-ligand bonds are generally polar. The molecular orbitals that participate in the luminescence processes are not equally delocalized between metal and ligands but predominantly located either at the side of the metal or of the ligand.

According to the localization, the following electronic transitions can be distinguished

- *Metal-centered* (MC) transition. They correspond mainly to d→d transitions of metals with not fully occupied d-level. They can be encountered for Cu(I)-compounds as well. Cu(I) has an electronic configuration of $3d^{10}$, however, upon transition an electron is promoted from the 3d level to the 4s level leaving vacancy in 3d level. [88]
- *Ligand-centered* (LC) or intraligand (IL) transition. They take place between two ligand-based orbitals, *i.e.* π→π*.
- *Ligand-to-ligand charge transfer (*LLCT) can be observed when a reducing and an oxidizing ligand are coordinated to a metal. In our studies we worked with homoleptic complexes, therefore, this case does not concern us.
- *Ligand-to-metal charge transfer* (LMCT) arises from electron transfer from the molecular orbital with ligand-like character to the one with metal-like character. It is favored when ligand has relatively high-energy lone pairs (*e. g.*, S-containing) or if the metal has low-lying empty orbitals. It can be formally seen as oxidation of the ligand and reduction of the metal. It is often occurs in Au(I)- and Ag(I)-compounds, however, it is known for Cu(I)-compounds as well. [89]
- *Metal-to-ligand charge transfer* (MLCT) arises from electron transfer from the molecular orbital with metal-like character to the one with ligand-like character. It is favored in compounds with metals that easily undergo oxidation (*e. g.*, Cu(I)). It can be seen as oxidation of the metal and reduction of the ligand. It is well known for Cu(I)-compounds, but it has been reported for Au(I)- and Ag(I)- as well. [90]
- *Metal-to-metal charge transfer* (MMCT, it can be encountered also as LMMCT or MMLCT). It happens once transfer from one metal atom to another metal atom occurs. It is often associated with a presence of metallophilic interactions.

Despite relatively obvious differences between these transitions, from the point of view of mechanism, in practice it is not always easy to distinguish between them. Sometimes the identification of the origin of luminescence can be pretty straightforward, while in other cases only the complex TD-DFT calculi can provide further information. To illustrate this point, let us

briefly discuss the luminescence properties and origin of two CPs studied in our team – $[Au(SPh)]_n$ and $[Au(p\text{-}SPhCO_2Me)]_n$.

$[Au(SPh)]_n$ case. [35] As mentioned above, $[Au(SPh)]_n$ is a CP formed by two intertwined -Au-S-Au- helices kept together through metallophilic interactions (**Figure I. 6** (e)). It shows a bright red emission at room temperature under the UV lamp (**Figure I. 17** (a)). The absorption band is centered at 278 nm and is assigned to the π-π* transition of the phenyl group. The excitation and emission maxima are located at 340 and 684 nm. The large Stokes shift of 14800 cm^{-1}, as well as, the micro-second range lifetime suggest a phosphorescent nature of the process. The quantum yield at room temperature in solid state was estimated to be as high as 5 %.

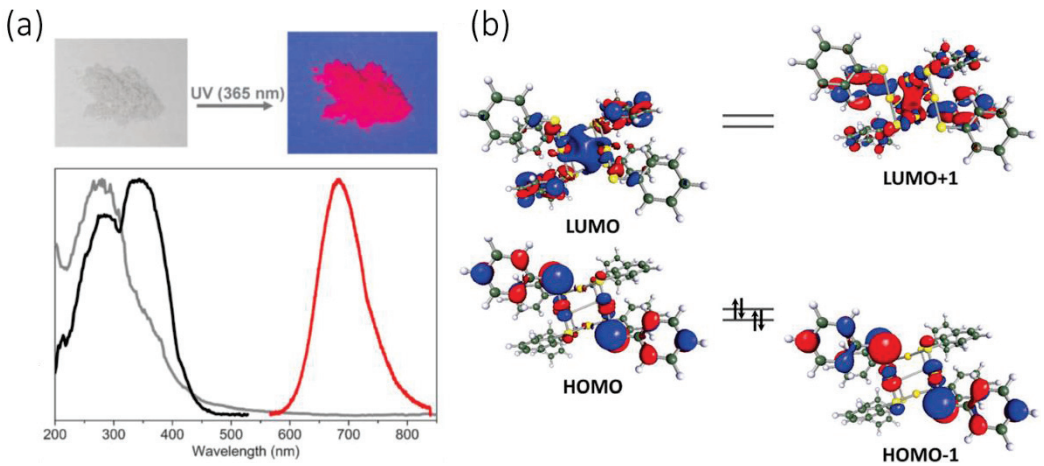

Figure I. 17 The photophysical properties of $[Au(SPh)]_n$: (a) top: photographs under ambient and UV light, bottom: absorption (gray), excitation (black) and emission (red) spectra measured at room temperature in the solid state; (b) frontier molecular orbitals for model system $[Au_6(SPh)_8]^{2-}$. Reprinted with permission from ref. [35]. Copyright 2015 The Royal Society of Chemistry.

The low energy emission of gold(I) thiolates is usually assigned to a LMCT or a LMMCT transition. [91] In order to get insight into photophysical behavior, a DFT calculus was performed. The highest occupied MOs (HOMOs) are mainly located at sulfur atoms of the thiolate ligands (pπ(S) character), with a small contribution from the phenyl rings and gold centers (dσ* character) connected to the corresponding thiolate group. The lowest unoccupied MOs (LUMOs) are mainly centered at the gold centers (pσ character), with some ligand contribution (**Figure I. 17** (b)). Therefore, the luminescent process can be summarized as ligand-to-metal-metal charge transfer ^{3}[pπ(S) → pσ(Au)] transition with a small contribution from a metal

centered ^{3}[dσ*(Au) → pσ(Au)] transition. As follows, the calculi are well in agreement with typically observed transition for gold(I)-thiolates. Hence, $[Au(SPh)]_n$ can be considered as a 'classical' case of gold(I)-thiolate emission.

$[Au(p\text{-}SPhCO_2Me)]_n$ case.[48] $[Au(p\text{-}SPhCO_2Me)]_n$ is a 2D CP formed by zig-zag -Au-S-Au- chains interacting through relatively short metallophilic interactions (3.199(5) Å) (**Figure I. 11**). It emits a very bright orange light at room temperature under the UV lamp (**Figure I. 18**). It has a rather large excitation band with a maximum at 370 nm and a shoulder at 290 nm. The emission maximum is at 645 nm. The large Stokes shift of 11000 cm^{-1} as well as micro-second range lifetime suggest a phosphorescent parentage of the excited states similarly to the previous case. The compound exhibits a very high quantum yield of 70 % at room temperature in the solid state.

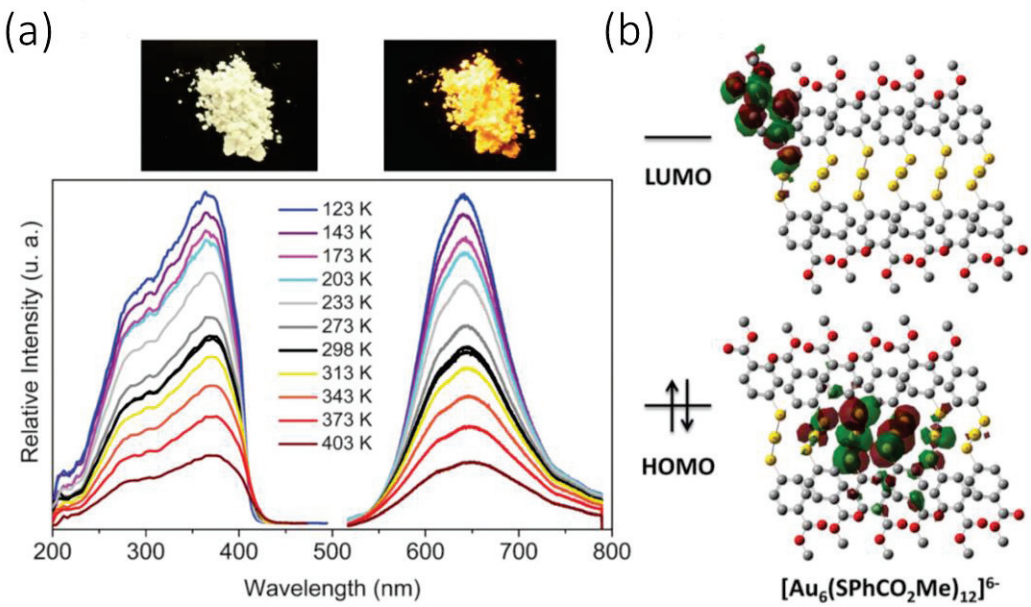

Figure I. 18 The photophysical properties of $[Au(p\text{-}SPhCO_2Me)]_n$: (a) top: photographs under ambient and UV light, bottom: emission and excitation spectra measured in the solid state at variable temperatures; (b) frontier molecular orbitals for model system $[Au_6(p\text{-}SPhCO_2Me)_{12}]^{6-}$ Adapted with permission from ref. [48]. Copyright 2016 The Royal Society of Chemistry.

Additionally, a low intensity emission peak at 488 nm appears at temperature below 233 K. It can be ascribed to a metal-perturbed IL transition, as a free standing ligand exhibits an emission at 500 nm.

In order to rationalize the origin of the emission, complex DFT calculations were undertaken. The results show that HOMOs are mainly located at the sulfur atoms with some contribution from the gold center and the phenyl ring, while LUMOs are mostly located at π*($PhCO_2Me$) orbitals. Hence, the overall process is described as ligand-metal-to-ligand charge transfer transition (LMLCT: AuS→$PhCO_2Me$). And interestingly, despite the short metallophilic contacts, no transition involving a MC or LMMCT, which are typical for gold(I)-compounds, has been found.

This case brings to light the fact that, the attribution of origin of the luminescence can be sometimes rather ambiguous. DFT calculus was not performed for the predominant majority of the CPs discussed in this work. The assignments made in the work should be taken with a pinch of salt and might be re-examined after further investigations.

I.4. Goals of the Work

As it was discussed above, a number of parameters is susceptible to cooperatively guide a structure formation of $[M(SR)]_n$ CPs. In this work, we performed a systematic investigation of the role of some of them, namely – the role of (i) the **metal's nature** (and as a result, propensity to form metallophilic interactions), (ii) the **hydrogen bonds** and (iii) the **steric hindrance**. [92] The synthesized CPs underwent photophysical studies in order to establish a correlation between luminescence properties of the corresponding structural arrangements, and even to potentially pinpoint their bond to the presence/absence of weak interactions that guided formation of these arrangements.

Keeping these goals in mind, it was decided to structure the work in the following way (**Table I. 4**):

- First chapter is dedicated to $[M(SPh)]_n$. While $[Cu(SPh)]_n$, $[Au(SPh)]_n$ and a tentative structural model for $[Ag(SPh)]_n$ have been reported, only $[Au(SPh)]_n$ underwent detailed photophysical study. Thus, the work start with a study targeting these known compounds in order to improve understanding of their luminescent properties. They serve as 'reference point' for comparison with other synthesized CPs with substituted arylthiolate ligands.

- Second chapter – $[M(p\text{-}SPhCO_2R)]_n$, where R = H, Me. These compounds illustrate effect of the substituents in *para*-position in comparison to the unsubstituted thiophenol. We tested both ligands with $–CO_2H$ and $–CO_2Me$ groups in order to prove the non-negligible role of the hydrogen bonds in the structure formation.
- Third and fourth chapters are dedicated to $[M(x\text{-}SPhCO_2H)]_n$, with *x* = *meta*, *ortho*, respectively. A displacement of the substituent from *para*- to *meta*- and then to *ortho*-position expose the potential influence of the steric hindrance near the coordinating sulfur atom on the formation of the extended system.
- Fifth chapter is dedicated to amorphous phases $a[Au(SPh)]_n$, $a[Au(SMePh)]_n$ and $a[Au(SEtPh)]_n$. $a[Au(SPh)]_n$ has been previously synthesized by our team, thus it was chosen as the first candidate for structural studies. The introduction of methyl or ethyl group spacer between sulfur atom and phenyl ring in $a[Au(SMePh)]_n$ or $a[Au(SEtPh)]_n$ relatively to $[Au(SPh)]_n$ was thought to favor the formation of the amorphous phase due to the increased flexibility of the ligand which prevents crystallization. The PDF-assisted structure investigation and photophysical properties for all three compounds were performed.

Table I. 4 Compounds studied through this works.

CHAPTER 1	CHAPTER 2	CHAPTER 3	CHAPTER 4	CHAPTER 5
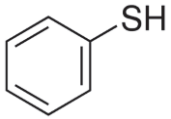	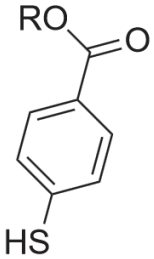	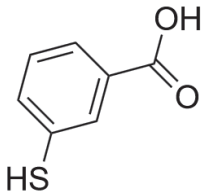	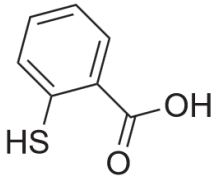	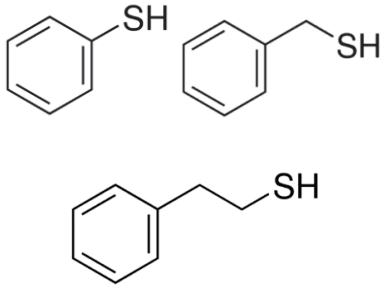
HSPh	*p*-HSPhCO$_2$R, R = H, Me	*m*-HSPhCO$_2$H	*o*-HSPhCO$_2$H	HSPh HSMePh HSEtPh
[M(SPh)]$_n$	[M(*p*-SPhCO$_2$R)]$_n$	[M(*m*-SPhCO$_2$H)]$_n$	[M(*o*-SPhCO$_2$H)]$_n$	*a*[Au(SPh)]$_n$ *a*[Au(SMePh)]$_n$ *a*[Au(SEtPh)]$_n$
		M = Cu, Ag, Au		

I.5 References

1. B. Rungtaweevoranit, C. S. Diercks, M. J. Kalmutzki and Omar M. Yaghi, *Faraday Discuss.*, 2017, **201**, 9-45.
2. O. M. Yaghi, M. O'Keeffe, N. W. Ockwig, H. K. Chae, M. Eddaoudi and J. Kim, *Nature*, 2003, **423**, 705-714.
3. M. Jansen and J. C. Schön, *Angew. Chem. Int. Ed.*, 2006, **45**, 3406-3412.
4. R. Robson, *Dalton Trans.*, 2008, 5113-5131.
5. M. G. Goesten, F. Kapteijn and J. Gascon, *CrystEngComm*, 2013, **15**, 9249-9257.
6. S. R. Batten, *J. Solid State Chem.*, 2005, **178**, 2475-2479.
7. G. I. Dzhardimalieva and I. E. Uflyand, *RSC Advances*, 2017, **7**, 42242-42288.
8. J. Jiang, Y. Zhao and O. M. Yaghi, *J. Am. Chem. Soc.*, 2016, **138**, 3255-3265.
9. K. A. Kacprzak, O. Lopez-Acevedo, H. Häkkinen and H. Grönbeck, *J. Phys. Chem. C*, 2010, **114**, 13571-13576.
10. O. Veselska and A. Demessence, *Coord. Chem. Rev.*, 2018, **355**, 240-270.
11. A. Bondi, *J. Phys. Chem.*, 1964, **68**, 441-451.
12. H. Schmidbaur and A. Schier, *Chem. Soc. Rev.*, 2012, **41**, 370-412.
13. G. Férey, *Chem. Soc. Rev.*, 2008, **37**, 191-214.
14. P. Rungthanaphatsophon, C. L. Barnes and J. R. Walensky, *Dalton Trans.*, 2016, **45**, 14265-14276.
15. A. Ciborska, Z. Hnatejko, K. Kazimierczuk, A. Mielcarek, A. Wiśniewska and A. Dołęga, *Dalton Trans.*, 2017, **46**, 11097-11107.
16. K. Tang, M. Aslam, E. Block, T. Nicholson and J. Zubieta, *Inorg. Chem.*, 1987, **26**, 1488-1497.
17. B. Becker, W. Wojnowski, K. Peters, E.-M. Peters and H. G. Von Schnering, *Polyhedron*, 1990, **9**, 1659-1666.
18. E. Block, H. Kang, G. Ofori-Okai and J. Zubieta, *Inorganica Chim. Acta*, 1990, **167**, 147-148.
19. I. Schröter-Schmid and J. Strähle, *Z. Naturforsch.*, 1990, **45b**, 1537-1542.
20. H. Yan, F. Yang, D. Pan, Y. Lin, J. N. Hohman, D. Solis-Ibarra, F. H. Li, J. E. P. Dahl, R. M. K. Carlson, B. A. Tkachenko, A. A. Fokin, P. R. Schreiner, G. Galli, W. L. Mao, Z.-X. Shen and N. A. Melosh, *Nature*, 2018, **554**, 505.
21. P. J. Bonasia, G. P. Mitchell, F. J. Hollander and J. Arnold, *Inorg. Chem.*, 1994, **33**, 1797-1802.
22. E. Block, M. Gernon, H. Kang, G. Ofori-Okai and J. Zubieta, *Inorg. Chem.*, 1989, **28**, 1263-1271.
23. P. J. Bonasia, D. E. Gindelberger and J. Arnold, *Inorg. Chem.*, 1993, **32**, 5126-5131.
24. W. Wojnowski, B. Becker, J. Saßmannshausen, E. M. Peters, K. Peters and H. G. Von Schnering, *Z. Anorg. Allg. Chem.*, 1994, **620**, 1417-1421.
25. D. Ohlmann, H. Pritzkow, H. Grützmacher, M. Anthamatten and R. Glaser, *J. Chem. Soc., Chem. Commun.*, 1995, 1011-1012.

26. I. Schröter and J. Strähle, *Chem. Ber.*, 1991, **124**, 2161-2164.
27. X. Jin, X. Xie, H. Qian, K. Tang, C. Liu, X. Wang and Q. Gong, *ChemComm*, 2002, 600-601.
28. M. R. Wiseman, P. A. Marsh, P. T. Bishop, B. J. Brisdon and M. F. Mahon, *J. Am. Chem. Soc.*, 2000, **122**, 12598-12599.
29. K. Tang, X. Jin, H. Yan, X. Xie, C. Liu and Q. Gong, *J. Chem. Soc., Dalton Trans*, 2001, 1374-1377.
30. S. S.-Y. Chui, R. Chen and C.-M. Che, *Angew. Chem. Int. Ed.*, 2006, **45**, 1621-1624.
31. C.-M. Che, C.-H. Li, S. S.-Y. Chui, V. A. L. Roy and K.-H. Low, *Chem. Eur. J.*, 2008, **14**, 2965-2975.
32. K. Tang, J. Yang, Q. Yang and Y. Tang, *J. Chem. Soc., Dalton Trans*, 1989, 2297-2302.
33. I. G. Dance, L. J. Fitzpatrick, D. C. Craig and M. L. Scudder, *Inorg. Chem.*, 1989, **28**, 1853-1861.
34. R. Bau, *J. Am. Chem. Soc.*, 1998, **120**, 9380-9381.
35. C. Lavenn, L. Okhrimenko, N. Guillou, M. Monge, G. Ledoux, C. Dujardin, R. Chiriac, A. Fateeva and A. Demessence, *J. Mater. Chem. C*, 2015, **3**, 4115-4125.
36. *Merck Index*, Merck & Co.: Rahway, NJ, 12th edn., 1996.
37. L. L. G. Al-Mahamad, O. El-Zubir, D. G. Smith, B. R. Horrocks and A. Houlton, *Nat. Commun.*, 2017, **8**, 720.
38. H. Yan, J. N. Hohman, F. H. Li, C. Jia, D. Solis-Ibarra, B. Wu, J. E. P. Dahl, R. M. K. Carlson, B. A. Tkachenko, A. A. Fokin, P. R. Schreiner, A. Vailionis, T. R. Kim, T. P. Devereaux, Z.-X. Shen and N. A. Melosh, *Nat. Mater.*, 2016, **16**, 349.
39. M. Baumgartner, H. Schmalle and C. Baerlocher, *J. Solid State Chem.*, 1993, **107**, 63-75.
40. K.-H. Low, C.-H. Li, V. A. L. Roy, S. S.-Y. Chui, S. L.-F. Chan and C.-M. Che, *Chem. Sci.*, 2010, **1**, 515-518.
41. I. G. Dance, *Inorganica Chim. Acta*, 1977, **25**, L17-L18.
42. Y. Zhang, T. Xia, K. M. Yu, F. Zhang, H. Yang, B. Liu, Y. An, Y. Yin and X. Chen, *ChemPlusChem*, 2014, **79**, 559-563.
43. J.-U. Kim, S.-H. Cha, K. Shin, J. Y. Jho and J.-C. Lee, *J. Am. Chem. Soc.*, 2005, **127**, 9962-9963.
44. S.-H. Cha, J.-U. Kim, K.-H. Kim and J.-C. Lee, *Chem. Mater.*, 2007, **19**, 6297-6303.
45. K.-H. Low, V. A. L. Roy, S. S.-Y. Chui, S. L.-F. Chan and C.-M. Che, *ChemComm*, 2010, **46**, 7328-7330.
46. A. T. Royappa, C. M. Tran, R. J. Papoular, M. Khan, L. E. Marbella, J. E. Millstone, M. Gembicky, B. Chen, W. Shepard and E. Elkaim, *Polyhedron*, 2018, **155**, 359-365.
47. H. L. Cuthbert, A. I. Wallbank, N. J. Taylor and J. F. Corrigan, *Z. Anorg. Allg. Chem.*, 2002, **628**, 2483-2488.
48. C. Lavenn, N. Guillou, M. Monge, D. Podbevšek, G. Ledoux, A. Fateeva and A. Demessence, *ChemComm*, 2016, **52**, 9063-9066.
49. E. A. Schriber, D. C. Popple, M. Yeung, M. A. Brady, S. A. Corlett and J. N. Hohman, *ACS Appl. Nano Mater.*, 2018, **1**, 3498-3508.

50. B. Trang, M. Yeung, D. C. Popple, E. A. Schriber, M. A. Brady, T. R. Kuykendall and J. N. Hohman, *J. Am. Chem. Soc.*, 2018, **140**, 13892-13903.
51. Y. Hao, C. Dai, L. Yu, S. Li, Y. Yu, B. Ju, M. Li and S. X.-A. Zhang, *CrystEngComm*, 2018, **20**, 181-188.
52. M. J. Baena, P. Espinet, M. C. Lequerica and A. M. Levelut, *J. Am. Chem. Soc.*, 1992, **114**, 4182-4185.
53. H. G. Fijolek, J. R. Grohal, J. L. Sample and M. J. Natan, *Inorg. Chem.*, 1997, **36**, 622-628.
54. F. Bensebaa, T. H. Ellis, E. Kruus, R. Voicu and Y. Zhou, *Langmuir*, 1998, **14**, 6579-6587.
55. A. N. Parikh, S. D. Gillmor, J. D. Beers, K. M. Beardmore, R. W. Cutts and B. I. Swanson, *J. Phys. Chem. B*, 1999, **103**, 2850-2861.
56. T. T. Chng, L. Polavarapu, Q.-H. Xu, W. Ji and H. C. Zeng, *Langmuir*, 2011, **27**, 5633-5643.
57. Y. X. Zhang and H. C. Zeng, *Adv. Mater.*, 2009, **21**, 4962-4965.
58. S.-H. Cha, K.-H. Kim, W.-K. Lee and J.-C. Lee, *J. Ind. Eng. Chem.*, 2010, **16**, 816-822.
59. H. Nie, M. Li, Y. Hao, X. Wang and S. X.-A. Zhang, *Chem. Sci.*, 2013, **4**, 1852-1857.
60. H. Nie, M. Li, Y. Hao, X. Wang, S. Gao, B. Yang, M. Gu, L. Sun and S. X.-A. Zhang, *J. Colloid Interface Sci.*, 2014, **434**, 104-112.
61. I. G. Dance, K. J. Fisher, R. M. H. Banda and M. L. Scudder, *Inorg. Chem.*, 1991, **30**, 183-187.
62. D. V. P. Massote and M. S. C. Mazzoni, *Appl. Phys. Lett.*, 2016, **109**, 133104.
63. Q. Xiao, J. A. Burg, Y. Zhou, H. Yan, C. Wang, Y. Ding, E. Reed, R. D. Miller and R. H. Dauskardt, *Nano Letters*, 2018, **18**, 4900-4907.
64. A. D. McNaught and A. Wilkinson, *Compendium of Chemical Terminology. - The Gold Book*, Blackwell Science, 2nd edn., 1997.
65. N. G. Connelly, T. Damhus, R. M. Hartshorn and A. T. Hutton, *Nomenclature of Inorganic Chemistry - IUPAC Recommendations 2005*, The Royal Society of Chemistry, 2005.
66. H. R. Khavasi, M. M. Barforoush and M. A. Fard, *CrystEngComm*, 2012, **14**, 7236-7244.
67. Z. Xie, T. Yu, J. Chen, E. Ubba, L. Wang, Z. Mao, T. Su, Y. Zhang, M. P. Aldred and Z. Chi, *Chem. Sci.*, 2018, **9**, 5787-5794.
68. J.-F. Song, S.-Z. Li, R.-S. Zhou, J. Shao, X.-M. Qiu, Y.-Y. Jia, J. Wang and X. Zhang, *Dalton Trans.*, 2016, **45**, 11883-11891.
69. S. Kitagawa, *Acc. Chem. Res.*, 2017, **50**, 514-516.
70. T. D. Bennett and A. K. Cheetham, *Acc. Chem. Res.*, 2014, **47**, 1555-1562.
71. R. E. Bachman and S. A. Bodolosky-Bettis, *Z. Naturforsch.*, 2009, **64b**, 1491-1499.
72. C. A. Simpson, C. L. Farrow, P. Tian, S. J. L. Billinge, B. J. Huffman, K. M. Harkness and D. E. Cliffel, *Inorg. Chem.*, 2010, **49**, 10858-10866.
73. Y. Zhao, K. Li and J. Li, *Z. Naturforsch. B Chem. Sci.*, 2010, **65**, 976-998.
74. K. D. M. Harris, M. Tremayne and B. M. Kariuki, *Angew. Chem. Int. Ed.*, 2001, **40**, 1626-1651.
75. M. Ladd and R. Palmer, *Structure Determination by X-ray Crystallography*, Springer, Boston, MA, 5th edn., 2013.

76. Topas V4.2: General Profile and Structure Analysis Software for Powder Diffraction Data, *Bruker AXS Ltd*, 2008.
77. T. Egami and S. J. L. Billinge, *Underneath the Bragg Peaks. Structural Analysis of Complex Materials*, Pergamon, 2003.
78. A. Mancini and L. Malavasi, *ChemComm*, 2015, **51**, 16592-16604.
79. F. Taulelle, B. Bouchevreau and C. Martineau, *CrystEngComm*, 2013, **15**, 8613-8622.
80. P. Juhas, T. Davis, C. L. Farrow and S. J. L. Billinge, *J. Appl. Crystallogr.*, 2013, **46**, 560-566.
81. C. L. Farrow, P. Juhas, J. W. Liu, D. Bryndin, E. S. Božin, J. Bloch, T. Proffen and S. J. L. Billinge, *Journal of Physics: Condensed Matter*, 2007, **19**, 335219.
82. J. Rodriguez-Carvajal and A. Bytchkov, *Institut Laue-Langevin, Grenoble, France*, 2016.
83. B. Valeur, *Molecular Fluorescence: Principles and Applications*, Wiley-VCH Verlag GmbH, 2001.
84. P. Atkins and P. d. Paula, *J. Atkins' Physical Chemistry*, Oxford University Press, 8th edn., 2006.
85. Jablonski diagram | What is it? | Edinburgh Instruments, https://www.edinst.com/blog/jablonski-diagram/).
86. M. A. Omary and H. H. Patterson, in *Encyclopedia of Spectroscopy and Spectrometry (Third Edition)*, eds. J. C. Lindon, G. E. Tranter and D. W. Koppenaal, Academic Press, Oxford, 2017, DOI: https://doi.org/10.1016/B978-0-12-803224-4.00193-X, pp. 636-653.
87. A. Vogler and H. Kunkely, in *Photosensitization and Photocatalysis Using Inorganic and Organometallic Compounds*, eds. K. Kalyanasundaram and M. Grätzel, Springer Netherlands, 1993, pp. 71-111.
88. C. Pedrini, *Phys. Status Solidi B*, 1978, **87**, 273-286.
89. V. W.-W. Yam and K. M.-C. Wong, *ChemComm*, 2011, **47**, 11579-11592.
90. V. W.-W. Yam, V. K.-M. Au and S. Y.-L. Leung, *Chem. Rev.*, 2015, **115**, 7589-7728.
91. E. R. T. Tiekink and J.-G. Kang, *Coord. Chem. Rev.*, 2009, **253**, 1627-1648.
92. E. R. T. Tiekink, *Coord. Chem. Rev.*, 2014, **275**, 130-153.

Chapter 1: $[M(SPh)]_n$

1.1 Introduction

In this chapter, we discuss the simplest arylthiolate-based CPs: thiophenolates of Cu(I), Ag(I) and Au(I).

The 1D column-like structure of $[Cu(SPh)]_n$ has been reported by C.-M. Che *et al.*[1] in 2008. Only brief note on luminescent properties was given later by the same authors in 2010. [2] It included emission-excitation spectra at 77 K and tentative attribution of emission origin to the triplet excited state of mixed MC and LMCT character.

For the $[Ag(SPh)]_n$ structural model was proposed by I. G. Dance *et al* (see State of the Art I.1.4). [3] The $[AgS]_n$ layer formed by quasi-hexagonal array where both silver and sulfur atom have coordination number 3. No luminescent properties have been reported.

Its selenoate counterpart $[Ag(SePh)]_n$, however, has been reported to have blue emission at the room temperature.[4] Nevertheless, it should be noted that in $[Ag(SePh)]_n$ silver and selenium atoms form different arrangement to one supposed for $[Ag(SPh)]_n$: silver atoms are in distorted tetrahedral coordination connected through μ_4-selenium atoms.

The $[Au(SPh)]_n$ structure was reported by our team in 2015.[5] It has 1D double helice structure with every gold atom being coordinated by two μ_2-sulfur atoms. This compound exhibits an intense red emission at the room temperature in the solid state due to a LMMCT transition with a small contribution from a MC transition. The study showed that the aurophilic interactions contribute to the luminescent process.

In this chapter, the results of an advanced structure investigation and polymorphism of $[Cu(SPh)]_n$ and $[Ag(SPh)]_n$ are presented. In-depth photophysical characterizations of their polymorphs as well as temperature-dependent study of $[Au(SPh)]_n$ are discussed.

The discussion of the properties of these compounds will serve as useful and convenient "reference point", once we study influence of substituents ($-CO_2H$ or $-CO_2Me$) on structures and properties of formed CPs in the following chapters.

1.2 $[Cu(SPh)]_n$ Polymorphs

1.2.1 Synthesis and PXRD Characterization

The $[Cu(SPh)]_n$ was synthesized according to the procedure adapted from [1]. The authors used phenyl disulfide that was reduced by $NaBH_4$, followed by the addition of Cu_2O. We used thiophenol as thiolate group precursor, thus there was no need for the reduction step. Rest of the procedure was performed according to the reported protocol (see 1.7 Experimental part). The formed product, denoted as **$[Cu(SPh)]_n$ A**, had a PXRD close to the reported one (**Figure 1. 1** (a)). However, it contained a considerable amount of unreacted Cu_2O. A complete reaction was achieved under solvothermal conditions (in the reported procedure, reflux was used). The product, denoted as **$[Cu(SPh)]_n$ 1**, was prepared in such way had better crystallinity than product **A**. This result points out the advantage of solvothermal conditions for better crystallinity.

An optimization of a synthetic procedure following the protocol similar to [6] was performed in order to improve the crystallinity of the product. The PXRD patterns of some samples, **$[Cu(SPh)]_n$: 2, 3** and **4** are presented in the **Figure 1. 1**(b). Interestingly, a new **4** was obtained (**Figure 1. 1** (b), inset). Following the peaks at 7.2° and 10.2°, we see how they get progressively broader for **2** and **3**, and then finally split into two for the compound **4**. Therefore, we have a case of two polymorphs **1** and **4** existing along with an "intermediate" polymorphic phases (**2** and **3**).

The crystallographic cell reported for $[Cu(SPh)]_n$ is $P4_2/n$ with a = 17.57(3) Å, c = 3.827(2) Å. The peaks at 7.2° and 10.2° that were split in two correspond to the planes with Miller indices of (110) and (200), respectively. Such splitting could originate from the lower symmetry of the compound; for example, from tetragonal to orthorhombic or monoclinic cell with two close parameters and β approaching 90°.

The indexing step for **4** did not converge unambiguously to any crystallographic cell. Few cells showed relatively good agreement with experimental data (*e. g.*, P-1 with a = 7.40(3) Å, b = 12.44(1) Å, c = 12.558(4) Å, α = 92.3(1)°, β = 88.5(2)°, γ = 107.3(2)°, Gof = 21 or $P2_1$ with a = 17.584(5) Å, b = 4.33(2) Å, c = 16.956(5) Å, β = 93.35(1)°, Gof = 15) (see comparison of these cells with the reported one in the **Figure 1. 2**). It was decided to continue the structure

investigation once experimental data of better quality would be collected and the indexing proposes a univocal solution.

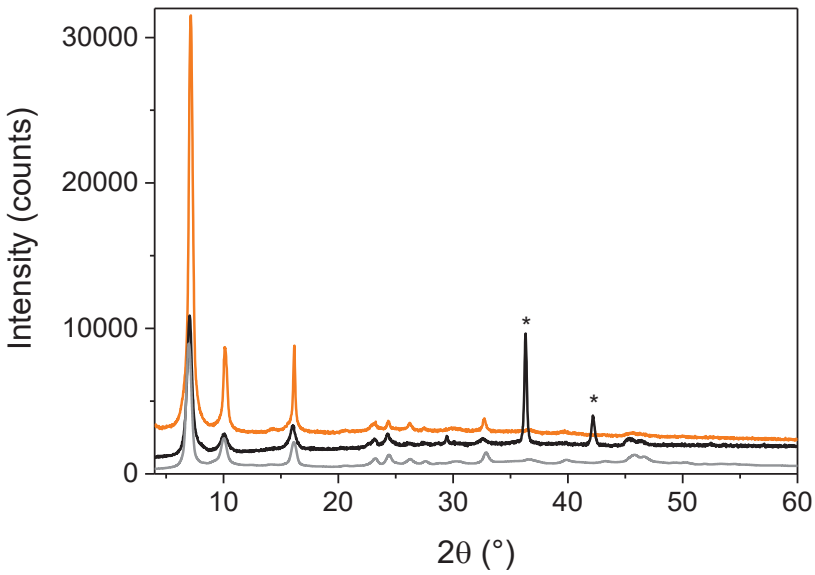

(a)

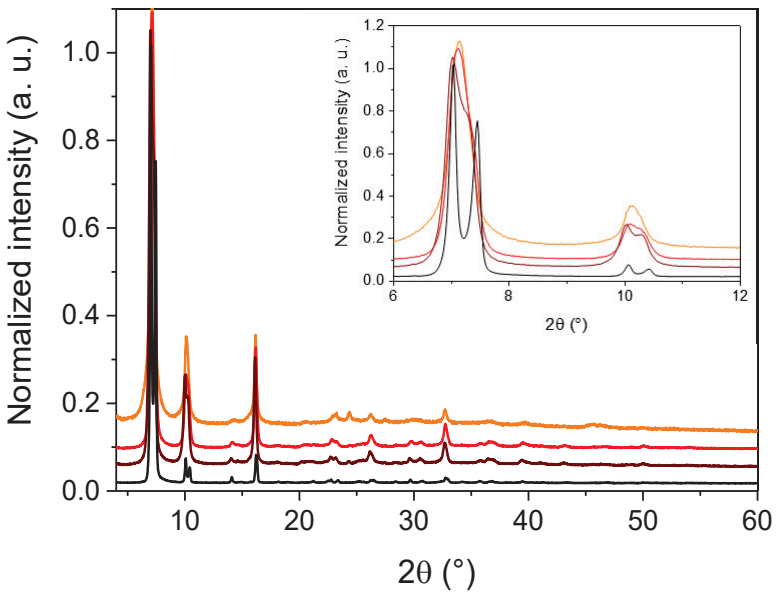

(b)

Figure 1. 1 The PXRD patterns of (a) reported $[Cu(SPh)]_n$ (grey line, digitized from Che *et al.*, 2008[1]) and synthesized samples – **A** (black) and **1** (orange), black asterisks correspond to unreacted Cu_2O; (b) synthesized samples **1** (orange), **2** (red), **3** (dark red) and **4** (black). A zoom at low angles is shown as inset.

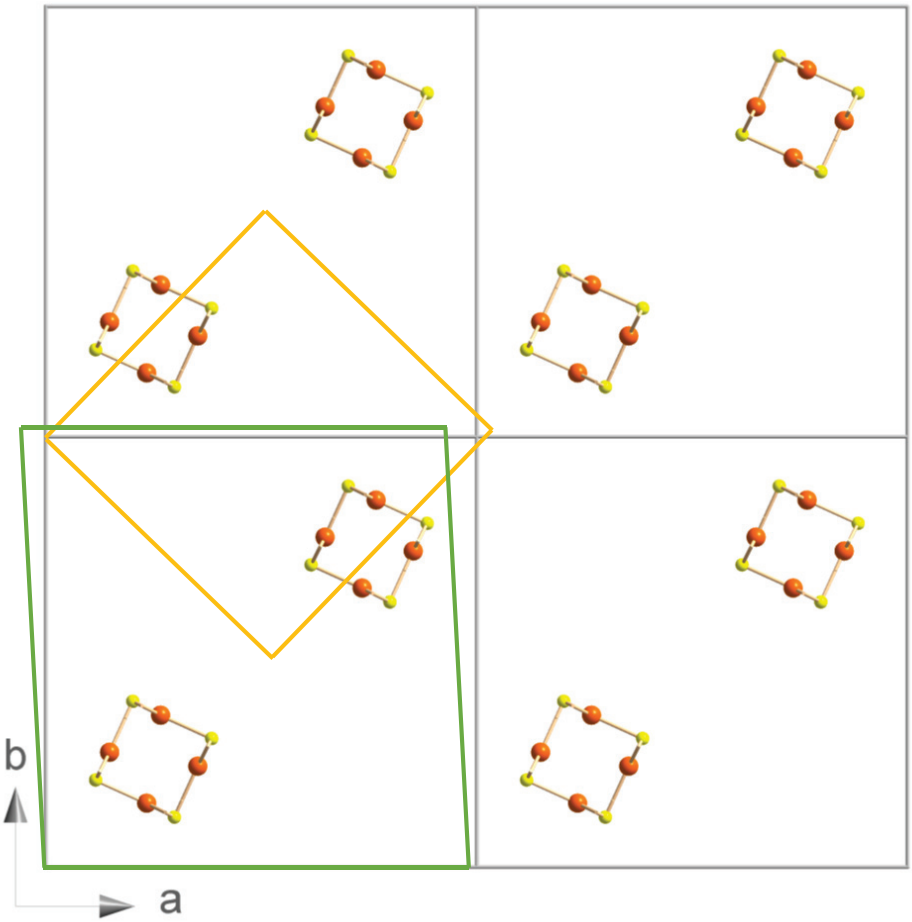

Figure 1. 2 The view on the $[Cu(SPh)]_n$ structure according along the *c* axis. In grey cell edges of the reported *P* $4_2/n$ cell are presented, in green – *P* 2_1 (a = 17.584(5) Å, b = 4.33(2) Å, c = 16.956(5) Å, β = 93.35(1)°, Gof = 15) and in yellow – *P* -1 a = 7.40(3) Å, b = 12.44(1) Å, c = 12.558(4) Å, α = 92.3(1)°, β = 88.5(2)°, γ = 107.3(2)°, Gof = 21). Orange and yellow spheres represent copper and sulfur atoms, respectively. Organic ligands are omitted for clarity.

Nevertheless, already at this point, some hypotheses concerning the new polymorph of $[Cu(SPh)]_n$ can be proposed: (i) the close positions of the first reflections in **1** and **4** polymorphs suggest similar general structural outline; (ii) the split of first two peaks supposes a disymetrization of the $[CuS]_n$ column; (iii) due to certain "flexibility" of the structure, "intermediate" polymorphic phases are possible (**2** and **3**). This shows the richness of different structures in this family of copper thiolates.

1.2.2 Characterizations

From the SEM images, the powders of all four samples are composed of thin needle-like crystallites of ~20 µm long (**Figure 1. 3**).

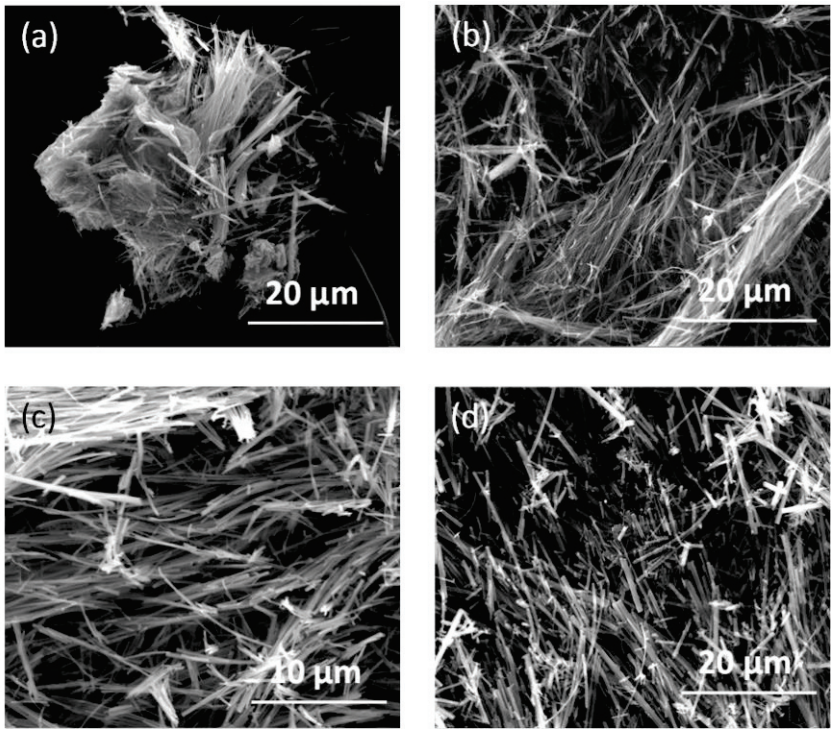

Figure 1. 3 SEM images of $[Cu(SPh)]_n$: (a) **1**, (b) **2**, (c) **3** and (d) **4**.

The FT-IR spectra of all four compounds are quasi-identical and show the characteristic peaks of a thiophenol (**Figure 1. 4**). No peak of S-H stretching vibration around 2550 cm^{-1} is observed, confirming the absence of the free ligand and its coordination to the copper atoms via thiolate groups.

The thermo-gravimetric analysis confirms the purity of the compounds with an expected metal and organic content. An increase of thermal stability is observed in the line: phase **1** (185°C) – intermediate phases **2** and **3** (220°C) – phase **4** (225°C) (**Figure 1. 5**).

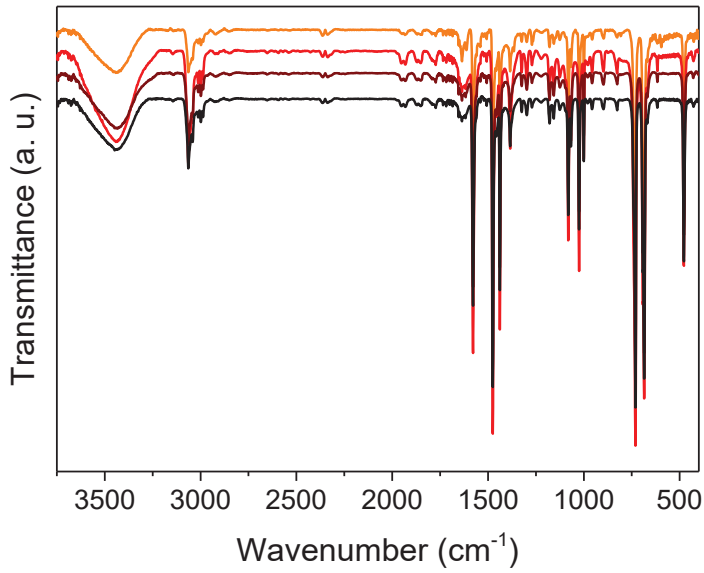

Figure 1. 4 FT-IR spectra of $[Cu(SPh)]_n$: **1** (orange), **2** (red), **3** (dark red) and **4** (black).

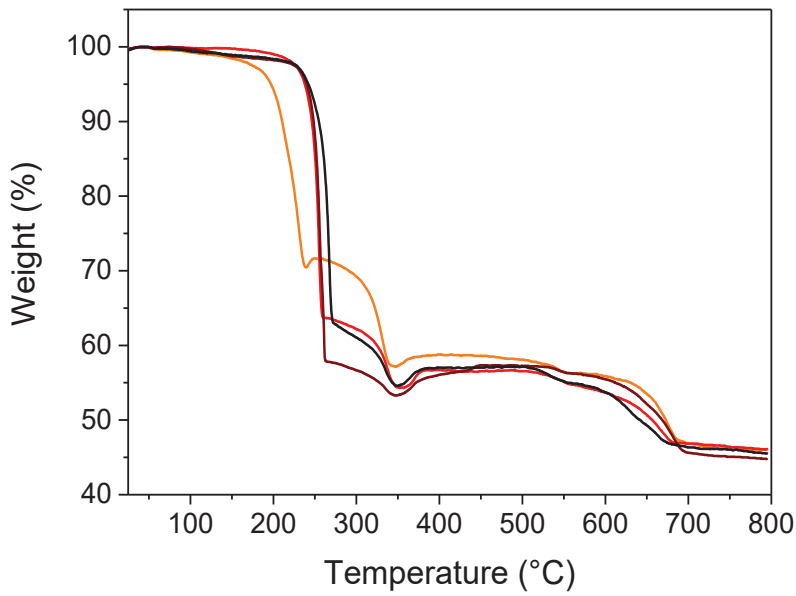

Figure 1. 5 The TGA performed under air at 10°C/min of $[Cu(SPh)]_n$: **1** (orange), **2** (red), **3** (dark red) and **4** (black).

1.2.3 Luminescent Properties

All four compounds have a broad absorption band extending from 200 to 500 nm responsible for the yellow sample color (**Figure 1. 6**). The measured optical band gap is 2.42 eV and is close to the reported value (2.59 eV).[1]

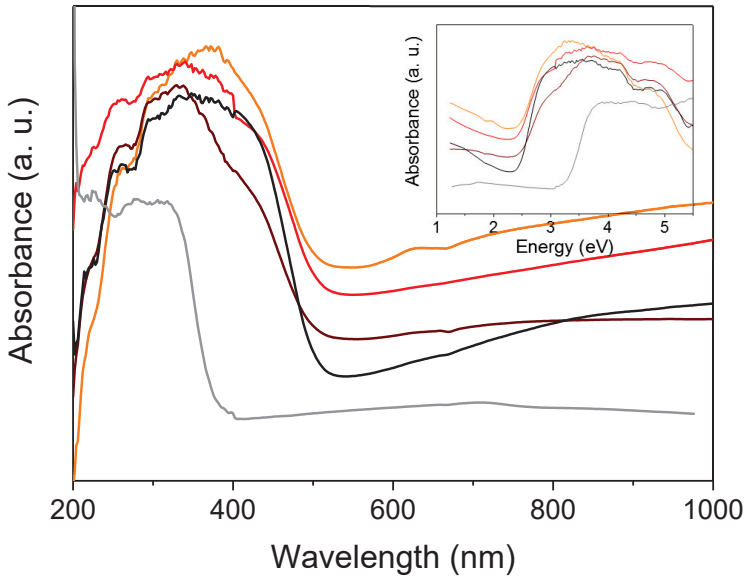

Figure 1. 6 UV-vis absorption spectra of $[Cu(SPh)]_n$: **1** (orange), **2** (red), **3** (dark red), **4** (black) and $(SPh)_2$ (gray) carried out in solid state at room temperature. UV-vis absorption spectra as function of energy are shown as inset.

The excitation of all four compounds with UV light in solid state at the room temperature results in bright orange emission (**Figure 1. 7** (a)). The measured excitation peak maxima are positioned at 440 nm with a broad shoulder at 375 nm for all the four compounds at 293 K (**Figure 1. 7** (b)). The emission peak maxima are positioned at 667 nm, 655 nm, 657 nm and 651 nm for **1**, **2**, **3** and **4** respectively. While the peak profiles are identical for **2**, **3** and **4**, phase **1** possesses a broad shoulder at 850 nm (**Figure 1. 7** (c), (d)).

The energies of the three separate apexes of the excitation peaks at 416, 440 and 464 nm are in agreement with the reported values of ^3D triplet sublevels of a free Cu(I) ion (compare reported 21929, 22847 cm^{-1} and 23988 to observed 21552, 22727 and 24038 cm^{-1}).[7] Thus, the MC $3d^9 4s^1$ transition is expected. The shoulder at 350 nm can be assigned to a π–π* transition of the phenyl group of the ligand.[8]

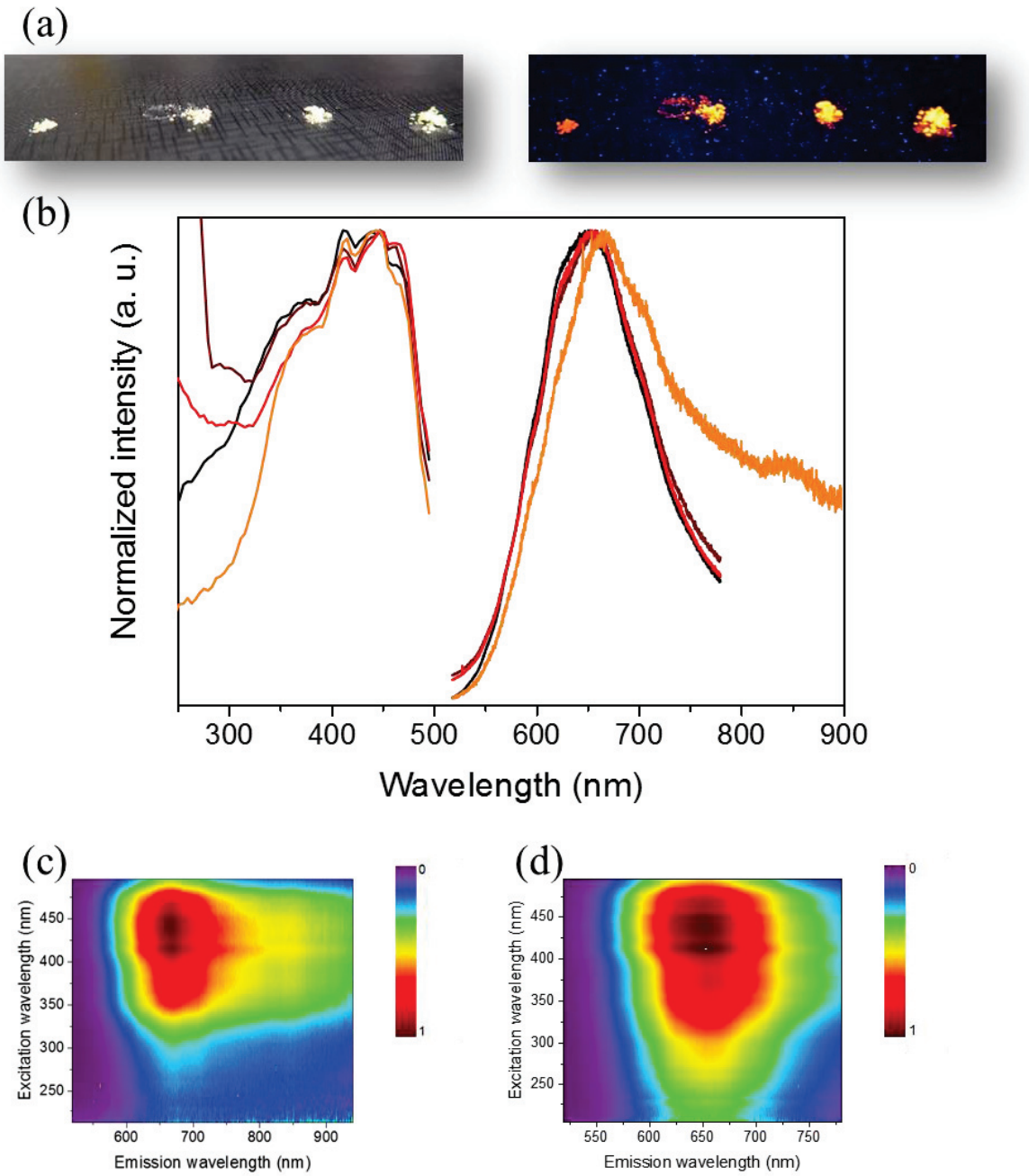

Figure 1. 7 Luminescent properties of $[Cu(SPh)]_n$: (a) photographs of products **1**, **2**, **3** and **4** from left to the right under ambient light (left) and UV lamp (right) in solid state at 293 K; (b) normalized emission-excitation spectra: **1** (orange), **2** (red), **3** (dark red) and **4** (black) obtained in the solid state at 293 K; 2D maps of the emission and excitation spectra obtained in the solid state at 93 K of phases (c) **1** and (d) **4**.

The broad unstructured emission peak at ~655 nm (for all the four compounds) and one at 850 nm (phase **1**) are tentatively assigned to originate from different sublevels of ^{3}LMCT. Assignement was made on the basis of good σ-donating capability of the thiolate ion. An admixture of ^{3}MC states modified by copper-copper interaction is possible.[9] In the reported

structure of $[Cu(SPh)]_n$, the shortest Cu-Cu contacts are of 2.956(4) Å,[1] and are bit too long for ground-state bonding interactions. However, they might contract in the excited state and cause the low-energy visible emissions, as it was suggested for other Cu(I) systems.[10]

If we compare reported emission peaks of $[Cu(SPh)]_n$ and $[Cu(SePh)]_n$,[2] we see that the one belonging to $[Cu(SePh)]_n$ has lower emission energy. This observation supports the assignment of the luminescence decay path through ^{3}LMCT states, considering that the filled ligand-based orbitals are at lower energy for thiolate than selenoate ligands.[11] This assignment is in agreement with one proposed by the authors.[2] It is also important to note that excitation peak maxima coincide for both compounds. Its independence from the ligands nature advocates the suggestion that excitation occurs via MC states.

During temperature decrease all the four compounds experience similar emission peak shift: firstly, when temperature is lowered from high temperature to ~213 K, peak is blue shifted, whereas at even lower temperatures it is red shifted (**Figure 1. 8** (a)-(e)).

Blue shift between 383 K and 213 K can be explained in terms of rigidochromism. The temperature decrease suppresses the geometry distortions. The geometry distortions are progressively more difficult to occur when temperature is lowered. This leads to the more important separations of MOs and blue shift of the emission maximum.[12] A suppression of thermal vibrations at low temperature can contribute to blue shift of emission as well.

During further temperature decrease (below 213 K) the emission peak maximum is red shifted. This observation is often encountered in coinage metal complexes.[13,14,15] It is caused by contraction of Cu-Cu contacts in crystalline structure at low temperature. Such contractions are known to lower the emission energy.[16] The red shift is the most pronounced for the intermediate phases **2** and **3**, it is less important for **1** and **4**. It can be speculated that **1** and **4** are structurally more stable and experience less Cu-Cu shortening than “intermediate”, more “flexible”, phases **2** and **3**.

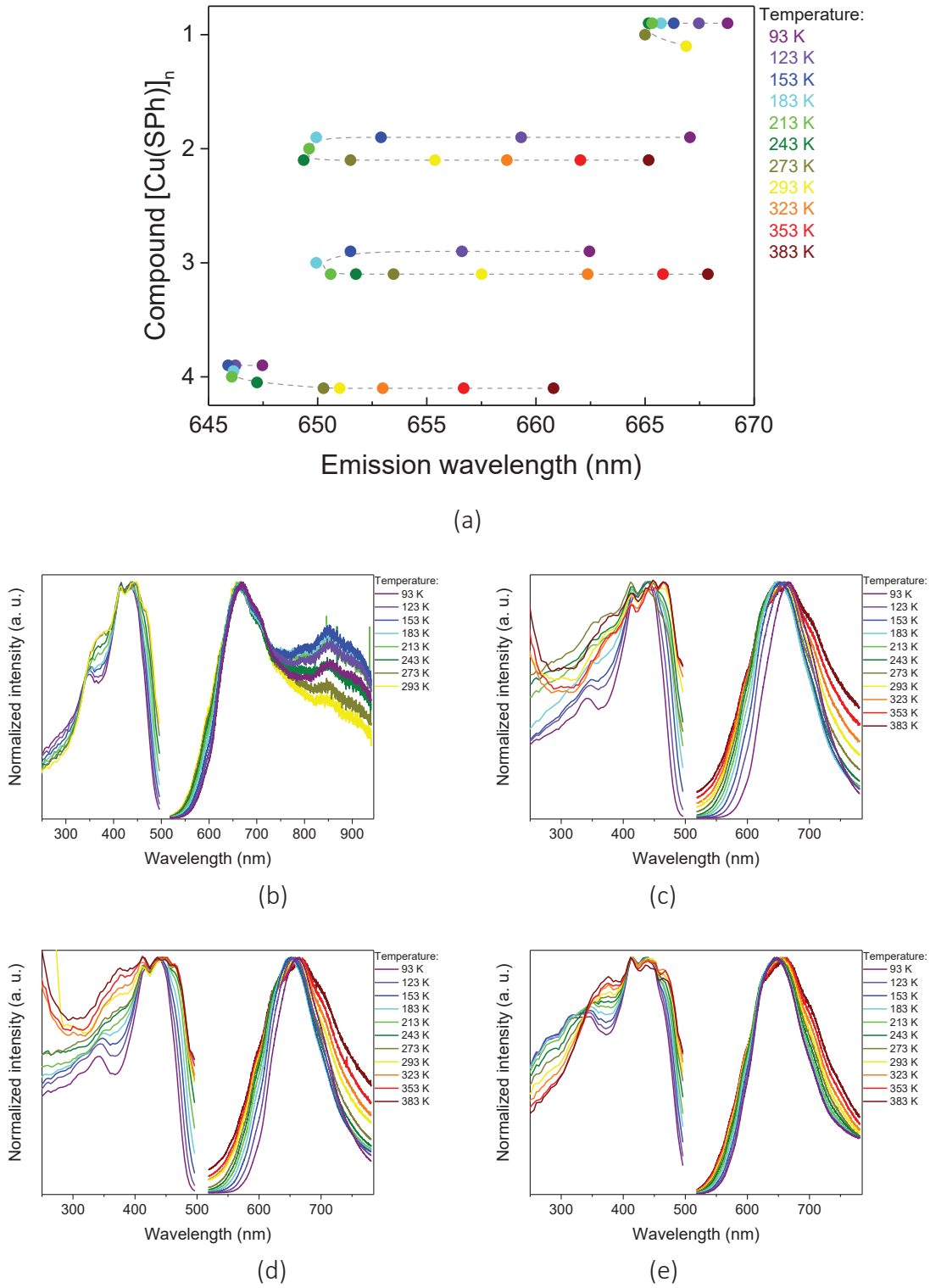

Figure 1. 8 Evolution of the luminescent properties of $[Cu(SPh)]_n$ at different temperatures in the solid state: (a) plot describing shift of the emission peak maximum, solid circles represent maxima' positions, whereas a color is indicator of temperature; normalized emission-excitation spectra of $[Cu(SPh)]_n$: **1** (b), **2** (c), **3** (d) and **4** (e).

The emission peak shift is a result of the competition between the rigidification of the structure and the metallophilic interactions, where the first one is dominant at high temperature (above 213 K), and the second one at low temperature (below 213 K). Such peculiar behavior has been observed previously in Cu(I)-alkynide clusters $[Cu_{16}(tBuC{\equiv}C)_{12}(CF_3COO)_4(CH_3OH)_2]$[17] and Ag(I)-based coordination network, $[Ag_2(pz)(bdc){\cdot}H_2O]_n$ (pz = pyrazine and H_2bdc = benzene-1,3-dicarboxylic acid).[18]

All four compounds have a predominant microsecond-range lifetime component (over 90 %) (**Figure 1. 9** and Appendix B). Microsecond-range lifetime, as well as significant values of Stokes shift (~7 300 cm^{-1}) confirm triplet emission parentage. It is worth paying attention to the fact that lifetime of intermediate phases **2** and **3** are significantly higher at low temperature than the ones of **1** and **4**.

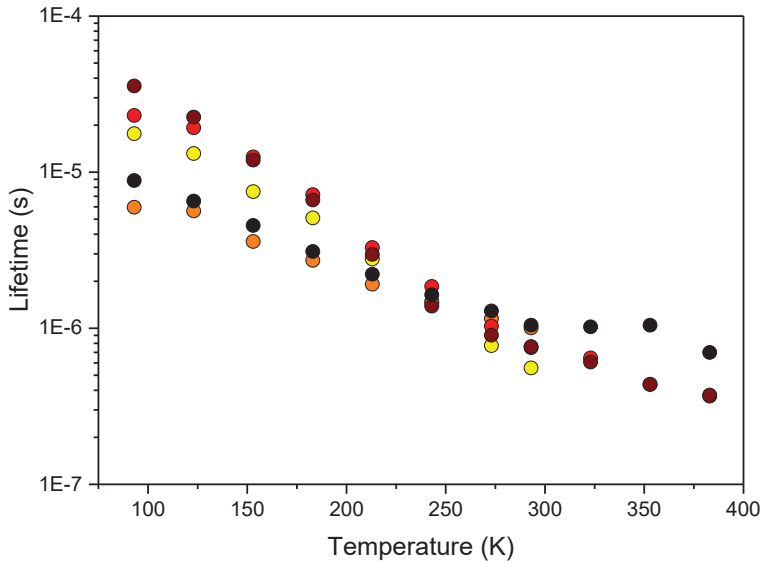

Figure 1. 9 Evolution of predominant lifetime component of $[Cu(SPh)]_n$: **1** (λ_{em} = 670 nm, orange filled circles; λ_{em} = 850 nm, yellow filled circles), **2** (red filled circles), **3** (dark red filled circles) and **4** (black circles) at various temperatures.

The lifetimes of all four compounds experience significant shortening with the temperature increase. This shortening is a typical temperature quenching behavior. It results from thermal activation of the non-radiative decay pathways.[19,20] The thermal quenching process of the emission can be described by following Arrhenius equation (1.1) (**Figure 1. 10**):

$$\tau_T = \frac{1}{\sum k + Ae^{-\frac{\Delta E}{k_B T}}} \quad \text{(Eq. 1.1)}$$

here, τ_T is an emission lifetime at the temperature *T*; $\sum k$ is the sum over all radiative and non-radiative rate constants, which do not involve an activation barrier, *A* is a pre-exponential factor, ΔE is the activation energy for the non-radiative decay and k_B is the Boltzmann constant.[21, 22] This equation is often used to describe the thermal lifetime behavior of transition metal complexes (Fe, Ru, Os).[21, 23, 24] Addition of another exponential term allows to account for more processes and to describe more complicate systems. For example, for Ru- and Os-complexes, Jablonski diagram is well understood and the nature of excited states is known. Therefore, it is possible to reconstruct relative energetic positions of excited states with the fitted data.[21,25, 26]

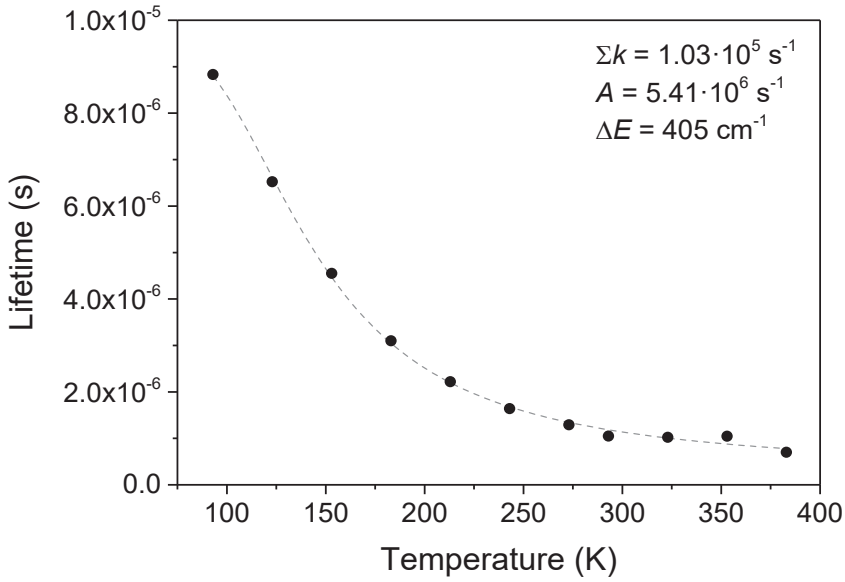

Figure 1. 10 Temperature dependent lifetime of $[Cu(SPh)]_n$ **4** (black circles). Gray dashed line represents a fit according to the Equation (1.1), with refined values displayed in top right corner in the figure.

Such fit was performed for phosphinine copper(I) halide complexes in order to interpret the temperature dependent lifetime behavior.[12] Activation energy for their non-radiative decay is close to the case of the compound $[Cu(SPh)]_n$ **4**. Similar situation with at least three-level system was described for the trinuclear copper(I) arenethiolate complex.[27] However, the extended systems are less understood because of the complexity of their luminescent processes. Such analysis will not be performed in further discussion.

Let us note, that emission peak of phase **1** at 850 nm has lifetime significantly different to the one from the main emission peak. The excitation profile of both peaks are similar (**Figure 1. 11**). It implies that the excitation route is the same for the two bands, but they decay independently. This is in agreement with assignment of emission to different sublevels of the emitting "triplet" excited state that is split by spin-orbit coupling.[10]

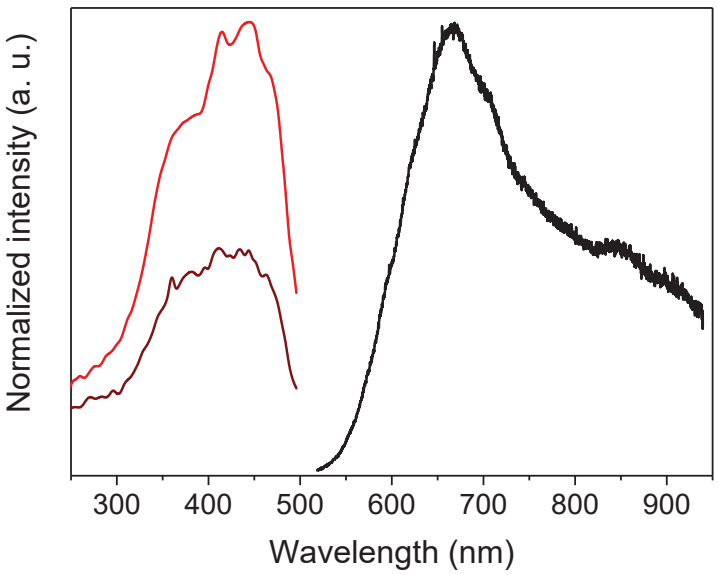

Figure 1. 11 Luminescent properties of $[Cu(SPh)]_n$ **1**: emission (black line, λ_{exc} = 440 nm) and excitation (red line, λ_{em} = 670 nm; dark red line, λ_{em} = 850 nm) carried out in the solid state at 293 K.

$[Cu(SPh)]_n$ provides a lot of interesting observations of photophysical behavior. Several assumptions were made in this discussion. In work to follow we expect to get deeper insight into the structure of all phases. It will help us to unambiguously correlate their structural variations (bond length, structure dissymetrization) and their photophysical properties.

1.3 $[Ag(SPh)]_n$ Phases

1.3.1 Synthesis and Structural Investigation

The structural model of $[Ag(SPh)]_n$ was proposed in 1991 by I. G. Dance *et al.*[3] In the same article, the synthetic procedure was described. The product was precipitated by addition of a solution of $AgNO_3$ in acetonitrile to a solution of the thiophenol in presence of trimethylamine.

In order to obtain a product of sufficient crystallinity for the structure determination, we tried to optimize the synthetic parameters. Polarity of solvents (H_2O, MeOH, DMF) and the temperature have impact on the formation of the product. This influence was studied and is depicted in **Figure 1. 12** (a)-(c) and **Table 1. 1**. The primary goal was to improve the crystallinity of the product. However, our study has shown that according to the conditions, three distinct polymorphs of lamellar structure with various spacing (14.0, 14.7 and 15 Å) are formed (see inset of **Figure 1. 12** (a)). From now, we will call them phase **1**, **2** and **3**, respectively.

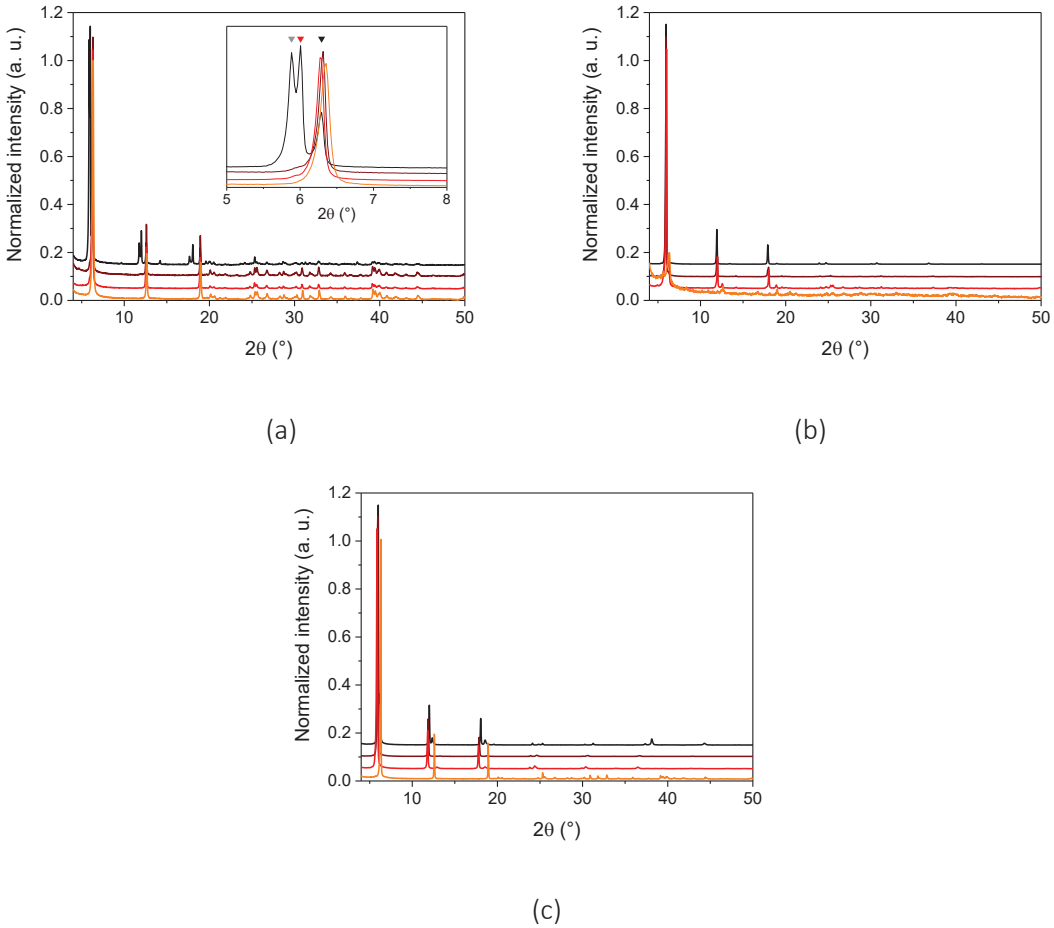

Figure 1. 12 The PXRD patterns of $[Ag(SPh)]_n$ synthesized in (a) H_2O (a zoom at low angles is shown as inset. Solid triangles indicate peaks corresponding to phase **1** (black), **2** (red) and **3** (grey)), (b) MeOH and (c) DMF at 120°C (black), 90°C (dark red), 60°C (red) and the room temperature (orange).

Table 1. 1 The formation of $[Ag(SPh)]_n$ phases in different synthetic conditions.

Solvent / Temperature	H_2O (1)†	MeOH (0.762)†	DMF (0.386)†
120°C	1, 2, 3	2	1, 2
90°C	1	2	2
60°C	1	1, 2′	**2**
Room temperature (~ 20°C)	**1**	2′′	1

† relative polarity, ′ traces,′ poor crystallinity

A formation of phase **1** is favored in water and low temperatures, whereas phase **2** is favored at higher temperatures and solvents of lower polarity. The formation of phase **3** was observed only in water at 120°C. We could isolate only phases **1** and **2**, thus in following only pure phases will be discussed (**Figure 1. 13**). The PXRD pattern of the phase **1** corresponds to the diffractogram reported by I. G. Dance *et al.*[3]

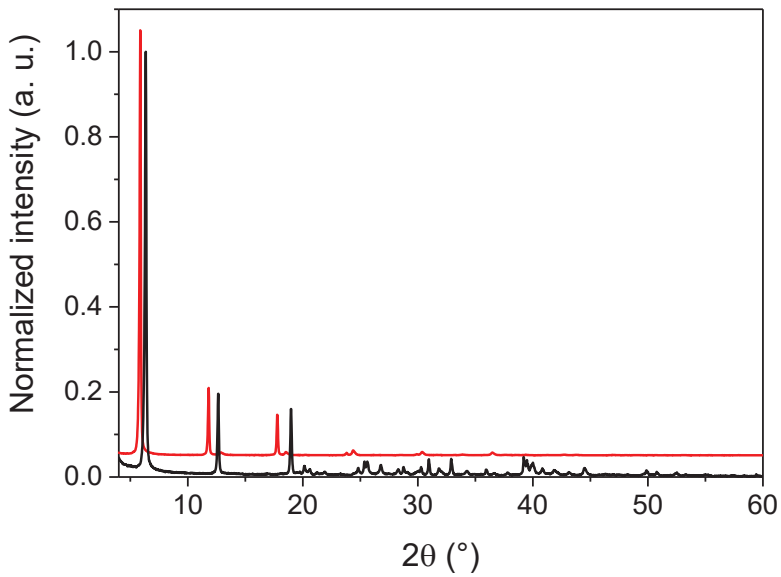

Figure 1. 13 The PXRD patterns of phases **1** (black line) and **2** (red line) of $[Ag(SPh)]_n$.

For both phases, high resolution X-ray powder diffraction data were collected at the CRISTAL beamline at Soleil Synchrotron (Gif-sur-Yvette, France). For the phase **1** the indexation converged unambiguously to a crystallographic cell, whereas for the phase **2** it did not. Thus, the structural determination could be performed only for the phase **1**.

Structure of [Ag(SPh)]$_n$ phase 1. The structure determination resulted in a $P2_1/c$ unit cell with a = 7.3316(1) Å, b = 5.91817(6) Å, c = 28.2311(4) Å, β = 93.700(4)°, what is different from the one reported by I. G. Dance (a = 8.70 Å, b = 14.06 Å, c = 4.35 Å, β = 120°). [3]

This structure is related to the one of [Ag(SePh)]$_n$.[4] Both compounds have a lamellar structure. The layers are composed of silver atoms in a distorted tetrahedral coordination. While in [Ag(SePh)]$_n$ all Ag-Se distances are close (**Figure 1. 14** (a)), in [Ag(SPh)]$_n$ one of Ag-S distances is too long to be considered a covalent bond (2.983(4) and 3.055(3) Å) (**Figure 1. 14** (b)). Thus, considered only the covalent bonds, we see a distorted hexagonal tile forming Ag(I)-S layers in [Ag(SPh)]$_n$ (**Figure 1. 14** (c)). The individual hexagons are folded along the shortest diagonal forming a dihedral angle ϕ of 134.9(1)°. It can be seen as highly distorted boat conformation (**Figure 1. 14** (d)). Therefore, the resolved structure still resembles the one proposed by I. G. Dance *et al.*[3] (see State of the Art I.1.4).

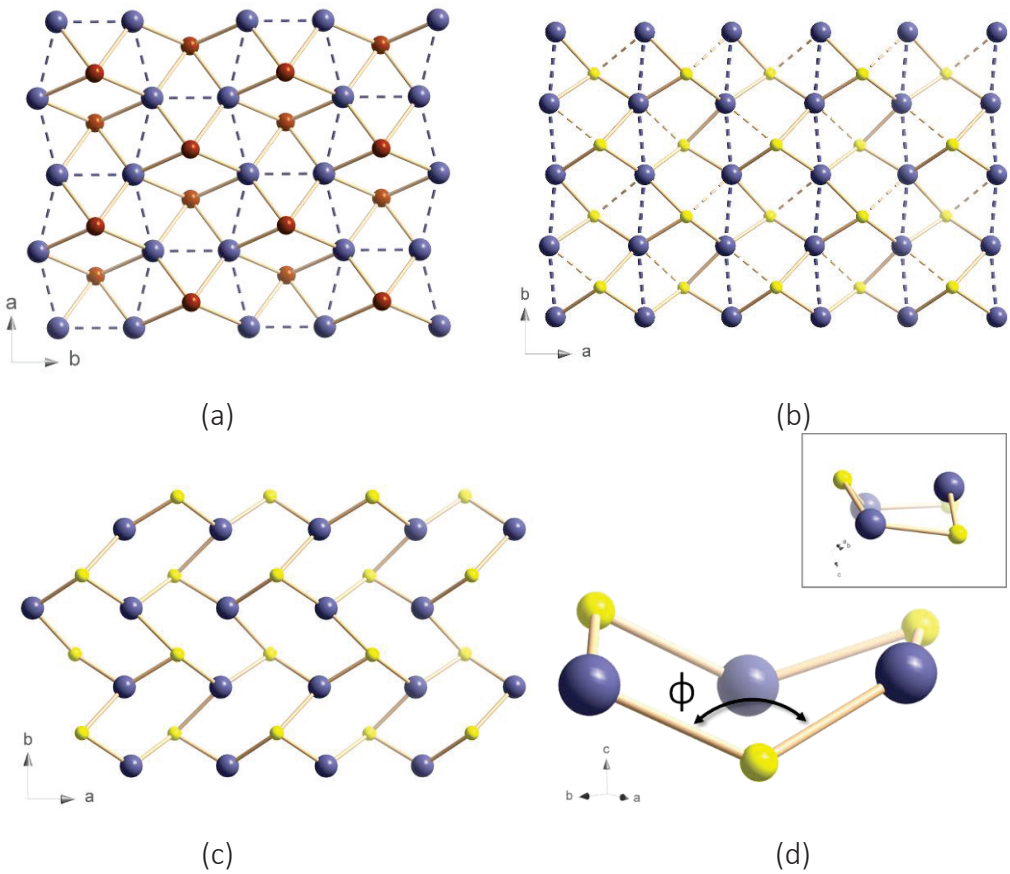

Figure 1. 14 Comparison of Ag-S/Se layers of (a) [Ag(SePh)]$_n$ and (b) [Ag(SPh)]$_n$ phase **1**, (c) view on underlying hexagonal arrangement of [Ag(SPh)]$_n$, (d) view on hexagon of [Ag(SPh)]$_n$, view on a boat conformation as inset. Blue, Ag; yellow, S; brown, Se. Blue dashed lines represent the metallophilic interactions. Tan dashed lines represent long Ag-S contacts.

The ligands are at ~80° angle to the Ag-S/Se plane and situated both above and below the plane without interpenetration of the phenyl groups in the interlayer space (**Figure 1. 15**). The long centroid–centroid distances between the adjacent phenyl rings imply an absence of π-π interactions (**Table 1. 2**). Short Ag-Ag contacts, which can be considered as metallophilic interactions, are found in both compounds.[28] In $[Ag(SPh)]_n$, they are 2.963(4) and 2.981(4) Å, and in $[Ag(SePh)]_n$ – 2.911(2) and 3.030(1) Å. However, their layout is different. While, in $[Ag(SePh)]_n$, Ag-Ag interactions form 2D-network composed of distorted Ag_6 hexagons, in $[Ag(SPh)]_n$, the Ag-Ag interactions form 1D-chain with quasilinear angles (169.3(2)°) (**Figure 1. 14** (c)).

Table 1. 2 Comparison of the main distances and angles in $[Ag(SPh)]_n$ (phase **1**) and $[Ag(SePh)]_n$.

Compound	Ag-E, Å	Ag-Ag, Å	E-Ag-E, °	Ag-E-Ag, °	π-π, Å
$[Ag(SPh)]_n$ phase 1	2.454(3)	2.963(4)†	87.4(1)′	62.9(1)′	5.918(1)
	2.490(3)	2.981(4)†	87.9(9)′	64.1(1)′	
	2.566(3)	3.687(5)†	94.9(1)	71.5(1)	
	2.577(3)	3.712(5)†	95.4(1)	72.0(1)	
	2.599(4)		102.6(1)′	81.4(1)′	
	2.614(3)		102.8(2)′	82.7(1)′	
	2.983(4)′		114.3(1)′	92.8(1)	
	3.055(3)′		118.7(1)′	95.3(1)	
			119.8(2)	122.7(1)	
			121.5(2)	123.2(1)	
			130.9(2)	127.4(1)′	
			136.1(2)	127.8(1)′	
$[Ag(SePh)]_n$	2.694(1)	2.911(2)†	75.6(3)	65.4(1)	4.685(3)
	2.698(1)	3.030(1)†	75.8(1)	67.1(1)	
	2.776(1)		112.8(1)	67.3(1)	
	2.782(1)		112.9(1)	104.3(1)	
			114.5(1)	117.7(1)	
			114.8(1)		
			117.7(1)		

† bridged by sulfur atoms.

′ long Ag-S contact involved.

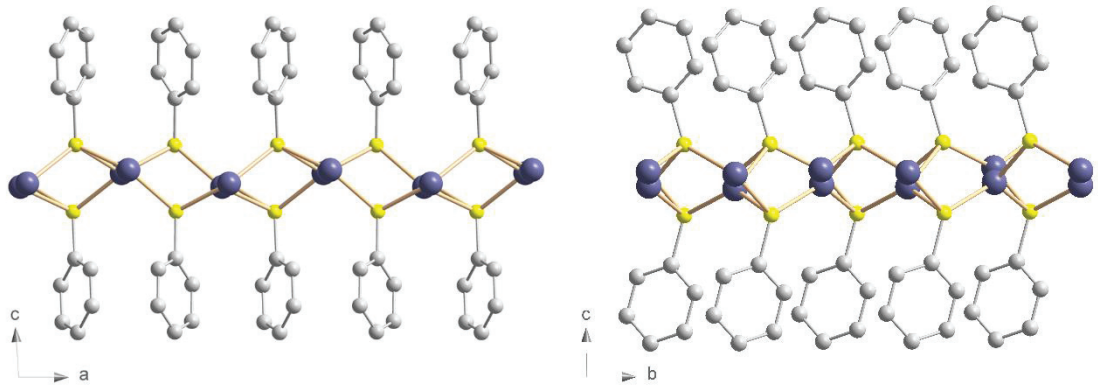

(a) (b)

Figure 1. 15 Structure representations of $[Ag(SPh)]_n$ phase **1**. Views on (a) *(ac)* and (b) *(bc)* plane. Blue, Ag; yellow, S; grey, C. Hydrogen atoms are omitted for clarity.

A structural unit of (μ_4-S)Ag(I) was described by V. W.-W. Yam *et al*. in 1996.[29] They have reported clusters formed by four silver(I) ions in a distorted rectangular array. They are quadruply bridged by an unsubstituted chalcogenido ligand. Discussed lamellar structure can be seen as highly distorted extended array formed by fusion of individual (μ_4-chalcogenoate)Ag(I) clusters. In average, Ag-Ag distances are *cca.* 3.1 Å in the cluster. The distances in Ag-Ag chain of $[Ag(SPh)]_n$, are only slightly shorter – *cca.* 3.0 Å, whereas distances between chains are 3.7 Å.

$[Ag(SPh)]_n$ phase 2. As it was stated above, the indexation did not converge unambiguously to any unit cell for the phase **2**. This prevented a further structure investigation. The structure of phase **2** is clearly lamellar. Slightly bigger interlamellar spacing in comparison to phase **1** suggest a quasi-perpendicular positioning of thiophenolate ligands relatively to Ag-S layer.

1.3.2 Characterizations

Based on the SEM images, the crystallites of the phase **1** are thin platelets of sub-micrometer size and of the phase **2** – elongated thin pellets of ~5 µm size (**Figure 1. 16**).

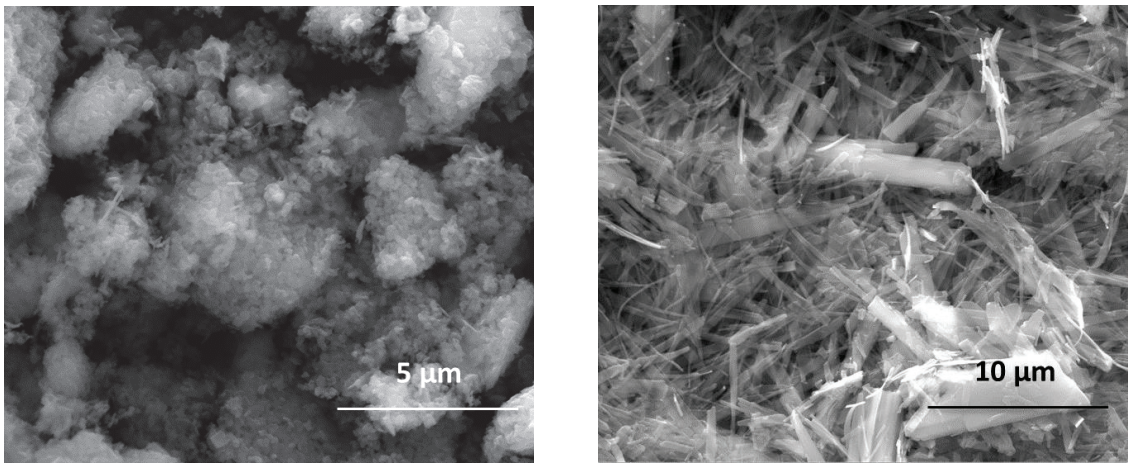

(a) (b)

Figure 1. 16 SEM images of $[Ag(SPh)]_n$: (a) phase **1** and (b) phase **2**.

FT-IR spectra of phases **1** and **2** and their comparison with spectrum of $[Cu(SPh)]_n$ show a number of important differences (**Figure 1. 17**). In particular, appearance, intensification and broadening of number peaks. The FT-IR spectra were recorded for a set of different batches of product. This excludes presence of impurities, dependence on synthetic procedure, etc. and confirms the reproducibility of the observations.

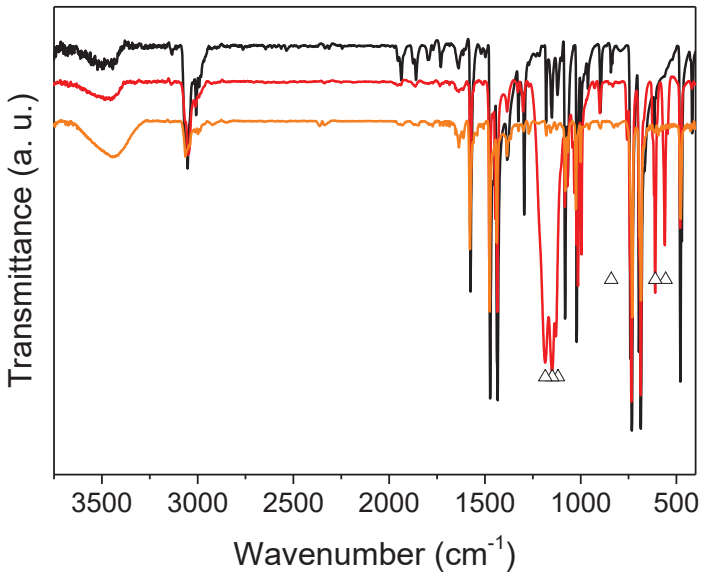

Figure 1. 17 Comparison of FT-IR spectra of $[Ag(SPh)]_n$: phase **1** (black) and phase **2** (red) with $[Cu(SPh)]_n$ (orange).

We have observed a specific category of peaks present in one or both $[Ag(SPh)]_n$ phases (556, 610, 840, 1118 cm^{-1}) which are quasi-absent in FT-IR of $[Cu(SPh)]_n$. They all belong to X-

sensitive vibrations (where X stands for substituent in monosubstituted benzene).[30,31] There are particularities of crystalline packing of lamellar 2D structure of silver-based coordination polymers relatively to copper-based monodimensional counterpart. These particularities seem to be related to the fact that all these vibrations are involving movement of substituent. Lamellar structure favors dipole moment change during vibration of concerned bonds, and thus could increase an intensity of these peaks.

Broadening and intensity increase of peaks at 1148 and 1184 cm^{-1} are observed in the case of the phase **2**. These peaks correspond to C-H in-plane deformation. This suggests particularity of crystalline packing of the phase **2** relatively to the phase **1**, and can be understood in terms of increased C-H interaction, for example.

Another hypothesis can be proposed to explain the different intensity ratios. Some of the vibrations were shown to have high dichroic ratios, meaning that their intensities are strongly dependent on the crystallite orientation. For example, a study performed on KBr pellet and crystals of biphenyl showed, that a change of the crystal orientation by 90° could cause some peaks to decrease their intensity from maximal value to practically zero intensity.[32] The crystallites of the phase **2** have high preferred orientation and they align themselves predominantly in the same direction once KBr pellet is exposed to the pressure, while orientation of the crystallites of phase **1** are more easily averaged out. Therefore, it is not unreasonable to suppose that the preferred orientation could cause the difference of FT-IR spectra of two phases.

The thermo-gravimetric analysis confirms the purity of the compounds with an expected metal and organic content. Both phases start the decomposition at 235°C (**Figure 1. 18**).

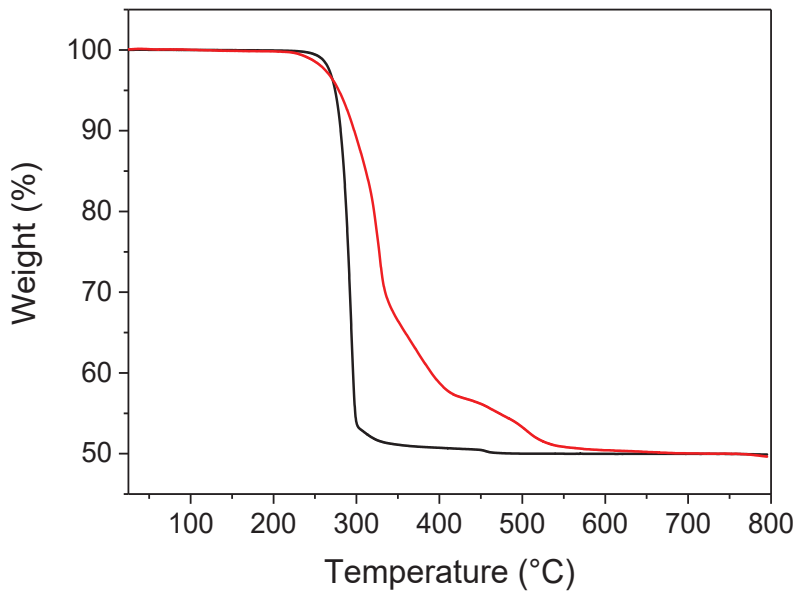

Figure 1. 18 The TGA performed under air at 10°C/min of $[Ag(SPh)]_n$: phase **1** (black) and phase **2** (red).

1.3.3 Luminescent Properties

Both compounds have a broad absorption band extending from 200 to 420 nm tentatively attributed to metal perturbed π–π* transition of the phenyl group of the ligand (**Figure 1. 19**). The measured optical band gap is 2.7 and 2.8 eV for the phases **1** and **2**, respectively.

Excitation of the **phase 1 of $[Ag(SPh)]_n$** with UV light in solid state, at room or low (93 K) temperature, does not result in visible emission. However, with extension of measurement time, emission-excitation spectra could be measured (**Figure 1. 20**). There are two excitation maxima at 380 and 432 nm resulting in closely positioned broad emission peaks at 830 and 810 nm, respectively. The presence of two excitation peaks corresponding to the close emission wavelength implies existence of two different excitation paths that decay from the same low-lying emissive state.

Despite structural resemblance with (μ_4-chalcogenoate)Ag(I) clusters, emission properties of the clusters and phase 1 are different. (μ_4-S)Ag(I) clusters emit at 536 nm in solid state at 77 K.[29] Therefore, in a transition from one isolated cluster unit to the fused $[AgS]_n$-system, an important red shift of the emission is observed.

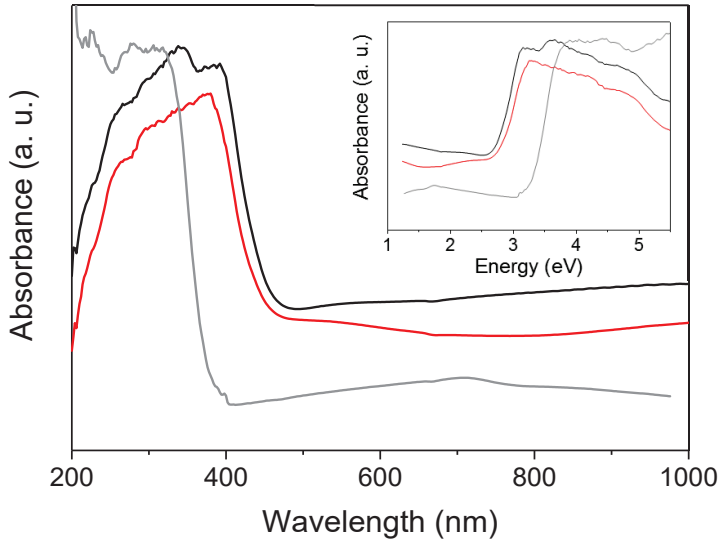

Figure 1. 19 UV-vis absorption spectra of $[Ag(SPh)]_n$: phase **1** (black), phase **2** (red) and $(SPh)_2$ (gray) obtained in solid state at the room temperature. UV-vis absorption spectra as function of energy are shown as inset.

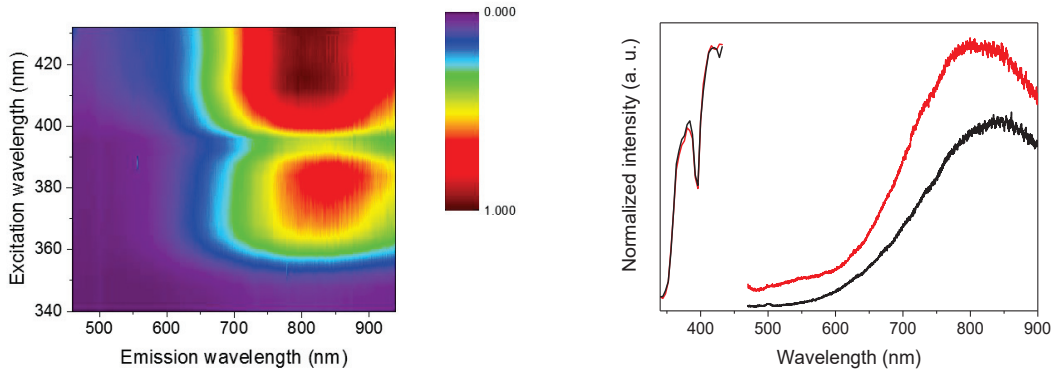

(a) (b)

Figure 1. 20 Luminescent properties of $[Ag(SPh)]_n$ phase **1**: (a) 2D map of the emission and excitation spectra and (b) normalized emission-excitation spectra (λ_{exc} = 380 nm, λ_{em} = 830 nm, black; λ_{exc} = 432 nm, λ_{em} = 810 nm, red) obtained in the solid state at 93 K.

Such a low energy emission is rarely reported for silver(I)-based coordination compounds.[33] Similar photophysical properties were reported for hexanuclear silver(I)thiolate complexes with bridging dppm ligands (bis(diphenylphosphino)methane).[34] They show excitation bands at *cca.* 345–415 nm. The complex with thiophenolate as a ligand, $[Ag_6(\mu\text{-dppm})_4(\mu_3\text{-SPh})_4](PF_6)_2$, exhibits a low energy emission at 746 nm in the solid state at 77 K. The emission origin was assigned to be derived from excited states with an admixture of MMLCT and MC (ds/dp) character. We believe that this assignment can be adopted in our case as well.

The red shift of the excitation and emission peaks for the phase **1** of $[Ag(SPh)]_n$, can be explained by the formation of an extended network of short Ag-Ag interactions.

Shorter metal-metal interactions, along with an increase of metal chain length are known to cause red-shift of an emission coming from MC excited states [16,35, 36 37] In the reported hexanuclear silver(I)thiolate complexes the shortest Ag-Ag distances are of *cca.* 3.3 Å, whereas, in our product, they are *cca.* 3.0 Å. They form quasi-linear infinite chains which contributes to the further ease of the interactions. Therefore, both excitation and emission peaks of $[Ag(SPh)]_n$ are observed at lower energy.

The emission energy of $[Ag(SPh)]_n$ is smaller than the one of $[Ag(SePh)]_n$. It is caused by the electron-richness of the chalcogenolate group: SPh < SePh. Considering the red shift of emission by 9365 cm^{-1} (from 467 nm to 830 nm) and significant drop of emission intensity ($[Ag(SePh)]_n$ is emissive at the room temperature), it seems unlikely that change of the nature of chalcogen atom is the only reason for such drastic change of properties. The change of array of metallophilic interactions from hexagonal tile to the quasi-linear arrangement could also intervene as into decrease of the emission energy. Nevertheless, it is possible, that the real reason escaped our attention.

The lifetime decay curves were registered for both peaks (Appendix B). The data in both cases were fitted with sum of two stretched exponentials. In the both cases the predominant component is the one with a shorter lifetime:

- λ_{exc} = 380 nm, λ_{em} = 830 nm : 0.1 µs (77 %), 71 µs (23 %)
- λ_{exc} = 432 nm, λ_{em} = 810 nm : 0.14 µs (61 %), 46 µs (39 %)

The microsecond-range lifetime and a large Stokes shift of 14270 and 10800 cm^{-1}, point to highly distorted excited states and triplet parentage of the emission.

The discussion of the luminescent properties of the phase **1** of $[Ag(SPh)]_n$ let us suggest that the formation of an extended $[MS]_n$-systems can be a good strategy for synthesis of CPs emitting in red-NIR part of the spectrum. Deeper understanding of the processes is necessary in order to improve the quantum yield and make the product emissive at ambient temperature.

The **phase 2 of $[Ag(SPh)]_n$** shows a photophysical behavior different from the **phase 1**. Excitation of the product by UV light in solid state and at the room temperature does not result

in visible emission. Once the sample is cooled it shows green emission. The excitation peak is quite narrow and its maximum is at 412 nm, whereas, the emission profile is quite broad with its maximum at 540 nm and a shoulder at 750 nm (**Figure 1. 21**). The Stokes shift for the maximum of emission is 6090 cm^{-1}, and for the shoulder – 10940 cm^{-1}.

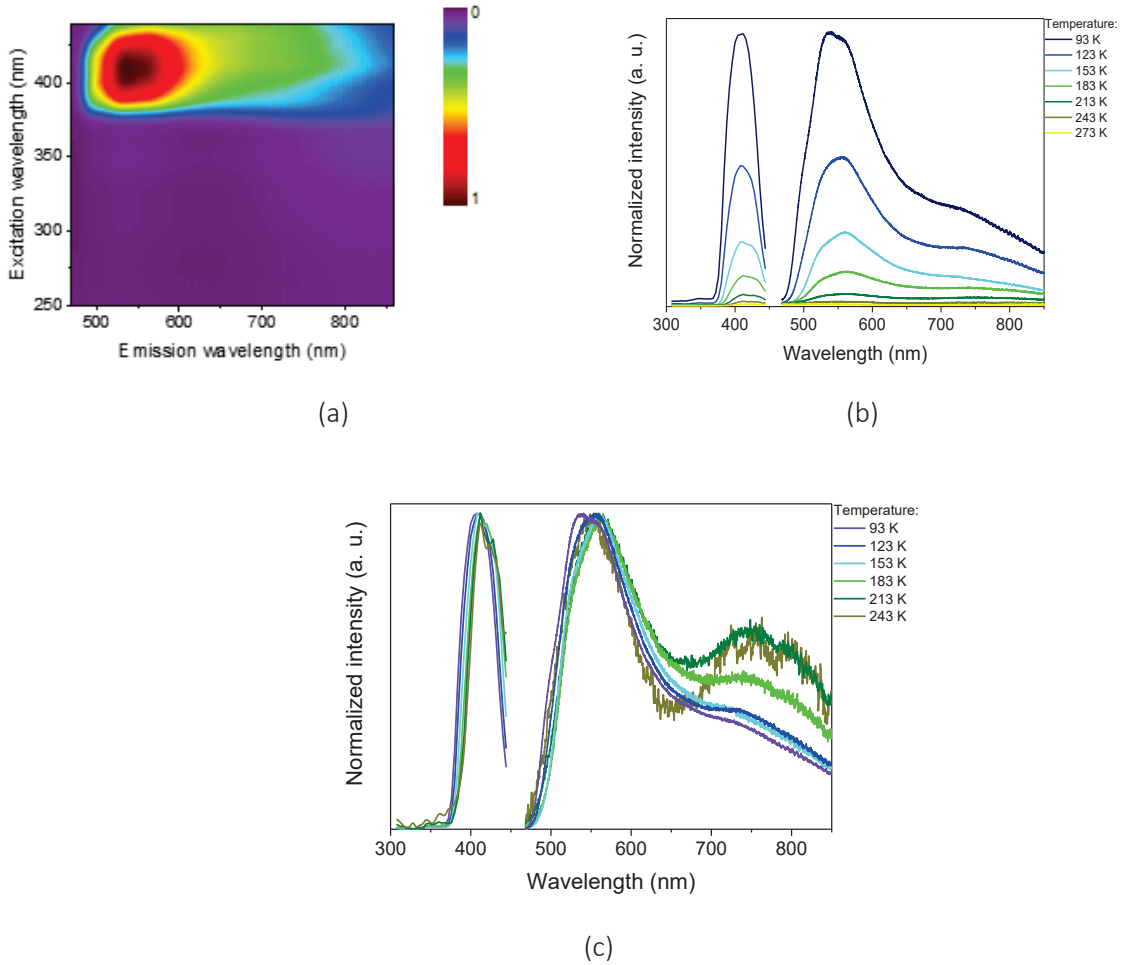

Figure 1. 21 Luminescent properties of $[Ag(SPh)]_n$ phase **2**: (a) 2D map of the emission and excitation spectra obtained in the solid state at 93 K and (b) emission-excitation spectra and (c) normalized emission-excitation spectra (λ_{exc} = 412 nm, λ_{em} = 550 nm) obtained in the solid state at various temperatures.

The lifetime decay curves were measured for both emission peak maximum (550 nm) and its shoulder (750 nm) (Appendix B). At 550 nm, two components are present: one of microsecond- (8.55 µs, 6 %) and one of millisecond-range (1.03 ms, 94 %). At low temperature, millisecond-range component is predominant, but its contribution substantially drops with temperature increase: 1.38 µs (98 %) and 0.92 ms (2 %) at 243 K (**Figure 1. 22**). At 750 nm, three components are present, with long lifetime components which are predominant

(millisecond-range). All lifetime decays for both wavelength experience temperature quenching.

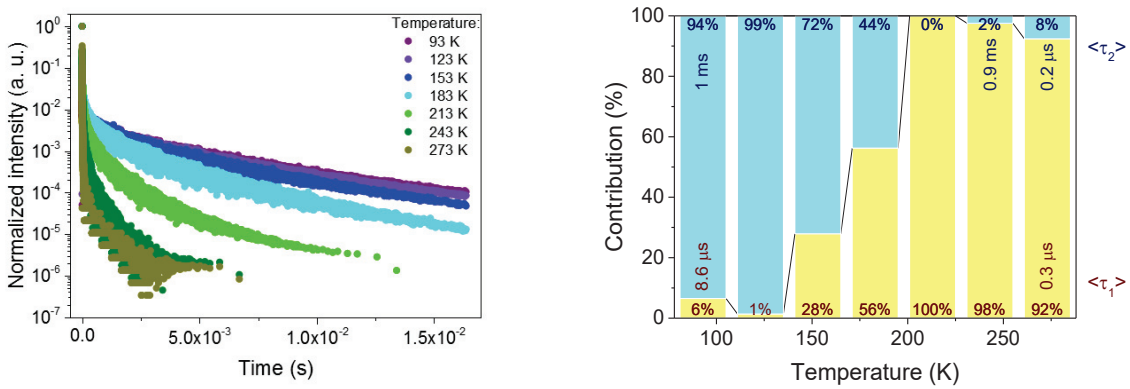

(a) (b)

Figure 1. 22 Temperature-dependent luminescence decays (λ_{exc} = 412 nm, λ_{em} = 550 nm) of the phase **2** of $[Ag(SPh)]_n$ (a) and evolution of contribution of two decay components at various temperatures (b).

By comparison of properties of the phase **1** and phase **2** of $[Ag(SPh)]_n$ (**Figure 1. 23**), it is easy to notice the closely lying absorption and excitation peaks of two phases. This implies a similarity of their excitation pathways. d-s transition of the free Ag^+ ion occurs at relatively low energy (39164 and 40741 cm^{-1} for the lowest energy spin-forbidden and spin-allowed transitions, respectively) [38]. It makes d-s states reasonable candidates for the excited states of these CPs. Ligand coordination is expected to rise s-orbital energies substantially. The metal-metal interactions can lead to substantial splitting of the d- (and especially s-) orbitals in a manner which may lead to marked effects on the expected molecular orbital energies. The stabilization of the lowest energy unfilled s-orbital and corresponding destabilization of the highest energy filled d-orbital lead to the decrease the d→s separation. [39]

Emission spectra are different (**Figure 1. 23**). The shoulder at 750 nm, in case of the phase **2**, has close energy to the emission of the phase **1** (830 nm). Supposedly, the similar decay path is involved in both cases. As explained below, its origin can be also ascribed to ^{3}MMLCT or ^{3}LMMCT states.[34,40] The emitting state at 550 nm can be assigned to mixed ^{3}MC and/or ^{3}LMCT character.[35,39,41] Nevertheless, LC emission origin cannot be completely excluded.

The assignment of emission's origin should be reviewed once the crystalline structure will be determined.

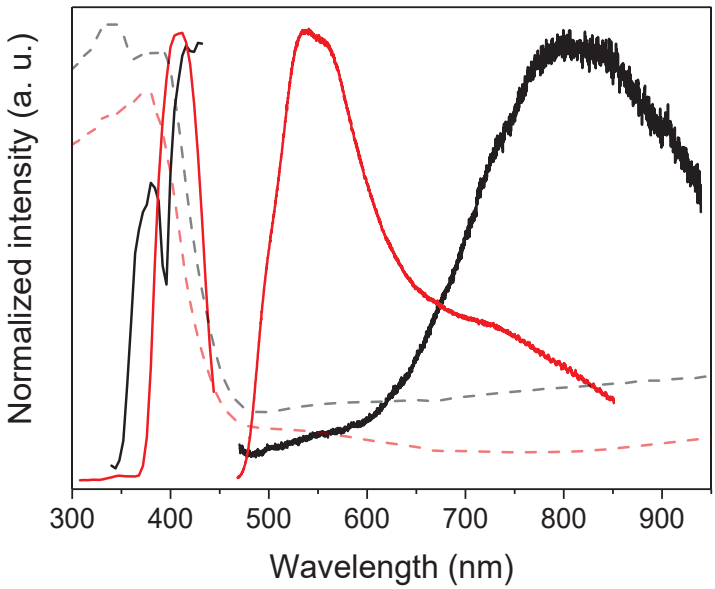

Figure 1. 23 Comparison of emission-excitation spectra of $[Ag(SPh)]_n$ – phase **1** (black line) and phase **2** (red line) obtained in the solid state at 93 K, and of their absorption spectra (in dashed line) measured in the solid state at the room temperature.

1.4 $[Au(SPh)]_n$

1.4.1 Characterizations

The synthetic procedure, photophysical properties and thermal behavior of $[Au(SPh)]_n$ were reported as early as in 2000.[42] Later, in 2009 two of the authors of the article, Robert E. Bachman and Sheri A. Bodolosky-Bettis, have published another study comparing two synthetic routes leading either to amorphous or crystalline $[Au(SPh)]_n$.[43] They identified a unique amorphous-to-crystalline phase change of $[Au(SPh)]_n$ and presented new products with their photophysical properties.

Finally, in 2015 in the framework of collaborative research of our team, the structure of $[Au(SPh)]_n$ was determined.[5] The study of previously mentioned thermally induced phase change was performed. Based on DFT-calculus, LMMCT emission origin was proposed.

Here we will briefly present the variation of photophysical properties with temperature.

The product was synthesized according to the procedure adapted from the article of C. Lavenn *et al.*, 2015.[5] The routine characterizations confirm the synthesis of the targeted product.

1.4.2 Luminescent Properties

Excitation of $[Au(SPh)]_n$ by UV light in solid state and at the room temperature results in bright red emission. At the room temperature excitation and emission maxima are at 340 and at 680 nm, with the Stokes shift of 14700 cm^{-1}. It confirms triplet parentage of the emission (**Figure 1. 24**).

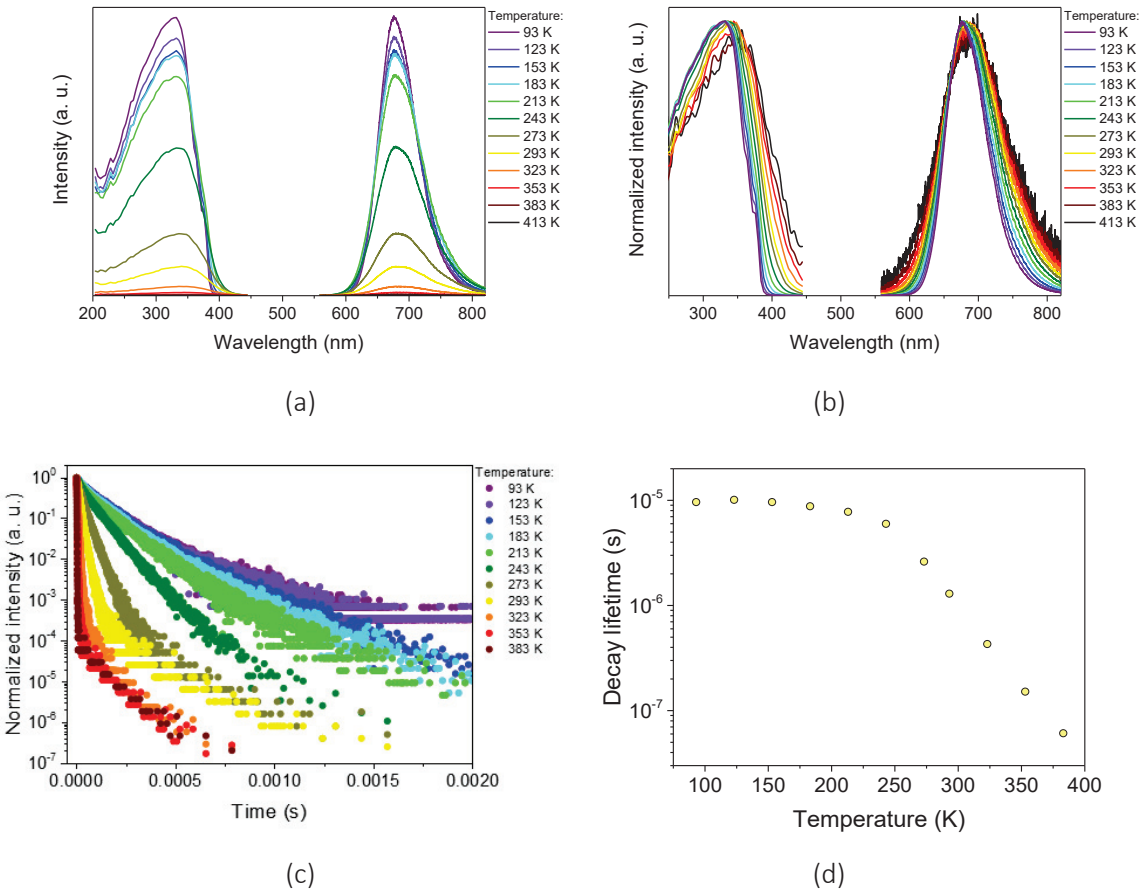

Figure 1. 24 Luminescent properties of $[Au(SPh)]_n$: (a) emission-excitation spectra and (b) normalized emission-excitation spectra obtained in solid-state with the temperature (λ_{exc} = 332 nm, λ_{em} = 675 nm), (c) observed lifetime decay curves and (d) evolution of lifetime of the predominant component with temperature.

Once sample is cooled down, the emission intensity increases, and the peak becomes sharper (**Figure 1. 24** (a)). It is due to the enhanced rigidity of the structure at low temperature

and faster intersystem (ISC) crossing process as a result. Faster ISC decreases energy loss via non-radiative decay. The emission maximum is slightly blue shifted to 676 nm once temperature reaches 93 K (Stokes shift of 15325 cm^{-1}). It happens due to the suppression of the vibrations and distortions in the excited state.[12] Inversely, at high temperature emission and excitation peak are red-shifted to 694 nm and 392 nm, respectively (Stokes shift of 14000 cm^{-1}) (**Figure 1. 24** (b)).

The lifetime decay curves were fitted with sum of two stretched exponentials (Appendix B). The predominant component (over 95 % at whole temperature range) is in microsecond range, the minor component is slightly shorter. Similarly to previously discussed compounds, temperature quenching is observed (**Figure 1. 24** (c), (d), Appendix B): lifetime goes from 9.63 µs at 93 K to 1.30 µs at 293 K, and to 0.06 µs at 383 K.

1.5 Potential Application: Lifetime Luminescence Thermometry

A significant lifetime shortening as a result of thermal quenching seems to be inherent characteristic of CPs based on thiolates of coinage metals. It will be observed further in the next chapters. This characteristic makes these materials potentially interesting for lifetime luminescence thermometry. Such materials are required in plenty domains, particularly for contactless measurements or temperature control systems where the spatial resolution of data is necessary. The list includes variety of applications from bioimaging to aerodynamics.

It is needless to say, that systems showing a significant change of lifetime decay for a given temperature range are required. In order to evaluate the potential of a given material the following parameters are calculated: relative sensitivity and/or normalized lifetime coefficient. Definitions of both terms can be found in the literature. [44, 45] They are reflecting the efficiency of the material as a thermometer.

Relative sensitivity is determined according to the equation (Eq. 1.2):

$$S_n = \frac{1}{\tau_n}\frac{\Delta\tau_n}{\Delta T} \cdot 100\ \% \quad \text{(Eq. 1.2)}$$

where τ_n is the decay time and $\Delta\tau_n$ represents its change for ΔT change of temperature.[44]

Normalized lifetime thermal coefficient is defined as following (Eq. 1.3):

$$\alpha_T = \frac{\Delta\tau_{nor}(T)}{\Delta T} \quad \text{(Eq. 1.3)}$$

where $\Delta\tau_{nor}(T)$ is the decay time at temperature T normalized to the room temperature value. [45]

In order to fit the experimental data, we used the function given by Equation (1.1) which describes thermal quenching. Both relative sensitivity and normalized lifetime coefficient were calculated for $[Au(SPh)]_n$ and $[Cu(SPh)]_n$ **4** (**Figure 1. 25**).

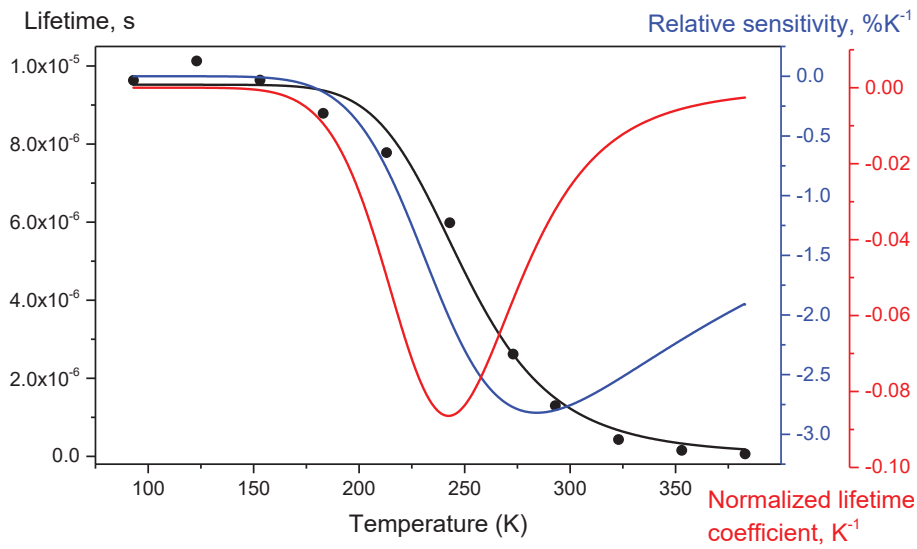

(a)

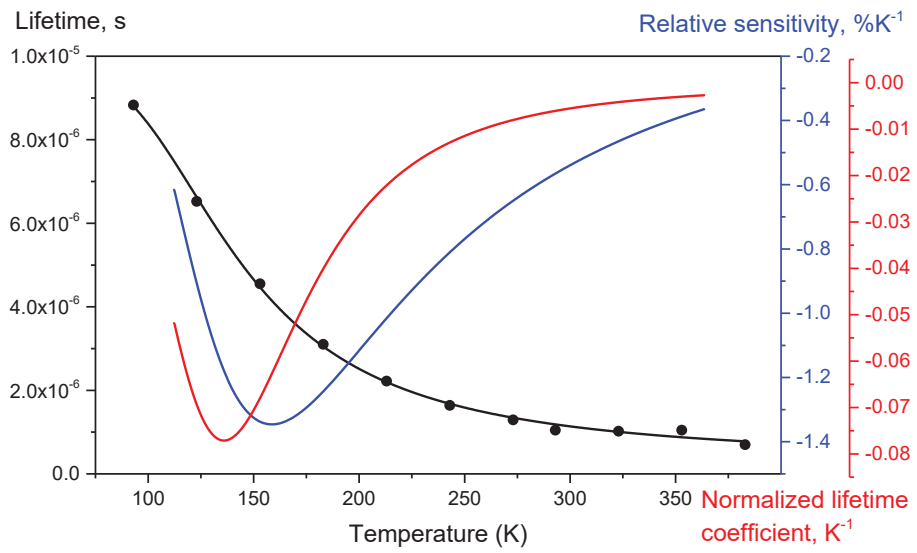

(b)

Figure 1. 25 The lifetime (black circles, experimental data; black line, fit), relative sensitivity (blue line) and normalized lifetime coefficient (red line) evolution with temperature of (a) $[Au(SPh)]_n$ and (b) $[Cu(SPh)]_n$ **4**.

$[Au(SPh)]_n$ has a maximal relative sensitivity of 2.8 %·K^{-1} (285 K) and a maximal normalized lifetime thermal coefficient of 0.086 K^{-1} (240 K) whereas for $[Cu(SPh)]_n$ **4** these values are 1.4 %·K^{-1} (145 K) and 0.077 K^{-1} (120 K). In addition, these compounds work well in an important temperature range (290 K for both compounds). While $[Cu(SPh)]_n$ **4** is more sensitive at low temperature (~93-225 K), $[Au(SPh)]_n$ works better for high temperature applications (~210-383 K).

Both compounds can present an appealing alternative to the widely reported materials for this application (*e. g.*, QDs, MOFs and inorganic matrices doped with rare earth or transition metal elements [46, 47]) because of their relatively low price, easy synthesis and high sensitivity.

The main drawbacks of $[Cu(SPh)]_n$ **4** and $[Au(SPh)]_n$ are: the nonlinear lifetime-temperature dependency and the complex lifetime decay (stretched, not strictly monoexponential).

1.6 Conclusions

In the chapter, we have discussed CPs based on Cu(I), Ag(I), Au(I) and thiophenolate as an organic ligand. Despite the fact, that the structures and properties of some of them have been already reported, these materials seem to be gifts that keep on giving.

Example of $[Cu(SPh)]_n$ and $[Ag(SPh)]_n$ showed that even in CPs with such a simple ligand, there is always a place for a structural diversity. The polymorphs of $[Cu(SPh)]_n$ and $[Ag(SPh)]_n$ give a unique opportunity to observe how a small structural change is translated into new photophysical properties. The structural investigation will continue with the goal to complete the studies.

The case of $[Ag(SPh)]_n$ phase **1** is a remarkable and rare example of Ag(I)-based coordination polymer emitting in NIR, despite it shows a very weak, low temperature emission.

All the discussed CPs have showed a significant lifetime shortening upon temperature decrease, as a result of the thermal quenching. This observation turns them into interesting candidate materials for lifetime luminescence thermometry.

In the three following chapters, we are going to investigate, how the introduction of a substituent in different positions of the phenyl ring can influence the structure and, therefore, the photophysical properties of the coinage metal thiolates.

1.7 Experimental part

1.7.1 Synthesis

Synthesis of $[Cu(SPh)]_n$ A: HSPh (250 µL, 1.15 mmol, 1.15 eq.) was added to 30 mL of aqueous solution of methanol (50 %). Cu_2O (144 mg, 1 mmol, 1 eq.) was added to the prepared solution, the reaction mixture was refluxed for 72 hours. The product was collected by filtration and washed by ethanol. The product is dark brown underlying a significant amount of unreacted Cu_2O.

Synthesis of $[Cu(SPh)]_n$ 1: 1 mL of **1 M HCl** was added to the solution of $CuCl_2{\cdot}2H_2O$ (126.8 mg, 0.74 mmol, 1 eq.) dissolved in 5 mL of **THF** and 5 mL of **DMF**, followed by the addition of HSPh (114 µL, 0.96 mmol, 1.3 eq.). The reaction was let to proceed for 18 h at **120°C** in a 20 mL sealed vial. Yellow precipitate was collected by filtration and washed by ethanol. The product was dried in air. Yield: 6 % (5 mg). Chemical Formula: C_6H_5CuS. Molecular Weight: 172.71. CuO content from TGA (calc.) wt%: 46.1 (46.1).

Synthesis of $[Cu(SPh)]_n$ 2: 1 mL of **0.1 M HCl** was added to the solution of $CuCl_2{\cdot}2H_2O$ (126.8 mg, 0.74 mmol, 1 eq.) in 10 mL **DMF**, followed by the addition of HSPh (114 µL, 0.96 mmol, 1.3 eq.). The reaction was let to proceed for 18 h at **100°C** in a 20 mL sealed vial. Yellow precipitate was collected by filtration and washed by ethanol. The product was dried in air. Yield: 53 % (44 mg). Chemical Formula: C_6H_5CuS. Molecular Weight: 172.71. CuO content from TGA (calc.) wt%: 46.1 (46.1).

Synthesis of $[Cu(SPh)]_n$ 3: 1 mL of **0.1 M HCl** was added to the solution of $CuCl_2{\cdot}2H_2O$ (126.8 mg, 0.74 mmol, 1 eq.) dissolved in 5 mL of **THF** and 5 mL of **DMF**, followed by the addition of HSPh (114 µL, 0.96 mmol, 1.3 eq.). The reaction was let to proceed for 18 h at **120°C** in a 20 mL sealed vial. Yellow precipitate was collected by filtration and washed by ethanol. The product was dried in air. Yield: 39 % (32 mg). Chemical Formula: C_6H_5CuS. Molecular Weight: 172.71. CuO content from TGA (calc.) wt%: 44.8 (46.1).

Synthesis of $[Cu(SPh)]_n$ 4: 1 mL of **0.1 M HCl** was added to the solution of $CuCl_2{\cdot}2H_2O$ (126.8 mg, 0.74 mmol, 1 eq.) in 5 mL of **THF** and 5 mL of **DMF**, followed by the addition of HSPh (114 µL, 0.96 mmol, 1.3 eq.). The reaction was let to proceed for 18 h at **100°C** in a 20 mL sealed vial. Yellow precipitate was collected by filtration and washed by ethanol. The product was

dried in air. Yield: 16 % (13 mg). Chemical Formula: C_6H_5CuS. Molecular Weight: 172.71. CuO content from TGA (calc.) wt%: 45.5 (46.1).

Synthesis of $[Ag(SPh)]_n$ phase 1: HSPh (60 µL, 0.59 mmol, 1 eq.) was added to the solution of $AgNO_3$ (100 mg, 0.59 mmol, 1 eq.) in H_2O (10 mL). The reaction was let to proceed for 18 h at ambient temperature with the steering. White precipitate was obtained and washed by 40 mL of ethanol for 6 times. The product was dried in air. Yield: 49 % (63 mg). Chemical Formula: C_6H_5AgS. Molecular Weight: 217.04. Silver content from TGA (calc.) wt%: 49.9 (49.7).

Synthesis of $[Ag(SPh)]_n$ phase 2: HSPh (60 µL, 0.59 mmol, 1 eq.) was added to the solution of $AgNO_3$ (100 mg, 0.59 mmol, 1 eq.) in DMF (10 mL). The reaction was let to proceed for 18 h at 60°C in a 20 mL sealed vial. White precipitate was obtained and washed by 40 mL of ethanol for 6 times. The product was dried in air. Yield: 60 % (76 mg). Chemical Formula: C_6H_5AgS. Molecular Weight: 217.04. Silver content from TGA (calc.) wt%: 49.6 (49.7).

Synthesis of $[Au(SPh)]_n$: HSPh (1200 µL, 10.13 mmol, 40.5 eq.) was added to the solution of $HAuCl_4 \cdot 3H_2O$ (100 mg, 0.25 mmol, 1 eq.) in EtOH (10 mL). The reaction was let to proceed for 18 h at 120°C in a 20 mL sealed vial. White precipitate was obtained and washed by large amount of ethanol for 6 times. The product was recovered by filtration. The product was dried in air. Yield: 80 % (62 mg). Chemical Formula: C_6H_5AuS, Molecular Weight: 306.16. Gold content from TGA (calc.) wt%: 63.6 (64.3).

1.7.2 PXRD structural determination of $[Ag(SPh)]_n$ phase 1

The structural determination of the phase **1** of $[Ag(SPh)]_n$ was carried out from High resolution X-ray powder diffraction data. The data was collected at the CRISTAL beamline at Soleil Synchrotron (Gif-sur-Yvette, France). A monochromatic beam was extracted from the U20 undulator beam by means of a Si(111) double monochromator. Its wavelength of 0.79276 Å was refined from a LaB6 (NIST Standard Reference Material 660a) powder diagram recorded prior to the experiment. The X-ray beam was attenuated, in order to limit radiation damage of the sample. High angular resolution was obtained, in the diffracted beam, using a 21 perfect crystal Si(111) multi-analyzers. The sample was loaded in a 0.7 mm capillary (Borokapillaren, GLAS, Schönwalde, Germany) mounted on a spinner rotating at about 5 Hz to improve the particles' statistics. Diffraction data were collected in continuous scanning mode. The

diffractogram was obtained by a precise superposition and addition of the data from 21 channels.

All structural investigation calculations were performed using the TOPAS program.[48] The LSI-indexing method converged unambiguously to a monoclinic unit cell. The direct space strategy was used to position silver atoms and the organic moieties, which were treated as rigid body in the simulated annealing process. The final Rietveld plot (**Figure 1. 26**) corresponds to satisfactory model indicator and profile factors (**Table 1. 3**).

Table 1. 3 Crystallographic data for $[Ag(SPh)]_n$ phase **1**.

	$[Ag(SPh)]_n$ phase 1
Empirical formula	$C_6H_5Ag_1S_1$
M_r	217.04
Crystal system	Monoclinic
Space group	$P2_1/c$
a (Å)	7.3316(1)
b (Å)	5.91817(6)
c (Å)	28.2311(4)
β (°)	93.700(4)
V (Å^3)	1222.37(4)
M_{20}	30
Z	8
λ (Å)	0.79276
Number of reflections	1009
Number of structural parameters	22
R_p, R_{wp}	0.051, 0.072
R_{Bragg}, GoF	0.018, 2.22

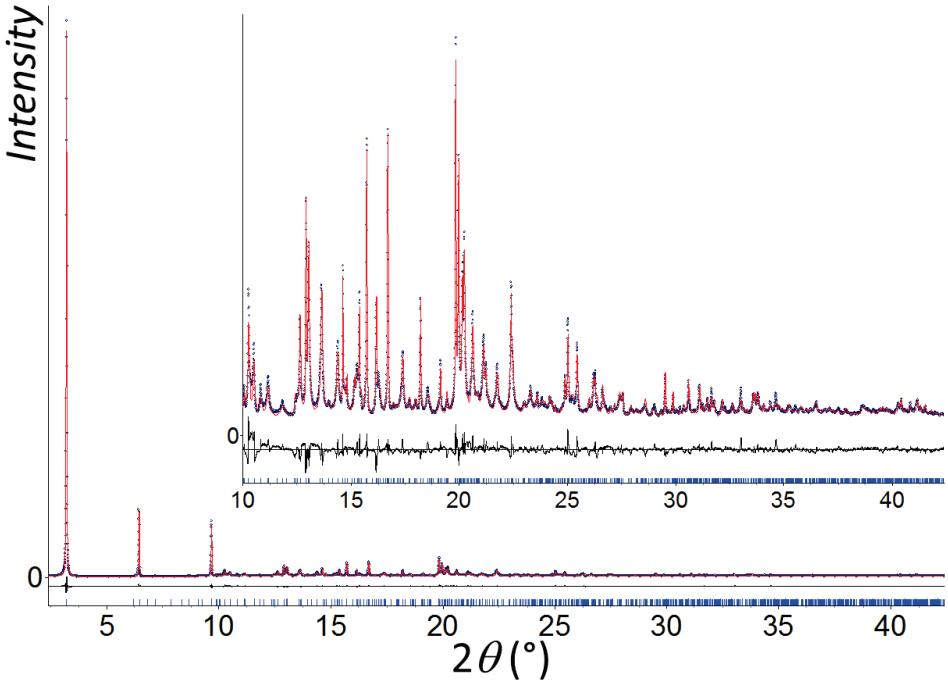

Figure 1. 26 Final Rietveld plot of $[Ag(SPh)]_n$ phase **1** showing observed (blue circles), calculated (red line), and difference (black line) curves. A zoom at high angles is shown as inset.

1.8 References

1. C.-M. Che, C.-H. Li, S. S.-Y. Chui, V. A. L. Roy and K.-H. Low, *Chem. Eur. J.*, 2008, **14**, 2965-2975.
2. K.-H. Low, C.-H. Li, V. A. L. Roy, S. S.-Y. Chui, S. L.-F. Chan and C.-M. Che, *Chem. Sci.*, 2010, **1**, 515-518.
3. I. G. Dance, K. J. Fisher, R. M. H. Banda and M. L. Scudder, *Inorg. Chem.*, 1991, **30**, 183-187.
4. H. L. Cuthbert, A. I. Wallbank, N. J. Taylor and J. F. Corrigan, *Z. Anorg. Allg. Chem.*, 2002, **628**, 2483-2488.
5. C. Lavenn, L. Okhrimenko, N. Guillou, M. Monge, G. Ledoux, C. Dujardin, R. Chiriac, A. Fateeva and A. Demessence, *J. Mater. Chem. C*, 2015, **3**, 4115-4125.
6. O. Veselska, D. Podbevšek, G. Ledoux, A. Fateeva and A. Demessence, *ChemComm*, 2017, **53**, 12225-12228.
7. C. E. Moore, *Atomic Energy Levels*, Washington D. C.: NSRDS-NBS 35, 1971.
8. J. S. Lim, H. Choi, I. S. Lim, S. B. Park, Y. S. Lee and S. K. Kim, *J. Phys. Chem. A*, 2009, **113**, 10410-10416.
9. V. W.-W. Yam, C.-H. Lam and K.-K. Cheung, *ChemComm*, 2001, 545-546.
10. H. V. R. Dias, H. V. K. Diyabalanage, M. A. Rawashdeh-Omary, M. A. Franzman and M. A. Omary, *J. Am. Chem. Soc.*, 2003, **125**, 12072-12073.
11. V. W.-W. Yam, K. K.-W. Lo and K.-K. Cheung, *Inorg. Chem.*, 1996, **35**, 3459-3462.
12. Y. Li, Z. Li, Y. Hou, Y.-N. Fan and C.-Y. Su, *Inorg. Chem.*, 2018, **57**, 13235-13245.
13. Q. Liu, M. Xie, X. Chang, Q. Gao, Y. Chen and W. Lu, *ChemComm*, 2018, **54**, 12844-12847.
14. R. Galassi, M. M. Ghimire, B. M. Otten, S. Ricci, R. N. McDougald, Jr., R. M. Almotawa, D. Alhmoud, J. F. Ivy, A.-M. M. Rawashdeh, V. N. Nesterov, E. W. Reinheimer, L. M. Daniels, A. Burini and M. A. Omary, *Proc. Natl. Acad. Sci. U.S.A.*, 2017, **114**, E5042-E5051.
15. I. Roppolo, E. Celasco, A. Fargues, A. Garcia, A. Revaux, G. Dantelle, F. Maroun, T. Gacoin, J.-P. Boilot, M. Sangermano and S. Perruchas, *J. Mater. Chem.*, 2011, **21**, 19106-19113.
16. V. W.-W. Yam and K. K.-W. Lo, *Chem. Soc. Rev.*, 1999, **28**, 323-334.
17. H.-Y. Zhuo, H.-F. Su, Z.-Z. Cao, W. Liu, S.-A. Wang, L. Feng, G.-L. Zhuang, S.-C. Lin, M. Kurmoo, C.-H. Tung, D. Sun and L.-S. Zheng, *Chem. Eur. J.*, 2016, **22**, 17619-17626.
18. Z.-H. Yan, X.-Y. Li, L.-W. Liu, S.-Q. Yu, X.-P. Wang and D. Sun, *Inorg. Chem.*, 2016, **55**, 1096-1101.
19. Y. Huang, J. Wang and H. J. Seo, *J. Electrochem. Soc.*, 2010, **157**, J429-J434.
20. L. Li, Y. Zhu, X. Zhou, C. D. S. Brites, D. Ananias, Z. Lin, F. A. A. Paz, J. Rocha, W. Huang and L. D. Carlos, *Adv. Funct. Mater*, 2016, **26**, 8677-8684.
21. R. Siebert, A. Winter, U. S. Schubert, B. Dietzek and J. Popp, *Phys. Chem. Chem. Phys.*, 2011, **13**, 1606-1617.
22. C. R. Hecker, A. K. I. Gushurst and D. R. McMillin, *Inorg. Chem.*, 1991, **30**, 538-541.

23. B. J. Coe, D. W. Thompson, C. T. Culbertson, J. R. Schoonover and T. J. Meyer, *Inorg. Chem.*, 1995, **34**, 3385-3395.
24. R. S. Lumpkin, E. M. Kober, L. A. Worl, Z. Murtaza and T. J. Meyer, *J. Phys. Chem.*, 1990, **94**, 239-243.
25. A. Amini, A. Harriman and A. Mayeux, *Phys. Chem. Chem. Phys.*, 2004, **6**, 1157-1164.
26. A. C. Benniston, G. Chapman, A. Harriman, M. Mehrabi and C. A. Sams, *Inorg. Chem.*, 2004, **43**, 4227-4233.
27. D. M. Knotter, G. Blasse, J. P. M. Vliet and G. van koten, *Inorg. Chem.*, 1992, **31**, 2196-2201.
28. A. Bondi, *J. Phys. Chem.*, 1964, **68**, 441-451.
29. V. W.-W. Yam, K. K.-W. Lo, C.-R. Wang and K.-K. Cheung, *Inorg. Chem.*, 1996, **35**, 5116-5117.
30. D. H. Whiffen, *J. Chem. Soc.*, 1956, 1350-1356.
31. J. H. S. Green, *Spectrochim. Acta A*, 1968, **24**, 1627-1637.
32. D. Steele and E. R. Lippincott, *J. Mol. Spectrosc.*, 1961, **6**, 238-264.
33. V. W.-W. Yam, V. K.-M. Au and S. Y.-L. Leung, *Chem. Rev.*, 2015, **115**, 7589-7728.
34. V. W.-W. Yam, E. C.-C. Cheng and N. Zhu, *New J. Chem.*, 2002, **26**, 279-284.
35. G. S. M. Tong, S. C. F. Kui, H.-Y. Chao, N. Zhu and C.-M. Che, *Chem. Eur. J.*, 2009, **15**, 10777-10789.
36. A. Burini, R. Bravi, J. P. Fackler, R. Galassi, T. A. Grant, M. A. Omary, B. R. Pietroni and R. J. Staples, *Inorg. Chem.*, 2000, **39**, 3158-3165.
37. T. Tanase, R. Otaki, T. Nishida, H. Takenaka, Y. Takemura, B. Kure, T. Nakajima, Y. Kitagawa and T. Tsubomura, *Chem. Eur. J.*, 2014, **20**, 1577-1596.
38. C. E. Moore, *Atomic Energy Levels*, Washington D. C.: NSRDS-NBS 35, 1971.
39. F. Sabin, C. K. Ryu, P. C. Ford and A. Vogler, *Inorg. Chem.*, 1992, **31**, 1941-1945.
40. E. C.-C. Cheng, W.-Y. Lo, T. K.-M. Lee, N. Zhu and V. W.-W. Yam, *Inorg. Chem.*, 2014, **53**, 3854-3863.
41. V. W.-W. Yam, W. K.-M. Fung and K.-K. Cheung, *Organometallics*, 1997, **16**, 2032-2037.
42. R. E. Bachman, S. A. Bodolosky-Bettis, S. C. Glennon and S. A. Sirchio, *J. Am. Chem. Soc.*, 2000, **122**, 7146-7147.
43. R. E. Bachman and S. A. Bodolosky-Bettis, *Z. Naturforsch.*, 2009, **64b**, 1491-1499.
44. Y. Cui, F. Zhu, B. Chen and G. Qian, *ChemComm*, 2015, **51**, 7420-7431.
45. D. Jaque and F. Vetrone, *Nanoscale*, 2012, **4**, 4301-4326.
46. L. Marciniak and K. Trejgis, *J. Mater. Chem. C*, 2018, **6**, 7092-7100.
47. Z. Ji, Y. Cheng, X. Cui, H. Lin, J. Xu and Y. Wang, *Inorg. Chem. Front.*, 2019, **6**, 110-116.
48. Topas V4.2: General Profile and Structure Analysis Software for Powder Diffraction Data, *Bruker AXS Ltd*, 2008.

Chapter 2: $[M(p\text{-}SPhCO_2R)]_n$, R = H, Me

2.1 Introduction

In this chapter, synthesis, structure, characterization and photophysical properties of *para*-mercaptobenzoic acid-based CPs are discussed. Only one Cu(I)-based CP with *para*-mercaptobenzoic acid has been reported so far. No example of Ag(I)-based compounds are known. In contrast, numerous Au(I)(p-$SPhCO_2H$)-based coordination compounds have been reported.[1]

The Cu(I)-based coordination polymer with p-$HSPhCO_2H$ as a ligand has been reported in 2008 by Che *et al*.[2] Later, in 2010, the same authors suggested a lamellar structure with an infinite covalent $[CuS]_n$ 2D network from PXRD. However, structural determination using powder XRD data was not successful. [3]

A significant number of phosphine *para*-carboxythiophenolate gold(I) complexes has been reported.[1] Among them, there are mainly the ones with tertiary monophosphines: $Au(R_3P)(p\text{-}SPhCO_2H)$ (R_3 = Me_3, Et_3, Ph_3, Ph_2Py,[4] Ph_2ferrocene,[5] Cy_3, [6] and Me_2Ph),[7] $[Au(p\text{-}SPhCO_2H)(PPh_3)]\cdot0.3$(acetone), $[Au(p\text{-}SPhCO_2H)(PPh_3)]\cdot0.5$(benzene),[8] $[\mu\text{-}(P\text{-}P)\{Au(p\text{-}SPhCO_2H)\}_2]$ (P-P = R-binap, S- binap).[9] Some complexes bearing biphosphines $[Au(p\text{-}SPhCO_2H)](R)$ (R = dppb or 1,4-bis(diphenylphosphino)butane; dppf or 1,1-bis(diphenylphosphino)ferrocene)[4] and a polyaurated product, $[(Ph_3PAu)_2(p\text{-}SPhCO_2H)]BF_4$, which have also been described.[4] Among the phosphine gold(I) complexes, structures of $Au(Et_3P)(p\text{-}SPhCO_2H)$, $Au(Ph_3P)(p\text{-}SPhCO_2H)$, $Au(Ph_2PyP)(p\text{-}SPhCO_2H)$,[4] $Au(Cy_3P)(p\text{-}SPhCO_2H)$,[6] $Au(Ph_2ferroceneP)(p\text{-}SPhCO_2H)$[5] and $Au(Me_2PhP)(p\text{-}SPhCO_2H)$[10] were solved. For all of them gold atom is coordinated by sulfur and phosphorus in linear fashion with an S-Au-P bond angle close to 180°. The complex $Au(Cy_3P)(p\text{-}SPhCO_2H)$ forms dimers via hydrogen bonds between the carboxylic acids (**Figure 2. 1** (a)).

Three other complexes, $Au(Et_3P)(p\text{-}SPhCO_2H)$, $Au(Ph_2PyP)(p\text{-}SPhCO_2H)$ and $Au(Ph_2ferroceneP)(p\text{-}SPhCO_2H)$, show similar packing with R_3P-Au-S units of neighboring molecules which are aligned head to tail and form [Au-S···Au-S] parallelograms via the

secondary Au···S interactions (**Figure 2. 1** (b)). The $[Au(R_3P)(p\text{-}SPhCO_2H)]_2$ dimers are then connected one to another through the hydrogen bonding between the carboxylic acid groups.

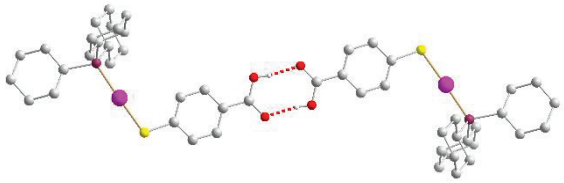

(a)

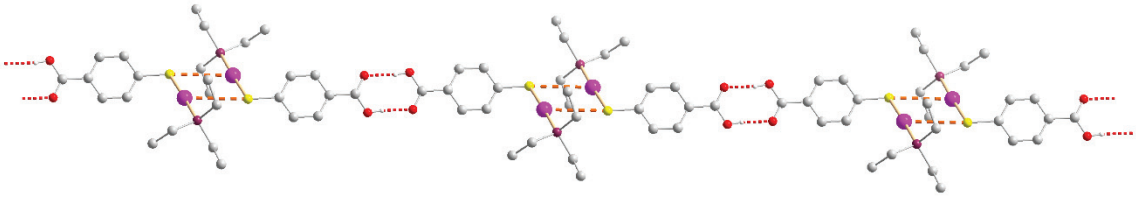

(b)

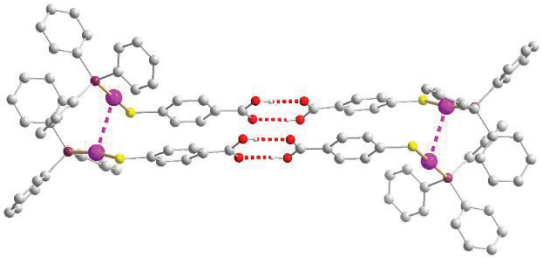

(c)

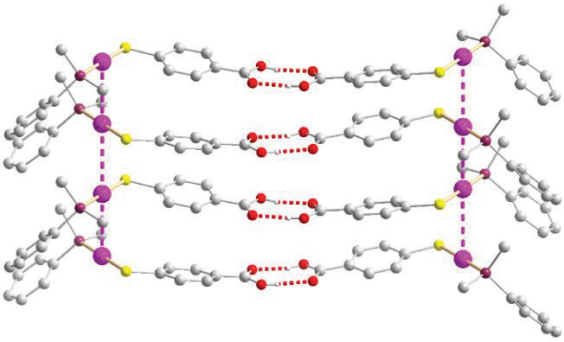

(d)

Figure 2. 1 Structure representations of (a) $Au(Cy_3P)(p\text{-}SPhCO_2H)$,[6] (b) $Au(Et_3P)(p\text{-}SPhCO_2H)$,[4] (c) $Au(Ph_3P)(p\text{-}SPhCO_2H)$[4] and (d) $Au(Me_2PhP)(p\text{-}SPhCO_2H)$.[10] Red dashed lines represent hydrogen bonding. Yellow dashed lines represent secondary Au···S interactions. Pink dashed lines represent aurophilic interactions. Pink, Au; violet, P; yellow, S; red, O; grey, C; white, H. Non-acidic hydrogen atoms are omitted for clarity.

In the case of $Au(Ph_3P)(p\text{-}SPhCO_2H)$ gold atoms form tetrameric units via the dimeric aurophilic interactions – Au(I)-Au(I) contacts of 3.076(1) Å – and dimeric hydrogen bonds (**Figure 2. 1** (c)). The P-Au-S units are rotated one relatively to another by an angle of ∼74°. The

complex Au(Me_2PhP)(*p*-$SPhCO_2H$) shows similar P-Au-S units which form an angle of ∼60°. They are connected through weak aurophilic interactions (3.534(2) Å). In this case, they form an extended quasi-linear array with Au(I)-Au(I)-Au(I) angles of ∼162° (**Figure 2.1**(d)). The two carboxylic acids form hydrogen bonds. The complexes, Au(Ph_3P)(*p*-$SPhCO_2H$) and Au(Ph_2ferroceneP)(*p*-$SPhCO_2H$), have been used for synthesis of heterometallic titanocene–gold complexes [(η-C_5H_5)$_2$TiMe(μ-)(*p*-$SPhCO_2$))Au(PR_3)], which have been shown to inhibit renal cancer cells both *in vitro* and *in vivo*.[5]

The complex, Au(Me_2PhP)(*p*-$SPhCO_2H$), has been reported to show luminescence properties.[10] The emission is structured, with at least three components (at *cca.* 478 nm, 533 nm and 570 nm). The lifetime decay is described by bi-exponential components with microsecond-range lifetime. The fast component corresponds to the emission at 478 nm, whereas the slow component corresponds to the emission at 530-580 nm. The multiple emission was tentatively assigned to several weakly coupled radiative relaxation channels, including different $^{1/3}$MC and LMCT excited states. The quantum yield was estimated to be 0.2-0.3 at 293 K. Moreover, this complex has served as a metalloligand for the synthesis of heterobimetallic Au^{I}/Zr^{IV} complexes.[10]

The aforementioned complex, [Au(*p*-$SPhCO_2H$)(PPh_3)]·0.3(acetone), has showed activity towards Gram-positive bacterium *Staphylococcus aureus*.[8]

The complexes [μ-(P-P){Au(*p*-$SPhCO_2H$)}$_2$] (P-P = R-binap, S- binap) have been used to generate supramolecular liquid-crystalline aggregates via hydrogen bonding interactions with 2,4,6-triaryl-1,3,5-triazine.[9]

The same team that studied heterometallic titanocene–gold complexes containing phosphine ligands, has synthesized four Au(*p*-$SPhCO_2H$) complexes with N-Heterocyclic Carbene Ligands (NHC). They were further used for the synthesis of [(η-C_5H_5)$_2$TiMe(μ-(*p*-$SPhCO_2H$)Au(NHC)] complexes that have been evaluated against renal, prostate, colon, and breast cancer cell lines. The [(NHC)Au(*p*-$SPhCO_2H$)] (NHC with two mesityl groups) complex was structurally characterized. It forms hydrogen-bonded carboxylic acid dimers, but no aurophilic or Au(I)-S secondary interactions have been observed, supposedly due to the steric bulkiness of the NHC ligand.[11]

Some other examples of reported complexes are following: $[N(PPh_3)_2][Au(p\text{-}SPhCO_2H)_2]$[4] and $Au(Ph_3P{=}S)(p\text{-}SPhCO_2H)$[4] and isocyanide complexes $[Au(p\text{-}SPhCO_2H)(RNC)]$ (R = tBu, 2,6-$Me_2C_6H_3$).[12]

It should be noted, that p-$HSPhCO_2H$ is a well-known stabilizing and protecting agent for numerous gold- and silver- based nanoparticles and nanoclusters (*e. g.*, $Au_{102}(p\text{-}SPhCO_2H)_{44}$[13] and $M_4Ag_{44}(p\text{-}SPhCO_2H)_{30}$[14,15]).[1] The p-$HSPhCO_2H$-based self-assembled monolayers (SAM) on gold and silver surfaces have also been of considerable interest.[1]

We saw that a number of architectures with different weak interactions (aurophilic, secondary Au···S interactions, hydrogen bonds) might be formed in dependence on the bulkiness of the auxiliary ligand. In this chapter we will investigate the homoleptic *para*-carboxythiophenolate-based CPs. We repeated yet another attempt (after Che *et al.*[2]) to elucidate the structure of $[Cu(p\text{-}SPhCO_2H)]_n$ as well as of Ag(I)- and Au(I)-based CPs. We attempted to find out how the metal-sulfur array is changed when the carboxylic group is introduced in aromatic cycle. We aimed to compare it with the case of unsubstituted thiophenolates discussed in the Chapter 1. In addition, CPs based on esterified *para*-mercaptobenzoic acid is be presented. A comparison between two groups of CPs (with $–CO_2H$ or $–CO_2Me$) help to illustrate the role of hydrogen bonds in structure formation. $[Au(p\text{-}SPhCO_2Me)]_n$[16] has been already reported by our team. Its characterization is completed with the temperature dependent studies of lifetime decay (Appendix B).

2.2 Structures

Five new coordination polymers ($[Cu(p\text{-}SPhCO_2H)]_n$, $[Cu(p\text{-}SPhCO_2Me)]_n$, $[Ag(p\text{-}SPhCO_2H)]_n$, $[Ag(p\text{-}SPhCO_2Me)]_n$ and $[Au(p\text{-}SPhCO_2H)]_n$) have been obtained. Highly crystalline powders were prepared under solvothermal conditions. Their PXRD patterns are shown in the Figure 2. 2.

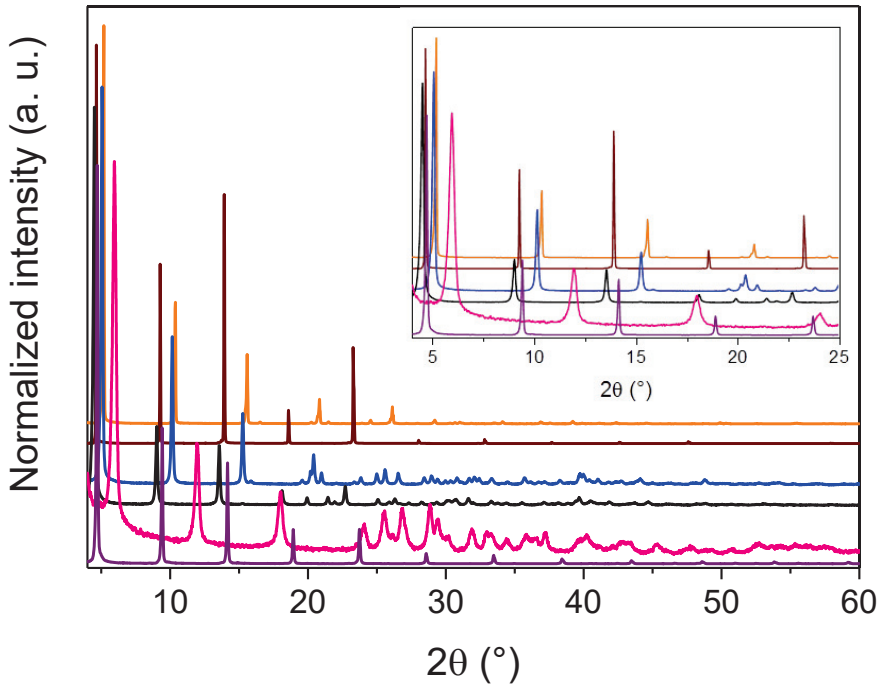

Figure 2. 2 The PXRD patterns of $[Cu(p\text{-}SPhCO_2H)]_n$ (orange), $[Cu(p\text{-}SPhCO_2Me)]_n$ (brown), $[Ag(p\text{-}SPhCO_2H)]_n$ (blue), $[Ag(p\text{-}SPhCO_2Me)]_n$ (black), $[Au(p\text{-}SPhCO_2H)]_n$ (pink), $[Au(p\text{-}SPhCO_2Me)]_n$ (violet). Zoom on low angles is shown as an inset.

We observe predominant (00*l*) reflections characteristic for the lamellar materials for all compounds. Position of the first diffraction peak can give us information about interlamellar spacing for each compound. In the case of compounds with ester group the spacing is bigger than for those cases with carboxylic group: 19.0 Å, 18.7 Å and 19.6 Å vs. 17.0 Å, 17.4 Å and 14.8 Å for Cu(I), Ag(I) and Au(I)-based compounds, respectively. This distance corresponds to M(I)-S layer and two layers of organic ligand without interpenetration. Interlamellar spacing is the smallest for Au(I)-based compounds. It is caused by a significant tilt angle between the organic ligand and M(I)-S layer in comparison to Cu(I)- and Ag(I)-based counterparts.

The structures of $[Cu(p\text{-}SPhCO_2H)]_n$ and $[Cu(p\text{-}SPhCO_2Me)]_n$ were resolved from single crystal data. The structures of $[Au(p\text{-}SPhCO_2H)]_n$, $[Ag(p\text{-}SPhCO_2H)]_n$, $[Ag(p\text{-}SPhCO_2Me)]_n$ were, however, solved from powder X-ray diffraction data.

2.2.1 [Cu(*p*-SPhCO$_2$H)]$_n$ Structure

Structure determination results into an orthorhombic centrosymetrical space group – *Pbca* with *a* = 6.858(2) Å, *b* = 5.771(2) Å, *c* = 33.909(7) Å. Solved lamellar structure is composed of 2D [CuS]$_n$ layers similar to [Cu(*p*-SPhOH)]$_n$. It is in agreement with hypothesis of Che *et al.* for the structure of [Cu(*p*-SPhCO$_2$H)]$_n$. [3]

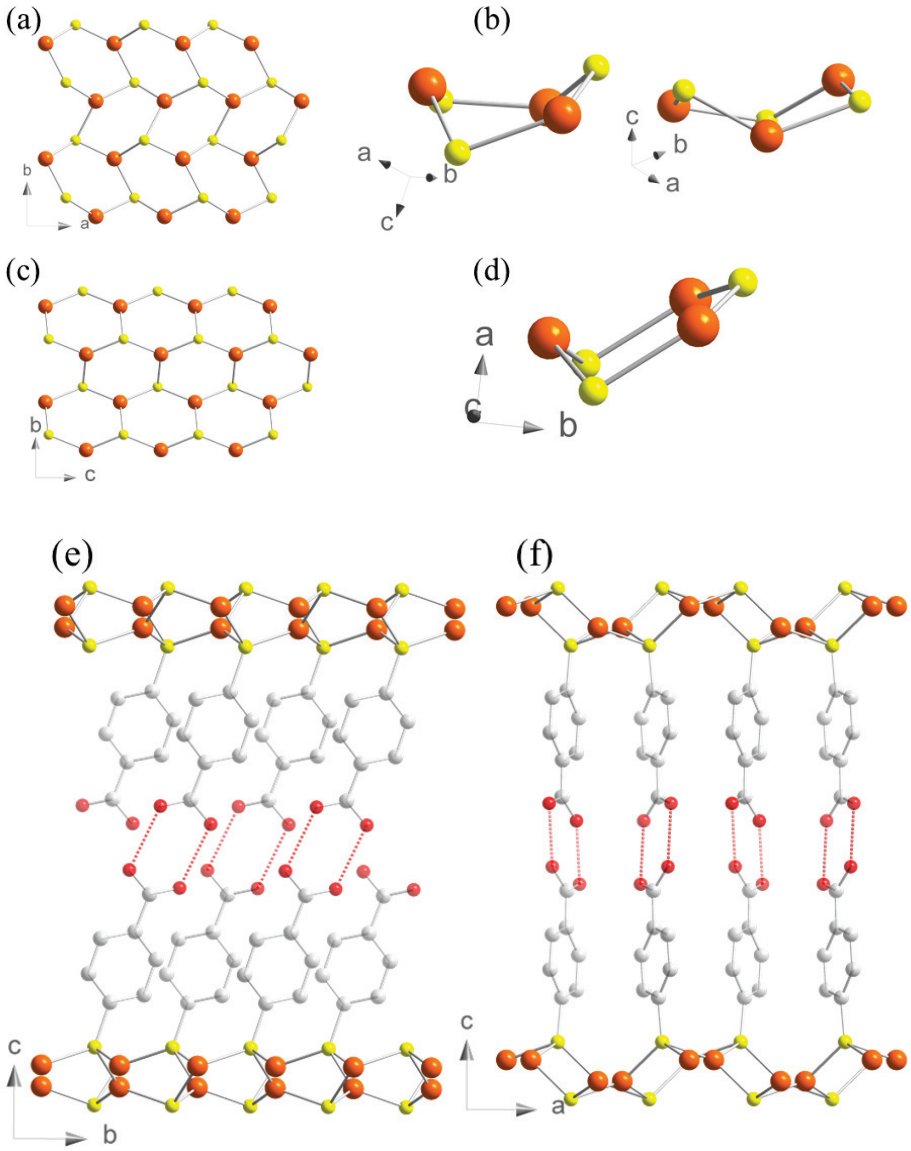

Figure 2. 3 Structure of [Cu(*p*-SPhCO$_2$H)]$_n$: (a) representation of the Cu_3S_3 network on the (*ab*) plane, (b) view of a Cu_3S_3 cycle. The [CuS]$_n$ layer of [Cu(*p*-SPhOH)]$_n$: (c) and (d) representation of the Cu_3S_3 network on the (*bc*) and plane view of Cu_3S_3 cycle of. Projections of the lamellar structure of [Cu(*p*-SPhCO$_2$H)]$_n$ on (e) (*bc*) and (f) (*ac*) planes, respectively. Red dashed lines represent hydrogen bonding. Orange, Cu; yellow, S; red, O; grey, C. Hydrogen atoms are omitted for clarity. Reprinted with permission from [17]. Copyright 2018 American Chemical Society.

Cu(I) atoms are in trigonal geometry. Each of them is linked to three sulfur atoms from thiolate ligands. Each sulfur atom, in turn, is connected to three copper atoms, giving rise to Cu_3S_3 hexagons. This hexagonal tiles form an infinite 2D layer propagating in the *(ab)* plane (**Figure 2. 3** (a), (b)). The main difference to [Cu(*p*-SPhOH)]$_n$ is the geometry of the hexagons. On one hand, in [Cu(*p*-SPhOH)]$_n$, five atoms Cu_2S_3 are located in one plane and the sixth atom – copper atom is pointing out of the plane (**Figure 2. 3** (c), (d)). On the other hand, the hexagons of [Cu(*p*-SPhCO$_2$H)]$_n$ are highly distorted (**Figure 2. 3** (a), (b)). The Cu-S distances are following 2.243(3) Å, 2.290(2) Å and 2.302(3) Å, and the S-Cu-S angles are 104.12(7)°, 126.0(2), 129.8(1)° (**Table 2. 1**). The Cu(I)-Cu(I) distance is 3.030(2) Å. It is longer than the sum of Van der Waals radii (2.80 Å). Therefore, no cuprophilic interactions are expected. The neighboring layers are connected via dimeric hydrogen bonds between the carboxylic acid groups (**Figure 2. 3** (e), (f)).

Table 2. 1 Comparison of the main distances and angles in discussed coordination polymers.

Compound	M-S, Å	M-M, Å	S-M-S, °	M-S-M, °	π-π, Å
[Cu(*p*-SPhCO$_2$H)]$_n$	2.243(3) 2.290(2) 2.302(3)	3.030(2)† 3.519(2)†	104.1(1) 126.0(1) 129.8(1)	83.6(1) 101.9(1) 116.4(1)	5.77(2)
[Cu(*p*-SPhCO$_2$Me)]$_n$	2.244(3) 2.255(3) 2.282(4)	3.313(3)† 3.493(3)†	114.0(2) 122.2(2) 123.6(2)	93.8(2) 101.0(2) 123.6(2)	3.966(1)
[Ag(*p*-SPhCO$_2$H)]$_n$	2.456(4) 2.493(4) 2.623(4)	2.936(2)† 3.687(2)†	97.2(2) 126.4(2) 131.3(2)	70.5(1) 96.3(2) 118.2(2)	5.82(1)
[Ag(*p*-SPhCO$_2$Me)]$_n$	2.437(5) 2.489(5) 2.627(5)	2.973(3)† 3.653(2)†	97.0(2) 124.4(2) 132.3(2)	71.8(2) 95.7(2) 120.2(2)	5.91(2)
[Au(*p*-SPhCO$_2$H)]$_n$	2.272(1) 2.272(8) 2.342(5) 2.367(1)	3.355(4) 3.422(6) 3.591(3)† 3.732(3)†	77.5(1) 124.0(1)	99.4(1) 110.4(1)	4.518(1)
[Au(*p*-SPhCO$_2$Me)]$_n$	2.307(1) 2.375(1)	3.199(5) 3.509(5)†	177.5(1)	97.1(1)	-

†bridged by sulfur atoms.

2.2.2 [Cu(*p*-SPhCO$_2$Me)]$_n$ Structure

Structure determination results into a monoclinic space group – *Pn* with a = 3.9655(5) Å, b = 19.103(3) Å, c = 5.2888(9) Å, β = 93.34(2)°. It has quasi-identical [CuS]$_n$-layout to previously mentioned [Cu(*p*-SPhOH)]$_n$. [3]

In $[Cu(p\text{-}SPhCO_2Me)]_n$, five atoms ($Cu_2S_3$) are located in one plane and the sixth atom – copper atom is pointing out of the plane. Therefore, it can be described as a half-chair conformation (**Figure 2. 4** (a), (b)). Formed dihedral angle is 106.5(1)° and it is only slightly different from $[Cu(p\text{-}SPhOH)]_n$ with 103.2(2)°. The Cu-S distances are 2.244(3) Å, 2.255(3) Å and 2.282(4) Å. The S-Cu-S angles are 93.8(2)°, 101.0(2)° and 123.6(2)° (**Table 2. 1**). The shortest Cu(I)-Cu(I) distances are of 3.313(3) Å and 3.493(3) Å. They are longer than the sum of Van der Waals radii (2.80 Å). No cuprophilic interactions are expected. The organic ligands occupy interlamellar space with parallel displaced π-stacking and no interpenetration (**Figure 2. 4** (c), (d)). The difference between $[Cu(p\text{-}SPhCO_2H)]_n$ and $[Cu(p\text{-}SPhCO_2Me)]_n$ arises from the presence of hydrogen bonds between the layers in the first case. It puts a constraint on the layer formation. Distorted Cu_3S_3-layout is generated.

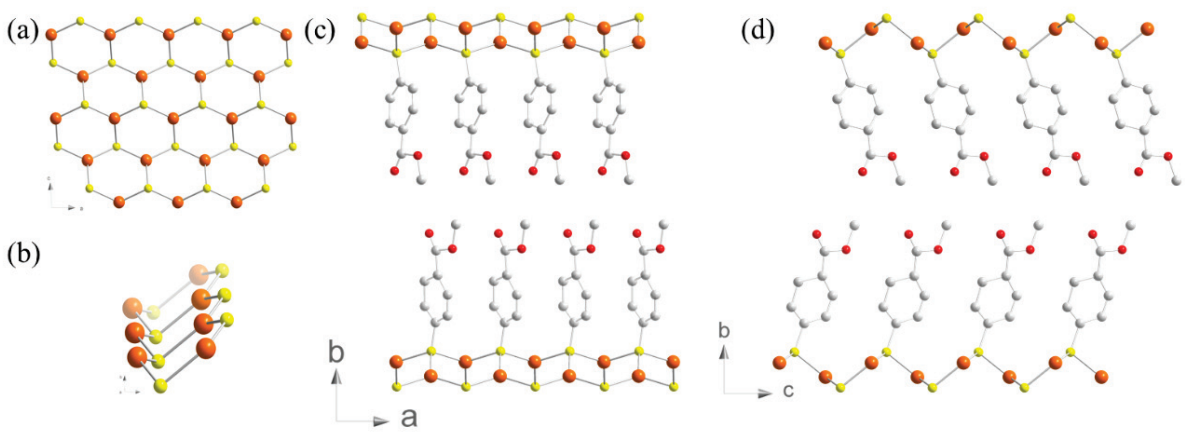

Figure 2. 4 Structure representations of $[Cu(p\text{-}SPhCO_2Me)]_n$: (a) View of the Cu_3S_3 hexagons of the inorganic sheet on *(ac)* plane. (b) View of the conformation of Cu_3S_3 hexagons. Views on (c) *(ab)* and (d) *(bc)* plane. Orange, Cu; yellow, S; red, O; grey, C. Hydrogen atoms are omitted for clarity. Reprinted with permission from ref. [18]. Copyright 2018 The Royal Society of Chemistry.

2.2.3 $[Ag(p\text{-}SPhCO_2H)]_n$ and $[Ag(p\text{-}SPhCO_2Me)]_n$ Structures

Structure of $[Ag(p\text{-}SPhCO_2H)]_n$ has an orthorhombic centrosymmetric space group *Pbca* (a = 7.2748(3) Å, b = 5.8158(3) Å, c = 34.7981(9) Å), while structure of $[Ag(p\text{-}SPhCO_2Me)]_n$ has an orthorhombic non-centrosymmetric space group – $Pca2_1$ (a = 7.21893(8) Å, b = 19.5651(3) Å, c = 5.90559(7) Å).

$[Ag(p\text{-}SPhCO_2H)]_n$ is isostructural with its copper-counterpart. It possesses the same M(I)-S-array formed with distorted hexagons M_3S_3. While $[Cu(p\text{-}SPhCO_2H)]_n$ and $[Cu(p\text{-}SPhCO_2Me)]_n$

show a difference in the M(I)-S-arrangement, it is not the case for [Ag(*p*-SPhCO$_2$H)]$_n$ and [Ag(*p*-SPhCO$_2$Me)]$_n$ (**Figure 2. 5** (a)). Silver and sulfur atoms form quasi-identical pattern with very close distances. The Ag-S distances are close in both structures: 2.456(4) Å, 2.493(4) Å, 2.623(4) Å and 2.437(5) Å, 2.489(5) Å, 2.627(5) Å in [Ag(*p*-SPhCO$_2$H)]$_n$ and [Ag(*p*-SPhCO$_2$Me)]$_n$, respectively. In addition, both structures are similar to the phase **1** of [Ag(SPh)]$_n$ (Chapter 1).

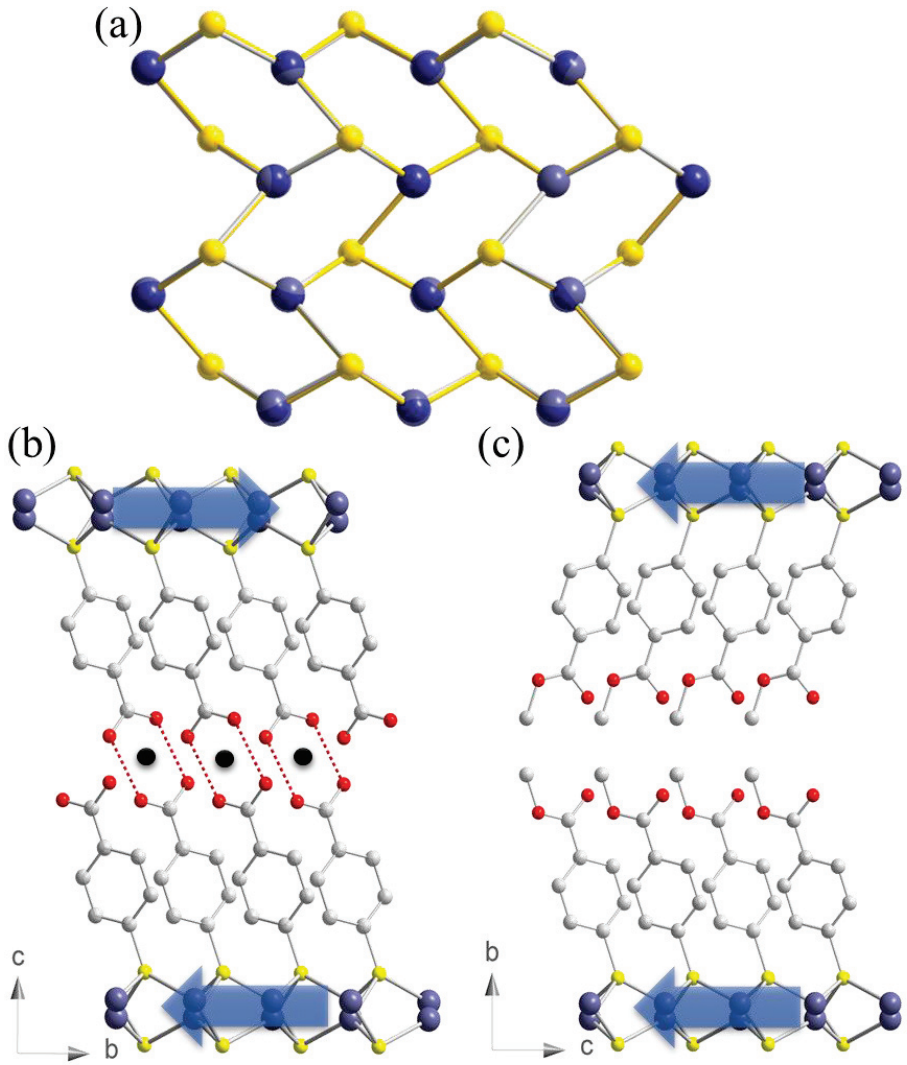

Figure 2. 5 Structure representations of [Ag(*p*-SPhCO$_2$H)]$_n$ and [Ag(*p*-SPhCO$_2$Me)]$_n$: (a) Superposition of the Ag$_3$S$_3$ hexagons in both compounds (gray lines – bonds of [Ag(*p*-SPhCO$_2$H)]$_n$ layer, yellow lines – bonds of [Ag(*p*-SPhCO$_2$Me)]$_n$ layer, dashed lines – short Ag-Ag contacts below 3.44 Å). Views on *(bc)* plane of (a) [Ag(*p*-SPhCO$_2$H)]$_n$ and (b) [Ag(*p*-SPhCO$_2$Me)]$_n$, respectively. Black sphere on (b) depicts inversion center. Blue arrows show the "orientation" of Ag-S layer. Red dashed lines represent the hydrogen bonds. Blue, Ag; yellow, S; red, O; grey, C. Hydrogen atoms are omitted for clarity. Adapted with permission from [19]. Copyright 2019 American Chemical Society.

The shortest Ag(I)-Ag(I) distances are of 2.936(2) Å and 2.973(3) Å in $[Ag(p\text{-}SPhCO_2H)]_n$ and $[Ag(p\text{-}SPhCO_2Me)]_n$, respectively. It is less than the sum of van der Waals atomic radii between two silver atoms (*cca*. 3.44 Å) and can be considered as argentophilic interactions (**Table 2. 1**).[20]

The organic part lies between the Ag(I)-S layers without interpenetration (**Figure 2. 5** (b) and (c)). In $[Ag(p\text{-}SPhCO_2H)]_n$, the presence of dimeric hydrogen bonds between the carboxylic acids is observed. The action of an inversion is demonstrated in the **Figure 2. 5** (b) and (c) for the two compounds. In $[Ag(p\text{-}SPhCO_2Me)]_n$, the neighboring Ag-S layers are oriented in the same direction. In $[Ag(p\text{-}SPhCO_2H)]_n$, the neighboring Ag-S layers are oriented in the opposite directions due to the presence of inversion center. Despite both CPs have the same $[AgS]_n$-array, influence of hydrogen-bonding on the overall structure is observed.

2.2.4 $[Au(p\text{-}SPhCO_2H)]_n$ Structure

The structure determination results into the triclinic space group – *P*1 with *a* = 4.5181(4) Å, *b* = 5.4084(4) Å, *c* = 14.8606(9) Å, α = 84.867(6)°, *β* = 86.292(6)°, γ = 88.256(6)°. It is a lamellar structure, however it is quite different from its reported esterified counterpart $[Au(p\text{-}SPhCO_2Me)]_n$.[21]

1D helical chains are composed of Au(I) atoms bridged by thiolate ligands with typical Au-S bonds in range between 2.27 Å and 2.37 Å. These chains are connected via zig-zag aurophilic interactions with Au-Au distances of 3.355(4) Å and 3.422(6) Å into 2D sheets (**Figure 2. 6** (a), **Table 2. 1**). The Au-S-Au angles have values expected for gold thiolate complexes (99.4(1)° and 110.4(1)°). In contrary, the S-Au-S angles are far from common linear ones: 77.5(1)° and 124.0(1)°. It is a first observation of S-Au-S angles of this range in a pure $[Au(SR)]_n$ structure. This non-linear angle can be found in gold(I) thiolate complexes with coordination number of three and four with phosphine or nitrogen-based molecules as ligands.[22-24] This significant distortion is partially governed by the formation of interchain Au-Au interactions. *Syn*, *syn* catemeric hydrogen bonds (between the carboxylic acid functions of the tilt and non-interpenetrated ligands) also contribute to the distortion (**Figure 2. 6** (b), (c)). This uncommon catemeric arrangement (as opposed to the common dimeric one)[25] is parallel to the -Au-S-helical chains. The distances between both oxygen atoms involved in the hydrogen interactions are 2.901(9) Å and 3.010(9) Å. These distances (of less than 3.4 Å) between the donor and

acceptor are in good accordance with the presence of hydrogen interactions. This catemeric hydrogen bonding is a rare example in CPs. They are sewing neighboring 2D-layers which results into formation of 3D-structure.

This structure is very different from the one of [Au(*p*-SPhCO$_2$Me)]$_n$ (see State of the Art I.1.3, **Figure I. 13**). This is a result of a complex interplay between different types of weak bonds: aurophilic and hydrogen interactions.

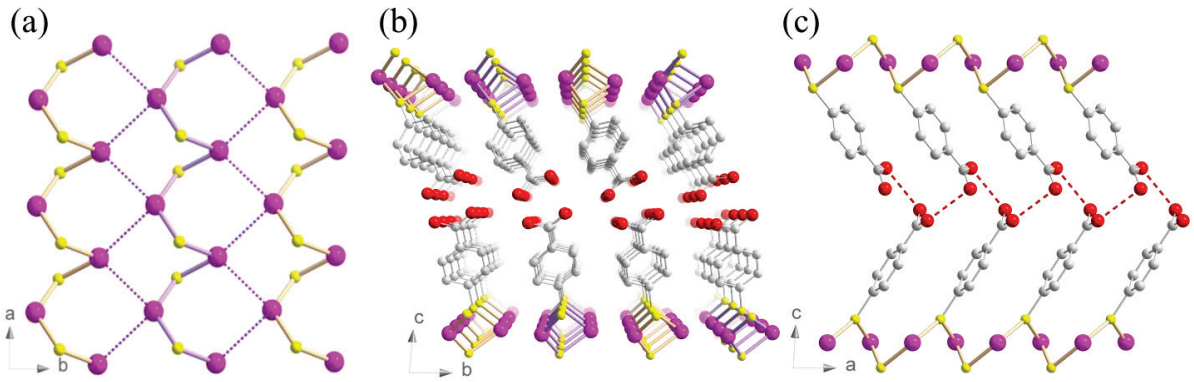

Figure 2. 6 Structure representations of [Au(*p*-SPhCO$_2$H)]$_n$: (a) View of gold-thiolate chains on *(ab)* plan. Views of the network on (b) *(bc)* and (c) *(ac)* plan. Red dashed lines represent hydrogen bonding. Violet dashed lines represent aurophilic interactions. Pink, Au; yellow, S; red, O; grey, C. Hydrogen atoms are omitted for clarity. Reprinted with permission from ref. [26]. Copyright 2017 The Royal Society of Chemistry.

2.2.5 Conclusion

The introduction of –CO$_2$R group (R = H, Me) in the *para*-position leads to the formation of different structural arrays in comparison to [M(SPh)]$_n$ CPs. It underlies its importance. The comparison of structures of three couples of compounds with –CO$_2$H and –CO$_2$Me groups in *para*-position (with or without hydrogen bonding) demonstrates non-negligible role of hydrogen bonding in the structure formation. Even for a quasi-identical [MS]$_n$-array in the case of [Ag(*p*-SPhCO$_2$H)]$_n$ and [Ag(*p*-SPhCO$_2$Me)]$_n$ the overall structures of the materials are different. Depending on the nature of the metal, and its ability to form metallophilic interactions, different [MS]$_n$-arrays can be formed (1D: helices or chains, or 2D with more or less distorted hexagons). These structures illustrate well the different possible cases.

2.3 Characterization

SEM images revealed that the crystallites of all compounds have pellet or platelet-like shapes of various sizes (**Figure 2. 7**). Such morphology is characteristic for lamellar compounds.

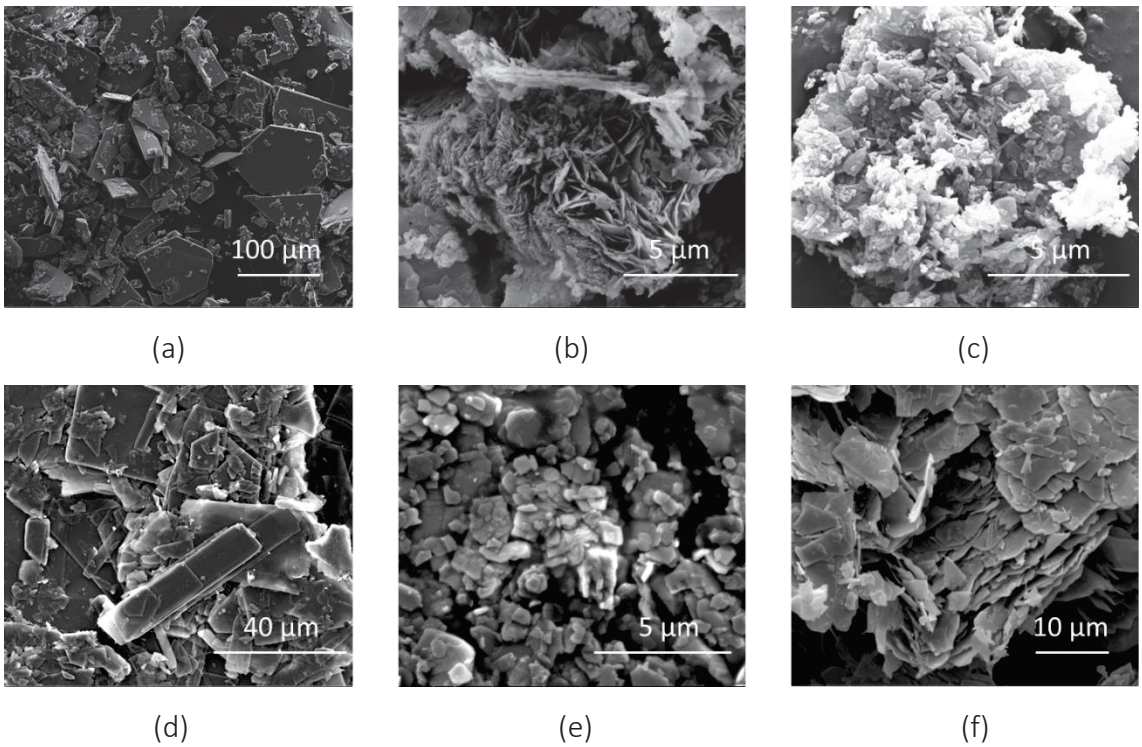

Figure 2. 7 SEM images of CPs $[Cu(p\text{-}SPhCO_2H)]_n$ (a), $[Ag(p\text{-}SPhCO_2H)]_n$ (b), $[Au(p\text{-}SPhCO_2H)]_n$ (c), $[Cu(p\text{-}SPhCO_2Me)]_n$ (d), $[Ag(p\text{-}SPhCO_2Me)]_n$ (e), $[Au(p\text{-}SPhCO_2Me)]_n$ (f). Adapted with permission from ref. [17,18,19,26]. Copyright 2018 & 2019 American Chemical Society. Copyright 2016 & 2017 The Royal Society of Chemistry.

FT-IR spectroscopy study (**Figure 2. 8**) has shown a presence of broad ν(OH) bands around 3000 and 2600 cm^{-1} in the case of following CPs: $[Cu(p\text{-}SPhCO_2H)]_n$, $[Ag(p\text{-}SPhCO_2H)]_n$ and $[Au(p\text{-}SPhCO_2H)]_n$. The observations are consistent with the presence of hydrogen bonds between the carboxylic acid functions. Antisymmetric vibration of the carboxylic acid group band is observed at 1687 cm^{-1}, similar to the free ligand and is in good accordance with non-coordinated acids. At 930 cm^{-1} relatively broad band of deformation (out of plane vibration of OC-OH) is present.[27] FT-IR spectra of $[Cu(p\text{-}SPhCO_2Me)]_n$, $[Ag(p\text{-}SPhCO_2Me)]_n$ and $[Au(p\text{-}SPhCO_2Me)]_n$ has shown presence of antisymmetric vibration of the carboxylic acid group band. It is observed at 1714 cm^{-1} and it confirms its esterification. A disappearance of the vibrations at 907 cm^{-1} and 2579 cm^{-1} is observed in comparison to the free ligand. They correspond to

deformation and stretching vibration of the SH-bond, respectively. Their disappearance confirms the coordination of the ligand to the metal via thiolate group.

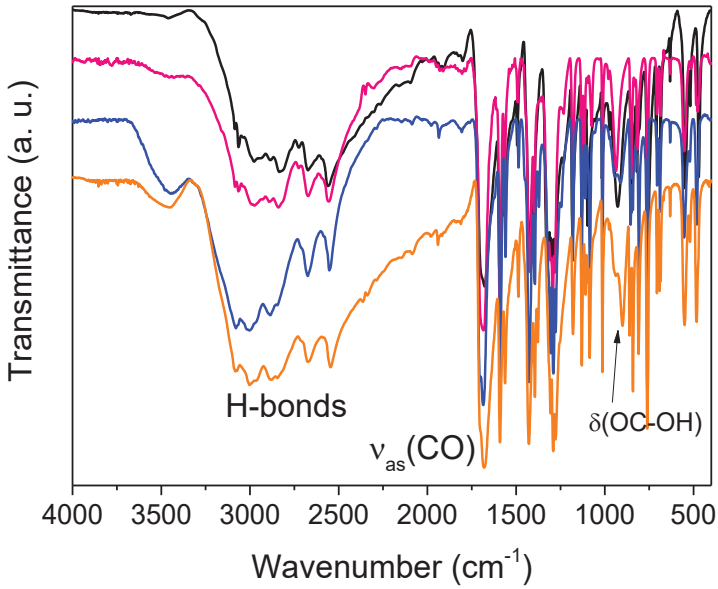

(a)

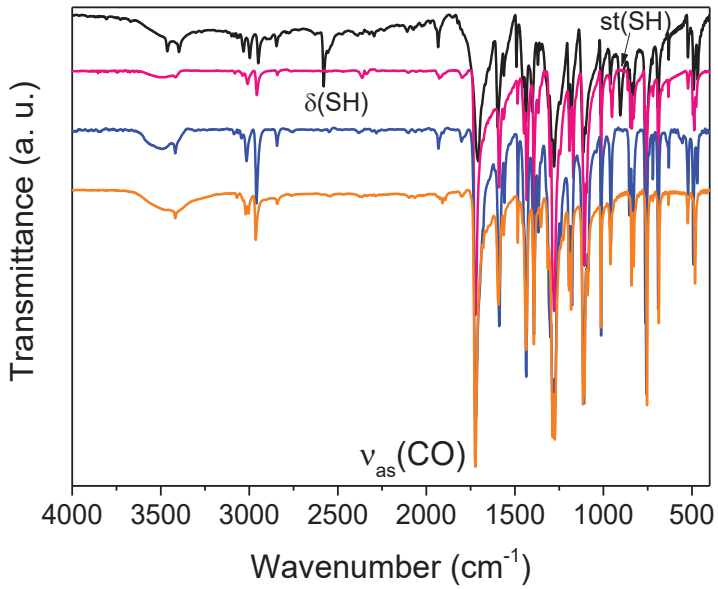

(b)

Figure 2. 8 FT-IR spectra of the free ligand (black), Cu(I)- (orange), Ag(I)- (blue) and Au(I)- (pink) based CPs formed with *para*-mercaptobenzoic acid (a) and its esterified version (b).

The thermo-gravimetric analysis confirms the purity of the compounds with an expected metal and organic content. We observe an increase of the thermal stability after the complexation of the metal in comparison to the free ligand (**Figure 2. 9**, **Table 2. 2**). After the

complexation of *p*-HSPhCO$_2$H by copper, silver and gold the decomposition temperature increases from 150°C to the values of 300°C, 340°C and 330°C, respectively. For the *p*-HSPhCO$_2$Me-based compounds, these values are rising from 100°C to 270°C, 290°C, 260°C, respectively. All CPs show relatively good thermal stability. For each couple of CPs (based on the same metal) an increase of thermal stability is observed in the presence of hydrogen bonding. It reinforces the structure. [Au(*p*-SPhCO$_2$Me)]$_n$ has lower stability than both the copper- and the silver-based counterparts. It occurs due to the difference of M-S arrangement: in copper- and silver-based compounds it forms a 2D covalent network. In case of the gold-based compound, it forms 1D chains connected through weak interactions in the 2D layers. In the case of [Au(*p*-SPhCO$_2$H)]$_n$, its stability is almost comparable to the silver counterpart, due to the presence of extended network of catemeric hydrogen bonds.

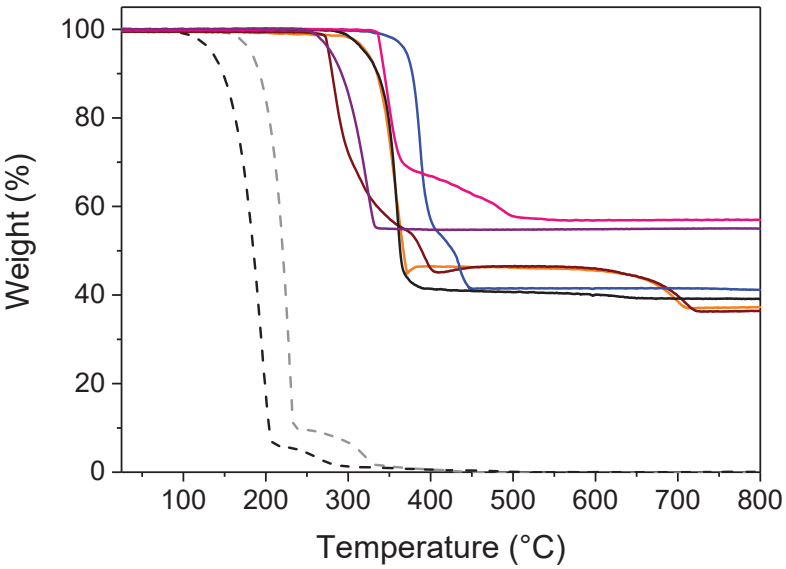

Figure 2. 9 The TGA performed under air at 10°C/min of free ligands: *p*-HSPhCO$_2$H (gray dashed line) and *p*-HSPhCO$_2$Me (black dashed line); and coordination polymers [Cu(*p*-SPhCO$_2$H)]$_n$ (orange), [Cu(*p*-SPhCO$_2$Me)]$_n$ (brown), [Ag(*p*-SPhCO$_2$H)]$_n$ (blue), [Ag(*p*-SPhCO$_2$Me)]$_n$ (black), [Au(*p*-SPhCO$_2$H)]$_n$ (pink), [Au(*p*-SPhCO$_2$Me)]$_n$ (violet).

Table 2. 2 The decomposition temperatures obtained from TGA experiments with the free ligands and the coordination polymers.

	p-HSPhCO$_2$R	[Cu(*p*-SPhCO$_2$R)]$_n$	[Ag(*p*-SPhCO$_2$R)]$_n$	[Au(*p*-SPhCO$_2$R)]$_n$
R = H	150	300	340	330
R = Me	100	270	290	260

2.4 Photophysical Properties

All compounds exhibit high-energy absorption between λ_{abs} = 250-350 nm, which can be assigned to a π–π* transition of the phenyl group of the ligand[28] (**Figure 2. 10**). The compound [Au(*p*-SPhCO$_2$Me)]$_n$ has a little different profile relatively to other CPs. It is supposedly due to the difference of [MS]$_n$ arrangement. The compound [Cu(*p*-SPhCO$_2$Me)]$_n$ also exhibits a less intense shoulder (between 400-450 nm). It is, presumably, a result of the M→S MLCT [29,30,31,32] or LMCT transition modified by the M⋯M contacts[33] which gives its yellow color.

The optical band gaps are following: [Cu(*p*-SPhCO$_2$H)]$_n$ – 2.79 eV, [Cu(*p*-SPhCO$_2$Me)]$_n$ – 2.68 eV, [Ag(*p*-SPhCO$_2$H)]$_n$ – 2.99 eV, [Ag(*p*-SPhCO$_2$Me)]$_n$ – 3.04 eV, [Au(*p*-SPhCO$_2$H)]$_n$ – 3.05 eV and [Au(*p*-SPhCO$_2$Me)]$_n$ – 2.84 eV.

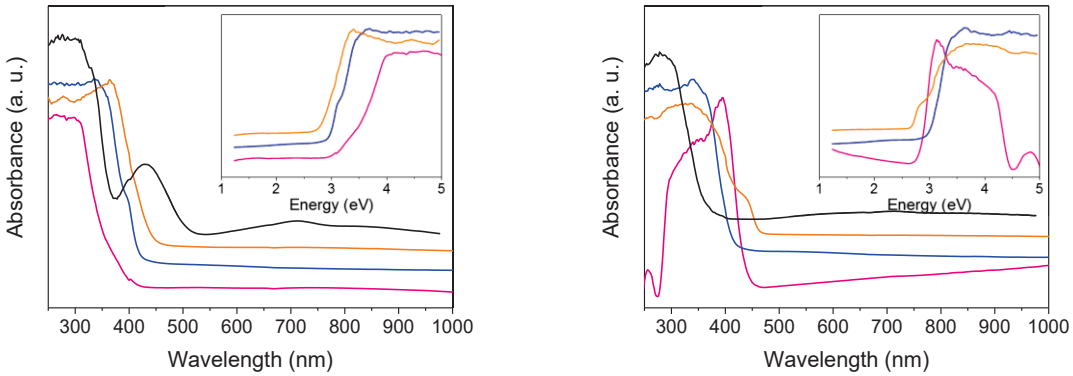

(a) (b)

Figure 2. 10 UV-vis absorption spectra of (a) [Cu(*p*-SPhCO$_2$H)]$_n$ (orange), [Ag(*p*-SPhCO$_2$H)]$_n$ (blue), [Au(*p*-SPhCO$_2$H)]$_n$ (pink), *p*-HSPhCO$_2$H (black); (b) [Cu(*p*-SPhCO$_2$Me)]$_n$ (orange), [Ag(*p*-SPhCO$_2$Me)]$_n$ (blue), [Au(*p*-SPhCO$_2$Me)]$_n$ (pink), *p*-HSPhCO$_2$Me (black) obtained in solid state at room temperature. UV-vis absorption spectra as function of energy are shown as inset.

2.4.1 [Cu(*p*-SPhCO$_2$H)]$_n$

[Cu(*p*-SPhCO$_2$H)]$_n$ shows rather complicated photophysical behavior with multiple emission peaks at different excitation wavelength. It is manifested in its thermoluminochromism that can be observed visually (**Figure 2. 11** (a)). The sample shows an intense yellow emission at 93 K, green emission between 153 K and 213 K, and it becomes again yellow-orange at 243 K. This can be well illustrated by the temperature dependent CIE (Commision Internationale de l'Eclairage) chromaticity diagram (**Figure 2. 11** (b)).

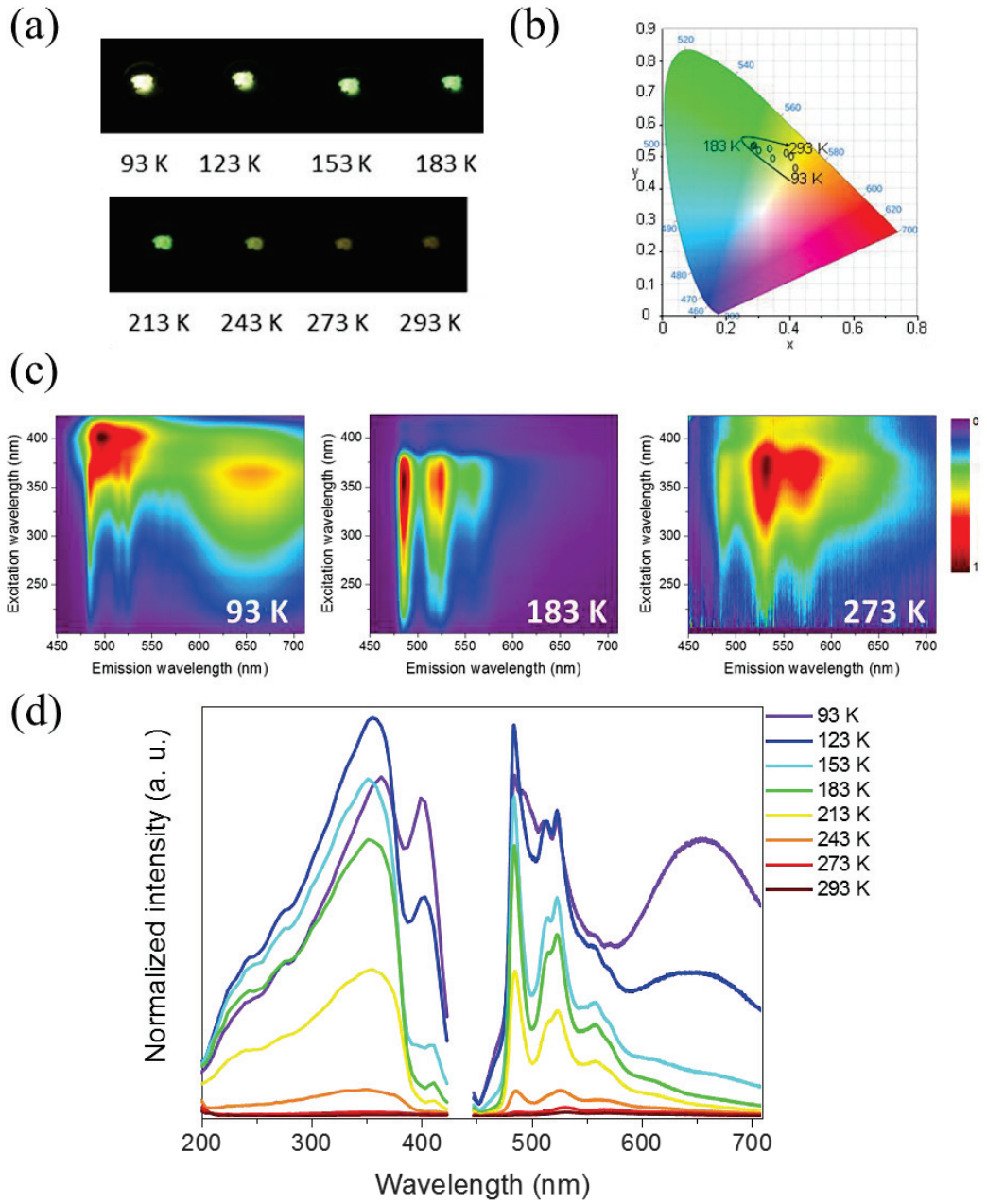

Figure 2. 11 (a) Photos of $[Cu(p\text{-}SPhCO_2H)]_n$ under UV light (380 nm) from 93 to 293 K; (b) CIE chromaticity diagram showing the temperature dependent luminescence color change in the 93–293 K temperature range (λ_{ex} = 352 nm); (c) 2D maps of the emission and excitation spectra obtained in the solid state at 93, 183 and 273 K, from left to right; (d) emission-excitation spectra (λ_{exc} = 360 nm, λ_{em} = 485 nm) obtained in the solid state at various temperatures. Adapted with permission from [17]. Copyright 2018 American Chemical Society.

The evolution of the emission-excitation spectra with temperature variation can be nicely represented with 2D maps (**Figure 2. 11** (c)). In section to follow, we adopt a convention that the positions of maxima are represented in form of 2D vectors (λ_{exc}, λ_{em}) in nanometers. At 273

K, $[Cu(p\text{-}SPhCO_2H)]_n$ exhibits an emission in green-yellow part of the spectrum with apexes at (370, 530) and less intense one at (370, 570). In the process of temperature decrease the peak at (350, 485) becomes predominant (from 213 to 123 K). Then, at 123 K, two other peaks appear at (400, 500) and (360, 660). The one at (400, 500) becomes predominant at 93 K. The presence of different emission and excitation maxima is clearly seen in the emission-excitation spectra collected at different temperatures (**Figure 2. 11** (d)).

In order to get deeper understanding of photophysical processes during temperature change, single crystal XRD analysis has been carried out at 120 K. At low temperature, no symmetry change is observed; the reduction of the cell volume is only 0.55 % in comparison to the data collected at 293 K (**Table 2. 4**). The thermoluminochromism is, therefore, not directly correlated to some prominent structural changes, as it has been often observed for Cu(I)-coordination compounds and Cu(I)-clusters. [34,35]

Lifetime decay measurements were performed under excitation of 379 nm at various temperatures. The data were fitted by four-exponential decay curve. At 273 K, the lifetime varies between 0.14 and 764 μs, while at 93 K it is between 44 μs and 9.2 ms (Appendix B). The lifetime shortening due to the thermal quenching is observed in this compound. It is similar to the CPs discussed in the Chapter 1. The long lifetimes are characteristic of phosphorescent processes.

The observed multiple emitting states are not very common case, but not unprecedented – thermoluminochromic systems with different emitting states of different origins have been already reported for other Cu(I)-compounds.[36,37,38]

The vibronic structure of the emission between 485 nm and 570 nm can be attributed to the intraligand transition ^{3}IL ($\pi \rightarrow \pi^*$) of the aromatic thiolates. Indeed, the free ligand shows an emission band centered around 530 nm in the same range of temperature (**Figure 2. 12**). The appareance of the vibronic structure can be explained by increased rigidity of the ligand when it is coordinated to the metal. Alternative explanation might lie in the perturbation of a CT due to the metal.

The emission band at LE, 660 nm, originates the most probably from the triplet states of ^{3}LMCT and/or ^{3}MLCT transitions, mixed with MC (ds/dp) states.

Therefore, luminescent properties of $[Cu(p\text{-}SPhCO_2H)]_n$ show a subtle equilibrium between LC (at HE) and MC (at LE) transitions.

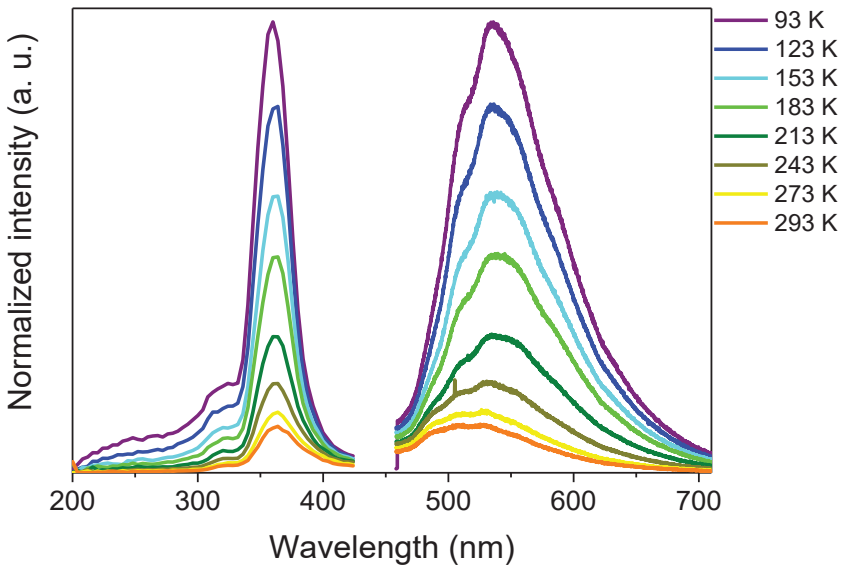

Figure 2. 12 Emission-excitation spectra (λ_{exc} = 360 nm, λ_{em} = 534 nm) of p-$HSPhCO_2H$ obtained in the solid state at various temperatures. Reprinted with permission from [17]. Copyright 2018 American Chemical Society.

2.4.2 $[Cu(p\text{-}SPhCO_2Me)]_n$

$[Cu(p\text{-}SPhCO_2Me)]_n$ exhibits thermoluminochromism similarly to $[Cu(p\text{-}SPhCO_2H)]_n$ (**Figure 2. 13** (a), (b)). However, it shows no emission dependence on the excitation wavelength (**Figure 2. 13** (c)). The emission profile is rather different from the one of $[Cu(p\text{-}SPhCO_2H)]_n$. At 93 K, a triple emission is observed with a blue peak at 460 nm, a green peak at 560 nm (the most intense) and a red peak at 740 nm. With temperature increase, each band decreases in intensity. The red emission band becomes predominant at 183 K, at the point where the blue emission is the most intense out of all – at 413 K (**Figure 2. 13** (d)). Visually, it manifests as emission color change from yellow at 93 K to pink at 273 K, and blue at 413 K. It is in agreement with temperature dependent CIE chromaticity diagram (**Figure 2. 13** (b)). While the blue and green peaks do not show any shift with the variation of the temperature, the red band shifts from 740 nm to 765 nm with the temperature increase.

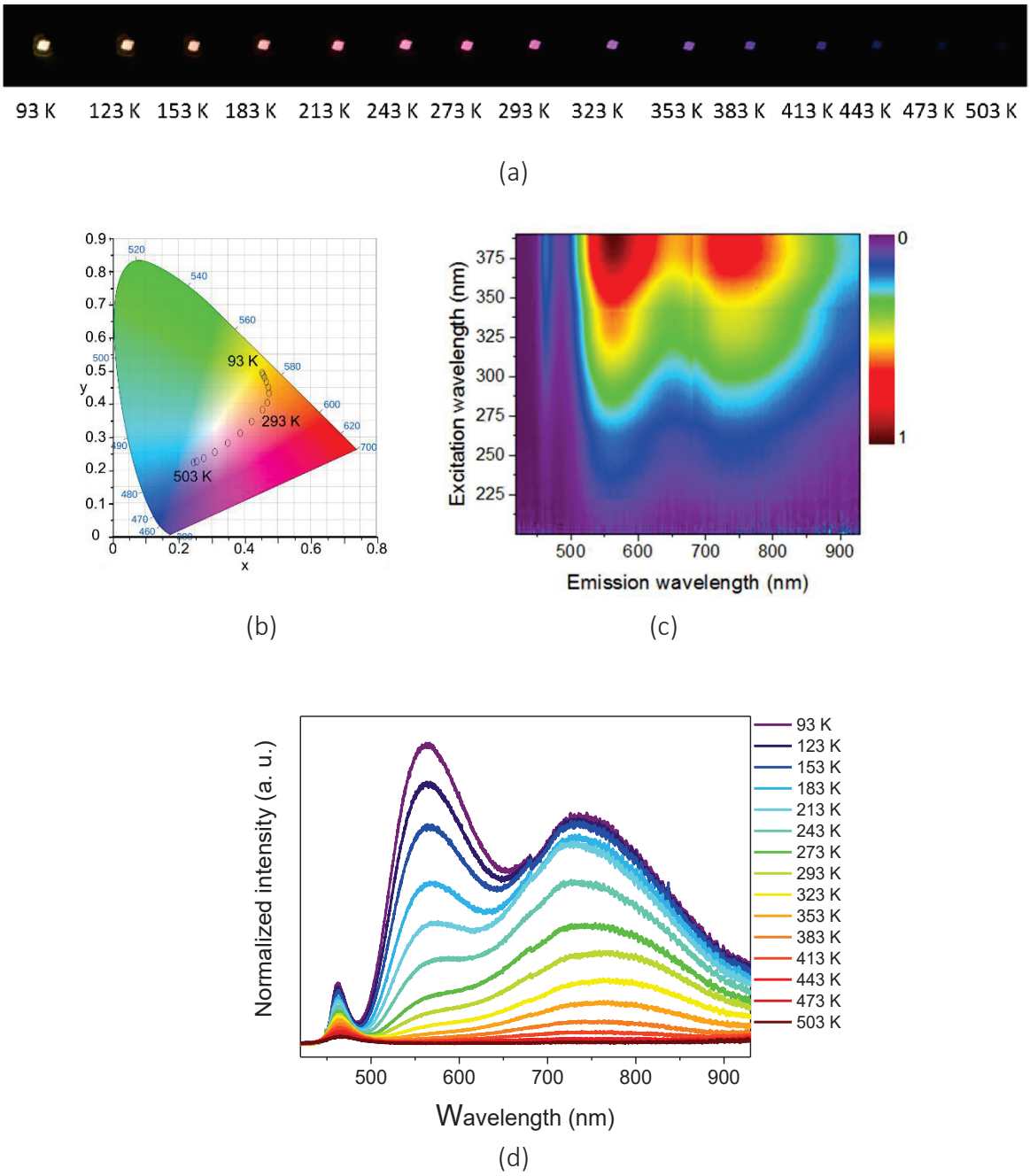

Figure 2. 13 Photophysical properties of $[Cu(p\text{-}SPhCO_2Me)]_n$:(a) photos at 93 K (left) to 503 K (right) under UV light (365 nm); (b) CIE chromaticity diagram showing the temperature dependent luminescence color change in the 93–503 K temperature range (λ_{exc} = 380 nm); (c) 2D map of the emission and excitation spectra obtained in the solid state at 93 K; (d) emission spectra (λ_{exc} = 380 nm) obtained in the solid state at various temperatures. Adapted with permission from ref. [18]. Copyright 2017 The Royal Society of Chemistry.

Such a well separated triple emissive behavior is unprecedented in Cu(I)-based materials. Intrinsic dual emission with well-separated peaks is well-known for various types of Cu(I) clusters, such as $[CuL]_6$[39] or $[Cu_4I_4L_4]$.[40] Their dual emission is usually attributed to a ^{3}CC (Cluster Centered CT) for the LE and a MLCT for the HE band. A couple of d^{10}-based coordination

compounds with peculiar photophysical properties have been reported. For example, Cu(I)–halide coordination polymers with thione-based ligands have been reported with up to seven red emission bands. The bands have not-well-separated vibronic character between 620–770 nm.[41] The multiemission in the 350–780 nm spectral domain originates from the ligand and LMCT.[42] Complicated photophysical behaviors with multiple origin emission have been reported for sulfido-phosphane Au(I) polynuclear complexes[43] and also for dithiolate gold phosphine complexes.[44]

The emission maximum of the free ligand, *p*-HSPhCO$_2$Me, is at 498 nm (**Figure 2. 14**). Taking into account the Cu(I)–thiolate-based compounds,[39,45,46,47,48] the origin of the triple emission of [Cu(*p*-SPhCO$_2$Me)]$_n$, is tentatively assigned to a complex mixture of various processes. It includes ILCT at HE, combined at LE with emission from ^{3}MLCT, ^{3}LMCT and/or MC (ds/dp) states.

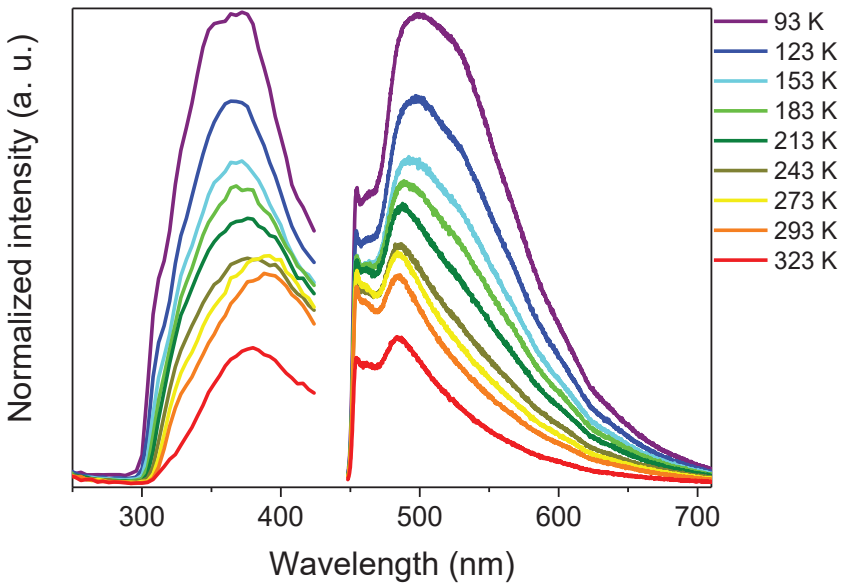

Figure 2. 14 Emission-excitation spectra (λ_{exc} = 356 nm, λ_{em} = 498 nm) of *p*-HSPhCO$_2$Me obtained in the solid state at various temperatures. Reprinted with permission from ref. [18]. Copyright 2017 The Royal Society of Chemistry.

2.4.3 [Ag(*p*-SPhCO$_2$H)]$_n$ and [Ag(*p*-SPhCO$_2$Me)]$_n$

The silver(I)-based compounds are not luminescent at the room temperature. A weak emission appears at 273 K for [Ag(*p*-SPhCO$_2$H)]$_n$ and at 243 K for [Ag(*p*-SPhCO$_2$Me)]$_n$ (**Figure 2. 15** (a) and **Figure 2. 16** (a)).

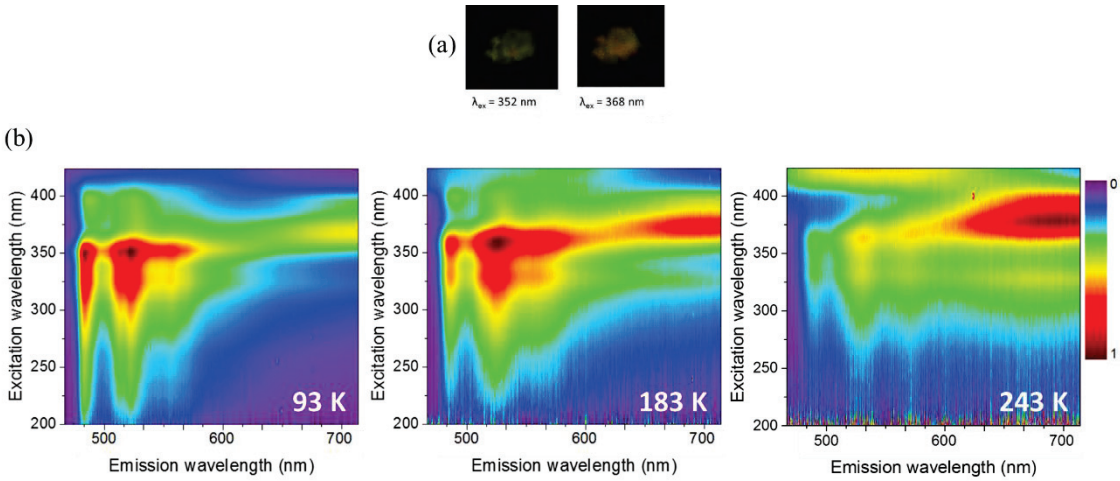

Figure 2. 15 (a) Photos of [Ag(*p*-SPhCO$_2$H)]$_n$ under UV light at 93 K and (b) 2D maps of the emission and excitation spectra, obtained in the solid state at 93, 183 and 243 K, from left to the right. Adapted with permission from [19]. Copyright 2019 American Chemical Society.

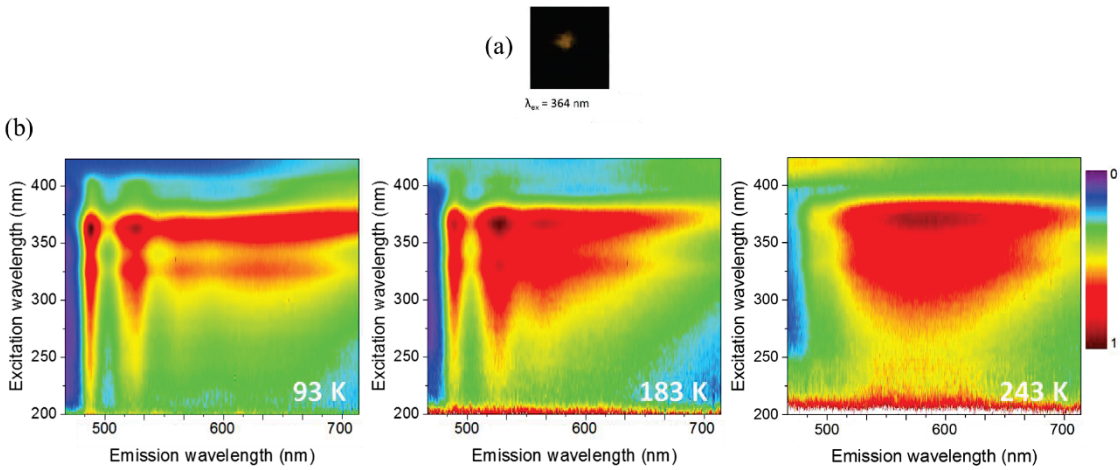

Figure 2. 16 (a) Photos of [Ag(*p*-SPhCO$_2$Me)]$_n$ under UV light at 93 K and (b) 2D maps of the emission and excitation spectra, obtained in the solid state at 93, 183 and 243 K, from left to the right. Adapted with permission from [19]. Copyright 2019 American Chemical Society.

This emission is centered in the LE range at (380, 700) and (368, 580) for [Ag(*p*-SPhCO$_2$H)]$_n$ and [Ag(*p*-SPhCO$_2$Me)]$_n$, respectively (**Figure 2. 15** (b), **Figure 2. 16** (b)). During the temperature decrease, some emission peaks in the HE range appears. At 93 K, the dominant peaks in [Ag(*p*-SPhCO$_2$H)]$_n$ are centered at (352, 484) and (352, 528). For [Ag(*p*-SPhCO$_2$Me)]$_n$ they are centered at (364, 489) and (364, 526). The LE bands are centered (at 93 K) at (368, 700) and (364, 650) for [Ag(*p*-SPhCO$_2$H)]$_n$ and [Ag(*p*-SPhCO$_2$Me)]$_n$, respectively. The intensification of the emission with the decrease of the temperature is due to the enhanced rigidity of the network, which effectively reduces the energy loss by non-radiative decay.

The emission is dependent on the excitation energy. For $[Ag(p\text{-}SPhCO_2H)]_n$, at λ_{exc} = 220-340 nm only the HE emission is present, while in case of λ_{exc} = 360 nm the LE emission appears. In the case of $[Ag(p\text{-}SPhCO_2Me)]_n$,, both HE and LE emissions are observed in the range of λ_{exc} = 220-360 nm. Starting from λ_{exc} = 380 nm, the LE energy increases and is red-shifted. The excitation-dependent emission is opposite to the classical case behavior in photophysics (Kasha rule). It is similar to the one observed for $[Cu(p\text{-}SPhCO_2H)]_n$.

The HE emission bands are well defined (**Figure 2. 17** (a), **Figure 2. 18** (a)) and have a vibronic spacing of ~1200 cm^{-1},characteristic for the vibrational modes of aromatic molecules. The HE emission bands can be assigned to the IL π-π* transition, since the free ligands exhibit an emission band in a given wavelength range. The vibronic structure of the aromatic rings (present in the silver thiolate compounds and absent in the non-coordinated ligands) is favored by the heavy-atom effect of silver[49] and by the rigidity of the network. It involves various weak intramolecular interactions.

These CPs are structurally similar to $[Ag(SPh)]_n$ phase **1**. Nevertheless, their emission belonging the red part of the spectra occurs at higher energy (700 nm and 650 nm vs. 810 nm for $[Ag(SPh)]_n$ phase **1**). Moreover, in $[Ag(SPh)]_n$ no emission is observed in the blue part of the spectra. These, along with higher quantum yield of $[Ag(p\text{-}SPhCO_2H)]_n$ and $[Ag(p\text{-}SPhCO_2Me)]_n$ (both emit at 243 K, while $[Ag(SPh)]_n$ emits only at 93K) seems to originate from the presence of the electron-withdrawing substituent on the cycle. Thus, an introduction of a substituent influences the electronic levels of the ligand and leads to different emission properties.

Lifetime measurements for $[Ag(p\text{-}SPhCO_2H)]_n$ and $[Ag(p\text{-}SPhCO_2Me)]_n$ were performed at 93 K in solid state (Appendix B). Measurements were done for both HE and LE emission peaks. The curves were fitted by a tri-exponential decay function, where one of components has a form of stretched exponential. The major component for the HE band is 182 ns (83 %) and 475 µs (94 %), for compounds $[Ag(p\text{-}SPhCO_2H)]_n$ and $[Ag(p\text{-}SPhCO_2Me)]_n$, respectively. The major component for the LE band is 191 µs (53 %) and 175 µs (70 %), respectively. In the case of both compounds, microsecond-range lifetime is dominant for HE and LE emission. These long lifetimes, are consistent with phosphorescence processes.

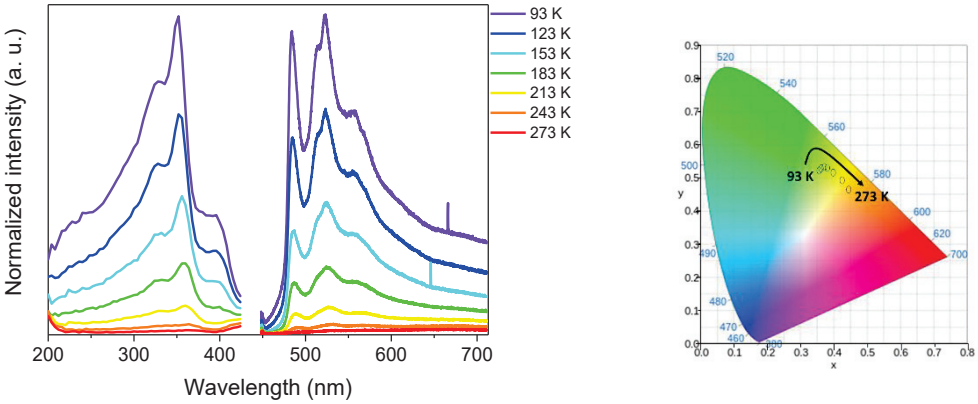

(a) (b)

Figure 2. 17 Photophysical properties of $[Ag(p\text{-}SPhCO_2H)]_n$: (a) emission-excitation spectra (λ_{ex} = 352 nm, λ_{em} = 522 nm) obtained in the solid state at various temperatures; (b) CIE chromaticity diagram showing the temperature dependent luminescence color change in the 93–273 K temperature range (λ_{ex} = 352 nm). Adapted with permission from [19]. Copyright 2019 American Chemical Society.

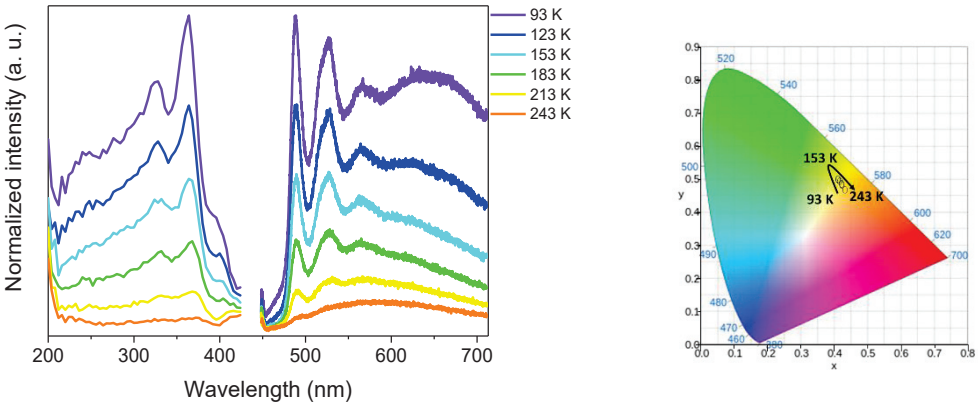

(a) (b)

Figure 2. 18 Photophysical properties of $[Ag(p\text{-}SPhCO_2Me)]_n$: (a) emission-excitation spectra (λ_{ex} = 364 nm, λ_{em} = 489 nm) obtained in the solid state at various temperatures; (b) CIE chromaticity diagram showing the temperature dependent luminescence color change in the 93–274 K temperature range (λ_{ex} = 364 nm). Adapted with permission from [19]. Copyright 2019 American Chemical Society.

The HE emission between 470 nm and 550 nm can be assigned to ^{3}IL $\pi \rightarrow \pi^*$ transitions. The formation of excimers, between aromatic-based ligands, cannot be proposed because of the long centroid-centroid distances between the adjacent benzyl rings (5.816(1) Å and 5.906(1) Å in $[Ag(p\text{-}SPhCO_2H)]_n$ and $[Ag(p\text{-}SPhCO_2Me)]_n$, respectively).[50, 51] The LE emission

bands, centered between 650 nm and 700 nm, originate the most probably from the triplet states of a LMCT or MLCT.[52-57]

CIE chromaticity diagram of $[Ag(p\text{-}SPhCO_2H)]_n$ shows a luminescence thermoluminochromism from yellow to green with the decrease of the temperature, while $[Ag(p\text{-}SPhCO_2Me)]_n$ exhibits a little color variation in the yellow area (**Figure 2. 17** (b), **Figure 2. 18** (b)).

The resemblance of the properties of $[Ag(p\text{-}SPhCO_2H)]_n$ and $[Ag(p\text{-}SPhCO_2Me)]_n$ is related to the structural similarity and comparable electronic effect of the substituents. $[Ag(p\text{-}SPhCO_2H)]_n$ shows emission at slightly higher temperature than $[Ag(p\text{-}SPhCO_2H)]_n$. It is probably due to the enhanced rigidity of the structure caused by the presence of the hydrogen bonds.

Both CPs have luminescence pattern similar to $[Cu(p\text{-}SPhCO_2H)]_n$. This is a manifestation of similar $[MS]_n$ arrangement and ligand stacking for all three compounds. The variance of the properties relatively to $[Cu(p\text{-}SPhCO_2Me)]_n$ underlines how sensible is the luminescence to the modifications of $[MS]_n$ array.

2.4.4 $[Au(p\text{-}SPhCO_2H)]_n$

$[Au(p\text{-}SPhCO_2H)]_n$ shows weak red emission at the room temperature under UV light. It turns yellow and then intense light blue at 223 K and 153 K, respectively (**Figure 2. 19** (a)). Visual observations are well in agreement with the evolution of emission observed on 2D maps. At 290 K, the compound exhibits a single peak centered at (345, 665). At 140 K, two additional peaks appear at (328, 490) and (384, 470). Finally at 80 K, these two peaks dominate over the first one (**Figure 2. 19** (b)). These multiple emission peaks resemble the emissive properties of $Au(Me_2PhP)(p\text{-}SPhCO_2H)$.[10]

HE emission peak (328, 490) has three apexes at 470 nm, 490 nm and 525 nm (**Figure 2. 20**). This corresponds to the vibronic progression of 870 cm^{-1} and 1360 cm^{-1}, typical for excited states of aromatic systems. Thus, this emission can be attributed to the IL transition, similarly to the previously discussed compounds.

The LE emission centered at 650 nm originates from the gold center and might be attributed to a LM(M)CT or sometimes to a LM-to-L charge transfer (LMLCT) transition.[21, 58]

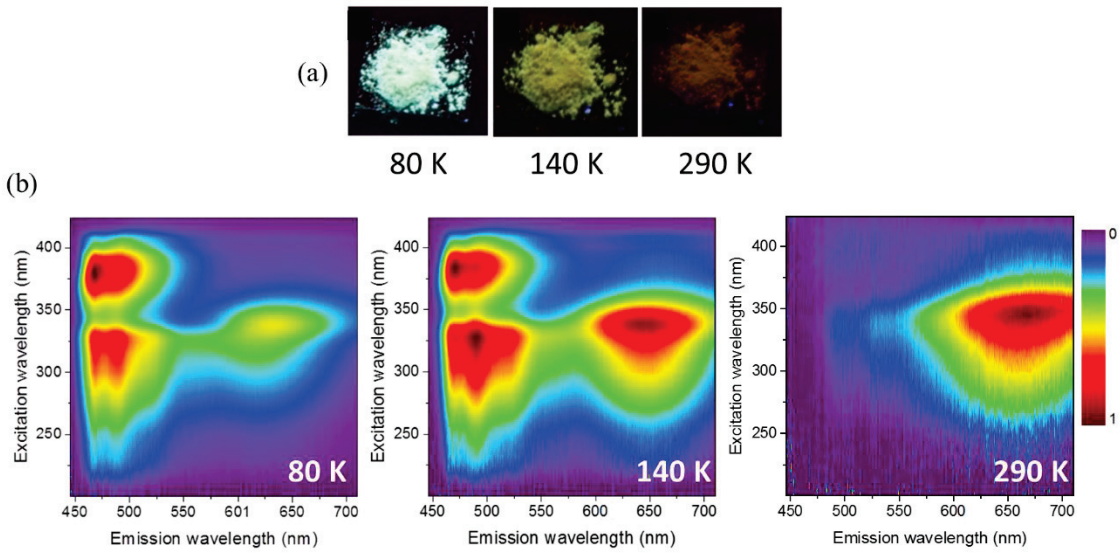

Figure 2. 19 Photophysical properties of $[Au(p\text{-}SPhCO_2H)]_n$:(a) photos at 80, 140 and 290 K under UV light; (b) 2D map of the emission and excitation spectra obtained in the solid state at 80, 140 and 290 K. Adapted with permission from ref. [26]. Copyright 2017 The Royal Society of Chemistry.

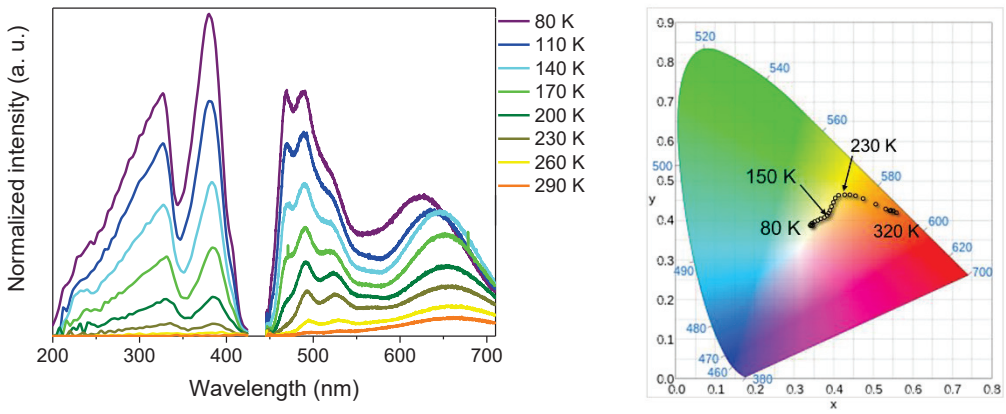

(a) (b)

Figure 2. 20 (a) Emission-excitation spectra (λ_{ex} = 328 nm, λ_{em} = 470 nm) of $[Au(p\text{-}SPhCO_2H)]_n$, obtained in the solid state at various temperatures; (b) CIE chromaticity diagram showing the temperature dependent luminescence color change of $[Au(p\text{-}SPhCO_2H)]_n$ in the 80–320 K temperature range (λ_{ex} = 328 nm). Adapted with permission from ref. [26]. Copyright 2017 The Royal Society of Chemistry.

Luminescence lifetime measurements were performed (Appendix B). The collected data were fitted with tri-exponential decay equation. Two main components are in the microsecond range – 2.56 µs (66 %) and 0.36 µs (29 %) at 293 K. At 93 K they are 9.94 µs (85 %) and 1.02 µs (14 %), respectively. Thermal quenching is observed. A third, weak lifetime component is present almost over the whole temperature range at around 0.04 µs (< 5 %).

The radiative lifetimes in the microsecond range point to triplet parentage of the emission. Thus, the HE emission is attributed to metal-perturbed intraligand phosphorescence ^{3}IL ($\pi \rightarrow \pi^*$). The LE peak might originate from triplet states of LMCT mixed with MC (ds/dp) states.

This kind of dual emission has already been observed for polynuclear Au(I) complexes. The HE bands arise from metal perturbated $\pi \rightarrow \pi^*$ IL transition and the LE peak originates from the mixture between LM(M)CT and MC (ds/dp) excited states. [43,59,60,61,62]

The $[Au(p\text{-}SPhCO_2H)]_n$ shows weak internal quantum yield (< 1 %) at the room temperature. It could be explained by relatively large distance between two gold atoms.[63]

The luminescence origin assignment of $[Au(p\text{-}SPhCO_2H)]_n$ was supported by TD-DFT calculus. However, latter will not be detailed here. The reader is invited to consult it in the following article: *J. Mater. Chem. C*, **2017**, 5, 9843-9848.[26]

2.4.5 Conclusion

The formation of extended 2D-networks of d^{10}-thiolate CPs leads to multiple emission properties.[a] $[Cu(p\text{-}SPhCO_2H)]_n$, $[Ag(p\text{-}SPhCO_2H)]_n$ and $[Ag(p\text{-}SPhCO_2Me)]_n$ are of very similar structure. They also possess very similar photophysical properties (**Figure 2. 21**). Despite the fact that the relative intensities of emission peaks vary, the emission wavelengths are almost the same for all of them.

Once we change the structure of $[MS]_n$ layer, it is possible to observe difference of the photophysical properties, *e. g.* in the case of $[Cu(p\text{-}SPhCO_2H)]_n$ and $[Cu(p\text{-}SPhCO_2Me)]_n$. If 2D-layers formed by distorted hexagons are exchanged to rather regular ones one can expect whole new emission profile. Unfortunately, the better understanding of the change of emission profile would require further studies.

Dissimilar structure of $[Au(p\text{-}SPhCO_2H)]_n$ gives the similar double emission as the one of $[Cu(p\text{-}SPhCO_2H)]_n$, $[Ag(p\text{-}SPhCO_2H)]_n$ and $[Ag(p\text{-}SPhCO_2Me)]_n$. The explanation probably lies in

[a] $[Au(p\text{-}SPhCO_2Me)]_n$ possesses one predominant emission peak (see State of the Art I.3.2). However, at the temperature below 233 K it shows second emission peak at 488 nm of relatively low intensity.

the highly distorted –S–Au–S– chains with an unusual values of S-Au-S angles. It makes them more similar to the compounds based on distorted hexagonal metal-sulfur arrangement.

All these observations demonstrate a future potential to employ these compounds as double (or multiple) emitters. A strong relationship between structure and photophysical properties is observed, but deeper understanding requires further theoretical investigations by means of TD-DFT calculus.

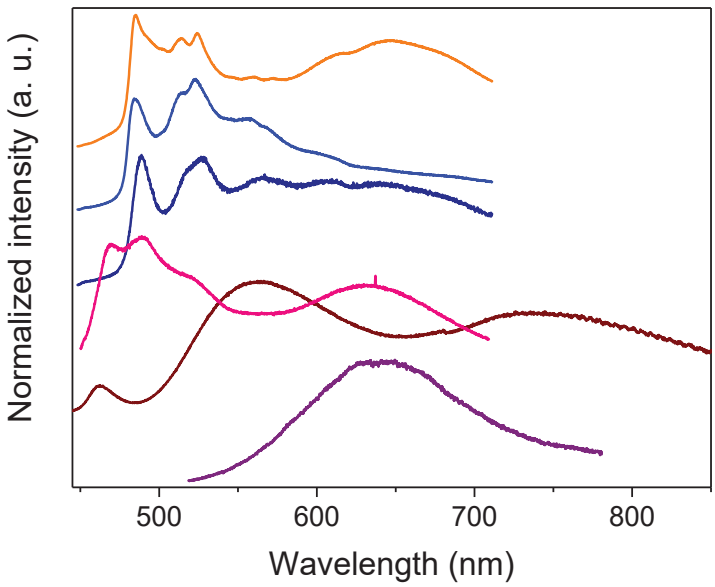

Figure 2. 21 The emission spectra of $[Cu(p\text{-}SPhCO_2H)]_n$ (orange), $[Cu(p\text{-}SPhCO_2Me)]_n$ (brown), $[Ag(p\text{-}SPhCO_2H)]_n$ (blue), $[Ag(p\text{-}SPhCO_2Me)]_n$ (black), $[Au(p\text{-}SPhCO_2H)]_n$ (pink), $[Au(p\text{-}SPhCO_2Me)]_n$ (violet) obtained in the solid state at 93 K.

2.5 Potential Application: Ratiometric Intensity Measurement Luminescence Thermometry

Observation of multiple emission peaks in spectra of discussed materials provide a possibility to use them for optical temperature determination. Ratio of emission peak intensities is a function of the temperature. Therefore, it is possible to use this quantity for the purpose of a temperature determination.

In order to evaluate the thermal sensitivity of such thermometer relative sensitivity is used (similar as in Chapter 1).[64, 65] It is defined in the Equation (2.1):

$$S_n = \frac{1}{I}\frac{\Delta I}{\Delta T} \cdot 100\ \% \quad \text{(Eq. 2.1)}$$

Here, I is the intensity ratio and ΔI represents its change for ΔT change of temperature.[64]

Here, the relative sensitivity was determined for [Au(*p*-SPhCO$_2$H)]$_n$ and [Cu(*p*-SPhCO$_2$Me)]$_n$.

For [Au(*p*-SPhCO$_2$H)]$_n$ the intensity ratio was defined as ratio of intensities of HE emission peak to LE emission peak: I_{Blue}/I_{Red}. For [Cu(*p*-SPhCO$_2$Me)]$_n$ intensities of all three peaks were taken into account; $(I_{Green} + I_{Red})/I_{Blue}$ (**Figure 2. 22**). The experimental data were fitted by a polynomial fit of seventh order for [Au(*p*-SPhCO$_2$H)]$_n$, and by Boltzmann sigmoidal fit for [Cu(*p*-SPhCO$_2$Me)]$_n$.[66]

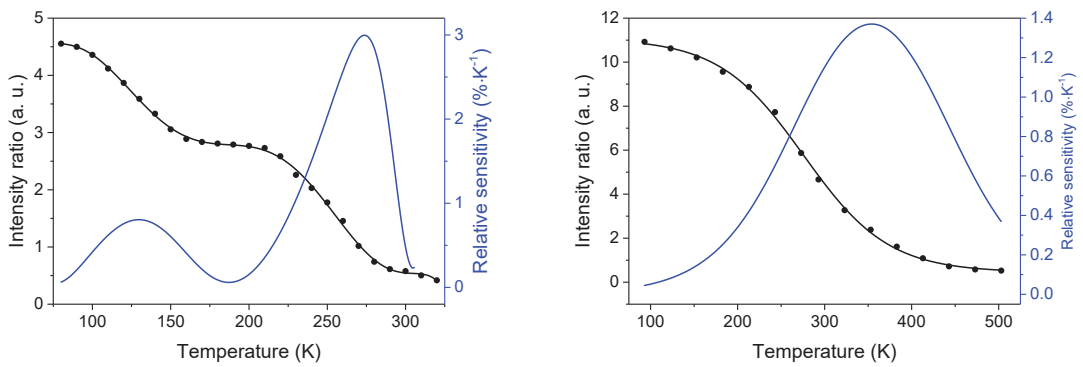

(a) (b)

Figure 2. 22 The intensity ratio (black circles, experimental data; black line, fit), relative sensitivity (blue line) evolution with temperature of (a) [Au(*p*-SPhCO$_2$H)]$_n$ and (b) [Cu(*p*-SPhCO$_2$Me)]$_n$.

The maximal relative sensitivity of [Au(*p*-SPhCO$_2$H)]$_n$ is ~3 % (at 260 K). For [Cu(*p*-SPhCO$_2$Me)]$_n$ the value is more modest – 1.4 % (at 353 K). Its working temperature range, however, is more important. For [Cu(*p*-SPhCO$_2$Me)]$_n$ it is 410 K (from 93 to 503 K), while for [Au(*p*-SPhCO$_2$H)]$_n$ it is only 240 K (from 80 to 320 K). As it can be seen in the **Figure 2. 23**, these two CPs show relatively significant sensitivity and important working temperature range in comparison to other reported CPs. Indeed, [Cu(*p*-SPhCO$_2$Me)]$_n$ shows large working temperature range which has never been seen before. More importantly, it works at the highest temperature region.[67-71]

If we take their low price and simple synthesis into consideration, d^{10} coinage metal-thiolated CPs definitely represent a better alternative to the widely reported materials for this application, such as MOFs with rare earth elements. In addition, these [M(SR)]n CPs exhibit

intrinsic photoluminescent properties that do not require doping, which typically introduces uncertainty of the ratio of the species.

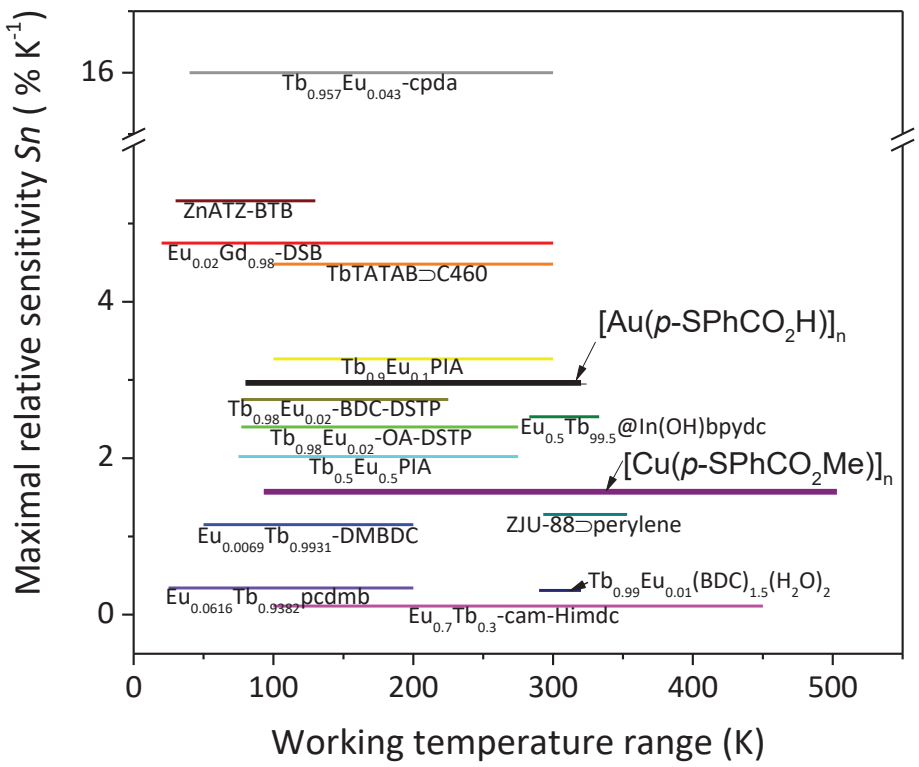

Figure 2. 23 Visual comparison of the maximum relative sensitivity values (S_n, %K^{-1}) with the working temperature ranges (K) of the reported ratiometric luminescent MOF-based thermometers with [Au(*p*-SPhCO$_2$H)]$_n$ and [Cu(*p*-SPhCO$_2$Me)]$_n$.[67-71] Adapted with permission from ref. [18]. Copyright 2017 The Royal Society of Chemistry.

2.6 Conclusions

Five new coordination polymers using *p*-$HSPhCO_2H$ and *p*-$HSPhCO_2Me$ ligand were synthesized. Use of these ligands systematically leads to the formation of lamellar structures which were successfully determined.

The emission-excitation spectra were obtained. All compounds show multiple emission peaks of different origin. HE emission is attributed to metal-perturbed IL transitions, and while LE emission is attributed to the mixture between LMCT/MLCT and MC excited states.

The resembling structures of $[Cu(p\text{-}SPhCO_2H)]_n$, $[Ag(p\text{-}SPhCO_2H)]_n$ and $[Ag(p\text{-}SPhCO_2Me)]_n$, as well as the one of $[Au(p\text{-}SPhCO_2H)]_n$ give rise to very similar double-emitting properties. At the current stage of the research, unfortunately, the origin of the triple emission of $[Cu(p\text{-}SPhCO_2Me)]_n$ is unclear, and the primary cause of its behavior different to other compounds is not clearly defined. These observations demonstrate that the emission of these compounds is dependent on a subtle balance between the metal center, the ligand and its packing. It is also dependent on the structure as whole, which determines the emission bands of different energy.

Properties of the studied materials show great potential to be employed as double/multiple emitters. Moreover, it makes them great candidates for ratiometric intensity measurement luminescence thermometry.

2.7 Note

For more detailed information on the structure and properties, the following articles should be consulted:

O. Veselska, L. Cai, D. Podbevšek, G. Ledoux, N. Guillou, G. Pilet, A. Fateeva, A. Demessence. Structural Diversity of Coordination Polymers Based on a Heterotopic Ligand: Cu(II)-Carboxylate vs Cu(I)-Thiolate. *Inorg. Chem*. 2018, **57**, 2736-2743.

O. Veselska, D. Podbevšek, G. Ledoux, A. Fateeva, A. Demessence. Intrinsic triple-emitting 2D copper thiolate coordination polymer as a ratiometric thermometer working over 400 K range *Chem. Commun*. 2017, **53**, 12225-12228.

O. Veselska, C. Dessal, S. Melizi, N. Guillou, D. Podbevšek, G. Ledoux, E. Elkaim, A. Fateeva, A. Demessence. New Lamellar Silver Thiolate Coordination Polymers with Tunable Photoluminescence Energies by Metal Substitution. *Inorg. Chem*. 2019, **58**, 99-105.

O. Veselska, L. Okhrimenko, N. Guillou, D. Podbevšek, G. Ledoux, C. Dujardin, M. Monge, D. M. Chevrier, R. Yang, P. Zhang, A. Fateeva, A. Demessence. An intrinsic dual-emitting gold thiolate coordination polymer, $[Au(+I)(p\text{-}SPhCO_2H)]_n$, for ratiometric temperature sensing. *J. Mater. Chem. C.* 2017, **5**, 9843-9848.

Simultaneously with these articles, an article describing $[Cu(p\text{-}SPhCO_2H)]_n$ and $[Cu(p\text{-}SPhCO_2Me)]_n$ was published by J. Troyano *et al*. We highly recommend the reader to consult it, particularly, for its first-principles DFT calculations and discussion about production of thin films of $[Cu(p\text{-}SPhCO_2R)]_n$@PVDF.

J. Troyano, O. Castillo, J. I. Martínez, V. Fernández-Moreira, Y. Ballesteros, D. Maspoch, F. Zamora, S. Delgado. Reversible Thermochromic Polymeric Thin Films Made of Ultrathin 2D Crystals of Coordination Polymers Based on Copper(I)-Thiophenolates. *Adv. Funct. Mater*. 2018, 1704040.

2.8 Experimental Part

2.8.1 Synthesis

Synthesis of [Cu(*p*-SPhCO$_2$H)]$_n$: a solution of 4-MBA (463 mg, 3.0 mmol) in DMF (3 mL) was added to 6 mL of THF followed by the addition of a solution of $CuCl_2 \cdot 2H_2O$ (170 mg, 1.0 mmol) in 1 mL of 1 M aqueous solution of HNO_3. The reaction was let to proceed for 24 h at 120°C in a 20 mL sealed vial. Colorless pellet-like crystals were obtained and washed by 20mL of DMF and by 20 mL of ethanol for 3 times. Crystals were recovered by centrifugation at 4000 rpm and then dried in the air. Yield: 65 % (100 mg). Chemical Formula: $C_7H_5CuO_2S$. Molecular Weight: 216.72. CuO content from TGA (calc.) wt%: 36.7 (36.7).

Synthesis of [Cu(*p*-SPhCO$_2$Me)]$_n$: H_2SO_4 solution (1 mL, 0.5 M) was added to a solution of $CuCl_2 \cdot 2H_2O$ (63 mg, 0.37 mmol) in 5 mL of DMF, then *p*-HSPhCO$_2$Me (43 mg, 0.25 mmol) dissolved in 5 mL of DMF was introduced. 20 mL vial was sealed and the mixture was kept at 120°C for 24h. Yellow pellet-like crystals were obtained and washed by 20mL of DMF and by 20 mL of acetone for 3 times. Crystals were recovered by centrifugation at 4000 rpm and then dried in the air. Yield: 81 % (24 mg). Chemical Formula: $C_8H_7CuO_2S$. Molecular Weight: 230.75. CuO content from TGA (calc.) wt%: 36.9 (34.5).

Synthesis of [Ag(*p*-SPhCO$_2$H)]$_n$: a solution of $AgNO_3$ (100 mg, 0.59 mmol) in H_2O (10 mL) was added to 4-MBA (90.9 mg, 0.59 mmol). The reaction was let to proceed for 16 h at 120 °C in a 20 mL sealed vial. White precipitate was obtained and washed by 20 mL of water, by 20 mL of ethanol and by 20 mL of acetone 2 times. Powder was recovered by centrifugation at 4000 rpm and then dried in the air. Yield: 90 % (139 mg). Chemical Formula: $C_7H_5AgO_2S$. Molecular Weight: 261.04. Elemental analysis (calc.) wt%: C, 31.89 (32.21); H, 1.9 (1.93); S, 12.15 (12.88). Silver content from TGA (calc.) wt%: 41.2 (41.3).

Synthesis of [Ag(*p*-SPhCO$_2$Me)]$_n$: a solution of $AgNO_3$ (100 mg, 0.59 mmol) in H_2O (10 mL) was added to *p*-HSPhCO$_2$Me (99.2 mg, 0.59 mmol). The reaction was let to proceed for 16 h at 120 °C in a 20 mL sealed vial. White precipitate was obtained and washed by 20 mL of water, by 20 mL of ethanol and by 20 mL of acetone 2 times. Powder was recovered by centrifugation at 4000 rpm and then dried in the air. Yield: 79 % (128 mg). Chemical Formula: $C_8H_7AgO_2S$. Molecular Weight: 275.07. Elemental analysis (calc.) wt%: C, 34.33 (34.93); H, 2.5 (2.57); S, 11.48 (11.66). Silver content from TGA (calc.) wt%: 39.1 (39.2).

Synthesis of [Au(*p*-SPhCO$_2$H)]$_n$: HAuCl$_4$·3H$_2$O (80 mg, 0.22 mmol) in 10 mL of H$_2$O was added to 4-mercaptobenzoic acid (200 mg, 1.32 mmol) The reaction was let to proceed for 16 h at 120 °C in a 20 mL sealed vial. White precipitate was obtained and washed by 20 mL of ethanol and by 20 mL of acetone 2 times. Powder was recovered by centrifugation at 4000 rpm and then dried in the air. Yield: 89 % (63 mg). Chemical Formula: C$_7$H$_5$AuO$_2$S, Molecular Weight: 350.14, Elemental Analysis (calc.) wt%: C, 24.4 (24.01); H, 1.4 (1.44); S, 9.3 (9.16). Gold content from TGA (calc.) wt%: 56.8 (56.3).

For **[Au(*p*-SPhCO$_2$H)]$_n$**, all characterizations (except structure determination) have been performed using the pure phase material synthesized at 120°C. For the structure determination, material synthesized at 180°C was used. It was a sample of higher crystallinity, which, however, contained some bulk gold.

2.8.2 Single Crystal Structure Determination of [Cu(*p*-SPhCO$_2$H)]$_n$ and [Cu(*p*-SPhCO$_2$Me)]$_n$

Single-crystal X-ray studies of [Cu(*p*-SPhCO$_2$H)]$_n$ and [Cu(*p*-SPhCO$_2$Me)]$_n$ were carried out by using Gemini diffractometer (MoKα radiation, λ = 0.71069 Å) and by the related analysis software, respectively.[72] For [Cu(*p*-SPhCO$_2$H)]$_n$, data were collected both at 293 and 120 K.

For the [Cu(*p*-SPhCO$_2$H)]$_n$ an absorption correction, which was based on the crystal faces was applied to the data sets (analytical).[73, 74] The [Cu(*p*-SPhCO$_2$H)]$_n$ structures were determined by direct methods using the SIR97 program.[75] It was combined with Fourier difference syntheses and refined against F using reflections with [I/σ(I)>3] by using the CRYSTALS program.[76]

For the [Cu(*p*-SPhCO$_2$Me)]$_n$, analytical absorption correction was applied based the modeled faces of the crystal. [77] The resulting set of hkl was used for structure determination and refinement. The structure was solved by direct methods using SIR97 [75] and the least-square refinement on F^2 was achieved by the CRYSTALS software. [76]

All the atomic displacement parameters for non-hydrogen atoms were refined using anisotropic terms. The hydrogen atoms were theoretically located on the basis of the conformation of the supporting atom. Presence of potential hydrogen bonds was taken into account. Hydrogen atoms have then refined by using the riding model.

CCDC-1822344, -1822345 and CCDC-1570642 files contain supplementary crystallographic data for compounds $[Cu(p\text{-}SPhCO_2H)]_n$ (120 K and 293 K) and $[Cu(p\text{-}SPhCO_2Me)]_n$, respectively. X-ray crystallographic data and refinement details are summarized in **Table 2. 3**.

Data for the comparison of main distances and angles of $[Cu(p\text{-}SPhCO_2H)]_n$ at 120 and 293 K are in the **Table 2. 4**.

2.8.3 PXRD Structure Determination of $[Ag(p\text{-}SPhCO_2H)]_n$ and $[Ag(p\text{-}SPhCO_2Me)]_n$

The structural determinations of $[Ag(p\text{-}SPhCO_2H)]_n$ and $[Ag(p\text{-}SPhCO_2Me)]_n$ were carried out thanks to high resolution X-ray powder diffraction data. They were collected at the CRISTAL beamline at Soleil Synchrotron (Gif-sur-Yvette, France). A monochromatic beam was extracted from the U20 undulator beam by means of a Si(111) double monochromator. Its wavelength of 0.79276 Å was refined from a LaB_6 (NIST Standard Reference Material 660a) powder diagram recorded prior to the experiment. The X-ray beam was attenuated in order to limit radiation damage of the samples. High angular resolution was obtained with, in the diffracted beam, a 21 perfect crystal Si(111) multi-analyzer. Typically, the sample was loaded in a 0.7 mm capillary (Borokapillaren, GLAS, Schönwalde, Germany) mounted on a spinner rotating at about 5 Hz to improve the particles' statistics. Diffraction data were collected in continuous scanning mode. The diffractogram was obtained by the precise superposition and addition of the 21 channels data.

All calculations of structural investigations were performed by the TOPAS program. [78] The LSI-indexing method converged unambiguously to orthorhombic unit cells with satisfactory figures of Merit for the two compounds. For $[Ag(p\text{-}SPhCO_2H)]_n$, similarities with unit cell parameters of $[Cu(p\text{-}SPhCO_2H)]_n$ led us to suppose that the two compounds were isotructural and structural model of $[Cu(p\text{-}SPhCO_2H)]_n$ was then used as a starting point of the Rietveld refinement of $[Ag(p\text{-}SPhCO_2H)]_n$.[79] Structural investigation of $[Ag(p\text{-}SPhCO_2Me)]_n$ was initialized using the charge flipping method. It allowed location of silver atoms. The direct space strategy was then used to complete the structural model and the organic moiety has been added to the fixed silver atomic coordinates. It was treated as rigid body in the simulated annealing process. For compound $[Ag(p\text{-}SPhCO_2H)]_n$, hydrogen atom for the carboxylic function was arbitrarily fixed to the O1 atom at 0.9 Å. The alignment of the carboxylate-carboxylate hydrogen bonding

has been considered to fix its torsion angle. The final Rietveld plots (**Figure 2. 24** and **Figure 2. 25**) correspond to satisfactory model indicators and profile factors (**Table 2. 3**). The use of a rigid organic moiety allowed to decrease the number of structural parameters to 16 (1 scale factor, 3 atomic coordinates for Ag atom, 6 parameters for the orientation and the translation of the organic moiety, 1 torsion angle for the carboxylate, 4 distances and 1 overall temperature factor) for $[Ag(p\text{-}SPhCO_2H)]_n$. In the case of $[Ag(p\text{-}SPhCO_2Me)]_n$ the number of parameters was18 (1 scale factor, 3 atomic coordinates for Ag atom, 6 parameters for the orientation and the translation of the organic moiety, 1 torsion angle for the ester, 6 distances and 1 overall temperature factor).

CCDC-1839578 and CCDC-1839581 files contain the supplementary crystallographic data for compounds $[Ag(p\text{-}SPhCO_2H)]_n$ and $[Ag(p\text{-}SPhCO_2Me)]_n$, respectively.

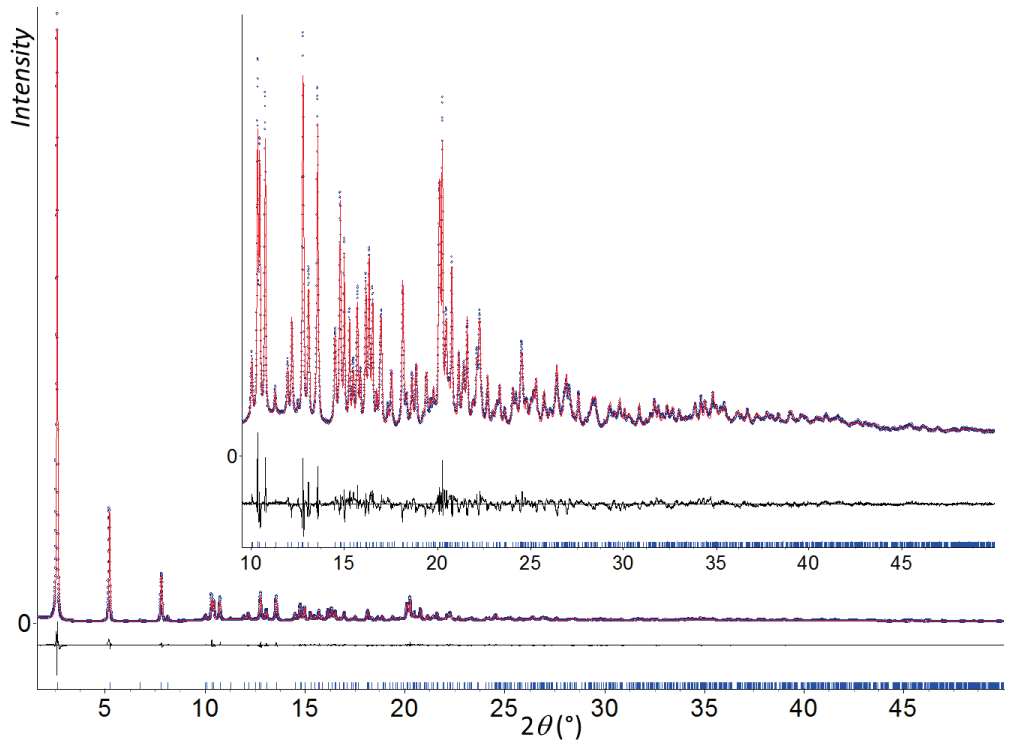

Figure 2. 24 Final Rietveld plot of $[Ag(p\text{-}SPhCO_2H)]_n$ showing observed (blue circles), calculated (red line), and difference (black line) curves. A zoom at high angles is shown as inset.

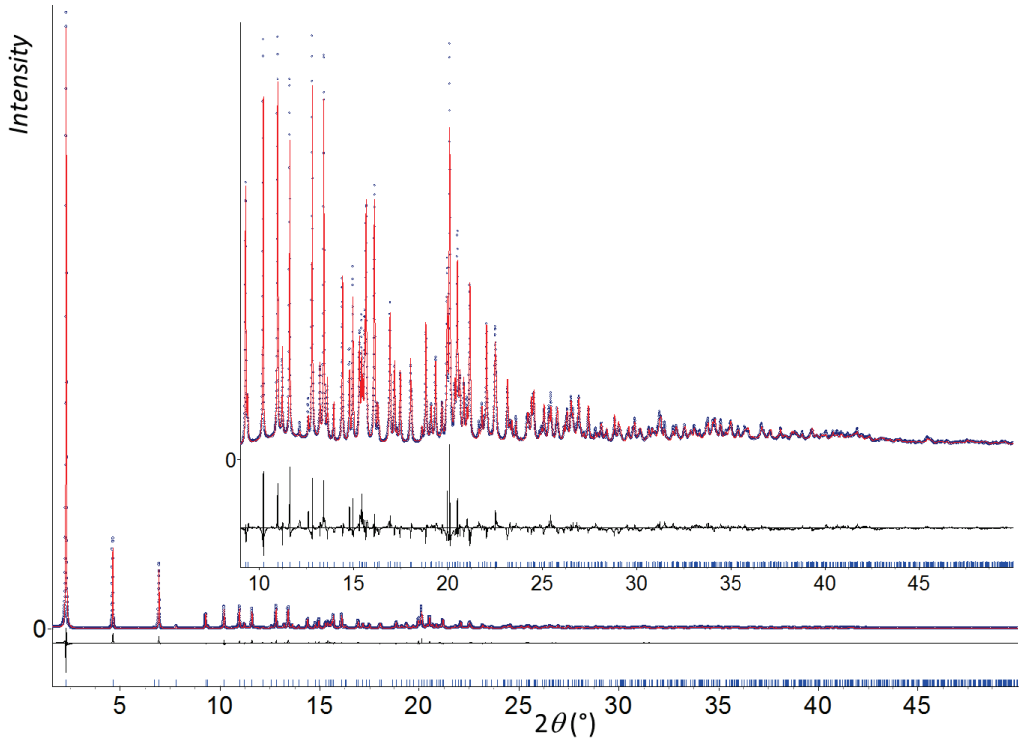

Figure 2. 25 Final Rietveld plot of [Ag(*p*-SPhCO$_2$Me)]$_n$ showing observed (blue circles), calculated (red line), and difference (black line) curves. A zoom at high angles is shown as inset.

2.8.4 PXRD Structure Determination of [Au(*p*-SPhCO$_2$H)]$_n$

The structural determination of [Au(*p*-SPhCO$_2$H)]$_n$ was carried with help of X-ray powder diffraction data. Sample synthesized at high temperature conditions (180°C) was used for this goal. Sample was introduced into a 0.5 mm capillary and spun during data collection to ensure good powder averaging. The pattern was scanned at the room temperature with a Bruker D8 Advance diffractometer with a Debye-Scherrer geometry, in the 2ϑ range of 2-100°. The D8 system is equipped with a Ge(111) monochromator producing Cu $K\alpha_1$ radiation (λ = 1.540598 Å) and a LynxEye detector. All calculations of structural investigation were performed by the TOPAS program.[80] The LSI-indexing method converged unambiguously to a triclinic unit cell. Unindexed lines observed on the powder pattern correspond to bulk gold. Its formation was favored by high temperature of the synthesis. Given the small number of lines, the presence of gold did not prevent us to solve the structure. At this stage the structural model of gold was taken into account and its contribution could be calculated by using the Rietveld method. The quantitative amount of bulk gold was estimated to be about 22 wt%. Structural investigation of [Au(*p*-SPhCO$_2$H)]$_n$ was initialized by use of the charge flipping method, which allowed location

of gold atoms. The direct space strategy was then used to complete the structural models and organic moieties have been added to the fixed gold atomic coordinates. They were treated as rigid bodies in the simulated annealing process. The final Rietveld plot corresponds to satisfactory model indicator and profile factors (**Figure 2. 26** and **Table 2. 1**).

CCDC-1539671 file contains the supplementary crystallographic data.

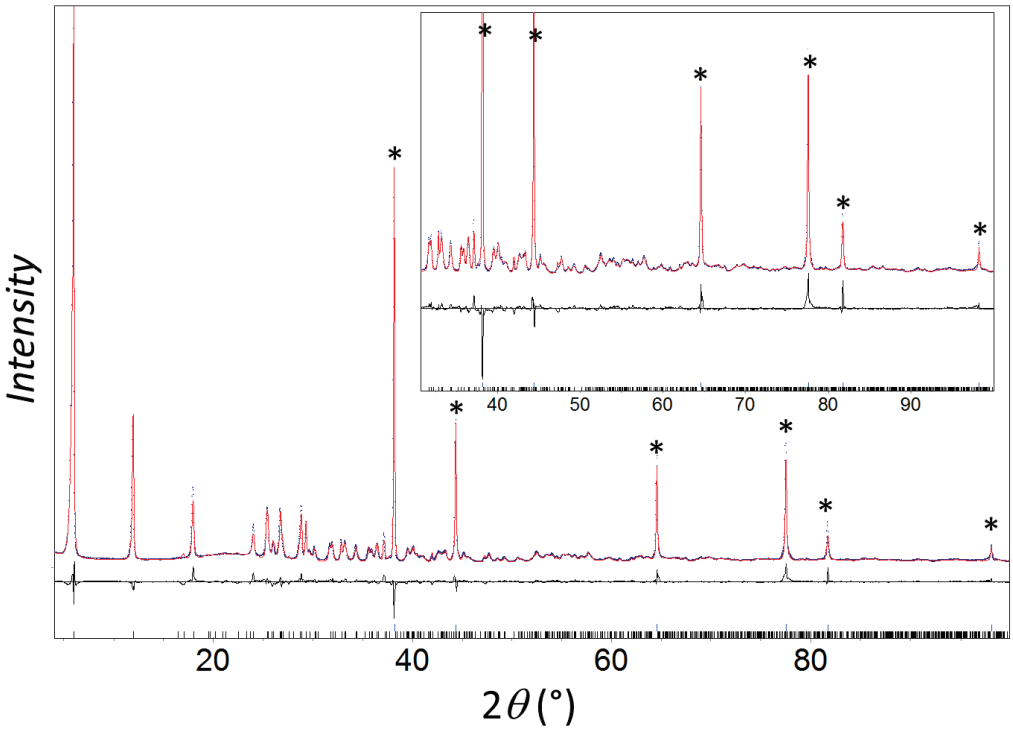

Figure 2. 26 Final Rietveld plot of $[Au(p\text{-}SPhCO_2H)]_n$ showing observed (blue circles), calculated (red line), and difference (black line) curves. A zoom at high angles is shown as inset. Black asterisks correspond to golf FCC present as impurity.

Table 2. 3 Crystallographic data for $[Cu(p\text{-}SPhCO_2H)]_n$, $[Cu(p\text{-}SPhCO_2Me)]_n$, $[Ag(p\text{-}SPhCO_2H)]_n$, $[Ag(p\text{-}SPhCO_2Me)]_n$ and $[Au(p\text{-}SPhCO_2H)]_n$.

Compound	$[Cu(p\text{-}SPhCO_2H)]_n$ 293 K	$[Cu(p\text{-}SPhCO_2H)]_n$ 120 K	$[Cu(p\text{-}SPhCO_2Me)]_n$ 293 K	$[Ag(p\text{-}SPhCO_2H)]_n$ 293 K	$[Ag(p\text{-}SPhCO_2Me)]_n$ 293 K	$[Au(p\text{-}SPhCO_2H)]_n$ 293 K
Empirical formula	$C_7H_5Cu_1O_2S_1$	$C_7H_5Cu_1O_2S_1$	$C_8H_7Cu_1O_2S_1$	$C_7H_5Ag_1O_2S_1$	$C_8H_7Ag_1O_2S_1$	$C_7H_5Au_1O_2S_1$
M_r	216.73	216.73	230.75	261.05	275.07	350.14
Crystal system	Orthorhombic	Orthorhombic	Monoclinic	Orthorhombic	Orthorhombic	Triclinic
Space group	*Pbca*	*Pbca*	*Pn*	*Pbca*	$Pca2_1$	*P*1
a (Å)	6.858(2)	6.886(2)	3.9655(5)	7.2748(3)	7.21893(8)	4.5181(4)
b (Å)	5.771(2)	5.707(2)	19.103(3)	5.8158(3)	19.5651(3)	5.4084(4)
c (Å)	33.909(7)	33.961(7)	5.2888(9)	34.7981(9)	5.90559(7)	14.8606(9)
α (°)	90.0	90.0	90.0	90.0	90.0	84.867(6)
β (°)	90.0	90.0	93.34(2)	90.0	90.0	86.292(6)
γ (°)	90.0	90.0	90.0	90.0	90.0	88.256(6)
V ($Å^3$)	1342.0(4)	1334.6(6)	400.0(2)	1472.3(1)	834.10(2)	360.80(5)
Z	8	8	2	8	4	2
λ (Å)	0.71073	0.71073	0.71073	0.79276	0.79276	1.540598
Number of reflections	1089	946	1325	960	615	757
Parameters[2]	100	100	110	16, 39	18, 39	29, 53
$R[F^2 > 2\sigma(F^2)]$	0.0613	0.0621	0.0562	0.045	0.055	0.052
$wR(F^2)$	0.0656	0.0713	0.02356	0.058	0.076	0.070
GoF	1.29	1.06	0.95	1.62	2.38	5.21

[2] Structural and profile parameters for structures solved from PXRD

Table 2. 4 Comparison of the main distances and angles in $[Cu(p\text{-}SPhCO_2H)]_n$ at 120 and 293 K.

Temperature, K	M-S, Å	M-M, Å	S-M-S, °	M-S-M, °	π-π, Å
293	2.243(3) 2.290(2) 2.302(3)	3.030(2)† 3.519(2)†	104.1(1) 126.0(1) 129.8(1)	83.6(1) 101.9(1) 116.4(1)	5.771(12)
120	2.254(2) 2.298(2) 2.302(3)	2.993(2) 3.535(2)	103.48(8) 126.54(8) 129.85(9)	82.16(7) 101.81(7) 115.96(8)	5.707(12)

2.8.5 CIE (Commision Internationale de l'Eclairage) Chromaticity Diagram[81, 82]

In this chapter, the colors of luminescence were presented in CIE diagram in the form of (x, y,) coordinates (**Figure 2. 27** (a)). They are functions of three tristimulus values *X*, *Y* and *Z* (Eq. 2.2(a) and (b)):

$$x = \frac{X}{X+Y+Z} \quad \text{(Eq. 2.2(a))}$$

$$y = \frac{X}{X+Y+Z} \quad \text{(Eq. 2.2(b))}$$

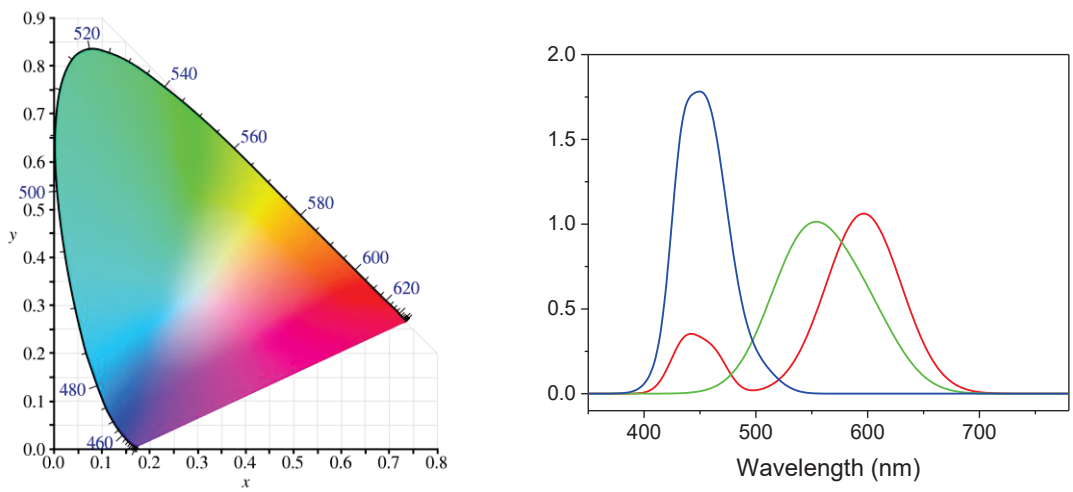

(a) (b)

Figure 2. 27 The CIE 1931 color space chromaticity diagram (a) and the CIE standard observer color matching functions (b).

The tristimulus values for a color of an emission *I(λ)* are given in terms of standard observer by (Eq 2.3 (a), (b) and(c)):

$$X = \int_{\lambda} I(\lambda)\bar{x}(\lambda)d\lambda \quad \text{(Eq. 2.3(a))}$$

$$Y = \int_{\lambda} I(\lambda)\bar{y}(\lambda)d\lambda \quad \text{(Eq. 2.3(b))}$$

$$Z = \int_{\lambda} I(\lambda)\bar{z}(\lambda)d\lambda \quad \text{(Eq. 2.3(c))}$$

where $\bar{x}(\lambda)$, $\bar{y}(\lambda)$ and $\bar{z}(\lambda)$ are the CIE's color matching functions (**Figure 2. 27** (b)). They are the numerical description of the chromatic response of the observer.

2.9 References

1. E. R. T. Tiekink and W. Henderson, *Coord. Chem. Rev.*, 2017, **341**, 19-52.
2. C.-M. Che, C.-H. Li, S. S.-Y. Chui, V. A. L. Roy and K.-H. Low, *Chem. Eur. J.*, 2008, **14**, 2965-2975.
3. K.-H. Low, V. A. L. Roy, S. S.-Y. Chui, S. L.-F. Chan and C.-M. Che, *ChemComm*, 2010, **46**, 7328-7330.
4. J. D. E. T. Wilton-Ely, A. Schier, N. W. Mitzel and H. Schmidbaur, *J. Chem. Soc., Dalton Trans*, 2001, 1058-1062.
5. J. Fernández-Gallardo, B. T. Elie, T. Sadhukha, S. Prabha, M. Sanaú, S. A. Rotenberg, J. W. Ramos and M. Contel, *Chem. Sci.*, 2015, **6**, 5269-5283.
6. D. de Vos, D. R. Smyth and E. R. T. Tiekink, *Met. Based Drugs*, 2002, **8**, 303-306.
7. U. Helmstedt, S. Lebedkin, T. Höcher, S. Blaurock and E. Hey-Hawkins, *Inorg. Chem.*, 2008, **47**, 5815.
8. K. Nomiya, S. Yamamoto, R. Noguchi, H. Yokoyama, N. C. Kasuga, K. Ohyama and C. Kato, *J. Inorg. Biochem.*, 2003, **95**, 208-220.
9. C. Domínguez, B. Heinrich, B. Donnio, S. Coco and P. Espinet, *Chem. Eur. J.*, 2013, **19**, 5988-5995.
10. U. Helmstedt, S. Lebedkin, T. Höcher, S. Blaurock and E. Hey-Hawkins, *Inorg. Chem.*, 2008, **47**, 5815-5820.
11. Y. F. Mui, J. Fernández-Gallardo, B. T. Elie, A. Gubran, I. Maluenda, M. Sanaú, O. Navarro and M. a. Contel, *Organometallics*, 2016, **35**, 1218-1227.
12. J. D. E. T. Wilton-Ely, H. Ehlich, A. Schier and H. Schmidbaur, *Helv. Chim. Acta*, 2001, **84**, 3216-3232.
13. Y. Levi-Kalisman, P. D. Jadzinsky, N. Kalisman, H. Tsunoyama, T. Tsukuda, D. A. Bushnell and R. D. Kornberg, *J. Am. Chem. Soc.*, 2011, **133**, 2976-2982.
14. B. E. Conn, A. Desireddy, A. Atnagulov, S. Wickramasinghe, B. Bhattarai, B. Yoon, R. N. Barnett, Y. Abdollahian, Y. W. Kim, W. P. Griffith, S. R. J. Oliver, U. Landman and T. P. Bigioni, *J. Phys. Chem. C*, 2015, **119**, 11238-11249.
15. A. Desireddy, B. E. Conn, J. Guo, B. Yoon, R. N. Barnett, B. M. Monahan, K. Kirschbaum, W. P. Griffith, R. L. Whetten, U. Landman and T. P. Bigioni, *Nature*, 2013, **501**, 399.
16. C. Lavenn, N. Guillou, M. Monge, D. Podbevšek, G. Ledoux, A. Fateeva and A. Demessence, *ChemComm*, 2016, **52**, 9063-9066.
17. O. Veselska, L. Cai, D. Podbevšek, G. Ledoux, N. Guillou, G. Pilet, A. Fateeva and A. Demessence, *Inorg. Chem.*, 2018, **57**, 2736-2743.
18. O. Veselska, D. Podbevšek, G. Ledoux, A. Fateeva and A. Demessence, *ChemComm*, 2017, **53**, 12225-12228.
19. O. Veselska, C. Dessal, S. Melizi, N. Guillou, D. Podbevšek, G. Ledoux, E. Elkaim, A. Fateeva and A. Demessence, *Inorg. Chem.*, 2019, **58**, 99-105.
20. H. Schmidbaur and A. Schier, *Angew. Chem. Int. Ed.*, 2015, **54**, 746.

21. C. Lavenn, N. Guillou, M. Monge, D. Podbevšek, G. Ledoux, A. Fateeva and A. Demessence, *Chem. Commun.*, 2016, **52**, 9063.
22. J. Chen, A. A. Mohamed, H. E. Abdou, J. A. Krause Bauer, J. P. Fackler, Jr., A. E. Bruce and M. R. M. Bruce, *Chem. Commun.*, 2005, 1575.
23. W. J. Hunks, M. C. Jennings and R. J. Puddephatt, *Inorg. Chem.*, 2002, **41**, 4590-4598.
24. M. C. Gimeno and A. Laguna, *Chem. Rev.*, 1997, **97**, 511.
25. L. D'Ascenzo and P. Auffinger, *Acta Cryst.*, 2015, **B71**, 164.
26. O. Veselska, L. Okhrimenko, N. Guillou, D. Podbevšek, G. Ledoux, C. Dujardin, M. Monge, D. M. Chevrier, R. Yang, P. Zhang, A. Fateeva and A. Demessence, *J. Mater. Chem. C*, 2017, **5**, 9843-9848.
27. E. Pretsch, P. Buhlmann and M. Badertscher, *Structure Determination of Organic Compounds*, Springer-Verlag Berlin Heidelberg, 4 edn., 2009.
28. J. S. Lim, H. Choi, I. S. Lim, S. B. Park, Y. S. Lee and S. K. Kim, *J. Phys. Chem. A*, 2009, **113**, 10410-10416.
29. J. C. Deaton, S. C. Switalski, D. Y. Kondakov, R. H. Young, T. D. Pawlik, D. J. Giesen, S. B. Harkins, A. J. M. Miller, S. F. Mickenberg and J. C. Peters, *J. Am. Chem. Soc.*, 2010, **132**, 9499-9508.
30. B. Hupp, C. Schiller, C. Lenczyk, M. Stanoppi, K. Edkins, A. Lorbach and A. Steffen, *Inorg. Chem.*, 2017, **56**, 8996-9008.
31. M. Z. Shafikov, A. F. Suleymanova, R. Czerwieniec and H. Yersin, *Inorg. Chem.*, 2017, **56**, 13274-13285.
32. J. Nitsch, C. Kleeberg, R. Fröhlich and A. Steffen, *Dalton Trans.*, 2015, **44**, 6944-6960.
33. V. W. W. Yam, E. C. C. Cheng and N. Zhu, *Angew. Chem.*, 2001, **40**, 1763-1765.
34. B. Li, H.-T. Fan, S.-Q. Zang, H.-Y. Li and L.-Y. Wang, *Coord. Chem. Rev.*, 2018, **377**, 307-329.
35. E. Cariati, E. Lucenti, C. Botta, U. Giovanella, D. Marinotto and S. Righetto, *Coord. Chem. Rev.*, 2016, **306**, 566-614.
36. H. V. R. Dias, H. V. K. Diyabalanage, M. G. Eldabaja, O. Elbjeirami, M. A. Rawashdeh-Omary and M. A. Omary, *J. Am. Chem. Soc.*, 2005, **127**, 7489-7501.
37. M. Vitale, C. K. Ryu, W. E. Palke and P. C. Ford, *Inorg. Chem.*, 1994, **33**, 561-566.
38. P. C. Ford, E. Cariati and J. Bourassa, *Chem. Rev.*, 1999, **99**, 3625-3648.
39. X.-C. Shan, F.-L. Jiang, D.-Q. Yuan, M.-Y. Wu, S.-Q. Zhang and M.-C. Hong, *Dalton Trans.*, 2012, **41**, 9411-9416.
40. S. Perruchas, C. Tard, X. F. Le Goff, A. Fargues, A. Garcia, S. Kahlal, J.-Y. Saillard, T. Gacoin and J.-P. Boilot, *Inorg. Chem.*, 2011, **50**, 10682-10692.
41. A. Gallego, O. Castillo, C. J. Gómez-García, F. Zamora and S. Delgado, *Inorg. Chem.*, 2012, **51**, 718-727.
42. D. Li, W.-J. Shi and L. Hou, *Inorg. Chem.*, 2005, **44**, 3907-3913.
43. J. R. Shakirova, E. V. Grachova, V. V. Sizov, G. L. Starova, I. O. Koshevoy, A. S. Melnikov, M. C. Gimeno, A. Laguna and S. P. Tunik, *Dalton Trans.*, 2017, **46**, 2516-2523.

44. F. M. Monzittu, V. Fernández-Moreira, V. Lippolis, M. Arca, A. Laguna and M. C. Gimeno, *Dalton Trans.*, 2014, **43**, 6212-6220.
45. R. Langer, M. Yadav, B. Weinert, D. Fenske and O. Fuhr, *Eur. J. Inorg. Chem.*, 2013, **21**, 3623-3631.
46. J.-F. Song, S.-Z. Li, R.-S. Zhou, J. Shao, X.-M. Qiu, Y.-Y. Jia, J. Wang and X. Zhang, *Dalton Trans.*, 2016, **45**, 11883-11891.
47. K. Shimada, A. Kobayashi, Y. Ono, H. Ohara, T. Hasegawa, T. Taketsugu, E. Sakuda, S. Akagi, N. Kitamura and M. Kato, *J. Phys. Chem. C*, 2016, **120**, 16002-16011.
48. X.-c. Shan, F.-l. Jiang, D.-q. Yuan, H.-b. Zhang, M.-y. Wu, L. Chen, J. Wei, S.-q. Zhang, J. Pan and M.-c. Hong, *Chem. Sci.*, 2013, **4**, 1484-1489.
49. H. Kunkely and A. Vogler, *Inorg. Chem. Commun.*, 2006, **9**, 866-868.
50. J. Chen, A. Neels and K. M. Fromm, *Chem. Commun.*, 2010, **46**, 8282-8284.
51. J. Chen, N. Voutier, J. Rajabi, A. Crochet, D. M. Bassani and K. M. Fromm, *CrystEngComm*, 2017, **19**, 5106.
52. A. Barbieri, G. Accorsi and N. Armaroli, *Chem. Commun.*, 2008, 2185.
53. S. Igawa, M. Hashimoto, I. Kawata, M. Hoshino and M. Osawa, *Inorg. Chem.*, 2012, **51**, 5805-5813.
54. V. W.-W. Yam and K. M.-C. Wong, *Chem. Commun.*, 2011, **47**, 11579-11592.
55. A. Kaeser, O. Moudam, G. Accorsi, I. Séguy, J. Navarro, A. Belbakra, C. Duhayon, N. Armaroli, B. Delavaux-Nicot and J.-F. Nierengarten, *Eur. J. Inorg. Chem.*, 2014, 1345-1355.
56. G. Moreno-Alcantar, A. Nacar-Anaya, M. Flores-Alamo and H. Torrens, *New J. Chem.*, 2016, **40**, 6577.
57. X.-Y. Li, Z. Wang, H.-F. Su, S. Feng, M. Kurmoo, C.-H. Tung, D. Sun and L.-S. Zhang, *Nanoscale*, 2017, **9**, 3601.
58. C. Lavenn, L. Okhrimenko, N. Guillou, M. Monge, G. Ledoux, C. Dujardin, R. Chiriac, A. Fateeva and A. Demessence, *J. Mater Chem. C*, 2015, **3**, 4115.
59. E. C.-C. Cheng, W.-Y. Lo, T. K.-M. Lee, N. Zhu and V. W.-W. Yam, *Inorg. Chem.*, 2014, **53**, 3854-3863.
60. E. M. Gussenhoven, J. C. Fettinger, D. M. Pham and A. L. Balch, *J. Am. Chem. Soc.*, 2005, **127**, 16338-16338.
61. V. W.-W. Yam, T.-F. Lai and C.-M. Che, *J. Chem. Soc., Dalton Trans*, 1990, 3747-3752.
62. V. W.-W. Yam, E. C.-C. Cheng and Z.-Y. Zhou, *Angew. Chem. Int. Ed.*, 2000, **39**, 1683-1685.
63. J. M. Forward, D. Bohmann, J. P. Fackler, Jr. and R. J. Staples, *Inorg. Chem.*, 1995, **34**, 6330.
64. Y. Cui, F. Zhu, B. Chen and G. Qian, *ChemComm*, 2015, **51**, 7420-7431.
65. D. Jaque and F. Vetrone, *Nanoscale*, 2012, **4**, 4301-4326.
66. L. Li, Y. Zhu, X. Zhou, C. D. S. Brites, D. Ananias, Z. Lin, F. A. A. Paz, J. Rocha, W. Huang and L. D. Carlos, *Adv. Funct. Mater*, 2016, **26**, 8677-8684.
67. Y. Cui, F. Zhu, B. Chen and G. Qian, *Chem. Commun.*, 2015, **51**, 7420.

68. H. Zhang, C. Lin, T. Sheng, S. Hu, C. Zhuo, R. Fu, Y. Wen, H. Li, S. Su and X. Wu, *Chem. Eur. J.*, 2016, **22**, 4460.
69. T. Xia, T. Song, Y. Cui, Y. Yang and G. Qian, *Dalton Trans.*, 2016, **45**, 18689.
70. T. Xia, Y. Cui, Y. Yang and G. Qian, *J. Mater Chem. C*, 2017, **5**, 5044.
71. L. Li, Y. Zhu, X. Zhou, C. D. S. Brites, D. Ananias, Z. Lin, F. A. Almedia Paz, J. Rocha, W. Huang and L. D. Carlos, *Adv. Funct. Mater.*, 2016, **26**, 8677.
72. CrysAlisPRO Software system Version 1.171.38.41, *Rigaku Oxford Diffraction*, 2015.
73. J. de Meulenaer and H. Tompa, *Acta Crystallogr.*, 1965, **19**, 1014-1018.
74. R. Blessing, *Acta Crystallogr. A*, 1995, **51**, 33-38.
75. A. Altomare, M. C. Burla, M. Camalli, G. L. Cascarano, C. Giacovazzo, A. Guagliardi, A. G. G. Moliterni, G. Polidori and R. Spagna, *J. Appl. Crystallogr.*, 1999, **32**, 115-119.
76. P. W. Betteridge, J. R. Carruthers, R. I. Cooper, K. Prout and D. J. Watkin, *J. Appl. Crystallogr.*, 2003, **36**, 1487.
77. R. C. Clark and J. S. Reid, *Acta Crystallogr. A*, 1995, **51**, 887-897.
78. Topas V4.2: General Profile and Structure Analysis Software for Powder Diffraction Data, *Bruker AXS Ltd*, 2008.
79. O. Veselska, L. Cai, D. Podbevšek, G. Ledoux, N. Guillou, G. Pilet, A. Fateeva and A. Demessence, *Inorg. Chem.*, 2018, **57**, 2736-2743.
80. L. Zhai, Z.-X. Yang, W.-W. Zhang, J.-L. Zuo and X.-M. Ren, *J. Mater. Chem. C*, 2018, **6**, 7030-7041.
81. J. S. Setchell, in *Colour Design (Second Edition)*, ed. J. Best, Woodhead Publishing, 2012, DOI: https://doi.org/10.1016/B978-0-08-101270-3.00004-7, pp. 99-129.
82. *CIE 015:2004 Colorimetry*, Commission Internationale de L'Eclairage, Vienna, Austria, 2004.

Chapter 3: $[M(m\text{-}SPhCO_2H)]_n$

3.1 Introduction

In Chapter 3, synthesis, structure, characterization and photophysical properties of *m*-$HSPhCO_2H$-based CPs are discussed.

There are extensive studies of *p*-$HSPhCO_2H$-based coordination compounds. In contrast, there is almost no examples of *m*-$HSPhCO_2H$ coordination complexes or CPs.[1]

Only two *m*-$HSPhCO_2H$-based coordination compounds are reported – $Cy_3PAu(m\text{-}SPhCO_2H)$ and $Ph_3PAu(m\text{-}SPhCO_2H)$.[2] The first one forms dimers via hydrogen bonds (**Figure 3. 1** (a)). $Ph_3PAu(m\text{-}SPhCO_2H)$ has a less bulky PPh_3 ligand comparing to PCy_3. Thanks to this fact, closer aggregation of gold centers are observed (**Figure 3. 1** (b)). It is caused by the presence of aurophilic interactions, O-H···S hydrogen bonds and π-π interactions between the phenyl rings of *m*-$HSPhCO_2H$ and triphenylphosphine (**Figure 3. 1** (c)). These two complexes nicely illustrate different crystal packing driven by co-operative action of all these weak interactions. The different aggregation patterns suggested that these interactions have comparable stabilizing potential in the condensed phase.

There are few examples of *m*-$HSPhCO_2H$ used in synthesis of protected nanoparticles and nanoclusters (NCs). The synthesis and luminescent properties were reported for Cu-NCs protected with *meta*-mercaptobenzoic acid.[3] The FT-IR spectrum confirms the formation of Cu-S bonds and no coordination of Cu with carboxylates was observed. Intermolecular hydrogen bonds were formed between the carboxylate groups on the surface of the NCs causing the formation of aggregates. The product possesses an absorption shoulder at around 340 nm and is weakly luminescent under UV irradiation. Its excitation peak is centered at 334 nm, and emission peak – at 668 nm. No tentative attribution of luminescent origin was proposed.

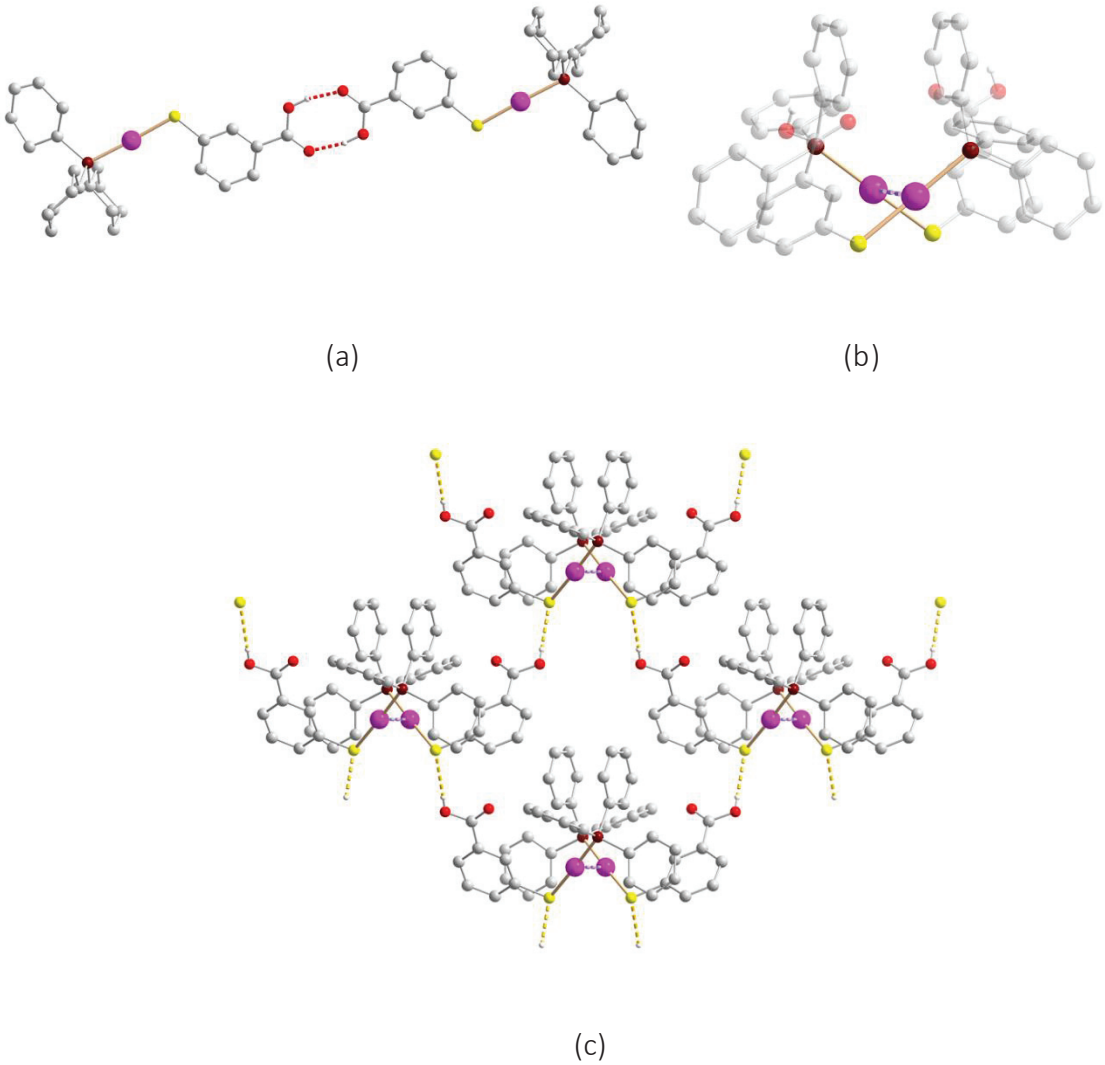

Figure 3. 1 Structure representations of (a) $Cy_3PAu(m\text{-}SPhCO_2H)$ and (b), (c) $Ph_3PAu(m\text{-}SPhCO_2H)$.[2] Red and yellow dashed lines represent hydrogen bonding. Violet dashed lines represent aurophilic interactions. Pink, Au; violet, P; yellow, S; red, O; grey, C; white, H. Non-acidic hydrogen atoms are omitted for clarity.

The study of the growth mechanism of *meta*-mercaptobenzoic acid-protected gold nanoclusters Au_{25} was reported.[4] A number of $Au_n(m\text{-}SPhCO_2H)_n$ and $[Au_n(m\text{-}SPhCO_2H)_nCl]^-$ precursors and stable NC intermediates were clearly identified. The follow up of those species let propose a reduction-growth mechanism of the NC formation. Furthermore, experimental and computational studies of $Au_{68}(m\text{-}SPhCO_2H)_{32}$ and $Au_{144}(m\text{-}SPhCO_2H)_{\sim 40}$ were reported.[5] The study shows their distinct characteristics, such as asymmetric metal core, weak interactions (within the ligand layer and at the ligand–gold interface – via π-Au interactions) and their potential interest as catalytic sites. Larger gold nanoparticles with this ligand were also reported.[6]

To conclude, few research has been done on coordination compounds of *meta*-mercaptobenzoic acid and coinage metals. Therefore, we decided to discuss the synthesis, characterizations, structures and photophysical properties of $[M(m\text{-}SPhCO_2H)]_n$ coordination networks, in this chapter.

3.2 Syntheses and Structures

We synthesized pure and highly crystalline *m*-$HSPhCO_2H$-based CPs under solvothermal conditions. Their PXRD patterns are shown in the **Figure 3. 2**. The predominant (00*l*) reflections underline the lamellar structure of these materials. The interlamellar distances are 15.1, 15.0, 16.3 Å for Cu-, Ag- and Au-based compounds respectively.

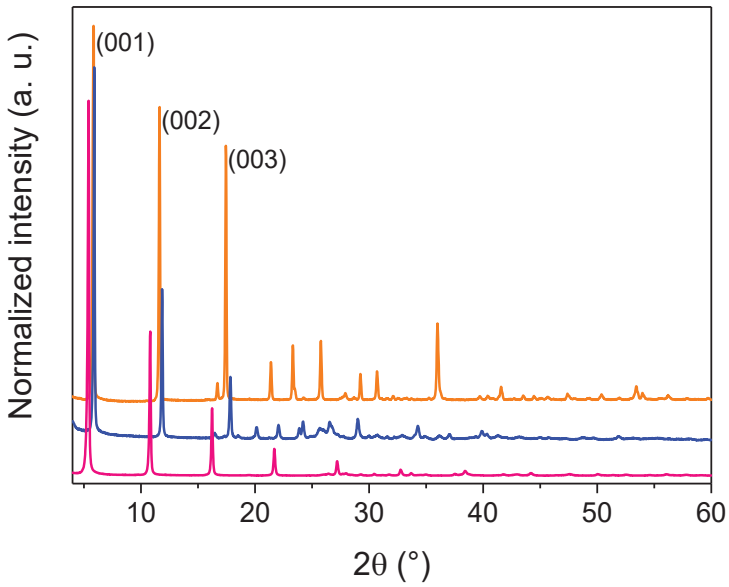

Figure 3. 2 The PXRD patterns of $[Cu(m\text{-}SPhCO_2H)]_n$ (orange), $[Ag(m\text{-}SPhCO_2H)]_n$ (blue) and $[Au(m\text{-}SPhCO_2H)]_n$ (pink).

In the case of $[Cu(m\text{-}SPhCO_2H)]_n$, crystals were big enough for single crystal structure determinations. Data was collected at the CRISTAL beamline at Synchrotron Soleil (Gif-sur-Yvette, France).

For $[Ag(m\text{-}SPhCO_2H)]_n$ and $[Au(m\text{-}SPhCO_2H)]_n$ high resolution X-ray powder diffraction data were also collected at the CRISTAL beamline. From these data, the structural determination

of [Au(*m*-SPhCO$_2$H)]$_n$ was performed. For [Ag(*m*-SPhCO$_2$H)]$_n$ the indexing did not converge unambiguously to any unit cell, what prevented further structural investigation.

3.2.1 Structure of [Cu(*m*-SPhCO$_2$H)]$_n$

The structure determination resulted into a $P2_1/n$ cell with a = 3.9047(2) Å, b = 30.438(3) Å, c = 5.6182(4) Å and β = 91.933(4)°. The long b parameter corresponds to two sets of Cu-S and organic layers. It is in agreement with the d_{hkl} spacing found from PXRD pattern (**Figure 3. 3**).

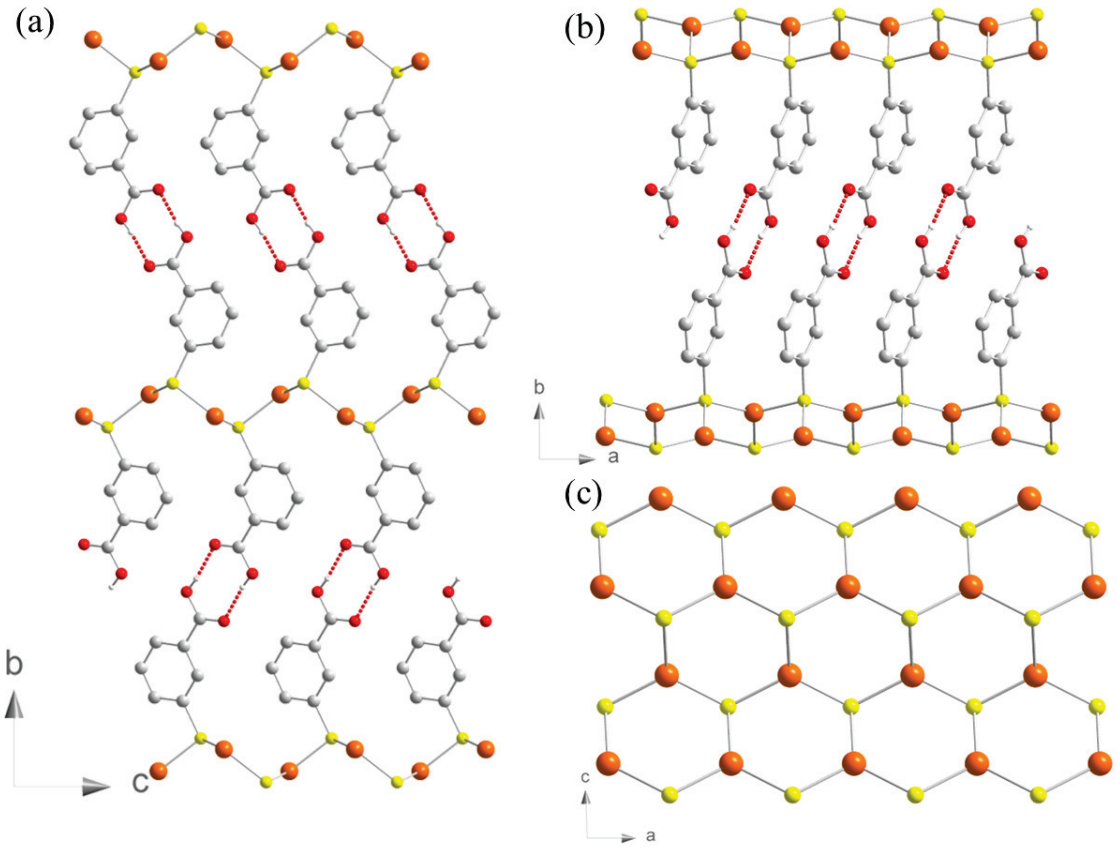

Figure 3. 3 Structure representations of [Cu(*m*-SPhCO$_2$H)]$_n$. Views on (a) *(bc)* and (b) *(ab)* planes. (c) View of the Cu_3S_3 hexagons of the inorganic sheet on *(ac)* plane. Orange, Cu; yellow, S; red, O; grey, C; white, H. Non-acidic hydrogen atoms are omitted for clarity.

Copper thiolate sheets are closely resembling the ones of [Cu(*p*-SPhCO$_2$Me)]$_n$ and [Cu(*p*-SPhOH)]$_n$.[7] (**Figure 3. 4**). Copper atoms are in a trigonal planar geometry. They are coordinated to μ_3-thiolate ligands, forming Cu_3S_3 hexagons in half-chair conformation. One copper atom sticks out of the plane containing five other atoms of the hexagon. It creates a dihedral angle of 61.3(1)° with the plane containing other 5 atoms of the hexagon. The Cu-S distances are

2.242(2), 2.244(2) and 2.294(2) Å, the angles of S-Cu-S are 116.3(1)°, 121.0(1)° and 121.1(1)° and of Cu-S-Cu are 100.7(1)°, 105.0(1)° and 121.0(1)°. These values are comparable to the ones of other similar 2D copper thiolates (**Table 3. 1**).[8] Cu-Cu distances of 3.494(1) and 3.599(2) Å are too long to be considered as cuprophilic interactions.[9] Ligand molecules occupy interlamellar space with parallel displaced π-stacking. The layers are connected via dimeric hydrogen bonds.

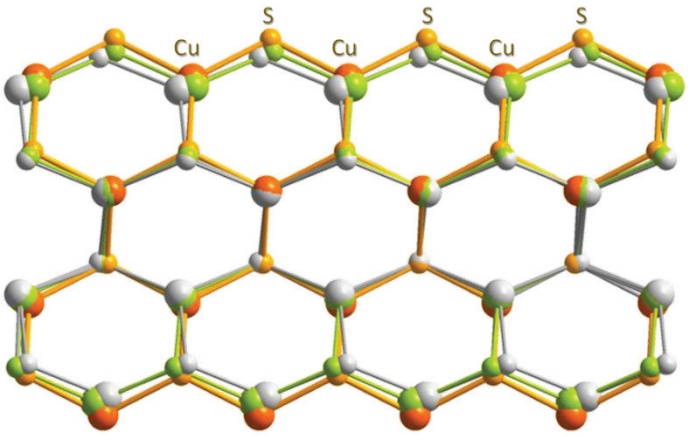

Figure 3. 4 Superposition of Cu-S layer of the three compounds: [Cu(*m*-SPhCO$_2$H)]$_n$ (orange), [Cu(*p*-SPhCO$_2$Me)]$_n$ (light green) and [Cu(*p*-SPhOH)]$_n$ (grey). It demonstrates a proximity of their structures.

Table 3. 1 Comparison of the main distances and angles in [Cu(*m*-SPhCO$_2$H)]$_n$, [Cu(*p*-SPhCO$_2$Me)]$_n$ and [Cu(*p*-SPhOH)]$_n$.

Compound	Cu-S, Å	Cu-Cu, Å	S-Cu-S, °	Cu-S-Cu, °	Dihedral angle in Cu_3S_3, °	π-π, Å
[Cu(*p*-SPhOH)]$_n$	2.252(4) 2.253(3)	3.238(5) 3.450(5) 4.001(4)	112.9(1) 121.9(1) 125.3(1)	91.9(1) 100.0(1) 125.3(1)	103.2(2)	4.001(1)
[Cu(*p*-SPhCO$_2$Me)]$_n$	2.244(3) 2.255(3) 2.282(4)	3.313(3) 3.492(3) 3.966(3)	114.0(2) 122.2(2) 123.6(2)	93.8(2) 101.0(2) 123.6(2)	106.5(1)	3.966(1)
[Cu(*m*-SPhCO$_2$H)]$_n$	2.242(2) 2.244(2) 2.294(2)	3.494(1) 3.599(2) 3.905(1)	116.3(1) 121.0(1) 121.1(1)	100.7(1) 105.0(1) 121.0(1)	118.7(1)	3.905(1)

3.2.2 Structure of [Ag(*m*-SPhCO$_2$H)]$_n$

The predominant (00*l*) reflections let us suppose a lamellar structure of this compound with interlamellar distances of 15.0 Å. It corresponds to Ag-S layer (*e. g.*, [Ag(SPh)]$_n$: 2.44 Å, [Ag(*p*-SPhCO$_2$H)]$_n$: 2.54 Å, [Ag(*p*-SPhCO$_2$Me)]$_n$: 2.49 Å) and two layers of ligand (*m*-SPhCO$_2$H) connected through dimeric hydrogen bonds with a tilt of ~65° to Ag-S layer.

3.2.3 Structure of [Au(*m*-SPhCO$_2$H)]$_n$

Structure determination gives a *P*1 cell with *a* = 4.7568(6) Å, *b* = 4.7635(6) Å, *c* = 16.3971(6) Å, α = 90.775(8)°, β = 89.128(6)°, γ = 92.658(4)°. This structure is similar to the previously discussed [Au(*p*-SPhCO$_2$H)]$_n$.

The lamellar structure of this compound consists of planes composed of of 1D helices of Au(I) atoms bridged by μ_2-S atoms (**Figure 3. 5**). The Au-S distances are between 2.251(8) and 2.367(8) Å (**Table 3. 2**). The Au-S-Au angles are 85.1(4)° and 90.9(4)°, while those formed by S-Au-S are 89.6(3)° and 150.3(4)°. The latter one are far from the linear angle which is usually observed for gold atoms and rather resemble the one of [Au(*p*-SPhCO$_2$H)]$_n$.

Table 3. 2 Comparison of the main distances and angles in [Au(*m*-SPhCO$_2$H)]$_n$ and [Au(*p*-SPhCO$_2$H)]$_n$.

Compound	Au-S, Å	Au-Au, Å	S-Au-S, °	Au-S-Au, °	O1-O2, Å	π-π, Å
[Au(*p*-SPhCO$_2$H)]$_n$	2.272(1) 2.273(1) 2.342(1) 2.367(1)	3.355(4) 3.422(6) 3.591(3)† 3.732(3)†	77.47(3) 124.00(1)	99.38(1) 110.41(4)	2.903(1) 3.011(1)	4.518(1)
[Au(*m*-SPhCO$_2$H)]$_n$	2.251(8) 2.355(8) 2.365(8) 2.367(8)	3.20(2)† 3.28(2)† 3.39(2) 3.61(2)	89.6(3) 150.3(4)	85.1(4) 90.9(4)	2.683(1) 3.035(1)	4.764(1)

† bridged by sulfur atoms.

Similarly to the case of [Au(*p*-SPhCO$_2$H)]$_n$, the formation of such unusual S-Au-S angles in [Au(*m*-SPhCO$_2$H)]$_n$ is directed by the formation of both, the catemeric hydrogen bonds and the aurophilic interactions. Interchain Au-Au distances are bit longer than in the case of [Au(*p*-SPhCO$_2$H)]$_n$: 3.39(2) and 3.61(2) Å vs. 3.36(1) and 3.42(1) Å. Inversely, intrachain Au-Au

distances are shorter than in the *para*-substituted counterpart (3.20(2) and 3.28 (2) Å vs. 3.59(1) and 3.72(1) Å).

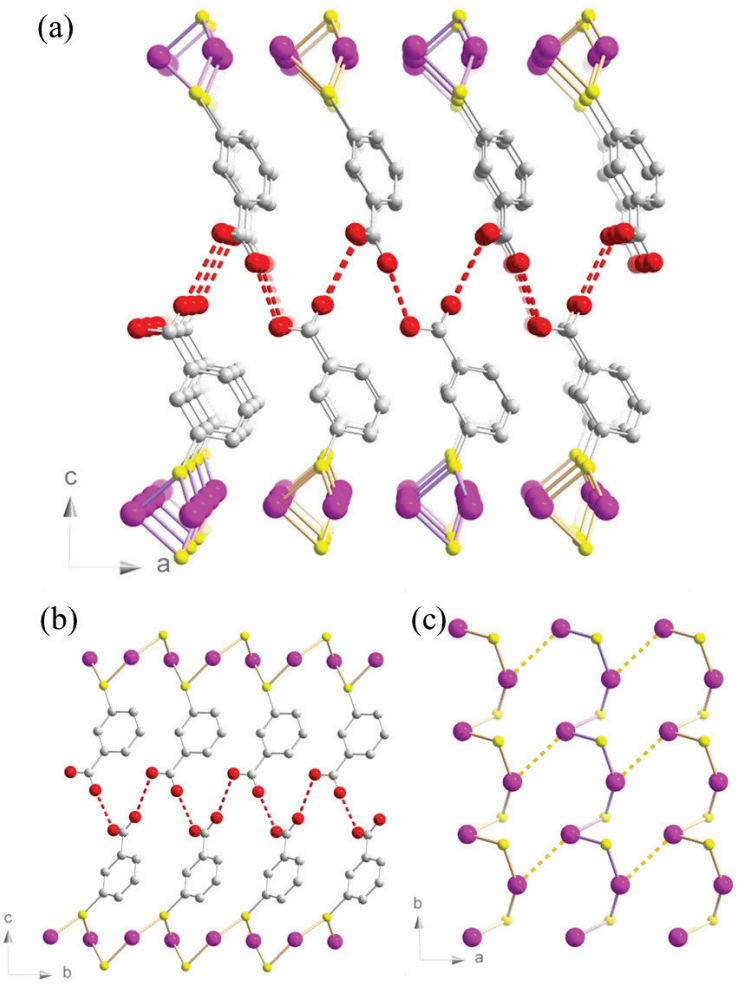

Figure 3. 5 Structure representations of $[Au(m\text{-}SPhCO_2H)]_n$. Views on (a) *(ac)* and (b) *(bc)* planes. (c) View of Au-S chains on the *(ab)* plane. Pink, Au; yellow, S; red, O; grey, C. Hydrogen atoms are omitted for clarity. Orange dotted lines represent the interchain aurophilic interactions.

3.3 Characterization

Based on the SEM images, of crystallites of all three CPs take form of thin pellets typical of lamellar compounds (**Figure 3. 6**).

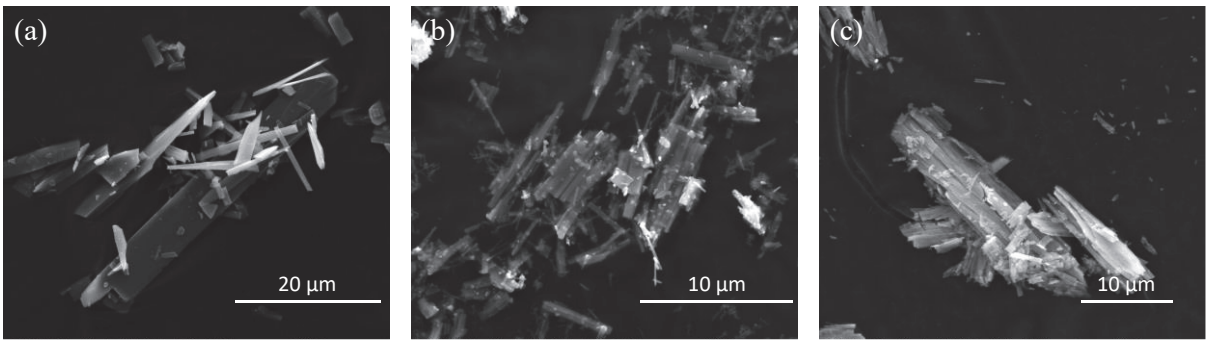

Figure 3. 6 SEM images of (a) $[Cu(m\text{-}SPhCO_2H)]_n$, (b) $[Ag(m\text{-}SPhCO_2H)]_n$ and (c) $[Au(m\text{-}SPhCO_2H)]_n$.

FT-IR spectroscopy showed presence of a band of antisymmetric vibration of CO of carboxylic acids. It is observed at 1683 cm^{-1}. Presence of the broad ν(OH) bands between 2560 and 3065 cm^{-1} is consistent with the presence of hydrogen bonds (**Figure 3. 7**).

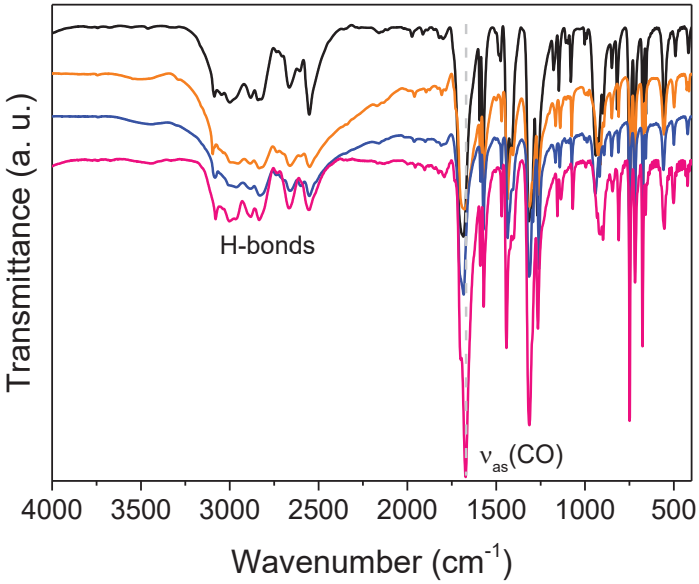

Figure 3. 7 FT-IR spectra of free ligand (black), $[Cu(m\text{-}SPhCO_2H)]_n$ (orange), $[Ag(m\text{-}SPhCO_2H)]_n$ (blue) and $[Au(m\text{-}SPhCO_2H)]_n$ (pink).

The thermo-gravimetric analysis confirms the purity of the compounds with an expected metal and organic content. We see an increase of thermal stability after the complexation of the metal in comparison to free ligand. All compounds show relatively good thermal stability around 300°C (**Figure 3. 8**).

Influence of weak bonding on decomposition temperature can be observed by comparison of $[Cu(m\text{-}SPhCO_2H)]_n$ (T_{dec} = 300°C) and $[Cu(p\text{-}SPhCO_2Me)]_n$ (T_{dec} = 280°C). Distances and angles in the $[CuS]_n$ layers are very close. Therefore, the presence of hydrogen bonding between the layers contributes to a higher thermal stability of $[Cu(m\text{-}SPhCO_2H)]_n$.

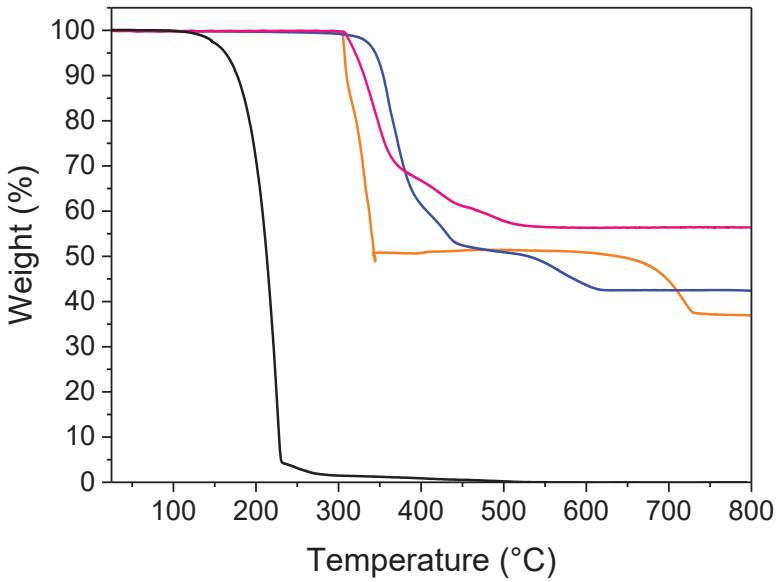

Figure 3. 8 The TGA performed under air at 10°C/min of the free ligand (black), $[Cu(m\text{-}SPhCO_2H)]_n$ (orange), $[Ag(m\text{-}SPhCO_2H)]_n$ (blue) and $[Au(m\text{-}SPhCO_2H)]_n$ (pink).

3.4 Photophysical Properties

$[Cu(m\text{-}SPhCO_2H)]_n$, a yellow compound, shows broad absorption band centered at 380 nm with far end that extends up to 500 nm (**Figure 3. 9**). Its measured optical band gap of 2.6 eV is close to the one of $[Cu(p\text{-}SPhCO_2Me)]_n$ (2.68 eV). Both silver- and gold-based compounds are white powders. Maxima of an absorption of $[Ag(m\text{-}SPhCO_2H)]_n$ is at 348 nm (optical band gap is 3.1 eV), similarly to $[Ag(p\text{-}SPhCO_2H)]_n$ (342 nm, 2.99 eV). The maximum of absorption of $[Au(m\text{-}SPhCO_2H)]_n$ is at 320 nm (optical band gap is 2.9 eV).

In case of free ligand, the absorption edge is located at 380 nm and the absorptions of CPs are red shifted. High-energy absorption of silver- and gold-based compounds (between λ_{abs} = 300-350 nm with its edge at 420 nm) is assigned to a π–π* transition of the phenyl group of the ligand.[10] Furthermore, a presence of broad, unstructured band (between λ_{abs} = 300-450 nm) was observed for copper-based compound. It is, presumably, a result of an electronic

transition from σ(M–S) orbital to an empty π* antibonding orbital. The latter is located on the phenyl group of the ligand. It gives the product its yellow color.[11] Nevertheless, it might also originate from the metal-perturbed IL or MLCT transition.[12,13]

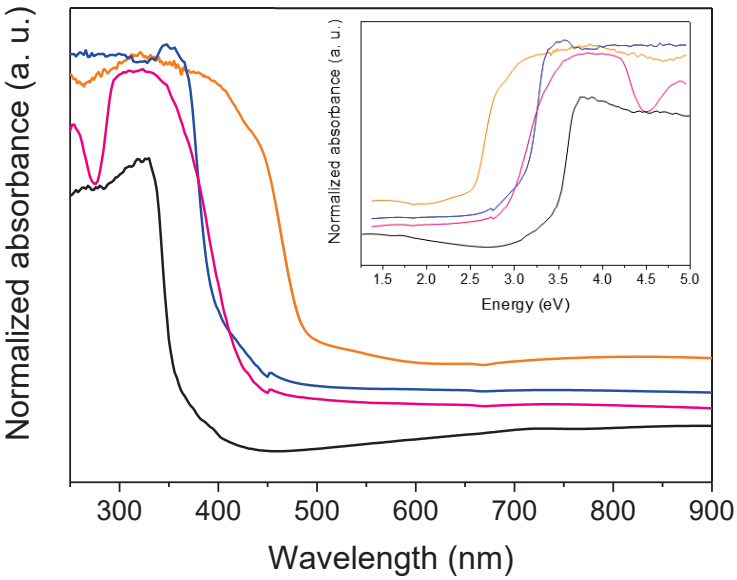

Figure 3. 9 UV-vis absorption spectra of $[Cu(m\text{-}SPhCO_2H)]_n$ (orange), $[Ag(m\text{-}SPhCO_2H)]_n$ (blue), $[Au(m\text{-}SPhCO_2H)]_n$ (pink) and $m\text{-}HSPhCO_2H$ (black) obtained in solid state at the room temperature. UV-vis absorption spectra as function of energy are shown as inset.

3.4.1 $[Cu(m\text{-}SPhCO_2H)]_n$

Excitation of the compound $[Cu(m\text{-}SPhCO_2H)]_n$ by UV light in solid state at the room temperature does not result in visible emission. Only at 93 K, very weak greenish emission can be seen (**Figure 3. 10**).

$[Cu(m\text{-}SPhCO_2H)]_n$ displays an emission band centered at 575 nm (**Figure 3. 10**). At low temperature, vibronic spacings of 1300 and 1495 cm^{-1} are seen. It is typical for the excited states of aromatic systems. Free ligand exhibits itself a blue emission centered at 447 nm with vibronic spacings of 1220 and 1145 cm^{-1} (**Figure 3. 11**). The red shift of emission peak maximum after complexation is observed (the same holds for excitation peak maximum: from 384 to 412 nm). It seems reasonable to associate it with metal-perturbed LC (ππ*) excited states.

Photophysical properties of $[Cu(m\text{-}SPhCO_2H)]_n$ coordination polymer are very different from reported Cu-NCs protected with *meta*-mercaptobenzoic acid.[3]

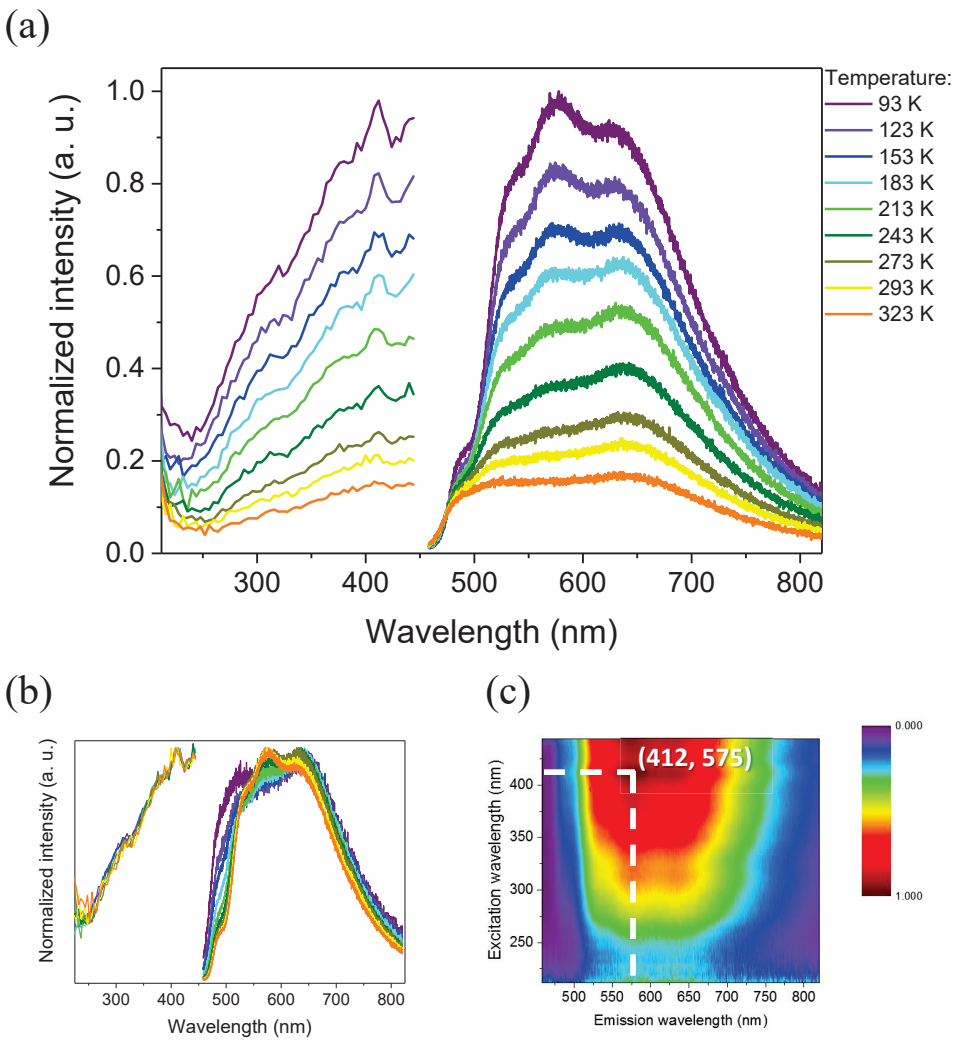

Figure 3. 10 Luminescent properties of $[Cu(m\text{-}SPhCO_2H)]_n$: (a) emission-excitation spectra (λ_{exc} = 412 nm, λ_{em} = 575 nm) and (b) normalized emission-excitation spectra obtained in the solid state at various temperatures; (c) 2D map of the emission and excitation spectra obtained in the solid state at 93 K.

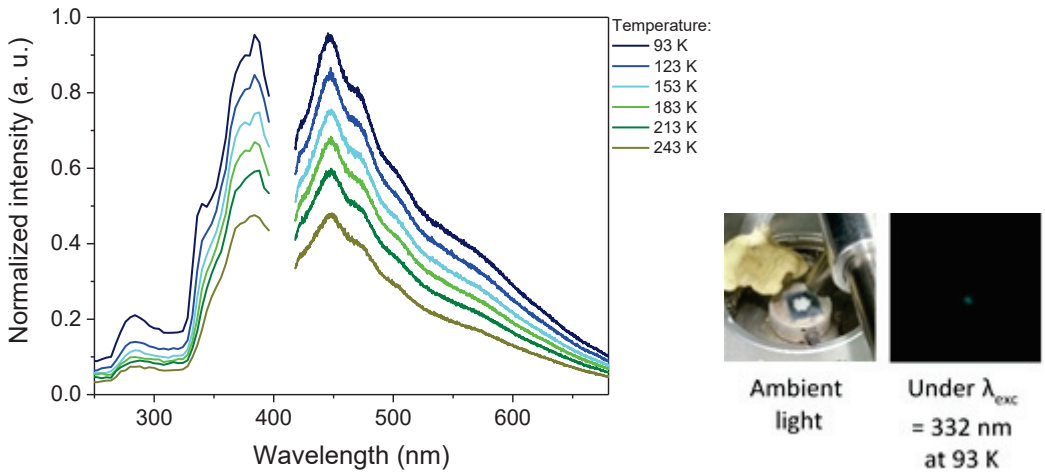

(a) (b)

Figure 3. 11 (a) Emission-excitation spectra (λ_{exc} = 384 nm, λ_{em} = 447 nm) of *m*-HSPhCO$_2$H obtained in the solid state at variable temperatures and (b) its photographs under ambient light (left) and UV lamp (right) in solid state at 93 K.

The luminescence lifetime decay in the solid-state were fitted by a triexponential curve with components of 0.19 µs (19 %), 11 ns (63 %) and 0.11 ms (17 %) at room temperature (**Figure 3. 12**, Appendix B). The contribution of ~80 % coming from faster components and ~20 % from slower components is preserved over all studied temperature range. Lifetime thermal quenching is observed.

The predominance of fast component and well resolved emission peak profile could be attributed to the fluorescent process. However, the Stokes shift of 6 900 cm^{-1} is too large to be a fluorescence. It implies its origin from a highly distorted excited state. Considering the complexity of the excited states of this class of CPs, it is not unreasonable to suppose a presence of few competing mechanisms. Therefore, origin of emission is tentatively assigned to the singlet and triplet states ^{1,3}IL.

It is interesting to compare emissive properties of [Cu(*m*-SPhCO$_2$H)]$_n$ and [Cu(*p*-SPhCO$_2$Me)]$_n$ which have similar structures (**Figure 3. 4**). On one hand, [Cu(*p*-SPhCO$_2$Me)]$_n$ exhibits two emission peaks at 460 and 560 nm, which we tentatively assigned to the intra-ligand/ligand–ligand CT. Furthermore, it also exhibits a peak at 740 nm assigned to the ^{3}MLCT/^{3}LMCT and/or MC (d*s*/d*p*) states. On the other hand, [Cu(*m*-SPhCO$_2$H)]$_n$ exhibits only one emission peak at 575 nm which is the most likely originating from metal-perturbed LC (ππ*) excited states.

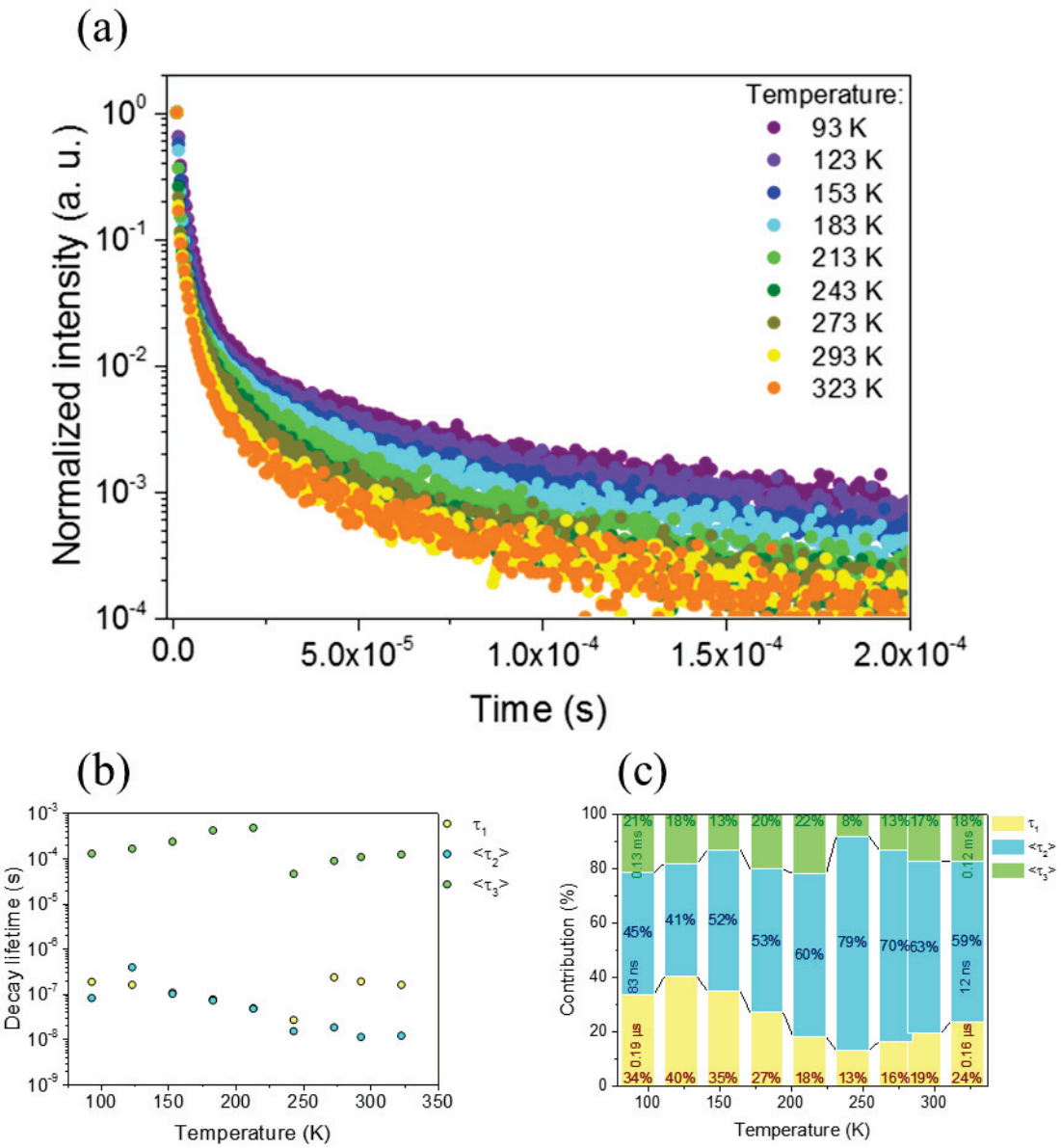

Figure 3. 12 Temperature-dependent luminescence decays (λ_{exc} = 412 nm, λ_{em} = 590 nm) of [Cu(*m*-SPhCO$_2$H)]$_n$ (a). Values of the lifetime decays (b) and of contributions of different components (c) at various temperatures.

Considering close distances and angles in Cu-S layer and π-π contacts, it seems, that the main reason for the observed properties comes from the modification of the electronic density of the ligand because of the position change of the substituent on the phenyl ring.

It is worth noting, that both compounds have closely lying maxima of emission: at 560 and 575 nm (**Figure 3. 13**). Nevertehless, in the case of [Cu(*m*-SPhCO$_2$H)]$_n$ it is well vibronically resolved, while peak of [Cu(*p*-SPhCO$_2$Me)]$_n$ is broad and lacks any structuration (even at low

temperature). The vibronic structure of the [Cu(*m*-SPhCO$_2$H)]$_n$ can be explained by higher relative rigidity of the CPs due to the presence of hydrogen bonds.

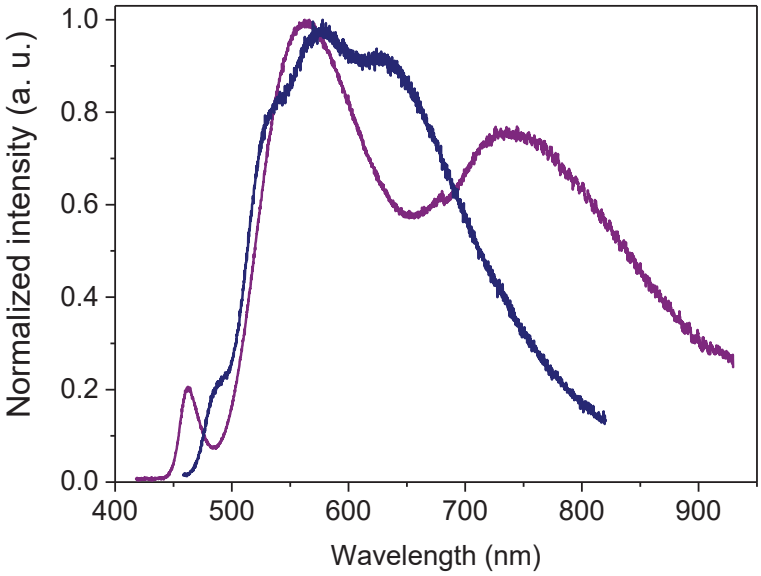

Figure 3. 13 Emission spectra of [Cu(*m*-SPhCO$_2$H)]$_n$ (λ_{exc} = 412 nm, dark blue) and [Cu(*p*-SPhCO$_2$Me)]$_n$ (λ_{exc} = 380 nm, purple) obtained in the solid state at 93 K.

3.4.2 [Ag(*m*-SPhCO$_2$H)]$_n$

The compound [Ag(*m*-SPhCO$_2$H)]$_n$ shows weak greenish emission at the room temperature when exposed to UV light. Once the temperature of the sample is decreased, emission color changes to blue and its intensity increases.

At 93 K, [Ag(*m*-SPhCO$_2$H)]$_n$ displays emission band with maximum at 482 nm and a tail reaching 700 nm (**Figure 3. 14**). In the process of the increase of the temperature (~ 273 K) the peak splits into two bands at 460 and 556 nm.

The excitation spectrum profile is a mirror image of the emission spectrum. The excitation maximum is at 352 nm at 93 K and it progressively shifts to lower energy, reaching 376 nm at 323 K. At the same time, during the temperature increase, excitation band at 316 nm becomes more distinct. Such behavior suggests the presence of two closely lying excited states that become further separated during the temperature increase, decay independently and produce two distinct emission bands.

These two emission bands resemble the emission properties of $[Ag(p\text{-}SPhCO_2H)]_n$ and $[Ag(p\text{-}SPhCO_2Me)]_n$ and they can be assigned in similar manner. The HE emission band has a Stokes shift of 4 860 cm^{-1} and can be associated to MC singlet states. The LE emission band with a Stokes shift of 13 360 cm^{-1} can be attributed to ^{3}LMCT perturbed by Ag-Ag contacts.[14]

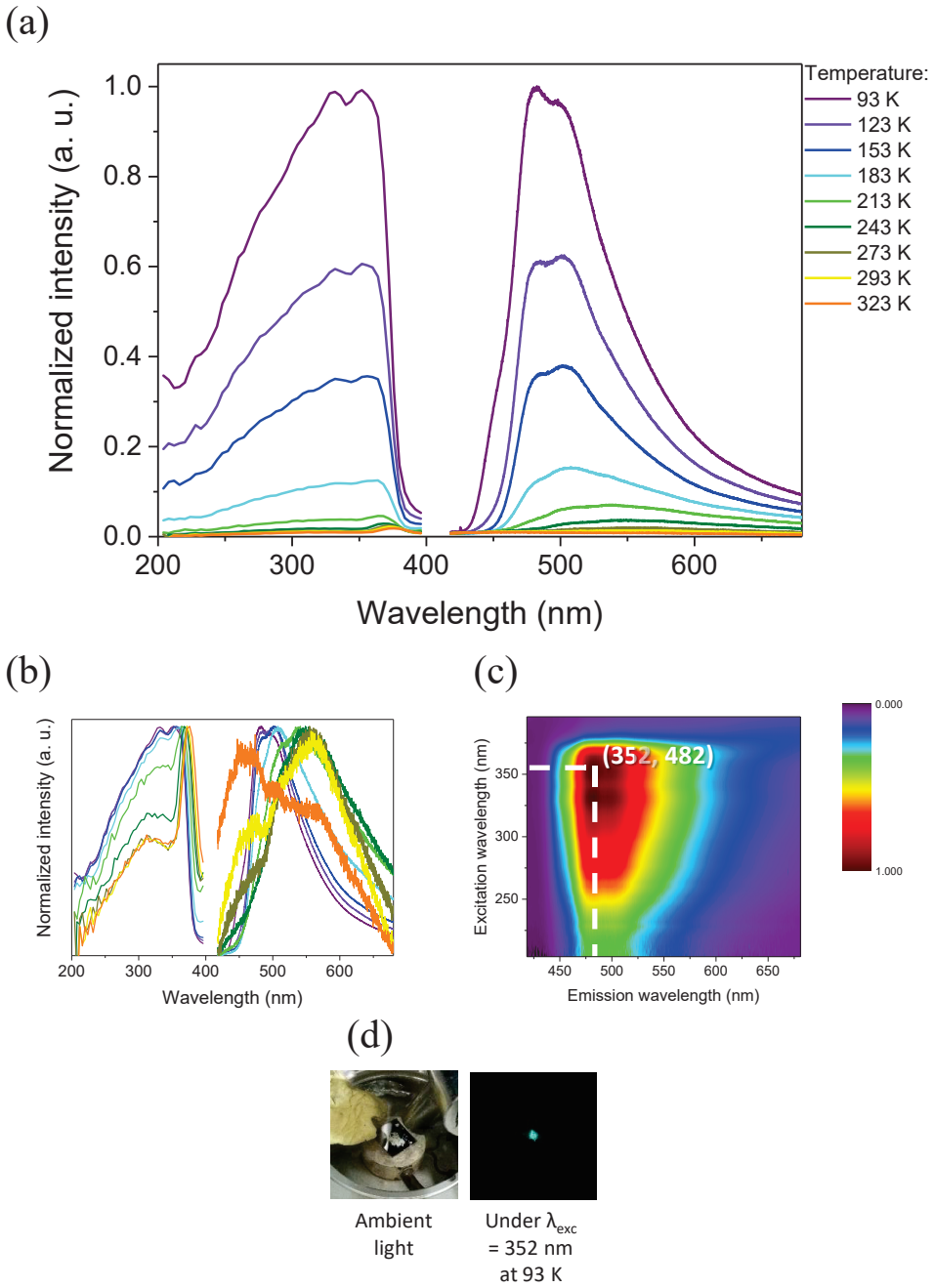

Figure 3. 14 Luminescent properties of $[Ag(m\text{-}SPhCO_2H)]_n$: (a) emission-excitation spectra (λ_{exc} = 352 nm, λ_{em} = 482 nm) and (b) normalized emission-excitation spectra obtained in the solid state at various temperatures; (c) 2D map of the emission and excitation spectra obtained in the solid state at 93 K; (d) photographs of $[Ag(m\text{-}SPhCO_2H)]_n$ under ambient light (left) and UV lamp (right) in solid state at 93 K.

The luminescence lifetime decay in the solid-state was fitted by a biexponential curve with two distinct components: dominant component is in the nanosecond range and minor one in the microsecond range (**Figure 3. 15**, Appendix B). First one is believed to correspond to the metal centered emission, and second one – to the LMCT. A thermal quenching of emission lifetime is observed.

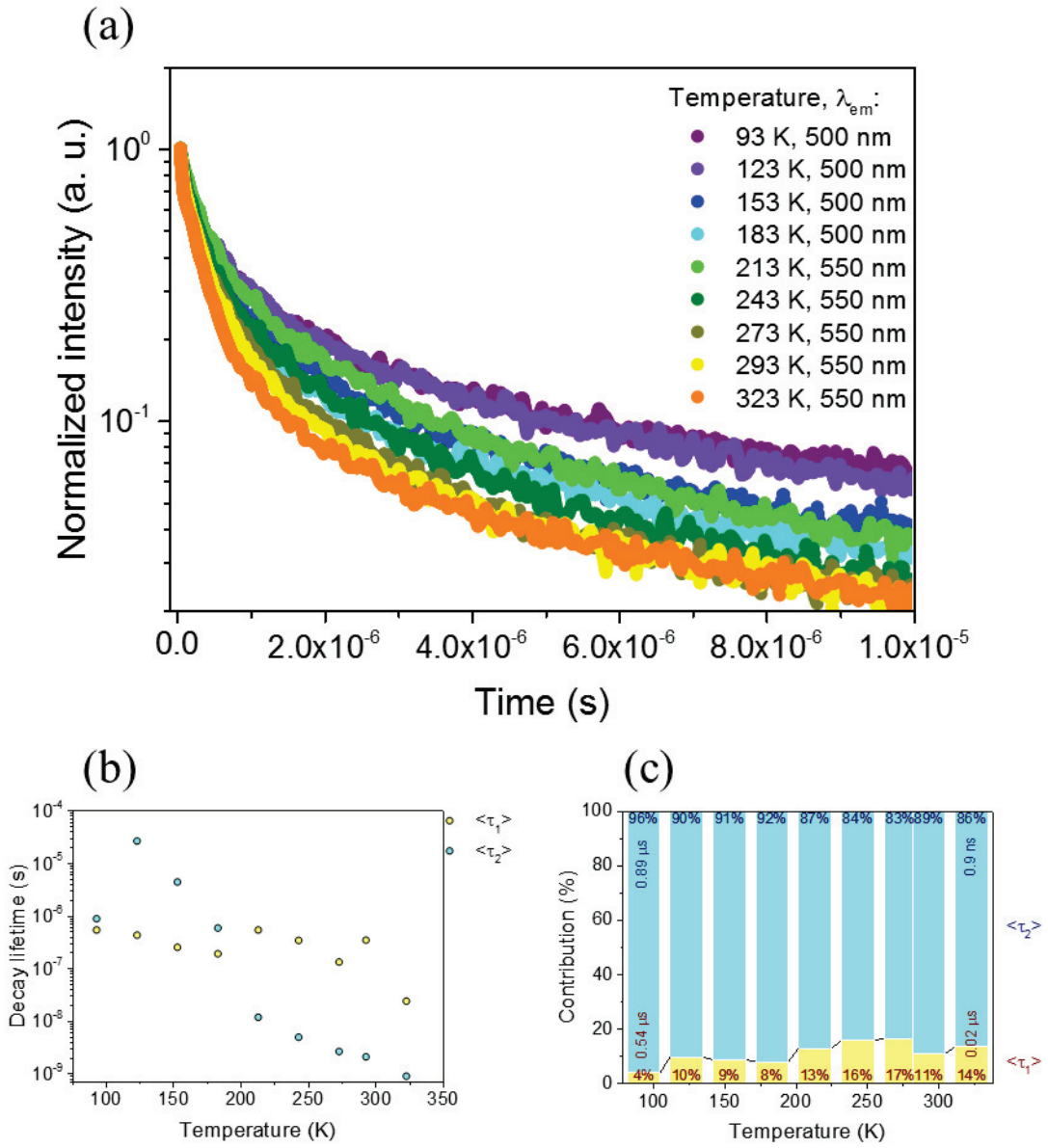

Figure 3. 15 Temperature-dependent luminescence decays (λ_{exc} = 352 nm, λ_{em} = 500/550 nm) of $[Ag(m\text{-}SPhCO_2H)]_n$ (a). Values of the lifetime decays (b) and of contributions of different components (c) at various temperatures.

Unfortunately, the impossibility of structural determination prevents an unambiguous discussion of 'structure-properties' correlation of $[Ag(m\text{-}SPhCO_2H)]_n$.

$[Ag(m\text{-}SPhCO_2H)]_n$ and phase **2** of $[Ag(SPh)]_n$ have similar emission profiles (**Figure 3. 16**). Emission, excitation and absorption spectra of $[Ag(m\text{-}SPhCO_2H)]_n$ are blue shifted relatively to the phase **2** of $[Ag(SPh)]_n$. It can be attributed to the electron-withdrawing effect of the carboxylic group on the ligand. It stabilizes the sulfur orbital, making the ligand more difficult to oxidize, thus leading to lowering of the LUMO and to the blue shift of the emission.[15] This interpretation is consistent with luminescence attribution of LMCT states.

It is tempting to attribute this similarity to the structural proximity. However, after the discussion about $[Au(m\text{-}SPhCO_2H)]_n$, it will be clear why one should not follow such precocious conclusions.

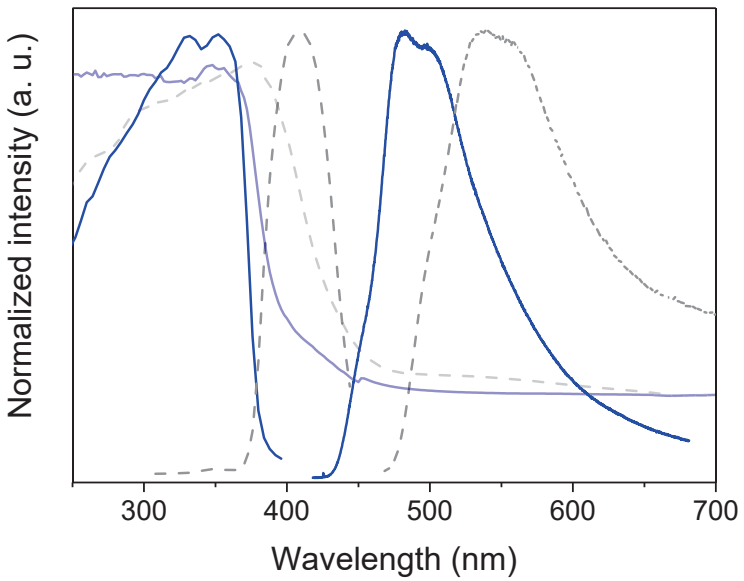

Figure 3. 16 Comparison of emission-excitation spectra of $[Ag(m\text{-}SPhCO_2H)]_n$ (blue solid line) and $[Ag(SPh)]_n$ phase **2** (gray dashed line) obtained in the solid state at 93 K, and of their absorption spectra (in half transparent) measured in the solid state at the room temperature.

3.4.3 $[Au(m\text{-}SPhCO_2H)]_n$

The compound $[Au(m\text{-}SPhCO_2H)]_n$ shows bright yellow-orange emission at the room temperature, and it persists even at high temperature (473 K, therefore almost up to the decomposition of the material). At the room temperature, emission and excitation maxima are lying at 615 nm and 352 nm, respectively. When the temperature is decreased, emission intensity increases with a soft refinement of the width and a shift of the emission maximum to

595 nm at 93 K (**Figure 3. 17**). When the temperature is increased, no significant shift of emission, relatively to the room temperature, is observed. In the same time, excitation maximum slightly shifts to 368 nm at 503 K.

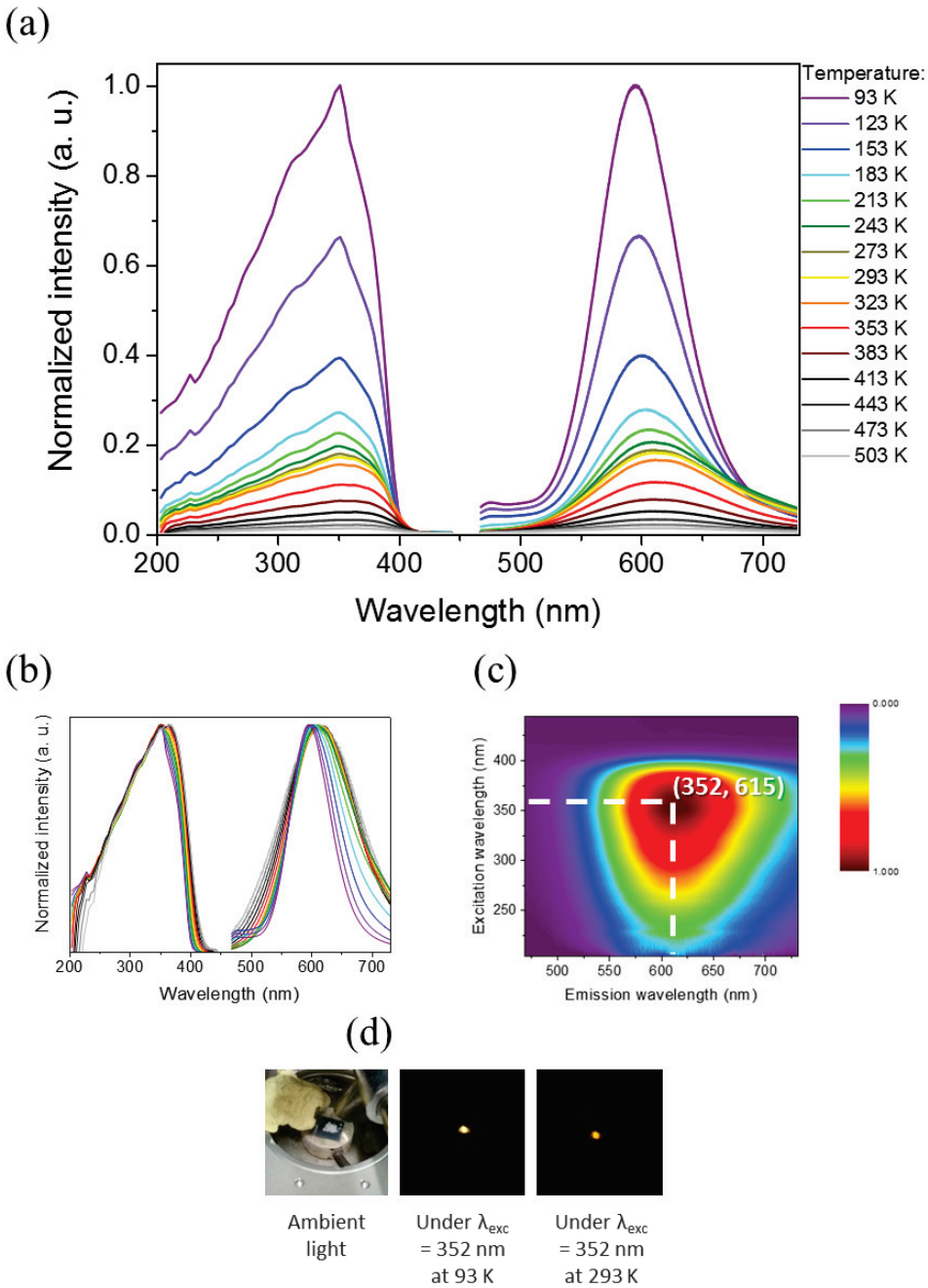

Figure 3. 17 Luminescent properties of $[Au(m\text{-}SPhCO_2H)]_n$: (a) emission-excitation spectra (λ_{exc} = 352 nm, λ_{em} = 596 nm) and (b) normalized emission-excitation spectra obtained in the solid state at various temperatures; (c) 2D map of the emission and excitation spectra obtained in the solid state at 293 K; (d) photographs of $[Au(m\text{-}SPhCO_2H)]_n$ under ambient light (left) and UV lamp (right) in solid state at 93 and 293 K.

There is a low intensity emission shoulder at 475 nm that appears below 213 K. Free ligand exhibits a large band of emission centered at 507 nm under the same excitation wavelength. Thus, this HE emission can be assigned to a metal-perturbed IL transition. Similar behavior has been observed before in Au(I) phosphane complexes containing 4-nitrophenylthiolate ligand[12] and dinuclear neutral thiolate Au(I) complexes with phenylene spacers.[16]

Luminescence lifetime decay in the solid-state has been fitted with a triexponential curve with components of 0.31 µs (88 %), 0.14 ms (10 %) and 2.3 ms (2 %) at the room temperature (Appendix B). Lifetime decay study at various temperatures (**Figure 3. 18**) shows shortening of lifetime of major components with temperature increase: at 93 K, the lifetime is 0.87 µs and at 503 K, it drops to 0.04 µs. Its contribution at low temperature stays at the level of 86 %, and it grows up to 94 % at high temperature. Two smaller components experience minor change of lifetime in the studied temperature range. The contribution of both decreases with temperature increase.

The long lifetime in the microsecond range and the large Stokes shift of 12 150 cm^{-1} (at the room temperature) are both characteristic for a phosphorescence process. The quantum yield is 18.9 ± 0.2 % in solid state at the room temperature.

The close emission and excitation energies, lifetime decay behavior, low-intensity emission shoulder and high quantum yield in the solid state make the photophysical properties of $[Au(m\text{-}SPhCO_2H)]_n$ strongly close to $[Au(p\text{-}SPhCO_2Me)]_n$.[17]

The overall luminescence process of $[Au(p\text{-}SPhCO_2Me)]_n$ was ascribed to a LMLCT transition (AuS → $PhCO_2Me$) based on DFT calculations.

Strong similarity of properties of two CPs, implies the same luminescence origin for $[Au(m\text{-}SPhCO_2H)]_n$ as the one proposed for $[Au(p\text{-}SPhCO_2Me)]_n$ – LMLCT. It supports the supposition previously made in [17]. The results of the paper point out to the presence of an electron withdrawing group precluding the possibility of LM(M)CT transitions, that are often ascribed to Au(I)-compounds.

Despite the fact that $[Au(m\text{-}SPhCO_2H)]_n$ is structurally related to $[Au(p\text{-}SPhCO_2H)]_n$, they both have very different luminescent properties. Moreover, the properties are close to the ones of $[Au(p\text{-}SPhCO_2Me)]_n$ which structurally differs and possesses disparate Au-S

arrangement (helices vs. zig-zags). The presence of aurophilic interactions and substituents on the organic ligand are often the main parameters that can help to trace the reason for the origin of the different photophysical properties.[15]

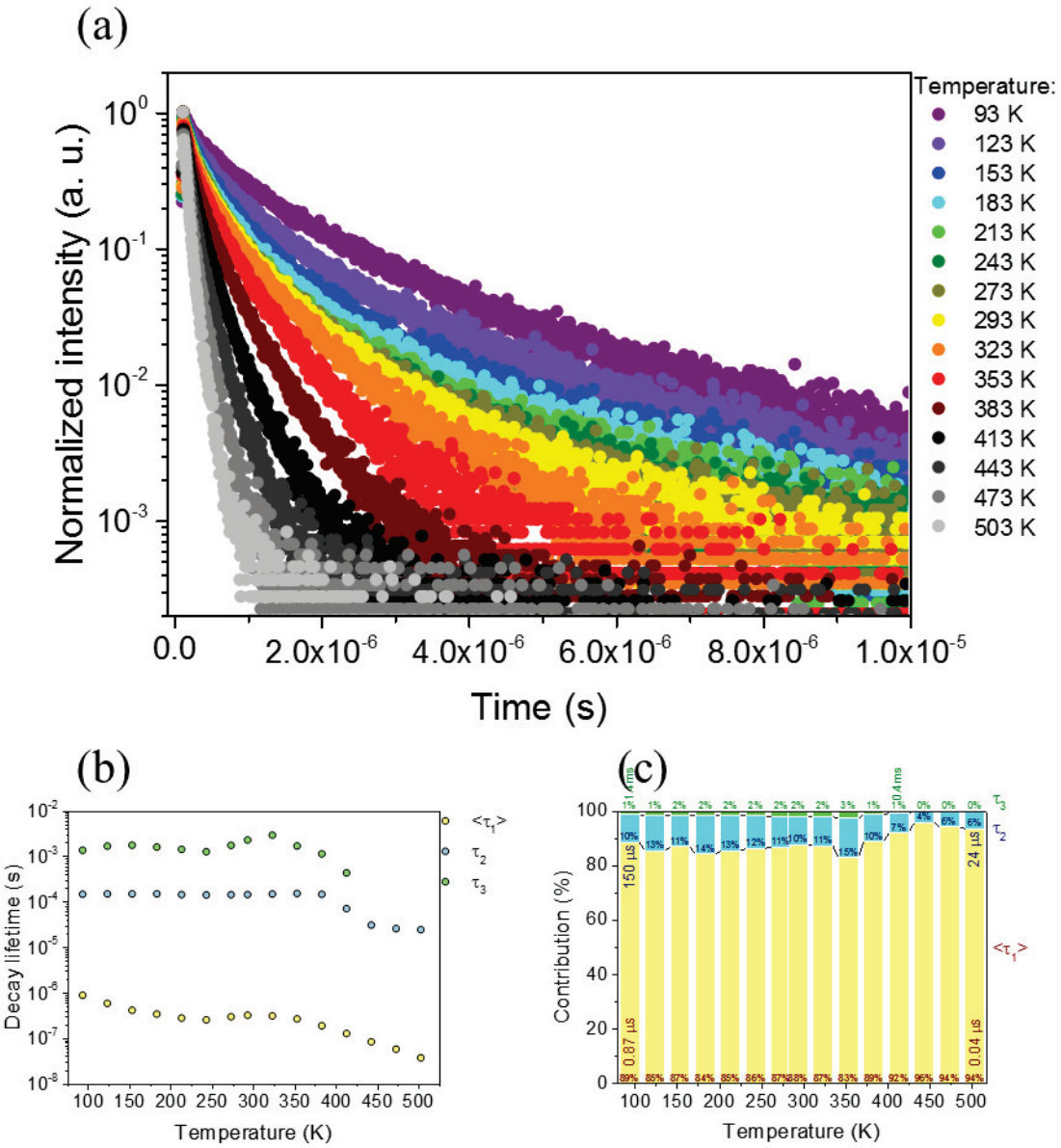

Figure 3. 18 Temperature-dependent luminescence decays (λ_{exc} = 352 nm, λ_{em} = 610 nm) of [Au(*m*-SPhCO$_2$H)]$_n$ (a). Values of the lifetime decays (b) and of contributions of different components (c) at various temperatures.

The Au-Au intrachain distances are shorter in *meta*-compound than in its *para*-counterpart: 3.20(2) and 3.28(2) Å vs. 3.59(1) and 3.72(1) Å. Normally, shorter Au-Au distances mean stronger interactions. This results in the lowering of the transition energy and consequently in the red shift of the emission.[15,18] However, it is not the case: [Au(*m*-SPhCO$_2$H)]$_n$

emission is centered at 615 nm, whereas [Au(*p*-SPhCO$_2$H)]$_n$ emission is centered at 665 nm (LE peak with LMCT origin) at the room temperature.

The interchain Au-Au distances of two compounds are comparable: 3.36(1) Å for [Au(*p*-SPhCO$_2$H)]$_n$ and 3.39(2) Å for [Au(*m*-SPhCO$_2$H)]$_n$. Thus, they cannot be responsible for the difference of properties.

The difference of properties, finally, might be explained by the change of substituent position on the phenyl ring and stronger effect of EWG –CO$_2$H in *meta*-position. EWG groups on the ligand stabilize the sulfur orbital. It makes the ligand more difficult to oxidize. This shifts the emission to higher energies.[15,19]

Unfortunately, without DFT calculations for [Au(*m*-SPhCO$_2$H)]$_n$, it is difficult to come up with unambiguous conclusion about the factors that direct properties in a way different from those of [Au(*p*-SPhCO$_2$H)]$_n$. So far, we can only speculate about the true reason behind the difference. Nevertheless, it is possible that we observe complex interplay between different factors. Either those, which we have already mentioned or even some other factors that were not covered in the chapter.

3.5 Conclusions

Three coordination polymers with *m*-$HSPhCO_2H$ were synthesized. For Cu- and Au-based compounds crystalline structures were successfully determined. The emission-excitation spectra and lifetime measurements at various temperatures let us conduct investigation of photophysical properties and tentatively assign the origin of their luminescence.

In the Chapter 2, we have seen that structural resemblance can be a reason to expect similar photophysical properties for a given couple of CPs ($[Ag(p\text{-}SPhCO_2H)]_n$ and $[Ag(p\text{-}SPhCO_2Me)]_n$ or $[Cu(p\text{-}SPhCO_2H)]_n$).

However, this chapter showed that such supposition is an oversimplification and should be used with precautions. The comparison of $[Cu(p\text{-}SPhCO_2Me)]_n$ and $[Cu(m\text{-}SPhCO_2H)]_n$ or $[Au(p\text{-}SPhCO_2H)]_n$, $[Au(p\text{-}SPhCO_2Me)]_n$ and $[Au(m\text{-}SPhCO_2H)]_n$ shows how difficult it is to unambiguously pinpoint structural parameter(s) responsible for the origin of certain properties. Weak interactions (hydrogen bond, π-π and/or metallophilic contacts), bond length and electronic effect of substituent should be investigated further.

$[Cu(m\text{-}SPhCO_2H)]_n$ is very weakly emissive even at low temperature, therefore, it presents few interest for its photophysical performance. Nevertheless, its structural similarity to $[Cu(p\text{-}SPhOH)]_n$ in combination with high reported conductivity of the$[Cu(p\text{-}SPhOH)]_n$ motivates future conductivity measurements for $[Cu(m\text{-}SPhCO_2H)]_n$.

$[Ag(m\text{-}SPhCO_2H)]_n$ is weakly emissive at the room temperature. Its emission intensity is not sufficient to consider it as a candidate for some real world application. Yet, we hope that its crystallographic structure will be elucidated and will eventually contribute to the understanding of the origin of luminescence in coinage metal (I)-thiolate CPs.

$[Au(m\text{-}SPhCO_2H)]_n$ is literally and figuratively a bright example of coinage metal (I)-thiolate based CP. The luminescent mechanism was identified through the comparison with $[Au(p\text{-}SPhCO_2Me)]_n$. High quantum yield of both makes them potentially interesting for application such as illumination. Nevertheless, the reason for difference of photophysical properties of $[Au(m\text{-}SPhCO_2H)]_n$ and $[Au(p\text{-}SPhCO_2H)]_n$ is yet to be understood.

3.6 Experimental Part

3.6.1 Synthesis

Synthesis of [Cu(*m*-SPhCO$_2$H)]$_n$: 1 mL of 0.1 M HCl was added to 5 mL of aqueous solution of $CuCl_2 \cdot 2H_2O$ (75 mg, 0.44 mmol, 1 eq.) followed by the addition of a solution of *m*-HSPhCO$_2$H (192 mg, 1.25 mmol, 2.8 eq.) in DMF (5 mL). The reaction was let to proceed for 18 h at 120°C in a 20 mL sealed vial. Yellow tiny pellet-like crystals were obtained and washed by 40 mL of ethanol for 3 times. The crystals were recovered by centrifugation at 4000 rpm. The product was dried in air. Yield: 85 % (84 mg). Chemical Formula: $C_7H_5CuO_2S$. Molecular Weight: 216.72. CuO content from TGA (calc.) wt%: 36.9 (36.7).

Synthesis of [Ag(*m*-SPhCO$_2$H)]$_n$: a solution of $AgNO_3$ (100 mg, 0.59 mmol, 1 eq.) in H_2O (10 mL) was added to *m*-HSPhCO$_2$H (91 mg, 0.59 mmol, 1 eq.). The reaction was let to proceed for 18 h at 120°C in a 20 mL sealed vial. White precipitate was obtained and washed by 40 mL of ethanol for 3 times. The powder was collected by centrifugation at 4000 rpm. The product was dried in air. Yield: 54 % (83 mg). Chemical Formula: $C_7H_5AgO_2S$. Molecular Weight: 261.05. Silver content from TGA (calc.) wt%: 42.2 (41.3).

Synthesis of [Au(*m*-SPhCO$_2$H)]$_n$: a solution of $HAuCl_4 \cdot 3H_2O$ (100 mg, 0.25 mmol, 1 eq.) in H_2O (10 mL) was added to *m*-HSPhCO$_2$H (178 mg, 1.15 mmol, 4.6 eq.). The reaction was let to proceed for 18 h at 120°C in a 20 mL sealed vial. White precipitate was obtained and washed with 40 mL of ethanol for 3 times. The powder was collected by centrifugation at 4000 rpm. The product was dried in air. Yield: 77 % (68 mg). Chemical Formula: $C_7H_5AuO_2S$, Molecular Weight: 350.14. Gold content from TGA (calc.) wt%: 56.4 (56.3).

3.6.2 Single Crystal Structure Determination of [Cu(*m*-SPhCO$_2$H)]$_n$

Single-crystal X-ray data of [Cu(*m*-SPhCO$_2$H)]$_n$ was collected at the CRISTAL beamline at Synchroton Soleil, using a set-up adapted for small crystals at 100.0 (1) K on a four-circle diffractometer equipped with an Atlas CCD detector. Data reduction was performed using CrysAlisPro. [20] An empirical absorption correction [21, 22] was applied using spherical harmonics on the basis of multiple scans of equivalent reflections, implemented in SCALE3 ABSPACK scaling algorithm. The structure was determined by direct methods using the SIR97 program[23] combined with Fourier difference syntheses and refined against F using all reflections by using

the CRYSTALS program.[24] All atomic displacement parameters for non-hydrogen atoms were refined with anisotropic terms. Hydrogen atoms were theoretically located on the basis of the conformation of the supporting atom or taking account the presence of potential hydrogen bonds. Hydrogen atoms have then been refined by using the riding model. CCDC-1906390 contains the supplementary crystallographic data.

X-ray crystallographic data and refinement details are summarized in**Table 3. 3**.

3.6.3 PXRD Structural Determination of $[Au(m\text{-}SPhCO_2H)]_n$

The structural determination of $[Au(m\text{-}SPhCO_2H)]_n$ was carried out from high resolution X-ray powder diffraction data. They were collected at the CRISTAL beamline at Soleil Synchrotron (Gif-sur-Yvette, France). A monochromatic beam was extracted from the U20 undulator beam by means of a Si(111) double monochromator. Its wavelength of 0.79276 Å was refined from a LaB_6 (NIST Standard Reference Material 660a) powder diagram recorded prior to the experiment. The X-ray beam was attenuated in order to limit radiation damage of the sample. High angular resolution was obtained with, in the diffracted beam, a 21 perfect crystal Si(111) multi-analyzer. The sample was loaded in a 0.7 mm capillary (Borokapillaren, GLAS, Schönwalde, Germany) mounted on a spinner rotating at about 5 Hz to improve the particles' statistics. Diffraction data were collected in continuous scanning mode and the diffractogram was obtained from the precise superposition and addition of the 21 channels data.

All calculations of structural investigation were performed using the TOPAS program.[25] The LSI-indexing method converged unambiguously to a triclinic unit cell. Structural investigation of $[Au(m\text{-}SPhCO_2H)]_n$ was initialized by using the charge flipping method, which allowed location of gold atoms. The direct space strategy was then used to complete the structural models and organic moieties have been added to the fixed gold atomic coordinates and treated as rigid bodies in the simulated annealing process. The final Rietveld plot corresponds to satisfactory model indicator and profile factors (**Figure 3. 19**, **Table 3. 3**).

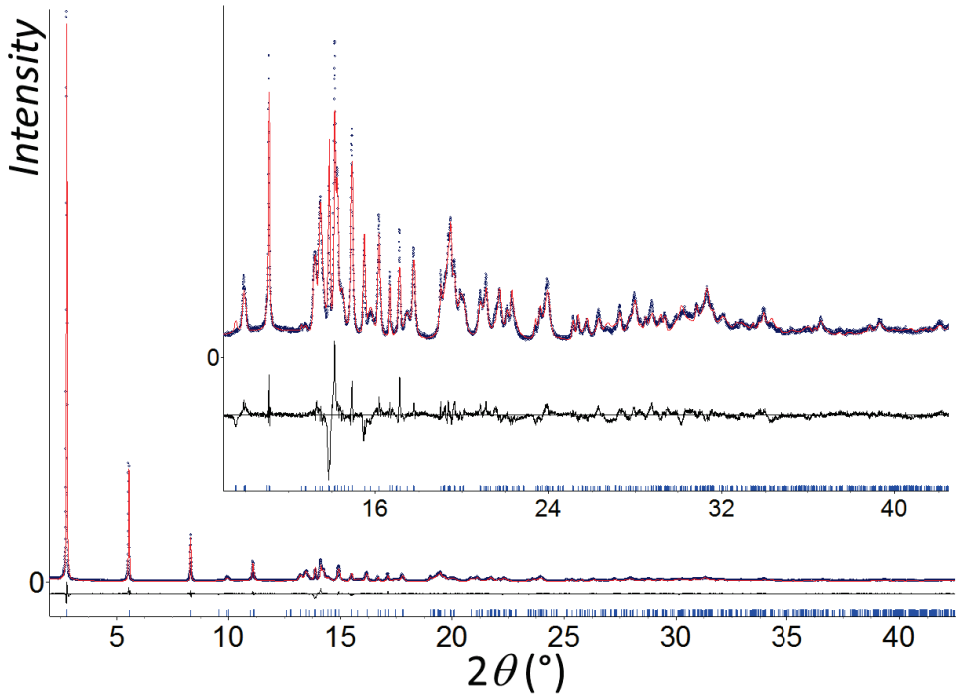

Figure 3. 19 Final Rietveld plot of $[Au(m\text{-}SPhCO_2H)]_n$ showing observed (blue circles), calculated (red line), and difference (black line) curves. A zoom at high angles is shown as inset.

Table 3. 3 Crystallographic data for $[Au(m\text{-}SPhCO_2H)]_n$ and $[Cu(m\text{-}SPhCO_2H)]_n$.

	$[Au(m\text{-}SPhCO_2H)]_n$	$[Cu(m\text{-}SPhCO_2H)]_n$
Empirical formula	$C_7H_5Au_1O_2S_1$	$C_7H_5Cu_1O_2S_1$
M_r	350.15	216.73
Crystal system	Triclinic	Monoclinic
Space group	*P*1	$P\ 2_1/n$
a (Å)	4.7568(6)	3.9047(2)
b (Å)	4.7635(6)	30.438(3)
c (Å)	16.3971(6)	5.6182(4)
α (°)	90.775(8)	90.0
β (°)	89.128(6)	91.933(4)
γ (°)	92.658(4)	90.0
V (Å^3)	371.07(7)	667.35(8)
Z	2	4
λ (Å)	0.79276	0.67173
Number of reflections	618	2574
Parameters	27[′]	105
$R[F^2 > 2\sigma(F^2)]$	0.063	0.1001
$wR(F^2)$	0.092	0.1324
GoF	1.72	0.9993
R_{Bragg}	0.018	-

[′]Number of structural parameters

3.7 References

1. E. R. T. Tiekink and W. Henderson, *Coord. Chem. Rev.*, 2017, **341**, 19-52.
2. D. R. Smyth, B. R. Vincent and R. T. Tiekink Edward, *Z. Kristallogr. Cryst. Mater.*, 2001, **216**, 298-302.
3. Y.-J. Lin, P.-C. Chen, Z. Yuan, J.-Y. Ma and H.-T. Chang, *ChemComm*, 2015, **51**, 11983-11986.
4. Z. Luo, V. Nachammai, B. Zhang, N. Yan, D. T. Leong, D.-e. Jiang and J. Xie, *J. Am. Chem. Soc.*, 2014, **136**, 10577-10580.
5. T.-R. Tero, S. Malola, B. Koncz, E. Pohjolainen, S. Lautala, S. Mustalahti, P. Permi, G. Groenhof, M. Pettersson and H. Häkkinen, *ACS Nano*, 2017, **11**, 11872-11879.
6. M. Azubel and R. D. Kornberg, *Nano Letters*, 2016, **16**, 3348-3351.
7. K.-H. Low, V. A. L. Roy, S. S.-Y. Chui, S. L.-F. Chan and C.-M. Che, *ChemComm*, 2010, **46**, 7328-7330.
8. O. Veselska and A. Demessence, *Coord. Chem. Rev.*, 2018, **355**, 240-270.
9. A. Bondi, *J. Phys. Chem.*, 1964, **68**, 441-451.
10. J. S. Lim, H. Choi, I. S. Lim, S. B. Park, Y. S. Lee and S. K. Kim, *J. Phys. Chem. A*, 2009, **113**, 10410-10416.
11. D. Sun, D.-F. Wang, F.-J. Liu, H.-J. Hao, N. Zhang, R.-B. Huang and L.-S. Zheng, *CrystEngComm*, 2011, **13**, 2833-2836.
12. C.-H. Li, S. C. F. Kui, I. H. T. Sham, S. S.-Y. Chui and C.-M. Che, *Eur. J. Inorg. Chem.*, 2008, **2008**, 2421-2428.
13. R. Langer, M. Yadav, B. Weinert, D. Fenske and O. Fuhr, *Eur. J. Inorg. Chem.*, 2013, **2013**, 3623-3631.
14. E. C.-C. Cheng, W.-Y. Lo, T. K.-M. Lee, N. Zhu and V. W.-W. Yam, *Inorg. Chem.*, 2014, **53**, 3854-3863.
15. J. M. Forward, D. Bohmann, J. P. Fackler and R. J. Staples, *Inorg. Chem.*, 1995, **34**, 6330-6336.
16. F. M. Monzittu, V. Fernández-Moreira, V. Lippolis, M. Arca, A. Laguna and M. C. Gimeno, *Dalton Trans.*, 2014, **43**, 6212-6220.
17. C. Lavenn, N. Guillou, M. Monge, D. Podbevšek, G. Ledoux, A. Fateeva and A. Demessence, *ChemComm*, 2016, **52**, 9063-9066.
18. A. Vogler and H. Kunkely, *Chem. Phys. Lett.*, 1988, **150**, 135-137.
19. G. L. Geoffroy and M. S. Wrighton, *Organometallic Photochemistry*, Academic Press: New York, 1979.
20. CrysAlisPRO Software system Version 1.171.38.41, *Rigaku Oxford Diffraction*, 2015.
21. J. de Meulenaer and H. Tompa, *Acta Crystallogr.*, 1965, **19**, 1014-1018.
22. R. Blessing, *Acta Crystallogr. A*, 1995, **51**, 33-38.
23. A. Altomare, M. C. Burla, M. Camalli, G. L. Cascarano, C. Giacovazzo, A. Guagliardi, A. Grazia, G. Moliterni, G. Polidori and R. Spagna, *J. Appl. Crystallogr.*, 1999, **32**, 115-119.

24. P. W. Betteridge, J. R. Carruthers, R. I. Cooper, K. Prout and D. J. Watkin, *J. Appl. Crystallogr.*, 2003, **36**, 1487.
25. *Topas V4.2: General Profile and Structure Analysis Software for Powder Diffraction Data, Bruker AXS Ltd, 2008.*

Chapter 4: $[M(o\text{-}SPhCO_2H)]_n$

4.1 Introduction

In Chapter 4, synthesis, structure, characterization and photophysical properties of *o*-$HSPhCO_2H$-based CPs are discussed. A great number of coordination compounds based on *o*-$HSPhCO_2H$ (also called thiosalicylic acid) and coinage metals (I) is known.[1] Here, we will briefly mention some of them.

Considering the ability of copper(II) to get reduced by thiolate species to copper(I) and disulfide, it could be expected that the copper thiosalicylates would presented mainly by the copper(I) compounds. However, a majority of reported compounds is based on copper(II).[1]

The mixed-valence copper(I)–copper(II) complex $[Cu(PPh_3)_2]_2[Cu(o\text{-}SPhCO_2)_2]$ has been reported. The copper(I)-based complex $[Cu(o\text{-}SPhCO_2H)(PPh_3)_3]$ was formed as an intermediate in its synthesis and has been structurally characterized. The complex has a distorted tetrahedral geometry with an S-bonded thiosalicylate ligand.[2]

Some mononuclear complexes of silver(I) thiosalicylate have been reported. Nevertheless, considering the ability of silver(I) to show coordination numbers of 2, 3 and 4 and ability of sulfur to coordinate to 2 or 3 silver ions, extensive aggregation processes are expected.[1] Indeed, number of polynuclear complexes is reported as well. Among mononuclear complexes are $[Ag(o\text{-}SPhCO_2H)(PPh_3)_3]$[3] and carborane-derived phosphine complex $[Ag(o\text{-}SPhCO_2H)(1,2\text{-}(PCy_2)_2\text{-}1,2\text{-}C_2B_{10}H_{10})_2]$.[4] They show tetrahedral and trigonal coordination sphere of silver atoms, respectively. Group of polynuclear species includes tetranuclear propeller-like cluster (with three "leaves") $[Ag(o\text{-}SPhCO_2H)(PPh_3)]_4$[5] and octanuclear aggregate $K_{12}[Ag_8(o\text{-}SPhCO_2H)_{10}]\cdot 12H_2O$ composed of two butterfly-type Ag_4S_4 subunits.[6]

A nonanuclear $[Ag_9(o\text{-}SPhCO_2)_9]^{9-}$ cluster with a triangular prism Ag_9-aggregate in the core has been reported (**Figure 4. 1** (a)).[7] It possesses both silver atoms of four-coordinated tetrahedral and two-coordinated linear geometries. The Ag-Ag contacts are in the range of 2.885(2)–3.307(1) Å, revealing possible existence of argentophilic interactions. In addition, four 3d-4d heterometallic coordination complexes were synthesized : a 1D Ag(I)–Cu(II) heterometallic coordination polymer $\{(NH_4)[Cu_4(eda)_8][Ag_9(o\text{-}SPhCO_2H)_9]\cdot 3H_2O\}$ and three

isolated Ag(I)–Zn(II) heterometallic clusters $\{(NH_4)_2(H_2eda)0.5[Zn_3(eda)_6][Ag_9(o\text{-}SPhCO_2H)_9]\cdot 7H_2O\}$, $\{[Zn_{4.5}(deta)_5][Ag_9(o\text{-}SPhCO_2H)_9]\cdot H_2O\}$ and $\{(NH_4)[Zn_3(pda)_2(Hpda)_2][Ag_9(o\text{-}SPhCO_2H)_9]\cdot 4H_2O\}$ (eda – ethylenediamine, deta – diethylenetriamine, pda – 1, 3–propanediamine). All complexes have HE absorption bands at *cca.* 300 nm, ascribed to the intraligand $\pi \rightarrow \pi^*$ transitions of the (o-$SPhCO_2H$)-moiety. For Zn(II)-based complexes, the low-energy bands (> 400 nm) are assigned to electronic transition from σ(Ag–S) orbital to an empty π* antibonding orbital located at the phenyl group of the thiosalicylate ligand. Moreover, Zn(II)-based complexes show solid state room temperature photoluminescence with maxima of emission bands of 579 nm, 585 nm and 562 nm. They were attributed to LMCT excited states which are probably mixed with a cluster-based MC (4d–5s/5p) excited state modified by metallophilic interactions.[7]

Another luminescent anionic cluster – of even higher nuclearity, $(NH_4)_{17}[(\mu_6\text{-}S)@Ag_{17}(o\text{-}SPhCO_2H)_{16}]\cdot 22H_2O$, has been synthesized thanks to reaction in ultrasonic conditions (**Figure 4. 1** (b)).[8] Silver(I) atoms show linear, trigonal-planar and tetrahedral coordination geometries and the presence of metallophilic interactions are observed. Similarly to aforementioned Zn(II)-heteronuclear complexes, this one shows a high-energy absorption band and a weak low-energy band, which have been assigned similarly. It exhibits a solid state room temperature photoluminescence in the same spectral range (maximum at 577 nm) with the same luminescence origin.

Some extended networks based on silver(I)-thiosalicylates have been also reported. For example, $[Ag_4(o\text{-}SPhCO_2)_2(eda)]_n$ forms an infinite monodimensional cylinder (**Figure 4. 1** (c)).[9] Silver(I) atoms are in tri- and tetrahedral coordination environment and connected to each other via metallophilic interactions. In that case, the silver atoms are coordinated through both thiolate and carboxylate groups. Interchain hydrogen bonds are present, forming 2D sheet which gives rise to a 3D supramolecular framework.

A lamellar structure of $[Ag_4(o\text{-}SPhCO_2)_2(H_2O)_2]_n$ has been reported (**Figure 4. 1** (d)).[10] Silver atoms are coordinated by both, the thiolate and the carboxylate groups. They adopt tri- or tetrahedral coordination environments. The compound shows absorption in the 200-400 nm range and a blue emission (λ_{em} = 468 nm) when excited by UV-radiation (in solid state at room temperature). It is assigned to LMCT. The compound has also semiconductive properties at room temperature (with a conductivity value of $3.24\cdot 10^{-5}$ Scm^{-1}).

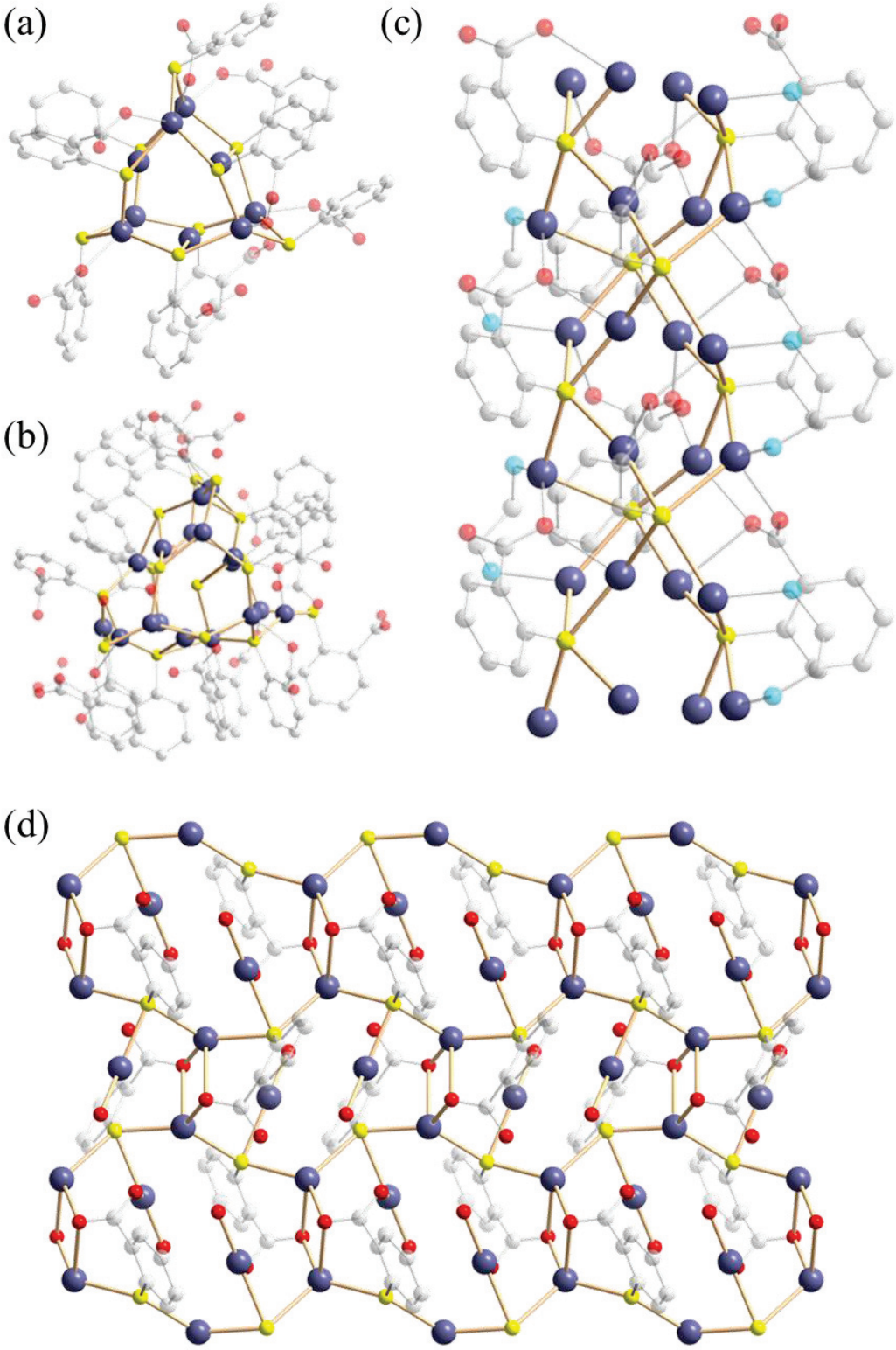

Figure 4. 1 Structure representations of (a) $[Ag_9(o\text{-}SPhCO_2)_9]^{9-}$ cluster from $\{[Zn_{4.5}(deta)_5][Ag_9(o\text{-}SPhCO_2H)_9]\cdot H_2O\}$;[7] (b) $[(\mu_6\text{-}S)@Ag_{17}(o\text{-}SPhCO_2H)_{16}]^{17-}$;[8] (c) $[Ag_4(o\text{-}SPhCO_2)_2(eda)]_n$[9] and (d) $[Ag_4(o\text{-}SPhCO_2)_2(H_2O)_2]_n$[10]. Blue, Ag; violet, P; yellow, S; red, O; grey, C; sky-blue, N; white, H. Hydrogen atoms are omitted for clarity.

There is a report on a polymeric orange product $[Ag(o\text{-}SPhCO_2H)]_n$. Its crystalline structure was not yet determined.[11] This CP could be converted to the form of salt, $\{Na[Ag(o\text{-}SPhCO_2H)\cdot H_2O]\}_n$, with n = 12-14, if one adds NaOH. Afterwards, it is possible to convert it back to the original CP by adding the acid solution. It was suggested, that the structure of $[Ag(o\text{-}SPhCO_2H)]_n$, resembles to the gold(I) thiomalate (Myocrisin),[12] composed by two interpenetrated chains. Both $[Ag(o\text{-}SPhCO_2H)]_n$ and its salt form showed antimicrobial activities for bacteria, yeast and mold.

Supramolecular structural chemistry of gold(I) thiosalicylate complexes has attracted considerable attention, due to the competition between aurophilic and hydrogen bonding interactions.[1] Numerous gold(I) thiosalicylate complexes, $R_3PAu(o\text{-}SPhCO_2H)$, with monodentate phosphines have been synthesized. Complexes with the following phosphines have been reported: PPh_3,[3] four different polymorphs with PCy_3,[13,14] and tri-*o*-tolyphosphine.[15] The last one shows an emission in the solid state at 78 K with its maximum at 576 nm and an additional long-tailed band at the low-energy side. Post-Hartree-Fock calculations were performed showing LMCT origin of the emission.[15] Among other reported complexes there are some with bidentate phosphines: bis(diphenylphosphine)ferrocene[16] and bis(diphenylphosphine)ethylene,[17] isonitrile linkers: $RNCAu(o\text{-}SPhCO_2H)$ (R =*t*Bu, mesityl)[18] as well as $[(Ph_3PAu)_2(o\text{-}SPhCO_2H)]BF_4$. [19] Gold(I) thiosalicylate complexes have been also used to generate supramolecular liquid-crystalline aggregates through hydrogen bonding interactions with 2,4,6-triaryl-1,3,5-triazine.[20]

Crystalline and amorphous polymeric products of $[Au(o\text{-}SPhCO_2H)]_n$ were reported. The amorphous product is not luminescent, while the crystalline is. It emits at 470 nm and 690 nm when excitated by radiation with wavelength of 350 nm. The emission was suggested to be due to MC triplet states.[21] Unfortunately, the structure was not determined. The salt form of a given coordination polymer ($[\{Ag(o\text{-}SPhCO_2Na)]\cdot H_2O\}_n$) was reported as well.[22] However, its structure was not elucidated either.

A vast variety of thiosalicylates of coinage metals has been reported, including some neutral polymeric networks $[M(o\text{-}SPhCO_2H)]_n$. However, structural studies for the latter ones, as well as in-depth photophysical analyses, are missing. Consequently, this chapter will be dedicated to their investigations.

4.2 Syntheses and structures

Three new thiosalicylate CPs have been obtained. Highly crystalline powders of compounds based on copper and silver were prepared in solvothermal conditions. For the gold-based compound, the use of solvothermal conditions did not improve its crystallinity, thus synthesis at room temperature was used. Their PXRD patterns are shown in the **Figure 4. 2**. The predominant (00*l*) reflections characteristic for the lamellar materials (see Chapter 2 and Chapter 3) are absent on PXRD patterns of $[M(o\text{-}SPhCO_2H)]_n$. The close positions of the first diffraction peaks (at 6.7°, 9.5°, 13.5° and 15.0°) suggest similarity of these three structures.

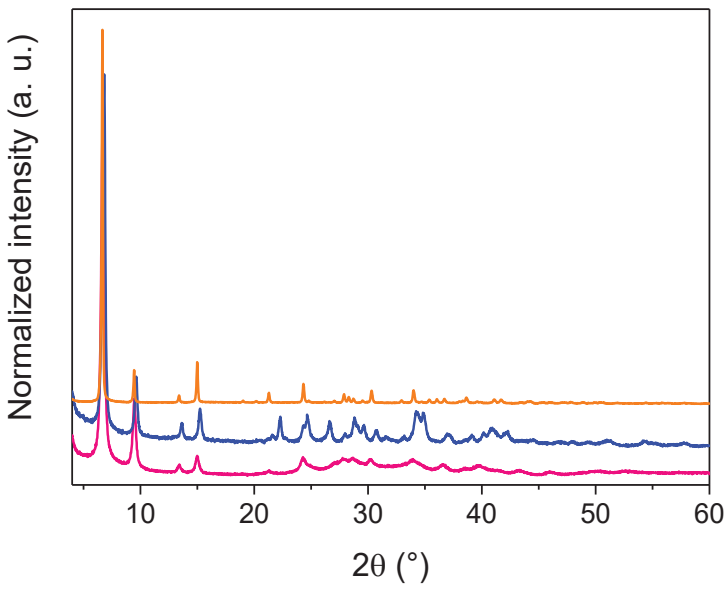

Figure 4. 2 The PXRD patterns of $[Cu(o\text{-}SPhCO_2H)]_n$ (orange line), $[Ag(o\text{-}SPhCO_2H)]_n$ (blue line)and $[Au(o\text{-}SPhCO_2H)]_n$ (pink line).

For all the three compounds, high resolution PXRD data were collected at the beamline ID15A of ESRF (Grenoble, France). From these data, the structural determinations of $[Cu(o\text{-}SPhCO_2H)]_n$ and $[Ag(o\text{-}SPhCO_2H)]_n$ were carried out. The structure determination of $[Au(o\text{-}SPhCO_2H)]_n$ was not possible from PXRD data, because of the poor crystallinity of the product. It is worth noting, that the positions of the first four most intense peaks coincide for all the three compounds, and overall PXRD patterns are highly resembling (**Figure 4. 2**). Therefore, the supposition about similarity of $[Au(o\text{-}SPhCO_2H)]_n$ to the silver and copper counterparts can be driven. In order to gain more information about the structure of $[Au(o\text{-}SPhCO_2H)]_n$, the pair distribution function (PDF) study was performed.

4.2.1 [Cu(*o*-SPhCO$_2$H)]$_n$ Structure

The structure determination gives a tetragonal space group – $P\,4_2/n$ with a = 18.5912(9) Å, c = 3.9622(2) Å. The space group and the structure are closely related to the previously reported 1D CPs, in particular – [Cu(SPh)]$_n$.[23] The monodimensional columns are made of aligned six-membered rings of Cu_3S_3. They are facing each other in an inverted position and they are connected through trigonal copper atoms and μ_3 bridging thiolates. The Cu-S distances and angles are summarized and compared with those of [Cu(SPh)]$_n$ in **Table 4. 1**, showing close resemblance of the two structures. The neighboring columns are connected through dimeric hydrogen bonds between the carboxylic acid groups (**Figure 4. 3**).

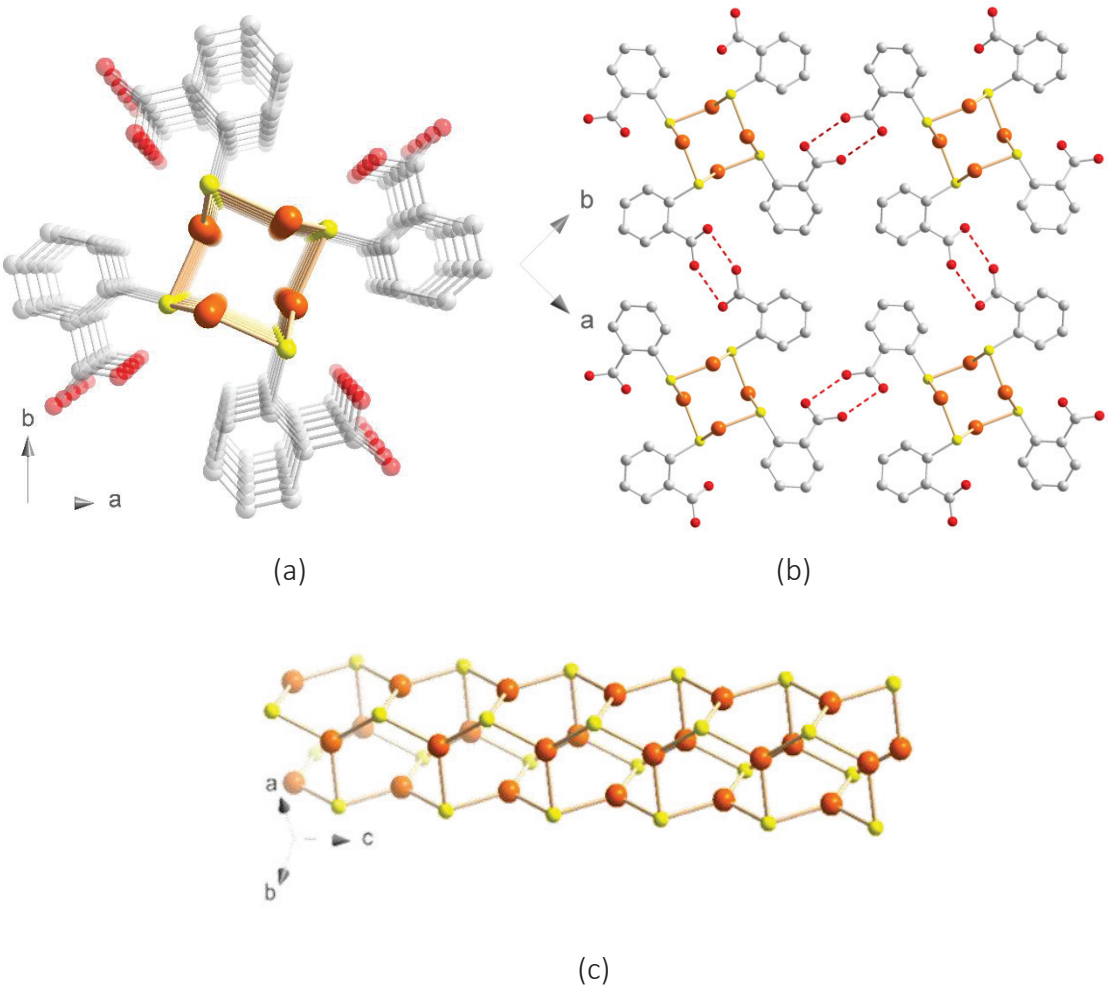

Figure 4. 3 Structure representations of [Cu(*o*-SPhCO$_2$H)]$_n$. (a) Central projection along the *c* axis. (b) View along the *c* axis representing hydrogen bonds network (c) View of the [CuS]$_n$ arrangement. Red dashed lines represent hydrogen bonding. Orange, Cu; yellow, S; red, O; grey, C. Hydrogen atoms are omitted for clarity.

Table 4. 1 Comparison of the main distances and angles in $[Cu(o\text{-}SPhCO_2H)]_n$ and $[Cu(SPh)]_n$.

Compound	Cu-S, Å	Cu-Cu, Å	S-Cu-S, °	Cu-S-Cu, °	Dihedral angle in Cu_3S_3, °	π-π, Å
$[Cu(o\text{-}SPhCO_2H)]_n$	2.261(5) 2.285(5) 2.400(5)	3.048(4)† 3.276(5) 3.962(3)†	117.4(2) 118.3(2) 121.3(2)	81.1(2) 81.6(2) 121.3(2)	74.7(3)	3.96(2)
$[Cu(SPh)]_n$	2.270(2) 2.298(2) 2.303(2)	2.965(3)† 3.437(3)† 3.593(5) 3.268(3)†	112.9(1) 113.6(1) 133.5(1)	80.0(1) 97.6(1) 113.6(1)	88.5(23)	3.827(2)

†bridged by sulfur atoms.

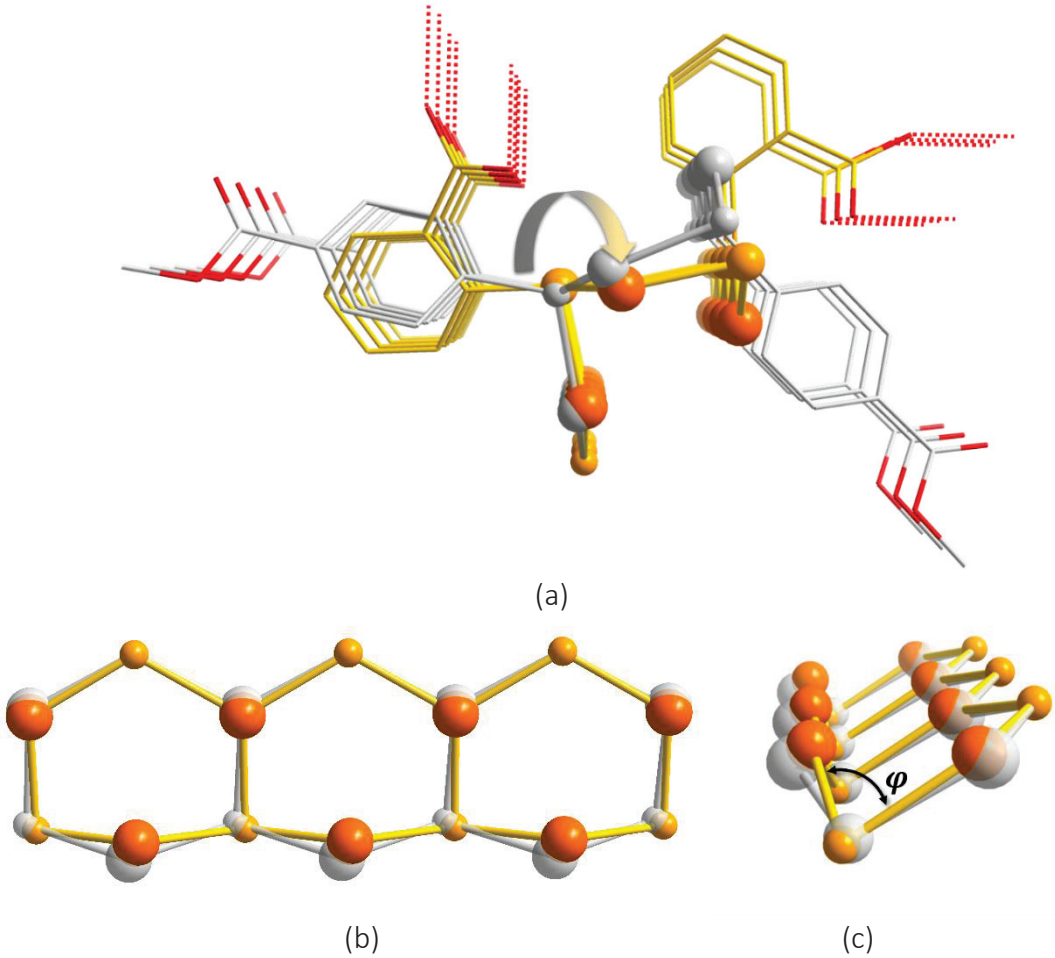

Figure 4. 4 Superimposed images of the compound **1** $[Cu(p\text{-}SPhCO_2Me)]_n$ (in gray) and $[Cu(o\text{-}SPhCO_2H)]_n$ (in orange) showing the bend direction of $[CuS]_n$ array (a) and fused Cu_3S_3 rings (b,c); on (c) dihedral angle φ is shown. Red dashed lines represent hydrogen bonding.

It is interesting to find the same fused Cu_3S_3 entities in both 1D and 2D CPs. In $[Cu(p\text{-}SPhCO_2Me)]_n$ or $[Cu(p\text{-}SPhOH)]_n$, Cu_3S_3 rings are arranged into infinite undulated 2D-planes. In $[Cu(o\text{-}SPhCO_2H)]_n$, the steric hindrance (introduced close to the coordination site) prevents the propagation into a 2D-plane. It decreases the dihedral angle φ from 106.5(1)° to 74.7(3)° (**Figure 4. 4**) giving rise to the bent arrangement and it forms a 1D column.

4.2.2 $[Ag(o\text{-}SPhCO_2H)]_n$ Structure

Structure determination shows, that the silver-based compound is isostructural to the copper-based counterpart. Its structure is described by a tetragonal space group – $P\,4_2/n$ with a = 18.420(2) Å, c = 4.434(1) Å. Slight increase of the c parameter when Cu(I) is replaced by Ag(I) is given by difference in atomic radius of silver (for silver it is larger than for copper). Ag-S distances and angles are summarized in **Table 4. 2**. The structure is shown in the **Figure 4. 5**.

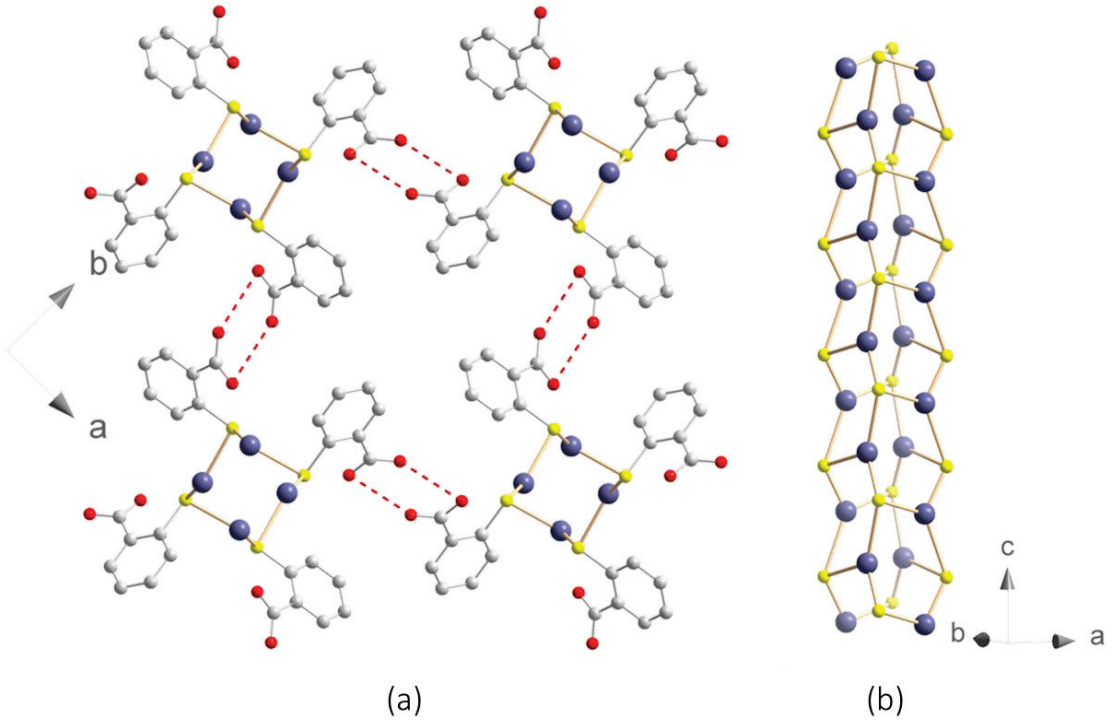

Figure 4. 5 Structure representations of $[Ag(o\text{-}SPhCO_2H)]_n$. (a) Central projection along the c axis. (b) View of the $[AgS]_n$ arrangement. Red dashed lines represent hydrogen bonding. Blue, Ag; yellow, S; red, O; grey, C. Hydrogen atoms are omitted for clarity.

Five neutral silver(I) thiolate CPs formed by chains ($[Ag(SPh\text{-}2,4,6\text{-}(iPr)_3)]_n$, [24] $[Ag(SAdamantane)]_n$, [25] $[Ag(SDiamantane)]_n$, [25] $[Ag(SCMeEt_2)]_n$ [26]) or columns ($[Ag(SCy)]_n$[27])

have been reported so far (see State of the Art **I.1.2**). However, it is the first time that this type of $[AgS]_n$ network with exclusively μ_3-S atoms is observed.

Table 4. 2 The main distances and angles in $[Ag(o\text{-}SPhCO_2H)]_n$.

Compound	Ag-S, Å	Ag-Ag, Å	S-Ag-S, °	Ag-S-Ag, °	Dihedral angle in Ag_3S_3, °	π-π, Å
$[Ag(o\text{-}SPhCO_2H)]_n$	2.486(8) 2.561(8) 2.641(7)	3.296(4)† 3.442(5) 4.434(3)†	114.8(3) 117.4(3) 122.9(3)	78.5(3) 79.8(2) 122.9(3)	70.2(3)	4.434(13)

†bridged by sulfur atoms.

4.2.3 $[Au(o\text{-}SPhCO_2H)]_n$ Structure

Poor crystallinity of the $[Au(o\text{-}SPhCO_2H)]_n$ precluded in-depth structural investigation using solely PXRD. However, the close positions of the first four most intense peaks of all the three $[M(o\text{-}SPhCO_2H)]_n$ compounds and the similar PXRD patterns, point out the proximity of $[Au(o\text{-}SPhCO_2H)]_n$ to the Cu and Ag CPs.

In order to gain more information about the structure of $[Au(o\text{-}SPhCO_2H)]_n$, the PDF study was performed. The comparison of the PDFs of the silver- and gold-based compound confirms the similarities of the structures[28] (**Figure 4. 6** (a)). Indeed, the peaks at 3.4 Å, 4.6 Å, 5.6 Å and 6.9 Å for $[Ag(o\text{-}SPhCO_2H)]_n$ and at 3.5 Å, 4.55 Å, 5.75 Å and 7.35 Å for $[Au(o\text{-}SPhCO_2H)]_n$ follow very close positioning pattern. This is also true for the peaks at larger distances. Nevertheless, the amplitude of oscillations for the Au compound is strongly damped due to the decrease of the structural coherence length. The same is observed for broad features centered at 17 Å, 30 Å, 43 Å, 58 Å and 70 Å corresponding to the distances between first-, second- and so follows neighboring $[MS]_n$ columns (**Figure 4. 6** (b)). Thus, the structure of $[Ag(o\text{-}SPhCO_2H)]_n$ (**Figure 4. 6** (c)) can be used as a starting model for the refinement of the structural model of $[Au(o\text{-}SPhCO_2H)]_n$.

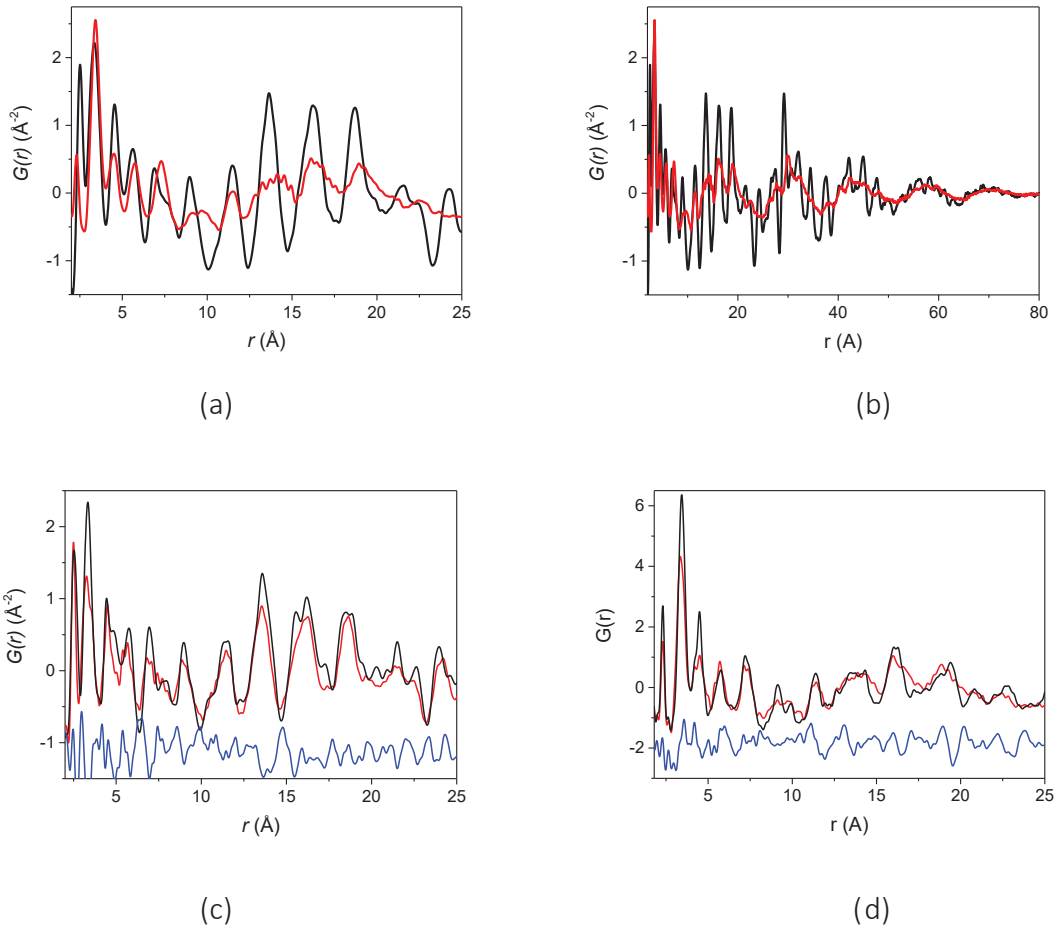

Figure 4. 6 Comparisons of the observed PDFs of $[Ag(o\text{-}SPhCO_2H)]_n$ (black) and $[Au(o\text{-}SPhCO_2H)]_n$ (red) (a) and (b); PDF refinements of $[Ag(o\text{-}SPhCO_2H)]_n$ (c) and $[Au(o\text{-}SPhCO_2H)]_n$ (d) showing observed (red line), calculated (black line), and difference (blue line) curves.

Silver atoms in $[Ag(o\text{-}SPhCO_2H)]_n$ were replaced by gold atoms. This model was used to refine the cell parameters and the positions of the heavy atoms (gold and sulfur) through the Rietveld method. One can find discrepancies in the Rietveld plot in comparison to the experimental data (**Figure 4. 21**, **Table 4. 4**). Nevertheless, the obtained structural model, including the $P\,4_2/n$ space group symmetry, was further used for the PDF refinement.

During MolPDF software processing,[29] the organic ligand was included in the structural model being fully constrained (*i.e.* considered as a rigid block molecule). Few information about the position of the phenyl ring compared to the Au(I)-S chains can be obtained with this method. There is a large difference in the atomic numbers between gold and sulfur atoms in comparison to carbon, oxygen and hydrogen atoms results in the PDF essentially originating from the gold and sulfur atoms. It makes a contribution of the carbon, oxygen and hydrogen

atoms to the PDF negligible. Obtained refinement shows a relatively good agreement in the range from 2 Å to 25 Å (**Figure 4. 6** (d)). Refined atomic positions showed that the Au(I)-S network is organized differently in comparison to the silver(I)-based compound. Indeed, each Au(I) atom is coordinated to two sulfur atoms and the thiolates are bridging two gold atoms. This coordination mode is well in agreement with common linear two-coordinated gold atom environment. This arrangement leads to the formation of a double interpenetrated helical chain similar to $[Au(SPh)]_n$ coordination polymer [12, 30] (**Figure 4. 7**). The intrachain contacts between neighbouring gold atoms are of 3.43(2) Å, while interchain contacts are of 3.64(1) Å. The comparison of PDF of $[Au(o\text{-}SPhCO_2H)]_n$ and $[Au(SPh)]_n$ confirms that Au-S arrangement is quasi-identical in both compounds (**Table 4. 3**, **Figure 4. 8**).

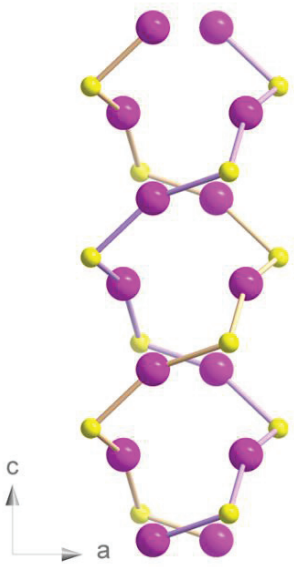

Figure 4. 7 Structural model of the $[Au(o\text{-}SPhCO_2H)]_n$ refined with PDF data: view of the double helices along the *b* axis; chains are represented in beige and purple colors. Pink and yellow spheres are gold and sulfur atoms, respectively. Organic ligands have been omitted for clarity.

Table 4. 3 Comparison of the main distances and angles in [Au(*o*-SPhCO$_2$H)]$_n$ (obtained by Rietveld and PDF refinement) and [Au(SPh)]$_n$.

Compound	Au-S, Å	Au-Au, Å	S-Au-S, °	Au-S-Au, °
[Au(*o*-SPhCO$_2$H)]$_n$ Rietveld	2.26(4) 2.31(4)	3.44(2) 3.64(1)	162(2)	98(2)
[Au(*o*-SPhCO$_2$H)]$_n$ PDF	2.29(1) 2.31(2)	3.43(2)† 3.64(1)	154.3(5)	96.4(4)
[Au(SPh)]$_n$	2.289(2) 2.332(2) 2.313(2) 2.345(2)	3.323(3)† 3.331(3) 3.369(3) 3.603(3) 3.610(3)†	171.57(9) 175.23(8)	91.36(7) 102.32(7)

† bridged by sulfur atoms.

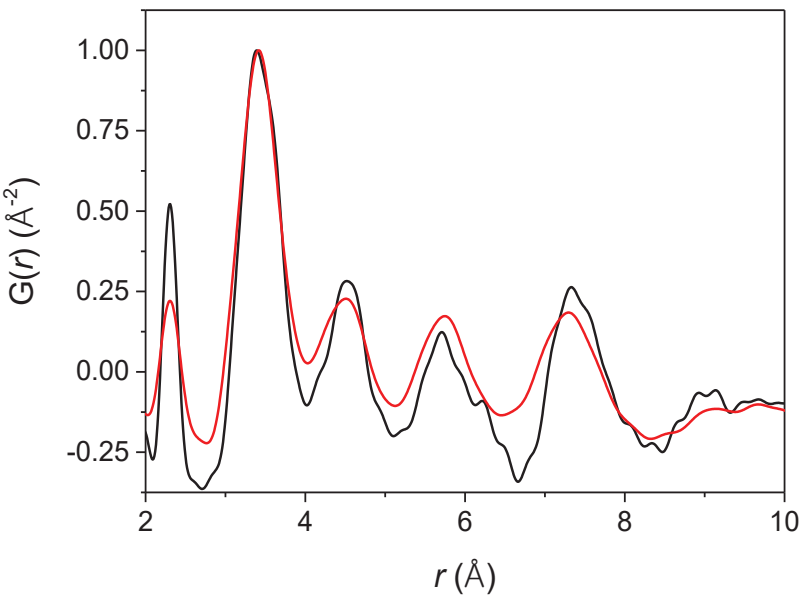

Figure 4. 8 Experimental PDF of [Au(*o*-SPhCO$_2$H)]$_n$ (red line) and [Au(SPh)]$_n$ (black line).

4.3 Characterization

From SEM images one can conclude that crystallites of the three CPs form 1D objects (**Figure 4. 9**): [Cu(*o*-SPhCO$_2$H)]$_n$ is composed of long needles with wide distribution in size (≈ 1-20 µm), [Ag(*o*-SPhCO$_2$H)]$_n$ is constituted of wires of diameter and length of 90 nm and 1 µm while [Au(*o*-SPhCO$_2$H)]$_n$ is composed of with long fibers of 250 nm in diameter.

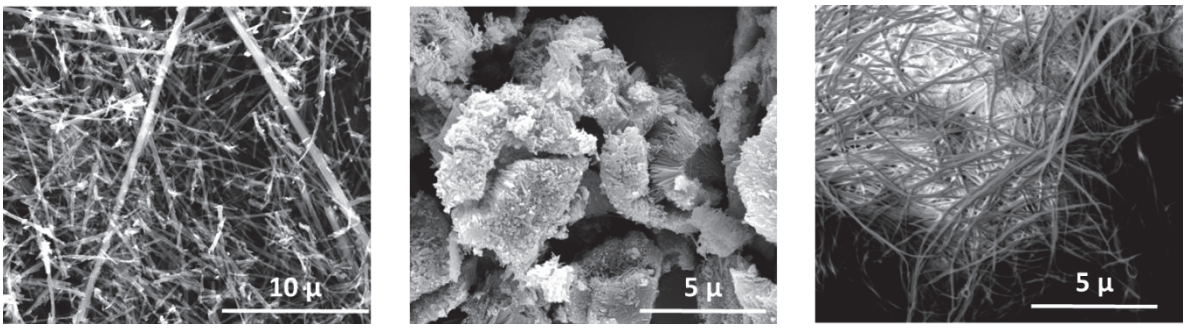

(a) (b) (c)

Figure 4. 9 SEM images of (a) $[Cu(o\text{-}SPhCO_2H)]_n$, (b) $[Ag(o\text{-}SPhCO_2H)]_n$ and (c) $[Au(o\text{-}SPhCO_2H)]_n$.

FT-IR spectroscopy (**Figure 4. 10**) showed existence of broad ν(OH) bands around 3000 and 2600 cm^{-1}. They are consistent with the presence of hydrogen bonds. Antisymmetric vibration of the carboxylic acid group band is observed at 1680 cm^{-1}. It is close to the free ligand and is in good accordance with non-coordinated acid group.

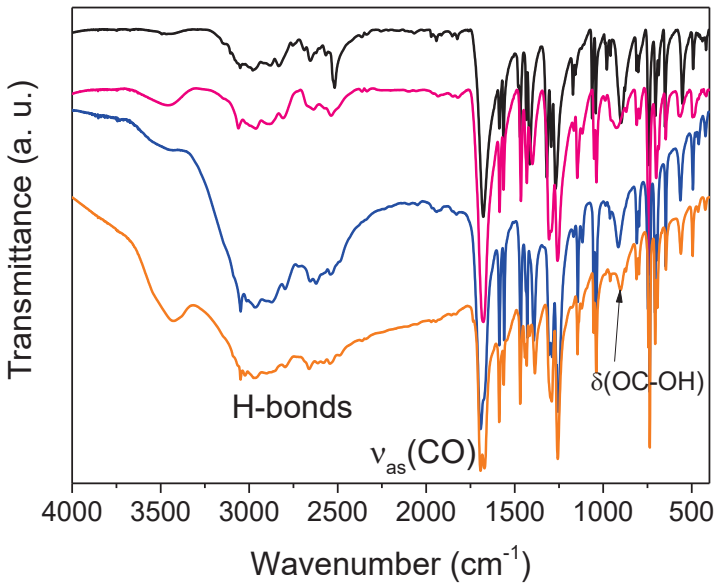

Figure 4. 10 FT-IR spectra of free ligand (black), $[Cu(o\text{-}SPhCO_2H)]_n$ (orange), $[Ag(o\text{-}SPhCO_2H)]_n$ (blue) and $[Au(o\text{-}SPhCO_2H)]_n$ (pink).

The thermo-gravimetric analysis confirms the purity of the compounds with an expected metal and organic content. We see an increase of thermal stability after the complexation of the metal in comparison to free ligand. All compounds show relatively good thermal stability (**Figure 4. 11**). The decomposition temperatures are 200°C, 260°C and 270°C for Cu(I)-, Ag(I)-

and Au(I)-based CPs, respectively. Thermal stability of $[Cu(o\text{-}SPhCO_2H)]_n$ is comparable to one of $[Cu(SPh)]_n$, while in the case of $[Au(o\text{-}SPhCO_2H)]_n$ it is higher than for $[Au(SPh)]_n$ (270°C vs. 200°C). It is due to the presence of hydrogen bonding which reinforces the structure.

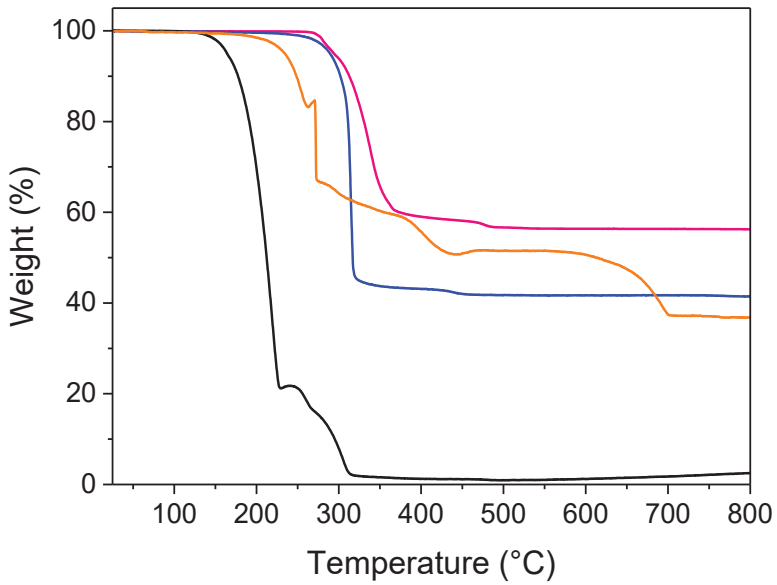

Figure 4. 11 The TGA performed under air at 10°C/min of free ligand (black), $[Cu(o\text{-}SPhCO_2H)]_n$ (orange), $[Ag(o\text{-}SPhCO_2H)]_n$ (blue) and $[Au(o\text{-}SPhCO_2H)]_n$ (pink).

Here, we successfully solved the structure of the product $[Ag(o\text{-}SPhCO_2H)]_n$ reported by K. Nomiya *et al.*.[11] It exhibits antimicrobial activities for bacteria, yeast and mold.[11]

4.4 Photophysical Properties

The compounds $[Cu(o\text{-}SPhCO_2H)]_n$ and $[Au(o\text{-}SPhCO_2H)]_n$ are pale yellow and pale beige powders. They exhibit high-energy absorption between λ_{abs} = 300-350 nm, which is assigned to π–π* transitions of the phenyl group of the ligand (**Figure 4. 12**).[31] The compound $[Cu(o\text{-}SPhCO_2H)]_n$ has also a less intense shoulder between 400-450 nm. It is presumably result of M→S MLCT [32,33,34,35] or LMCT transition modified by M···M contacts.[36] It gives a similar profile to the isostructural $[Cu(SPh)]_n$[23]. The compound $[Ag(o\text{-}SPhCO_2H)]_n$ shows a broad unstructured band between λ_{abs} = 300-450 nm, presumably as a result of an electronic transition from the σ(Ag–S) orbital to an empty π* antibonding orbital located at the phenyl group of the ligand.[7] It is in good accordance with its intense orange color.

The optical band gaps are 2.43 eV, 2.23 eV and 2.83 eV for Cu(I)-, Ag(I)- and Au(I)-based CPs (**Figure 4. 12**), respectively. Band gap of $[Cu(o\text{-}SPhCO_2H)]_n$ is comparable to another reported copper(I)-based 1D-MOCS (2.23-2.68 eV),[23] and the one of $[Au(o\text{-}SPhCO_2H)]_n$ is fairly close to the one of $[Au(SPh)]_n$ (2.8 eV). [30]

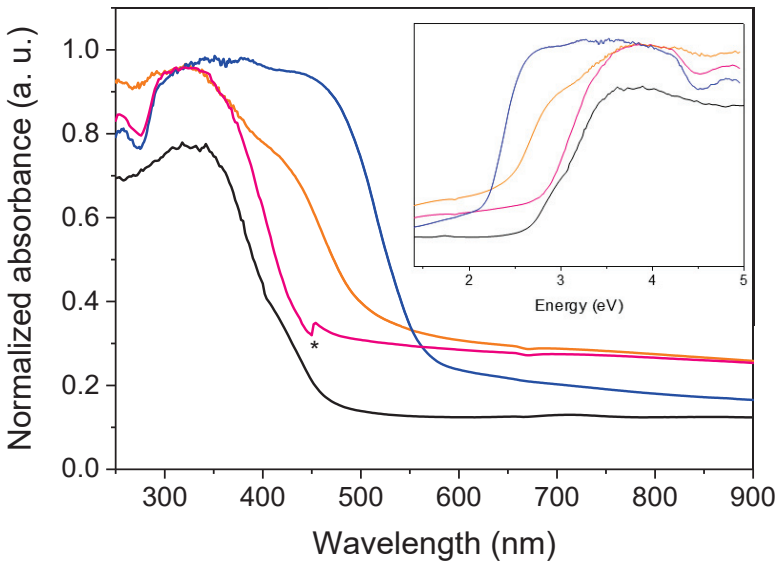

Figure 4. 12 UV-vis absorption spectra of $[Cu(o\text{-}SPhCO_2H)]_n$ (orange), $[Ag(o\text{-}SPhCO_2H)]_n$ (blue) and $[Au(p\text{-}SPhCO_2H)]_n$ (pink) obtained in solid state at the room temperature. UV-vis absorption spectra as function of energy are shown as inset. Asterisk marks an instrumental artefact.

Excitation of the compound $[Ag(o\text{-}SPhCO_2H)]_n$ (λ_{exc} = 379 nm) in solid state at room temperature results in intense orange emission. Compounds $[Cu(o\text{-}SPhCO_2H)]_n$ and $[Au(o\text{-}SPhCO_2H)]_n$ show weak dark red emission (**Figure 4. 13** (a)). The emission spectra have broad featureless profiles centered at 700 nm, 634 nm and 787 nm for $[Cu(o\text{-}SPhCO_2H)]_n$, $[Ag(o\text{-}SPhCO_2H)]_n$ and $[Au(o\text{-}SPhCO_2H)]_n$, respectively. Maxima of the excitation are centered at 412 nm, 484 nm and 376 nm (**Figure 4. 13** (b)). Large Stokes shifts of 9988 cm^{-1}, 5060 cm^{-1} and 13886 cm^{-1} point out of highly distorted excited states.

All compounds show a bathochromic shift of the emission once they were cooled to 93 K (**Figure 4. 14** and **Figure 4. 15**). Emission maximum of $[Cu(o\text{-}SPhCO_2H)]_n$ shifts from 697 nm to 719 nm (Δ = 22 nm, 439 cm^{-1}, 0.054 eV) between 413 K and 93 K. In the case of $[Ag(o\text{-}SPhCO_2H)]_n$ the emission shifts from 627 nm to 655 nm (Δ = 28 nm, 682 cm^{-1}, 0.85 eV) between

443 K and 93 K. For [Au(*o*-SPhCO$_2$H)]$_n$ the emission shifts from 756 nm to 813 nm (Δ = 57 nm, 928 cm^{-1}, 0.115 eV) between 473 K to 93 K.

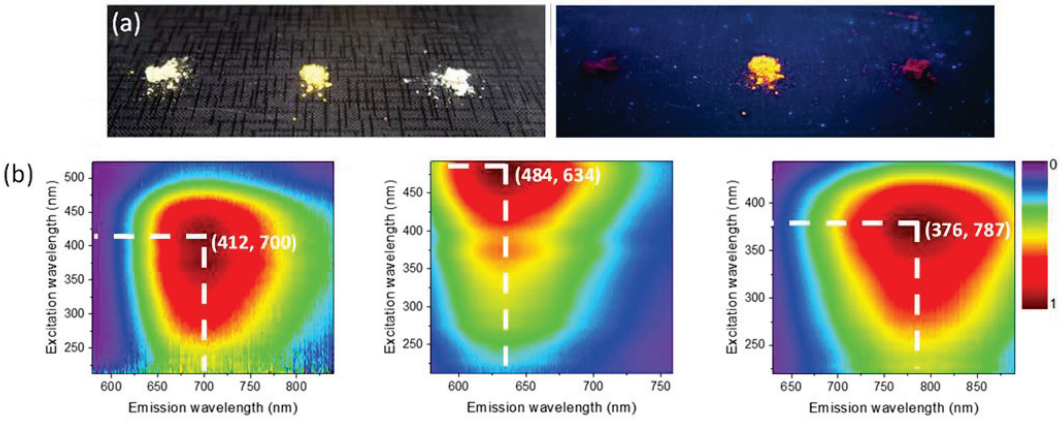

Figure 4. 13 (a) Photographs of [Cu(*o*-SPhCO$_2$H)]$_n$, [Ag(*o*-SPhCO$_2$H)]$_n$ and [Au(*o*-SPhCO$_2$H)]$_n$ (from left to right) under ambient light (left) and UV lamp (right) in solid state at room temperature. (b) From the left to the right: 2D maps of the emission and excitation spectra of the compounds [Cu(*o*-SPhCO$_2$H)]$_n$, [Ag(*o*-SPhCO$_2$H)]$_n$ and [Au(*o*-SPhCO$_2$H)]$_n$, respectively, obtained in the solid state at 293 K.

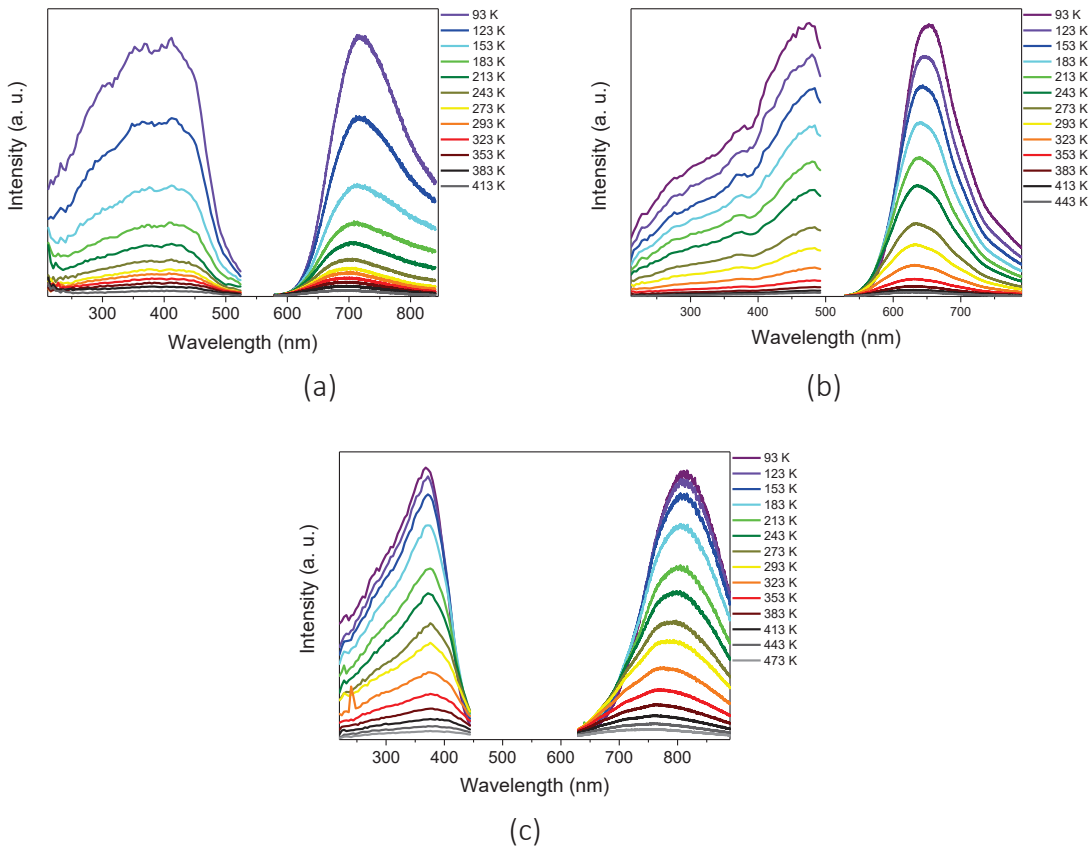

Figure 4. 14 Evolution of emission-excitation spectra of (a) [Cu(*o*-SPhCO$_2$H)]$_n$ (λ_{exc} = 412 nm, λ_{em} = 715 nm), (b) [Ag(*o*-SPhCO$_2$H)]$_n$ (λ_{exc} = 484 nm, λ_{em} = 650 nm) and (c) [Au(*o*-SPhCO$_2$H)]$_n$ (λ_{exc} = 376 nm, λ_{em} = 810 nm) in solid-state as a function of temperature.

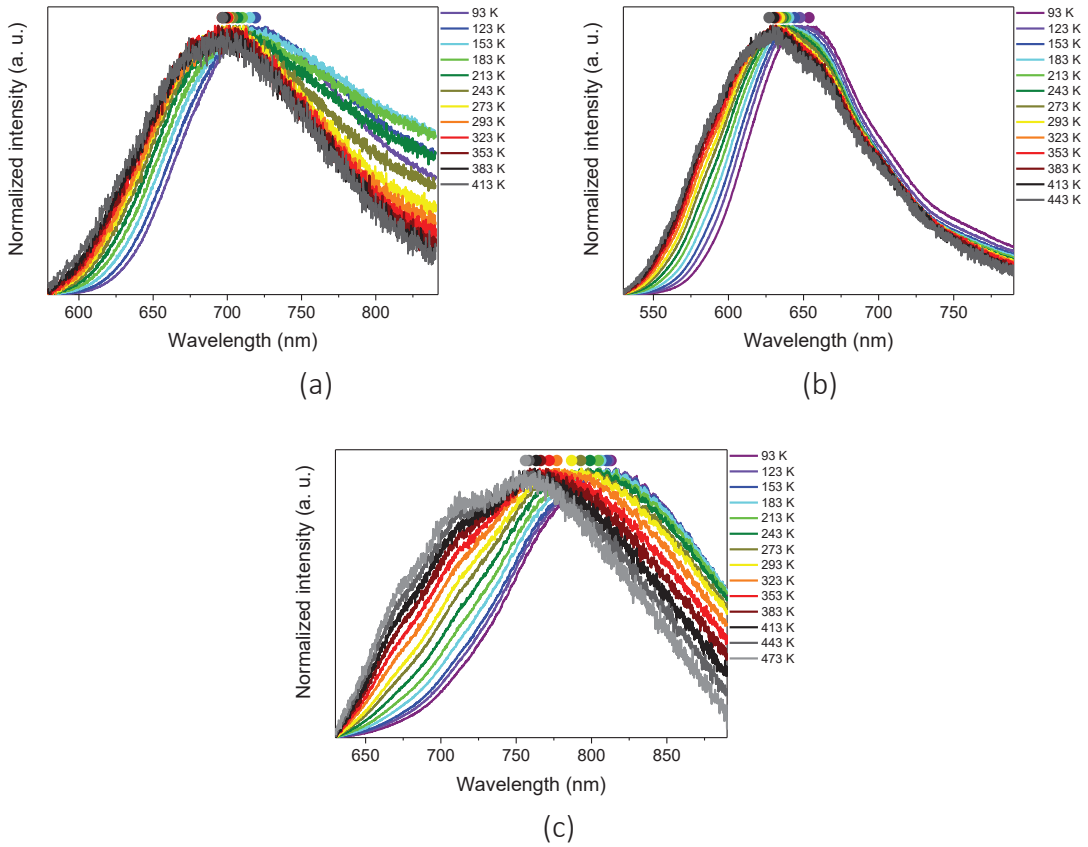

Figure 4. 15 Normalized intensities of emission spectra of (a) $[Cu(o\text{-}SPhCO_2H)]_n$ (λ_{exc} = 412 nm), (b) $[Ag(o\text{-}SPhCO_2H)]_n$ (λ_{exc} = 484 nm) and (c) $[Au(o\text{-}SPhCO_2H)]_n$ (λ_{exc} = 376 nm) in solid-state as function of temperature. Filled colored circles above the spectra indicate the position of the maximum of the peak at corresponding temperature.

For the $[Cu(o\text{-}SPhCO_2H)]_n$ (**Figure 4. 17** (a), Appendix B), at 93 K, the contribution of the short component is 48 %, and it reaches 97 % at 273 K. Its lifetime decreases from 0.8 µs at 93 K to 1.9 ns at 413 K. The shortening of the decay lifetime by factor of 400 is observed. Lifetime decay of the long component experiences significant decrease as well: from 36 µs at 93 K to 1 µs at 413 K. For the compound $[Ag(o\text{-}SPhCO_2H)]_n$ (**Figure 4. 17** (b), Appendix B), the shortening of both long and short components is observed. Longer component drops from 19 ms at 93 K to 16 ms at 443 K and shorter component changes from 37 µs to 7 ns. It is meaning a difference by factor of 5000! Differently to the case of the compound $[Cu(o\text{-}SPhCO_2H)]_n$, the contribution of the short component of the compound $[Ag(o\text{-}SPhCO_2H)]_n$ decreases from 100 % at 93 K to only 11 % at 443 K. The lifetime decay of the compound $[Au(o\text{-}SPhCO_2H)]_n$ (**Figure 4. 17** (c), Appendix B) stays monoexponential in the majority of the studied temperature range. It changes from 5.5 µs to 84 ns between 93 K and 473 K. Lifetime is decreased by “modest” factor

of 66. The slow component, with lifetime in the microsecond range, appears at 383 K and its contribution does not exceed 2 %.

Quantum yield was measured at the room temperature. Compound $[Cu(o\text{-}SPhCO_2H)]_n$ exhibits low quantum yield of 0.17 ± 0.01 %. Compounds $[Ag(o\text{-}SPhCO_2H)]_n$ and $[Au(o\text{-}SPhCO_2H)]_n$ exhibit higher quantum yield of 51.55 ± 1.75 and 7.30 ± 0.02 %, respectively. It makes them interesting for potential applications.

Possible assignment of the emission origin involves MC d → s transition with admixture of either MLCT or LMCT transitions.

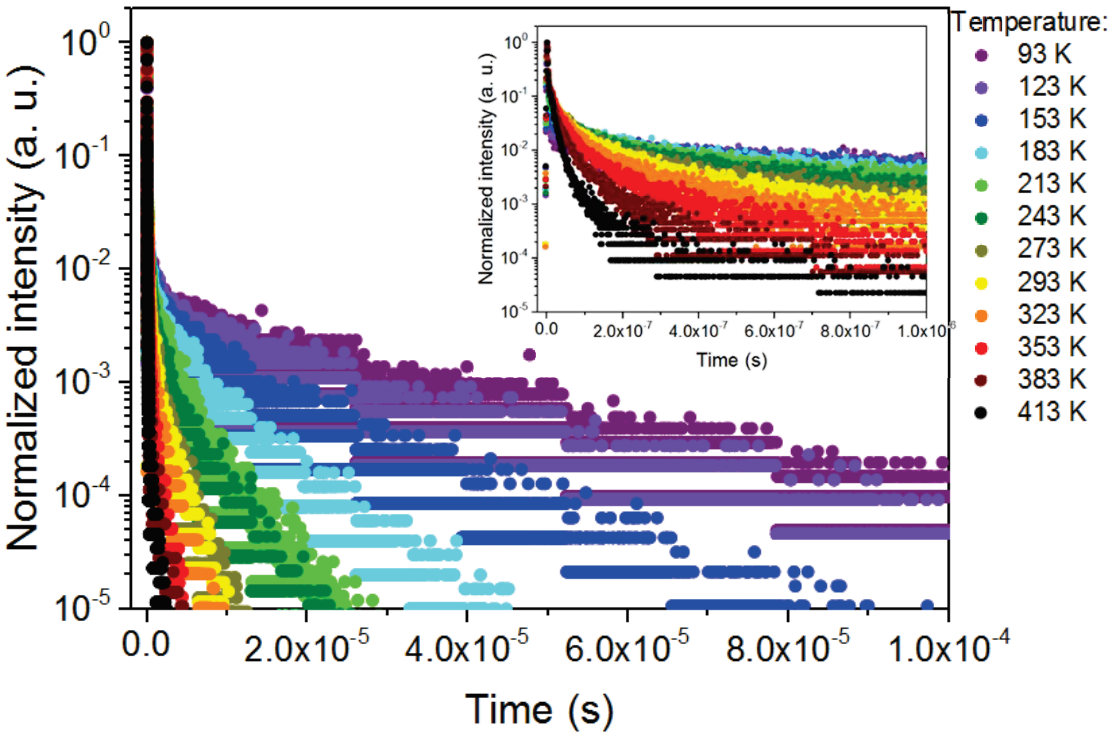

(a)

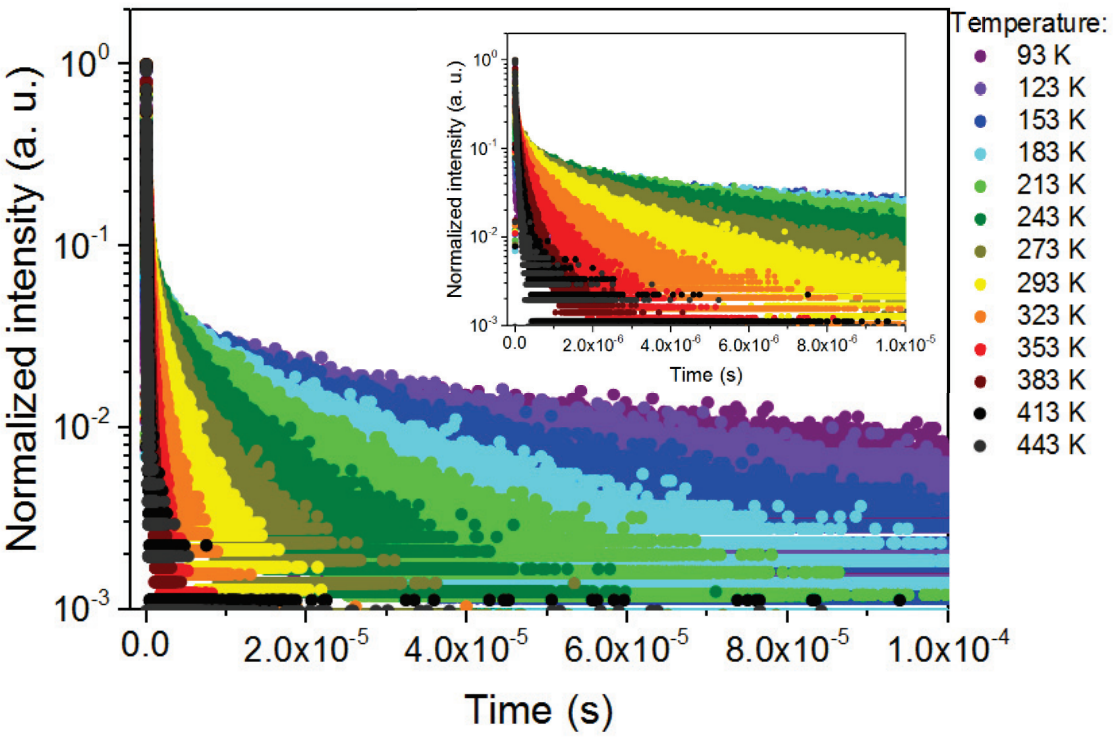

(b)

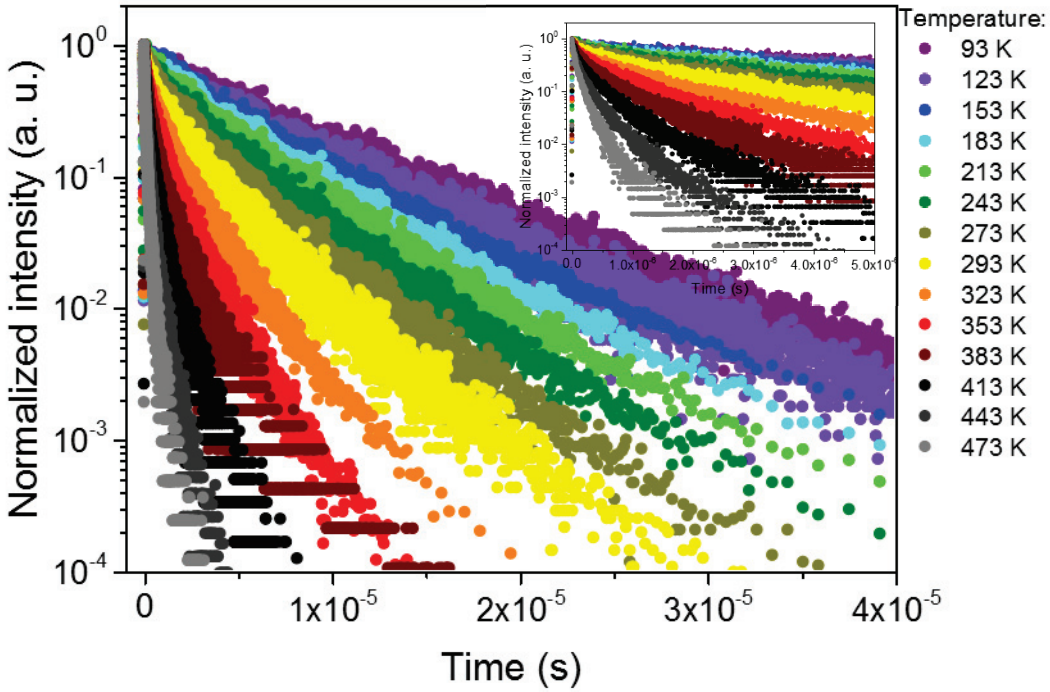

(c)

Figure 4. 16 Temperature-dependent luminescence decays of $[Cu(o\text{-}SPhCO_2H)]_n$ (a), $[Ag(o\text{-}SPhCO_2H)]_n$ (b) and $[Ag(o\text{-}SPhCO_2H)]_n$ (c). Zoom on shorter time is shown as inset.

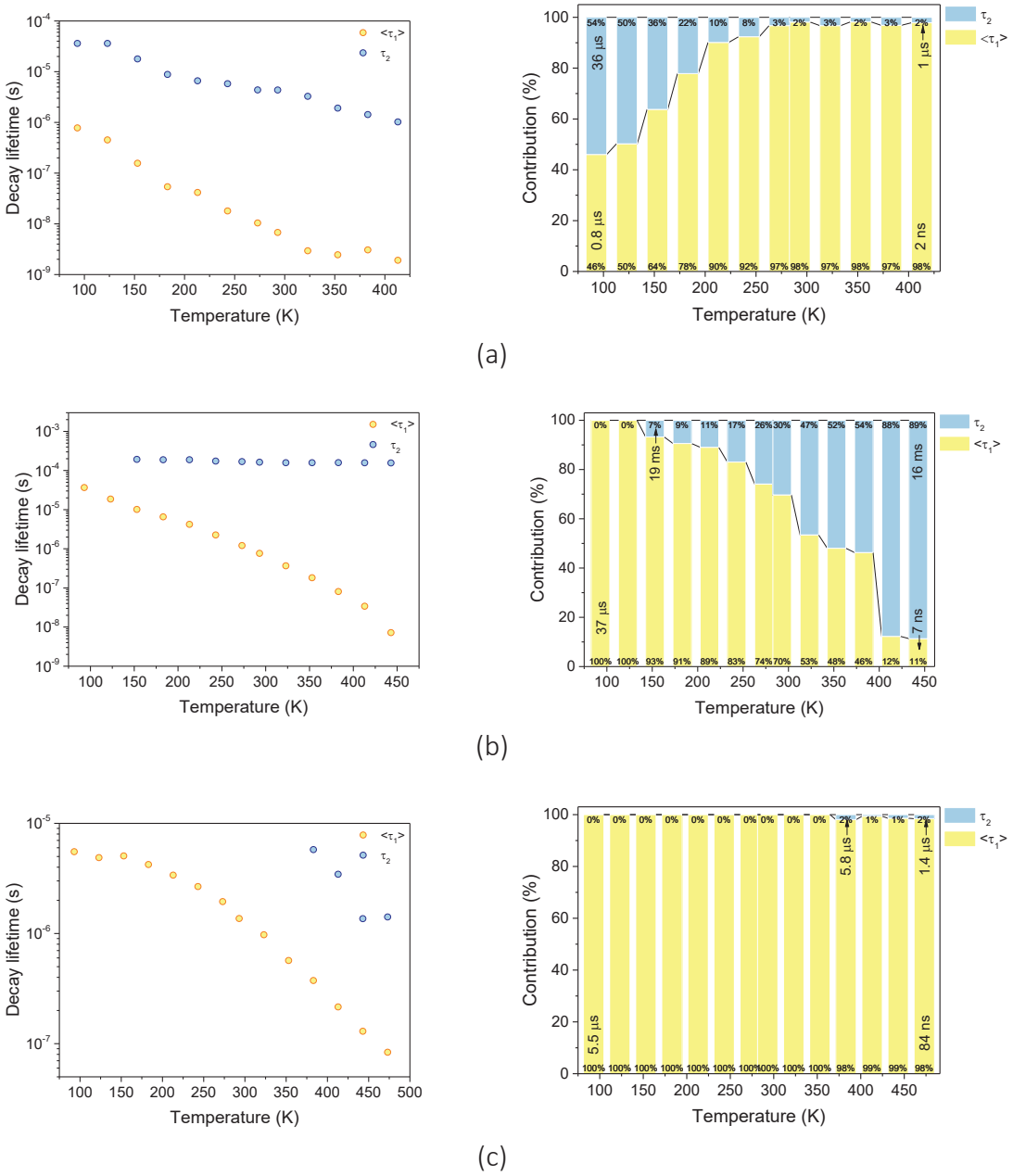

Figure 4. 17 Temperature dependence of the emission decays (left) and of contributions of different components (right) of $[Cu(o\text{-}SPhCO_2H)]_n$ (a), $[Ag(o\text{-}SPhCO_2H)]_n$ (b) and $[Au(o\text{-}SPhCO_2H)]_n$ (c).

Emission assignment done for the previously discussed $[Au(SPh)]_n$ and $[Cu(SPh)]_n$ can serve as a good starting point for the discussion of luminescence origin. One can build on their structural similarity to the corresponding $[M(o\text{-}SPhCO_2H)]_n$. If the same emission mechanism, LMCT or LMMCT, is preserved for $[Cu(o\text{-}SPhCO_2H)]_n$ and $[Au(o\text{-}SPhCO_2H)]_n$, the introduction of electron-withdrawing ($-CO_2H$) group on the ligand should have blue shift effect.[37] However, the

opposite was observed. The emission was red-shifted by 1360 cm^{-1} for Cu(I)-based and by 2490 cm^{-1} for Au(I)-based compounds (at low temperature).

The factor which is known to contribute to red shift of emission in the CPs of coinage metals is the decrease of the metal-metal distances. Actually, stronger metallophilic interactions lower the transition energy and they red shift the emission.[37] Interestingly, the metal-metal distances in $[M(o\text{-}SPhCO_2H)]_n$ are not shorter than in the case of$[M(SPh)]_n$ (**Table 4. 1**, **Table 4. 3**, **Figure 4. 8**).

Main structural difference between the compounds based on thiophenolate and thiosalycilic acid lies in the presence of hydrogen bonds. Hydrogen bonds between the $[MS]_n$-columns rigidify the structure and limit the excited state distortion process (rigidochromic effect). It leads to the blue shift of the emission.

None these hypotheses justify the red shift of the emission, therefore another emission mechanism has to be involved. There is a good reason to propose the possibility of MLCT. Indeed, a significant number of Cu(I)-based compounds with MLCT emission is known. To lesser extent it also applies to Au(I)-based compounds. MLCT emission is considered to be uncommon for Ag(I)-based compounds. Nevertheless, few compounds with low-lying emissive MLCT states are known.[38] This is due to higher oxidation potential of the Ag^+ ion in comparison to Cu^+ ion (173329 cm^{-1} vs. 163670 cm^{-1}, respectively).[39] As a result, the 4d orbitals of silver complexes mostly lie below LC orbitals. This leads to low-lying states of LC character. The use of ligands with highly donating properties, *e. g.* phosphine, has recently proved itself to be a strategy to create Ag(I)-based compounds exhibiting MLL'CT or (M+L)L'CT emission.[34,40,41] Therefore, in silver-thiolate CP, MLCT emission could be potentially expected as well.

The emission energy of $[Cu(o\text{-}SPhCO_2H)]_n$ is lower than that of $[Ag(o\text{-}SPhCO_2H)]_n$. This aligns with assignment of MLCT emissive state. Still, the difference of emission energy can be used to discriminate between MLCT and LMCT origin of the emission.[42] As Cu^+ is easier to oxidize than Ag^+, the MLCT transition for Cu(I) should occur at lower energy than for Ag(I). Considering the fact, that the ionization energy of Ag^+ is 9660 cm^{-1} larger than that of Cu^+, an assignment of MLCT is less likely, if we take into account the difference of emission energies of only 1487 cm^{-1}.

A similar red shift in the case of silver(I) to copper(I) chalcogenolate clusters has been reported (2180 cm^{-1}). In these cases, mixed d→s/LMCT origin has been supported by molecular orbital calculations.[43,44, 45,46,47] For trinuclear silver(I) and copper(I) acetylide complexes (red shift of 2340 cm^{-1} and 2660 cm^{-1}), and for silver(I) and copper(I) thiocarbamate clusters (red shift of 2500 cm^{-1}), LMCT origin was suggested in framework of small energy differences.[42, 48] In the case of silver(I) and copper(I) dinuclear phosphine-phosphine oxide complexes, ^{3}MLCT origin was suggested. Energy difference was in this case more significant than in our case (3444 cm^{-1}).[49] For silver(I) and copper(I) 1,2-bis(diphenylphosphino)benzene bisphosphine complexes, ^{3}MLCT origin was also suggested, while the energy difference was very small (343 cm^{-1}). It should be noted, that no calculus was provided to support this assignment.[50]

It seems impossible to attribute unambiguously the emission origin without theoretical calculus. We tend to assign the emission to MLCT triplet parentage mixed with MC states. The perturbation, due to metallophilic interactions, might be also involved. M(I)-M(I) contacts for $[Cu(o\text{-}SPhCO_2H)]_n$ and $[Ag(o\text{-}SPhCO_2H)]_n$ are too long for ground-state interactions. Nevertheless, it is reasonable to suppose that they might contract in the excited state and cause low-energy emission.[51] This would explain well the emission energy decrease in a row Ag – Cu – Au with their increasing tendency to form metallophilic interactions which are red shifting the emission.

The question of hydrogen bonds can be discussed separately. Recent advances in femtosecond time-resolved spectroscopy and accurate quantum chemistry calculations allow to study electronic excited-state hydrogen-bonding dynamics. It can also show the significant role of electronic excited-state of the hydrogen bonds on the internal conversion, fluorescence quenching, intramolecular charge transfer and MLCT.[52] It is reasonable to suppose, that introduction of the hydrogen bonds could influence the luminescent properties significantly. So far, only few studies were done on contribution of the hydrogen bonds on MLCT or LMCT excited states. Thus, it is difficult to estimate, to what extent the hydrogen bonds could influence the emission of the discussed CPs.

If we compare $[Ag(o\text{-}SPhCO_2H)]_n$ to other silver(I)- thiosalicylate complexes, it shows relative red shift of the emission.[7,8] It can be explained by increased metallophilic chain length in CPs relatively to the metallophilic oligomers in isolated clusters. This is known to decrease the HOMO-LUMO gap for the emission coming from MC excited states.[53]

In the process of temperature decrease, a bathochromic shift of the emission peak was observed for the three compounds. It can be explained by the shortening of the M-M contacts in the crystalline structure at low temperature. This shortening is known to lower the emission energy.[54] The phenomenon is often encountered in coinage metal compounds, and also in $[Cu(SPh)]_n$ and $[Au(SPh)]_n$.[55,56,57]

Both compounds, the $[Cu(o\text{-}SPhCO_2H)]_n$ and the $[Ag(o\text{-}SPhCO_2H)]_n$ show biexponential decay. Compound $[Au(o\text{-}SPhCO_2H)]_n$, however, shows monoexponential decay in the majority of the studied temperature range. The presence of the two lifetimes is indicative of two thermally non-equilibrated states. They are tentatively assigned to different sublevels of the emitting "triplet" excited states that are split by the spin-orbit coupling. Crosby[58] suggested that such sublevels behave independently and decay differently in metal complexes, even if only one emission band is observed.[51]

The three compounds show a lifetime shortening when the temperature is increased. This is a typical temperature quenching behavior resulting from the thermal activation of the non-radiative decay pathway.[59] The reasonable fit for the shorter lifetime components of $[Cu(o\text{-}SPhCO_2H)]_n$ and $[Ag(o\text{-}SPhCO_2H)]_n$ can be achieved using the (Eq. 1.1) (**Figure 4. 18**). The fit does not converge neither for the longer components, nor for the compound $[Au(o\text{-}SPhCO_2H)]_n$. This fact points out to the presence of two or more different non-radiative decay mechanisms.

Even though, the lifetime of the compound $[Cu(o\text{-}SPhCO_2H)]_n$ and $[Au(o\text{-}SPhCO_2H)]_n$ is on nanoscale range at high temperature, we still attribute the emission to the triplet parentage. Despite of the short lifetime, emission is still coming from the same triplet excited state.

The compound $[Ag(o\text{-}SPhCO_2H)]_n$ exhibits a high quantum yield, making it an attractive candidate material for sustainable and efficient illumination. It is also worth noting, that compound $[Au(o\text{-}SPhCO_2H)]_n$ represents interesting properties in comparison to other Au(I)-based NIR-emitters. The latter are known to be very rare and have faint luminescence.[60] One of the known examples are polynuclear chalcogenolate clusters (S- and Se-based).[36,61,62,63] Nevertheless, $[Au(o\text{-}SPhCO_2H)]_n$ shows the highest quantum yield among all of them.

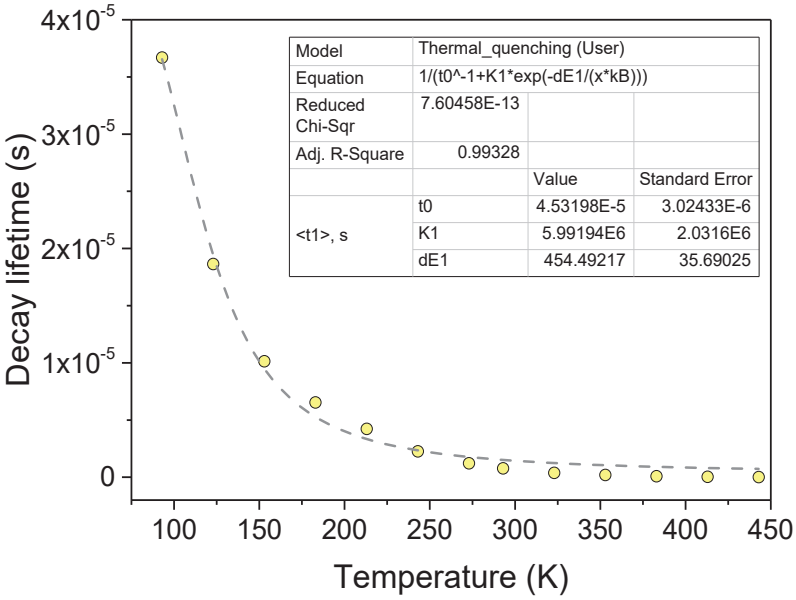

(a)

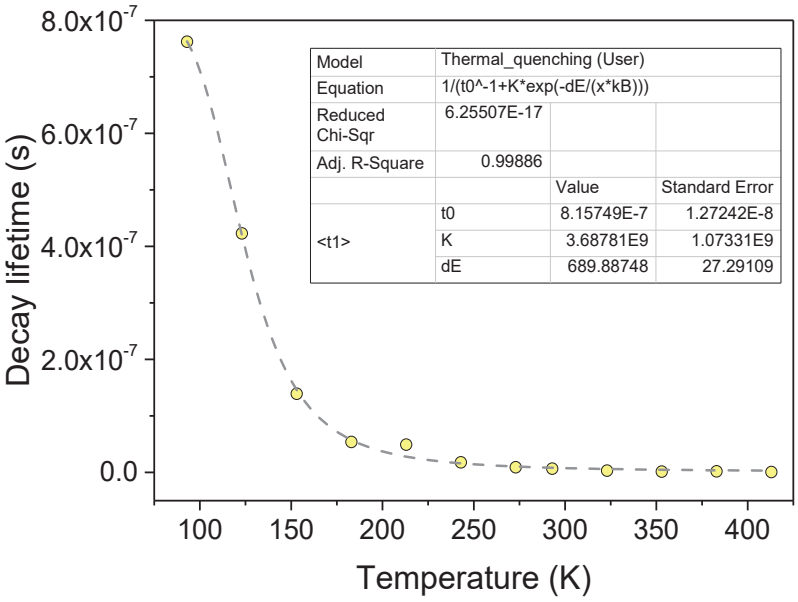

(b)

Figure 4. 18 Luminescence decay time of short component <τ_1> plotted versus temperature with a fit of (Eq. 1. 1) for $[Cu(o\text{-}SPhCO_2H)]_n$ (a) and $[Ag(o\text{-}SPhCO_2H)]_n$ (b). Yellow circles, experimental data; gray dashed line, fit; fitted parameters are given as inset.

4.5 Conclusions

Three coordination polymers with *o*-$HSPhCO_2H$ serving as a ligand were synthesized. The structure of Cu- and Ag-based compounds were successfully solved. The structural model based on PXRD and PDF data was proposed for Au-based compound. The emission-excitation spectra and lifetime measurements at various temperatures let us conduct investigation of the photophysical properties and assign tentatively the origin of luminescence.

This chapter shows that the introduction of a steric hindrance close to the coordination site of a ligand prevents the formation of extended networks as it was in the case of the *para*- and *meta*-mercaptobenzoic based CPs. 1D $[MS]_n$ arrangements are formed for all three investigated coinage metals. The major difference is the environment of the metal and sulfur. It is tribonding in the case of $[Cu(o\text{-}SPhCO_2H)]_n$ and $[Ag(o\text{-}SPhCO_2H)]_n$, and dibonding in the case of $[Au(o\text{-}SPhCO_2H)]_n$.

The three materials have low-energy emission, similar to the CPs discussed in the first chapter, *i. e.* $[Cu(SPh)]_n$ and $[Au(SPh)]_n$. Unexpected red shift of the emission is observed after the introduction of electro-withdrawing group on the ligand. Despite the full photophysical characterization, an unambiguous assignment of emission origin could not be done. The emission was assigned tentatively to mixed MC and LMCT or MLCT excited states of triplet parentage.

$[Cu(o\text{-}SPhCO_2H)]_n$ shows very weak emission at the room temperature. The quantum yields of $[Ag(o\text{-}SPhCO_2H)]_n$ and $[Au(o\text{-}SPhCO_2H)]_n$ reach promising values. They fully reveal the great potential of 1D CPs based on thiolates of coinage metals to be highly efficient emitters in orange-NIR part of the spectra.

4.6 Experimental Part

4.6.1 Synthesis

Synthesis of [Cu(*o*-SPhCO$_2$H)]$_n$: 1 mL of 0.5 M H_2SO_4 was added to a solution of $Cu(CH_3CO_2)_2$ (50 mg, 0.28 mmol) in THF (5 mL) followed by addition of 5 mL of 2-MBA (110 mg, 0.71 mmol) in DMF. The reaction was let to proceed for 18 h at 100°C in a 20 mL sealed vial. Yellowish precipitate was obtained and washed by 40 mL of ethanol for 2 times. A powder was recovered by centrifugation at 4000 rpm. Yield: 96 % (58 mg). Chemical Formula: $C_7H_5CuO_2S$. Molecular Weight: 216.72. Elemental analysis (calc.) wt%: C, 39.5 (38.8); H, 2.45 (2.33); S, 14.47 (14.80). CuO content from TGA (calc.) wt%: 36.7 (36.7).

Synthesis of [Ag(*o*-SPhCO$_2$H)]$_n$: a solution of $AgNO_3$ (100 mg, 0.59 mmol) in H_2O (10 mL) was added to 2-MBA (82 mg, 0.53 mmol). The reaction was let to proceed for 40 min at 90°C in a 20 mL sealed vial. Bright orange precipitate was obtained and washed by 40 mL of ethanol for 2 times. A powder was recovered by centrifugation at 4000 rpm. Yield: 80 % (123 mg). Chemical Formula: $C_7H_5AgO_2S$. Molecular Weight: 261.05. Elemental analysis (calc.) wt%: C, 34.0 (32.2); H, 2.06 (1.93); S, 12.64 (12.28). Silver content from TGA (calc.) wt%: 41.4 (41.3).

Synthesis of [Au(*o*-SPhCO$_2$H)]$_n$: a solution of $HAuCl_4 \cdot 3H_2O$ (300 mg, 0.76 mmol) in iPrOH (50 mL) was added to 2-MBA (715 mg, 4.64 mmol). The reaction was let to proceed for 72 h at room temperature. Pale beige precipitate was obtained and washed by 40 mL of ethanol for 2 times. A powder was recovered by centrifugation at 4000 rpm. Yield: 91 % (242 mg). Chemical Formula: $C_7H_5AuO_2S$. Molecular Weight: 350.15. Elemental analysis (calc.) wt%: C, 25.3 (24); H, 1.37 (1.44); S, 9.38 (9.16). Gold content from TGA (calc.) wt%: 56.2 (56.3).

4.6.2 PXRD and Total Scattering Measurements

Finely powdered samples of the three products were loaded into 0.7 mm diameter borosilicate glass capillaries. Room temperature X-ray data were collected at the ID22 beamline of the ESRF, Grenoble, France, at a wavelength of λ = 0.17965 Å (70 keV) using a Perkin-Elmer flat panel detector located at 100 cm and 45 cm away from the sample, respectively.

Diffraction images were corrected and transformed to 1D diffraction patterns using the PyFAI software[64] (Q_{max} = 25 Å^{-1}).

Data from a standard sample (CeO_2) was collected and used to characterize the instrumental resolution function.

The reciprocal space data were converted to PDFs using the PDFgetX3 software.[65]

4.6.3 PXRD Structure Determination of [Cu(*o*-SPhCO$_2$H)]$_n$ and [Ag(*o*-SPhCO$_2$H)]$_n$

All calculations of structural investigations were performed using the TOPAS program.[66] The LSI-indexing method converged unambiguously to a tetragonal unit cell for a [Ag(*o*-SPhCO$_2$H)]$_n$. The direct space strategy was used to position silver atoms and the organic moieties, which were treated as rigid body in the simulated annealing process. The final Rietveld plot (**Figure 4. 19**) corresponds to satisfactory model indicator and profile factors (**Table 4. 4**).

For [Cu(*o*-SPhCO$_2$H)]$_n$, similarities with unit cell parameters of [Ag(*o*-SPhCO$_2$H)]$_n$ led us to suppose that the two compounds were isostructural. The structural model of **2** was then used as a starting point of the Rietveld refinement of **1**. Final Rietveld plot (**Figure 4. 20**) corresponds to satisfactory model indicator and profile factors (**Table 4. 4**).

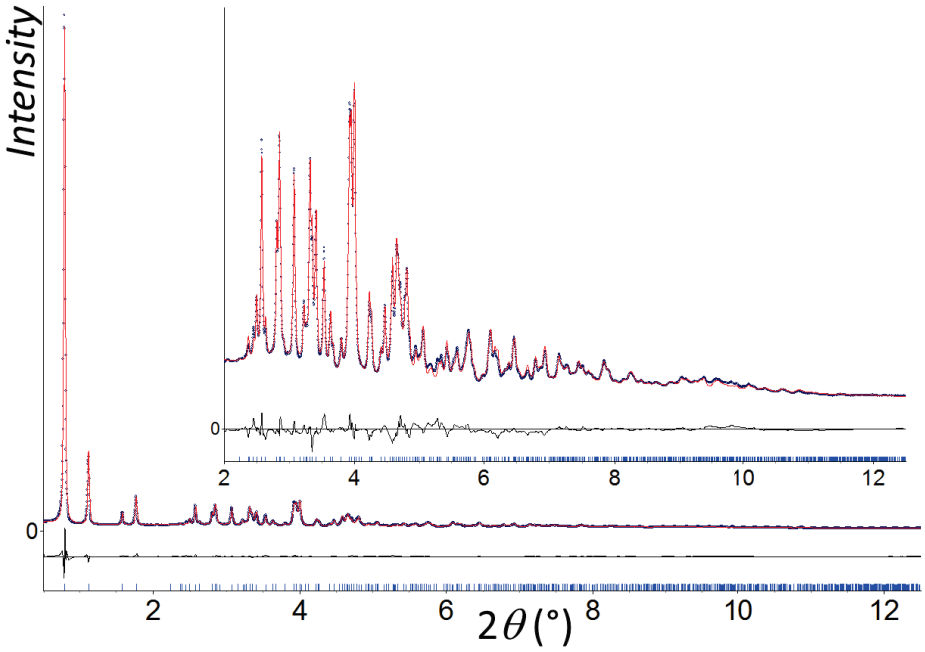

Figure 4. 19 Final Rietveld plot of $[Ag(o\text{-}SPhCO_2H)]_n$ showing observed (blue circles), calculated (red line), and difference (black line) curves. A zoom at high angles is shown as inset.

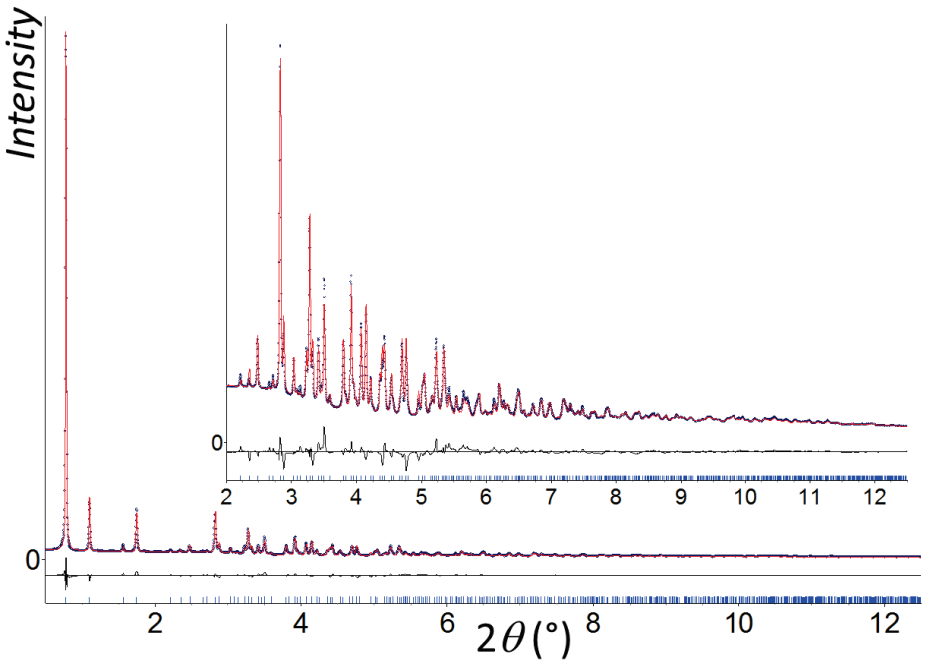

Figure 4. 20 Final Rietveld plot of $[Cu(o\text{-}SPhCO_2H)]_n$ showing observed (blue circles), calculated (red line), and difference (black line) curves. A zoom at high angles is shown as inset.

Table 4. 4 Crystallographic data for $[Cu(o\text{-}SPhCO_2H)]_n$, $[Ag(o\text{-}SPhCO_2H)]_n$ and $[Au(o\text{-}SPhCO_2H)]_n$.

	$[Cu(o\text{-}SPhCO_2H)]_n$	$[Ag(o\text{-}SPhCO_2H)]_n$	$[Au(o\text{-}SPhCO_2H)]_n$
Empirical formula	$C_7H_5Cu_1O_2S_1$	$C_7H_5Ag_1O_2S_1$	$C_7H_5Au_1O_2S_1$
M_r	216.72	261.05	350.15
Crystal system	Tetragonal	Tetragonal	Tetragonal
Space group	$P4_2/n$	$P4_2/n$	$P4_2/n$
a (Å)	18.5912(9)	18.420(2)	18.795(8)
c (Å)	3.9622(2)	4.4344(4)	4.564(2)
V (Å^3)	1369.5(2)	1504.5(3)	1612.0(15)
M_{20}	58	65	16
Z	8	8	8
λ (Å)	0.15965	0.15965	0.15965
No of structural parameters	18	18	17
Number of reflections	1421	1587	899
R_p, R_{wp}	0.035, 0.049	0.033, 0.046	0.059, 0.075
R_{Bragg}, GoF	0.025, 0.57	0.017, 0.67	0.018, 1.40

4.6.4 PDF Analysis of $[Au(o\text{-}SPhCO_2H)]_n$ Structure

Prior to the refinement of the structural model based on the PDF data, the Rietveld refinement on PXRD data was performed (**Figure 4. 22**).

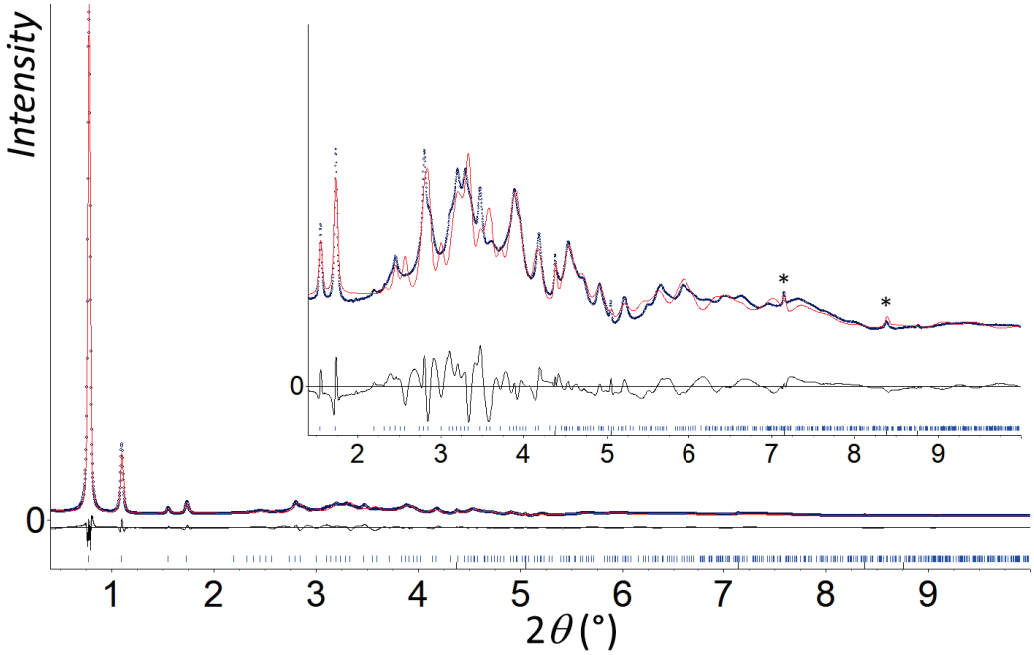

Figure 4. 21 Rietveld plot of [Au(*o*-SPhCO$_2$H)]$_n$ showing observed (blue circles), calculated (red line), and difference (black line) curves. A zoom at high angles is shown as inset. Black asterisks correspond to golf FCC present as impurity.

The refinement was performed by the MolPDF software. [29] The organic ligand was included in the structural model and it was fully constrained (*i. e.* considered as a rigid block molecule). Following refined parameters were used: the scale factor, cell parameters, atomic positions and thermal displacement parameter of gold atoms (it was fixed for the atoms of organic ligand – sulfur, carbon, oxygen – because its refinement was leading to the divergence of the fit). A refinement of the standard sample (CeO_2) PDF (**Figure 4. 23** (a)) allowed us to determine the parameters characterizing the instrumental resolution function (Q_{damp} = 0.01637; Q_{broad} = 0.01023). They were fixed later during sample refinement. The *spdiameter* was chosen and fixed at 48 Å in order to mimic the observed decay of the sample PDF at high *r* values (**Figure 4. 23** (b)).

All the used parameters are listed in the **Table 4. 5**.

Table 4. 5 The parameters used for the refinement of the PDF of $[Au(o\text{-}SPhCO_2H)]_n$ with MolPDF software.

Profile and instrumental resolution parameters					
Scale factor	0.929(7)	Q_{damp}	0.01637	*spdiameter*, Å	48.0
Q_{max}, Å^{-1}	25.0	Q_{broad}	0.01023		
Structural parameters					
Space group: P 4_2/n					
Cell: 18.796(10)	18.796(10)	4.521(3)	90.0000	90.0000	90.0000
Atom	Type	x/a	y/b	z/c	B_{iso}
Au1	Au	0.2055(4)	0.6640(3)	0.554(2)	3.25(9)
S1	S	0.3816(3)	0.8122(4)	-0.101(2)	0.10(5)
C11	C	0.4679(3)	0.7877(4)	-0.337(3)	1.00
C12	C	0.5218(4)	0.8363(5)	-0.364(3)	1.00
C13	C	0.5814(5)	0.8189(7)	-0.526(4)	1.00
C14	C	0.5866(7)	0.7546(9)	-0.663(5)	1.00
C15	C	0.5346(7)	0.7045(8)	-0.629(5)	1.00
C16	C	0.4733(5)	0.7211(6)	-0.487(4)	1.00
C17	C	0.5156(4)	0.9091(5)	-0.210(2)	1.00
O11	O	0.4657(4)	0.9181(5)	0.042(2)	1.00
O12	O	0.5511(4)	0.95912(6)	-0.295(2)	1.00

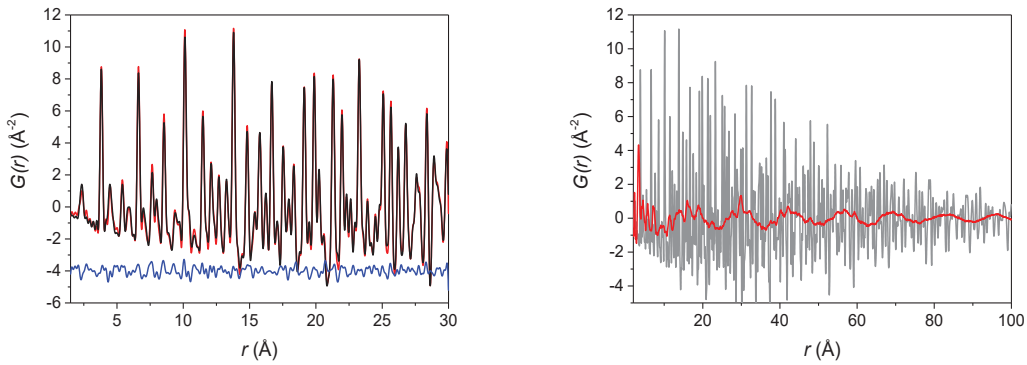

(a) (b)

Figure 4. 22 (a) A refinement of the standard sample (CeO_2) PDF: observed curve (red line), calculated (black line), and difference (blue line) curves; (b) decay of the sample PDF at high *r* values: CeO_2 (gray line), $[Au(o\text{-}SPhCO_2H)]_n$ (red line).

4.7 References

1. T. Wehr-Candler and W. Henderson, *Coord. Chem. Rev.*, 2016, **313**, 111-155.
2. R. C. Bott, P. C. Healy and D. S. Sagatys, *ChemComm*, 1998, 2403-2404.
3. K. Nomiya, N. C. Kasuga, I. Takamori and K. Tsuda, *Polyhedron*, 1998, **17**, 3519-3530.
4. L.-G. Yang, C.-C. Zhu, D.-P. Zhang, D.-C. Li, D.-Q. Wang and J.-M. Dou, *Polyhedron*, 2011, **30**, 1469-1477.
5. R. Noguchi, A. Hara, A. Sugie, S. Tanabe and K. Nomiya, *Chem. Lett.*, 2005, **34**, 578-579.
6. K. Nomiya, R. Noguchi and C. Kato, *Chem. Lett.*, 2000, **29**, 162-163.
7. D. Sun, D.-F. Wang, F.-J. Liu, H.-J. Hao, N. Zhang, R.-B. Huang and L.-S. Zheng, *CrystEngComm*, 2011, **13**, 2833-2836.
8. D. Sun, F.-J. Liu, R.-B. Huang and L.-S. Zheng, *Inorg. Chem.*, 2011, **50**, 12393-12395.
9. D. Sun and Z.-H. Yan, *Acta Crystallogr. C*, 2012, **68**, m229-m232.
10. D. Sun, G.-G. Luo, N. Zhang, Q.-J. Xu, Y.-C. Jin, Z.-H. Wei, C.-F. Yang, L.-R. Lin, R.-B. Huang and L.-S. Zheng, *Inorg. Chem. Commun.*, 2010, **13**, 306-309.
11. K. Nomiya, Y. Kondoh, K. Onoue, N. C. Kasuga, H. Nagano, M. Oda, T. Sudoh and S. Sakuma, *J. Inorg. Biochem.*, 1995, **58**, 255-267.
12. R. Bau, *J. Am. Chem. Soc.*, 1998, **120**, 9380-9381.
13. D. R. Smyth, B. R. Vincent and E. R. T. Tiekink, *Cryst. Growth Des.*, 2001, **1**, 113-117.
14. P. D. Cookson and E. R. T. Tiekink, *J. Coord. Chem.*, 1992, **26**, 313-320.
15. S.-S. Yun, J.-K. Kim, J.-S. Jung, C. Park, J.-G. Kang, D. R. Smyth and E. R. T. Tiekink, *Cryst. Growth Des.*, 2006, **6**, 899-909.
16. D. R. Smyth, J. Hester, J. V. G. Young and E. R. T. Tiekink, *CrystEngComm*, 2002, **4**, 517-521.
17. D. R. Smyth, B. R. Vincent and E. R. T. Tiekink, *CrystEngComm*, 2000, **2**, 115-120.
18. W. Schneider, A. Bauer and H. Schmidbaur, *Organometallics*, 1996, **15**, 5445-5446.
19. A. Sladek, W. Schneider, K. Angermaier, A. Bauer and H. Schmidbaur, *Z. Naturforsch. B Chem. Sci.*, 1996, **51b**, 765-773.
20. C. Domínguez, B. Heinrich, B. Donnio, S. Coco and P. Espinet, *Chem. Eur. J.*, 2013, **19**, 5988-5995.
21. R. E. Bachman and S. A. Bodolosky-Bettis, *Z. Naturforsch.*, 2009, **64b**, 1491-1499.
22. K. Nomiya, H. Yokoyama, H. Nagano, M. Oda and S. Sakuma, *J. Inorg. Biochem.*, 1995, **60**, 289-297.
23. C.-M. Che, C.-H. Li, S. S.-Y. Chui, V. A. L. Roy and K.-H. Low, *Chem. Eur. J.*, 2008, **14**, 2965-2975.
24. K. Tang, J. Yang, Q. Yang and Y. Tang, *J. Chem. Soc., Dalton Trans*, 1989, 2297-2302.
25. H. Yan, F. Yang, D. Pan, Y. Lin, J. N. Hohman, D. Solis-Ibarra, F. H. Li, J. E. P. Dahl, R. M. K. Carlson, B. A. Tkachenko, A. A. Fokin, P. R. Schreiner, G. Galli, W. L. Mao, Z.-X. Shen and N. A. Melosh, *Nature*, 2018, **554**, 505.
26. I. G. Dance, L. J. Fitzpatrick, D. C. Craig and M. L. Scudder, *Inorg. Chem.*, 1989, **28**, 1853-1861.

27. S.-H. Hong, A. Olin and R. Hesse, *Acta Chem. Scand.*, 1979, **A29**, 582-589.
28. C. A. Simpson, C. L. Farrow, P. Tian, S. J. L. Billinge, B. J. Huffman, K. M. Harkness and D. E. Cliffel, *Inorg. Chem.*, 2010, **49**, 10858-10866.
29. J. Rodriguez-Carvajal and A. Bytchkov, *Institut Laue-Langevin, Grenoble, France*, 2016.
30. C. Lavenn, L. Okhrimenko, N. Guillou, M. Monge, G. Ledoux, C. Dujardin, R. Chiriac, A. Fateeva and A. Demessence, *J. Mater. Chem. C*, 2015, **3**, 4115-4125.
31. J. S. Lim, H. Choi, I. S. Lim, S. B. Park, Y. S. Lee and S. K. Kim, *J. Phys. Chem. A*, 2009, **113**, 10410-10416.
32. J. C. Deaton, S. C. Switalski, D. Y. Kondakov, R. H. Young, T. D. Pawlik, D. J. Giesen, S. B. Harkins, A. J. M. Miller, S. F. Mickenberg and J. C. Peters, *J. Am. Chem. Soc.*, 2010, **132**, 9499-9508.
33. B. Hupp, C. Schiller, C. Lenczyk, M. Stanoppi, K. Edkins, A. Lorbach and A. Steffen, *Inorg. Chem.*, 2017, **56**, 8996-9008.
34. M. Z. Shafikov, A. F. Suleymanova, R. Czerwieniec and H. Yersin, *Inorg. Chem.*, 2017, **56**, 13274-13285.
35. J. Nitsch, C. Kleeberg, R. Fröhlich and A. Steffen, *Dalton Trans.*, 2015, **44**, 6944-6960.
36. V. W. W. Yam, E. C. C. Cheng and N. Zhu, *Angew. Chem.*, 2001, **40**, 1763-1765.
37. J. M. Forward, D. Bohmann, J. P. Fackler and R. J. Staples, *Inorg. Chem.*, 1995, **34**, 6330-6336.
38. V. W.-W. Yam, V. K.-M. Au and S. Y.-L. Leung, *Chem. Rev.*, 2015, **115**, 7589-7728.
39. *CRC Handbook of Chemistry and Physics*, CRC Press LLC: Boca Raton, 84th edn., 2003.
40. M. Z. Shafikov, A. F. Suleymanova, R. Czerwieniec and H. Yersin, *Chem. Mater.*, 2017, **29**, 1708-1715.
41. M. Z. Shafikov, A. F. Suleymanova, A. Schinabeck and H. Yersin, *J. Phys. Chem. Lett.*, 2018, **9**, 702-709.
42. V. W.-W. Yam, W. K.-M. Fung and K.-K. Cheung, *Organometallics*, 1997, **16**, 2032-2037.
43. V. W.-W. Yam, K. K.-W. Lo and K.-K. Cheung, *Inorg. Chem.*, 1996, **35**, 3459-3462.
44. V. W.-W. Yam, K. K.-W. Lo, C.-R. Wang and K.-K. Cheung, *Inorg. Chem.*, 1996, **35**, 5116-5117.
45. V. W.-W. Yam, W.-K. Lee and T.-F. Lai, *J. Chem. Soc., Chem. Commun.*, 1993, 1571-1573.
46. C.-R. Wang, K. K.-W. Lo and V. W.-W. Yam, *Chem. Phys. Lett.*, 1996, **262**, 91-96.
47. C.-R. Wang, K. Kam-Wing Lo and V. Wing-Wah Yam, *J. Chem. Soc., Dalton Trans*, 1997, 227-230.
48. F. Sabin, C. K. Ryu, P. C. Ford and A. Vogler, *Inorg. Chem.*, 1992, **31**, 1941-1945.
49. T. M. Dau, B. D. Asamoah, A. Belyaev, G. Chakkaradhari, P. Hirva, J. Jänis, E. V. Grachova, S. P. Tunik and I. O. Koshevoy, *Dalton Trans.*, 2016, **45**, 14160-14173.
50. A. Kaeser, O. Moudam, G. Accorsi, I. Séguy, J. Navarro, A. Belbakra, C. Duhayon, N. Armaroli, B. Delavaux-Nicot and J.-F. Nierengarten, *Eur. J. Inorg. Chem.*, 2014, **2014**, 1345-1355.
51. H. V. R. Dias, H. V. K. Diyabalanage, M. A. Rawashdeh-Omary, M. A. Franzman and M. A. Omary, *J. Am. Chem. Soc.*, 2003, **125**, 12072-12073.

52. G.-J. Zhao and K.-L. Han, *Acc. Chem. Res.*, 2012, **45**, 404-413.
53. G. S. M. Tong, S. C. F. Kui, H.-Y. Chao, N. Zhu and C.-M. Che, *Chem. Eur. J.*, 2009, **15**, 10777-10789.
54. V. W.-W. Yam and K. K.-W. Lo, *Chem. Soc. Rev.*, 1999, **28**, 323-334.
55. Q. Liu, M. Xie, X. Chang, Q. Gao, Y. Chen and W. Lu, *ChemComm*, 2018, **54**, 12844-12847.
56. R. Galassi, M. M. Ghimire, B. M. Otten, S. Ricci, R. N. McDougald, Jr., R. M. Almotawa, D. Alhmoud, J. F. Ivy, A.-M. M. Rawashdeh, V. N. Nesterov, E. W. Reinheimer, L. M. Daniels, A. Burini and M. A. Omary, *Proc. Natl. Acad. Sci. U.S.A.*, 2017, **114**, E5042-E5051.
57. I. Roppolo, E. Celasco, A. Fargues, A. Garcia, A. Revaux, G. Dantelle, F. Maroun, T. Gacoin, J.-P. Boilot, M. Sangermano and S. Perruchas, *J. Mater. Chem.*, 2011, **21**, 19106-19113.
58. K. W. Hipps and G. A. Crosby, *Inorg. Chem.*, 1974, **13**, 1543-1544.
59. Y. Huang, J. Wang and H. J. Seo, *J. Electrochem. Soc.*, 2010, **157**, J429-J434.
60. A. Barbieri, E. Bandini, F. Monti, V. K. Praveen and N. Armaroli, *Top. Curr. Chem.*, 2016, **374**, 47.
61. H. Xiang, J. Cheng, X. Ma, X. Zhou and J. J. Chruma, *Chem. Soc. Rev.*, 2013, **42**, 6128-6185.
62. E. C.-C. Cheng, W.-Y. Lo, T. K.-M. Lee, N. Zhu and V. W.-W. Yam, *Inorg. Chem.*, 2014, **53**, 3854-3863.
63. S. Lebedkin, T. Langetepe, P. Sevillano, D. Fenske and M. M. Kappes, *J. Phys. Chem. B*, 2002, **106**, 9019-9026.
64. J. Kieffer and D. Karkoulis, *J. Phys. Conf. Ser.*, 2013, **425**, 202012.
65. P. Juhas, T. Davis, C. L. Farrow and S. J. L. Billinge, *J. Appl. Crystallogr.*, 2013, **46**, 560-566.
66. Topas V4.2: General Profile and Structure Analysis Software for Powder Diffraction Data, *Bruker AXS Ltd*, 2008.

Chapter 5: *a*[Au(SR)]$_n$

5.1 Introduction

Gold(I)-thiolate CPs represent a huge crystallization challenge, due to high affinity between gold and sulfur atoms and poor solubility of the formed product. While a few crystalline [Au(SR)]$_n$ CPs were characterized structurally, the structural studies of amorphous products were precluded for a long time, because of the instrumental limitations.

Nowadays, due to the rise of accessibility of new characterization techniques, one can finally get an insight into the structure of these phases.

An article by the team of D. E. Cliffel, [1] is the only structural study of the amorphous gold(I)-thiolate CPs to our knowledge. This work studies the thiolate- protected oligomers, with tiopronin as the ligand. Thanks to the PDF refinement, the authors succeeded to show the formation of [Au(tiopronine)]$_4$ ring, after testing different cycle and chain models.

Thanks to the previous experience with amorphous products during the work on [Au(SPh)]$_n$ [2] in our team, it was decided to conduct its structural investigation to understand the amorphous-crystalline phase change. The study of the series of three products was performed: [Au(SPh)]$_n$, [Au(SMePh)]$_n$ and [Au(SEtPh)]$_n$. The use of methyl and ethyl group between the phenyl ring and the thiol function targeted an increase of the flexibility of the ligand. This could preclude crystallization due to the difficulty of formation of periodic crystalline packing. Thus, it could lead to an amorphous phase. Photophysical characterizations of these three phases were performed. Here, we present the pioneering study of 'structure-properties' correlation of amorphous gold(I)-thiolate CPs.

5.2 Synthesis and Characterization

The amorphous gold thiolates were synthesized via redox reaction between $HAuCl_4$ and excess of the corresponding thiol, thiophenol (HSPh), phenylmethanethiol (HSMePh) and phenylethanethiol (HSEtPh) in methanol, at room temperate or 60°C, similarly to the reported procedure. [2] Pale yellow to white powders *a*[Au(SPh)]$_n$, *a*[Au(SMePh)]$_n$, *a*[Au(SEtPh)]$_n$ were

obtained. Thus, the loss of the color appears to be directly related to the addition of $–CH_2–$ motif.

The PXRD patterns of the three powders exhibit similar features (**Figure 5. 1**): a sharp peak at low angle and a broad diffuse halo between 20 and 40° in 2θ characteristic of a poorly crystallized materials. Further in the text we will call them amorphous.

By application of Bragg's law to the first broad peak, the distances of 1.14 nm, 1.23 nm and 1.31 nm for *a*[Au(SPh)]$_n$, *a*[Au(SMePh)]$_n$, *a*[Au(SEtPh)]$_n$, respectively, were calculated. For *a*[Au(SPh)]$_n$, this distance is close to the distance between helical chains of the crystalline phase. Thus, one can hypothesize, that the structure of the amorphous phase is composed of highly distorted helical chains similar to the ones of the crystalline phase. Gradual shift of the position from *a*[Au(SPh)]$_n$ to *a*[Au(SEtPh)]$_n$ follows the length increase of the ligand and corresponds to a stacking of the organic moieties without interpenetration of the aromatic rings.

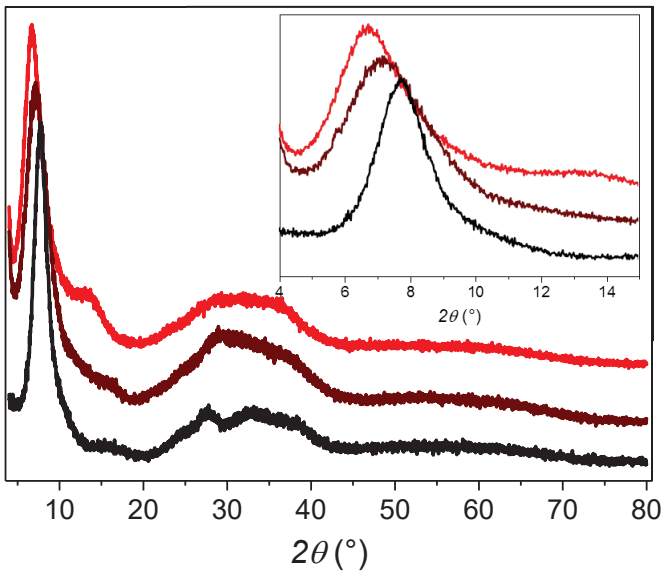

Figure 5. 1 The PXRD patterns of *a*[Au(SPh)]$_n$ (black), *a*[Au(SMePh)]$_n$ (dark red) and *a*[Au(SEtPh)]$_n$ (red). A zoom at low angles is shown as inset.

Based on the SEM images (**Figure 5. 2**), we can state that *a*[Au(SPh)]$_n$ forms large aggregates of around 500 nm, while *a*[Au(SMePh)]$_n$ and *a*[Au(SEtPh)]$_n$ form well-defined spherical nanoparticles of around 80 and 50 nm, respectively.

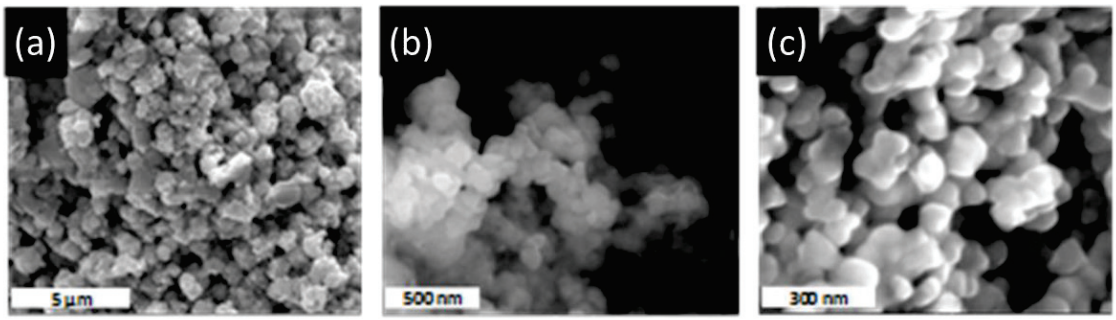

Figure 5. 2 SEM images of (a) *a*[Au(SPh)]$_n$, (b) *a*[Au(SMePh)]$_n$ and (c) *a*[Au(SEtPh)]$_n$.

The FT-IR spectra show characteristic bands of aromatic rings and alkane functions (**Figure 5. 3**). No peak of S-H stretching vibration around 2550 cm^{-1} is observed, confirming the absence of the free ligand and its coordination to the gold via thiolate group.

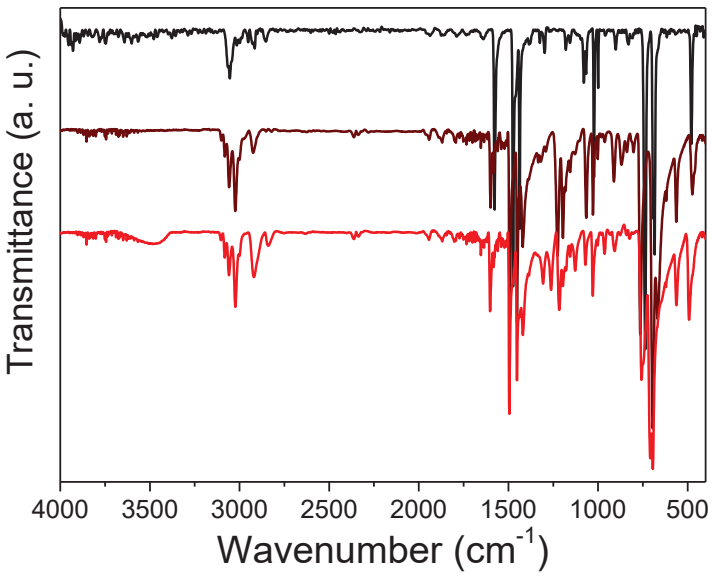

Figure 5. 3 FT-IR spectra of *a*[Au(SPh)]$_n$ (black), *a*[Au(SMePh)]$_n$ (dark red) and *a*[Au(SEtPh)]$_n$ (red).

The thermo-gravimetric analysis confirms the purity of the compounds with an expected metal and organic content. The compounds *a*[Au(SPh)]$_n$, *a*[Au(SMePh)]$_n$ and *a*[Au(SEtPh)]$_n$ start to decompose at 240, 184 and 225 °C, respectively (**Figure 5. 4**).

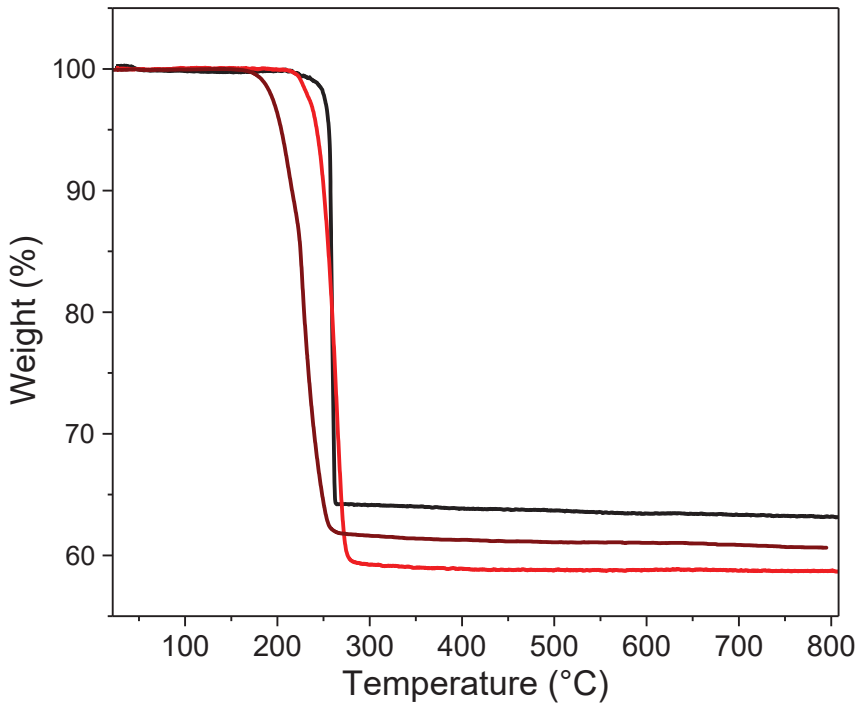

Figure 5. 4 The TGA performed under air at 10°C/min of *a*[Au(SPh)]$_n$ (black), *a*[Au(SMePh)]$_n$ (dark red) and *a*[Au(SEtPh)]$_n$ (red).

5.3 PDF Analysis of Crystalline and Amorphous [Au(SPh)]$_n$

Structural characterization of the samples in the reciprocal space is greatly challenged due to the poor crystallinity of the samples. To overcome this difficulty we analyzed the PDF obtained by total scattering measurements.

Similarly to study of D. E. Cliffel, [1] we investigated structural models of amorphous phase composed by isolated rings and by helical chains.

Firstly, we discuss the PDF of crystalline [Au(SPh)]$_n$ and compare it to the amorphous counterpart *a*[Au(SPh)]$_n$. Secondly, the PDFs of *a*[Au(SMePh)]$_n$ and *a*[Au(SEtPh)]$_n$ is compared to that of *a*[Au(SPh)]$_n$.

Reduced structure functions *G(r)* and *F(Q)* [3] of samples [Au(SPh)]$_n$ and *a*[Au(SPh)]$_n$ are shown in the **Figure 5. 5**. A qualitative inspection of the figure indicates that crystalline sample of [Au(SPh)]$_n$ has well-defined Bragg peaks and PDF oscillations extending over 250 Å. It indicates that the size of the structure coherent domains exceed this value. Observed decay of PDF with increasing *r* is essentially due to the relatively modest spatial resolution of the

diffraction experiment. For *a*[Au(SPh)]$_n$, the Bragg peaks in *F(Q)* are replaced by broad oscillations, characteristic for amorphous or disordered materials.

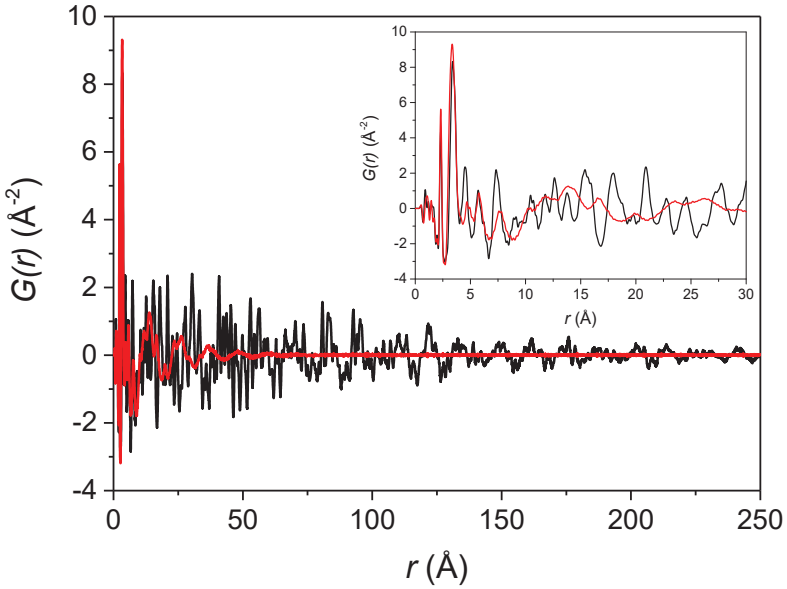

(a)

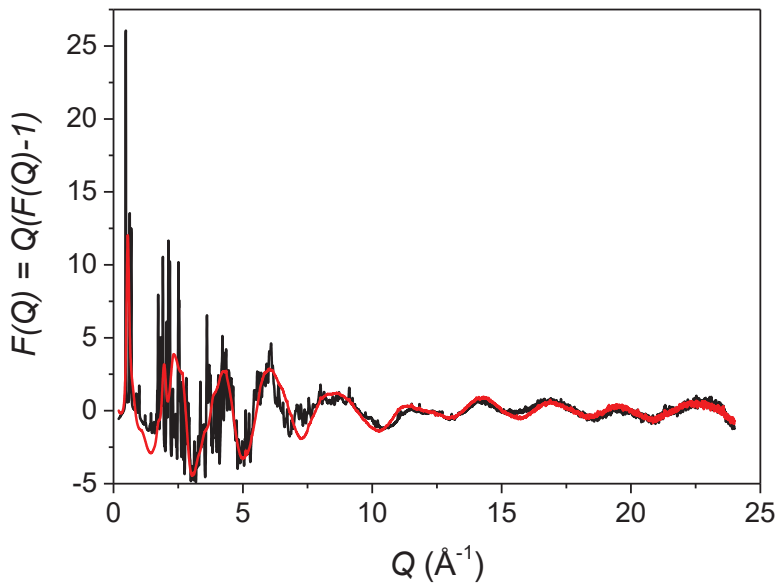

(b)

Figure 5. 5 Pair distribution function *G(r)* (a) and reduced structure function *F(Q)* (b) of samples *a*[Au(SPh)]$_n$ (red) and crystalline [Au(SPh)]$_n$ (black). The short r part of the PDFs up to 30 Å is shown in the inset of (a).

In the PDFs of *a*[Au(SPh)]$_n$ and crystalline [Au(SPh)]$_n$, the two first peaks, with maximum at 2.3 Å and 3.4 Å correspond to the shortest Au-S and Au-Au bonds, respectively. They are almost identical for the two samples (**Figure 5. 6** and **Table 5. 1**). The most significant difference lies in the exchange of the well-defined oscillations of the crystalline phase to the broad features of amorphous phase that are present up to 50 Å. This distance corresponds to the maximum of structural coherence length. It indicates, that the global structural arrangement is markedly modified in the amorphous phase compared to the crystalline one. Nevertheless, some level of structural coherence is retained up to relatively large distances (several tens of Å). This could be interpreted as the persistence of positional correlations between the double helical chains (up to 50 Å), with a short structural coherence along the double helical chains (up to 9 Å). In order to verify that the crystal structure of [Au(SPh)]$_n$, determined by standard crystallographic techniques, is also valid at the local scale, we have performed a refinement of its PDF using the MolPDF software. [4]

Table 5. 1 Main Au-S and Au-Au distances (Å) at short *r*-range from PDF data and MolPDF refinement.

Distance	Crystalline [Au(SPh)]$_n$			Amorphous *a*[Au(SPh)]$_n$	
	Reported average structure[5]	Observed PDF	Model refined in MolPDF	Observed PDF	Model refined in MolPDF
A	2.289(2) 2.332(2)	2.31(1)	2.276(9) 2.33(1)	2.32(1)	2.27(3) 2.32(5)
B	3.323(3) 3.331(3)× 3.369(3)× 3.603(3)× 3.610(3)	3.3(2) 3.5(2) 3.64(8)	3.318(8) 3.359(9)× 3.457(7)× 3.555(8)× 3.685(7)	3.20(4) 3.52(4)	3.19(3) 3.27(3)× 3.34(2)× 3.55(3)× 3.68(2)
C	4.031(3) 4.533(4)	4.16(6) 4.54(4)	4.160(6) 4.523(8)	4.77(4)◊	3.81(2) 4.69(2)
D	5.648(4) 6.066(3)	5.71(9)	5.634(8) 6.145(7)	5.8(6)◊	5.71(3) 6.04(2)

× Interchain distances; ◊ obtained from the weighted arithmetic mean of several peaks.

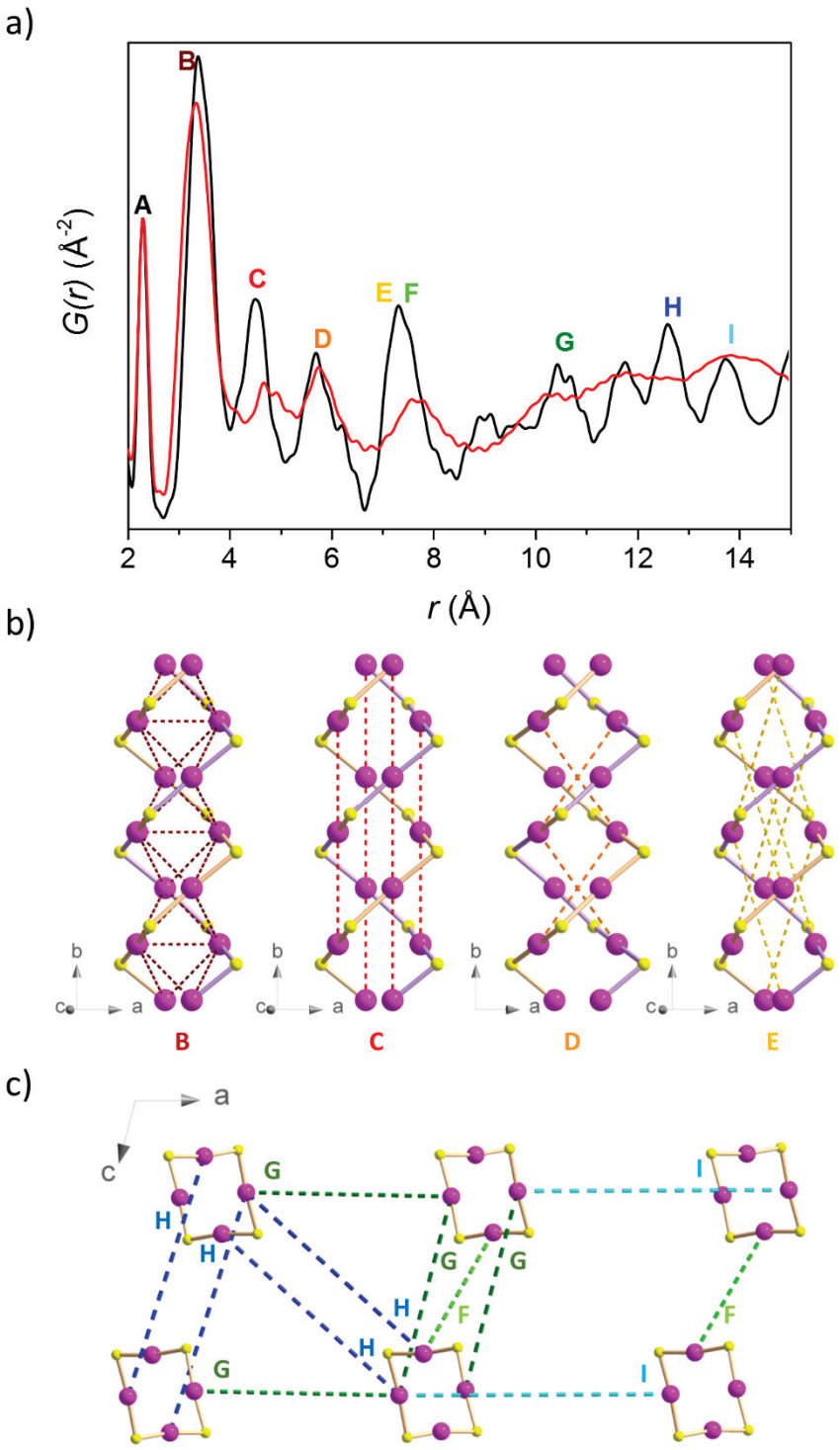

Figure 5. 6 (a) PDF data for *a*[Au(SPh)]$_n$ (red) and crystalline [Au(SPh)]$_n$ (black). B-E peak labels correspond to the indicated Au-Au distances in the double helix (b), while F-I correspond to some distances between Au atoms of neighboring helices (c). Pink, Au; yellow, S; C and H are omitted.

The PDF mainly originates from the gold and the sulfur atoms. Consequently, most features of the PDF correspond to the contribution of Au-Au atomic pairs. The only exception

is the first peak at 2.3 Å which arises solely due to the Au-S pairs (see Experimental Part, **Figure 5. 14**). Known crystallographic structure of $[Au(SPh)]_n$ solved in *C* 2/*c* space group was used as starting model for the refinement, disregarding the hydrogen atoms.[5] First neighbor C-C distances, the C-C-C and C-C-S angles were constraint to their starting values. Atoms of the same elements had equal isotropic thermal parameters, which were varied along with the atomic positions, cell parameters, scale factor and a sharpening factor. It allows to account for difference between the Debye-Waller factor of intramolecular and other distances. It was applied to the restrained C-C bonds. The refinement was carried out between 1.7 and 30.0 Å. The results are reported in the **Table 5. 1** and the refinement plot in the **Figure 5. 7** (a). The figure shows a relatively satisfactory agreement for this type of soft material with distances between the refined positions and the original ones from reference.[2] They do not exceed 0.2 Å for gold and sulfur atoms. The main difference lies in relatively small rotations of the molecules (**Figure 5. 7** (b)). They are difficult to confirm, given the weak contribution of the molecules to the refined patterns. Both for the present PDF refinement and the original Rietveld refinement of reference.[2] However, the present PDF analysis confirms the validity of the crystallographic structure at the local scale.

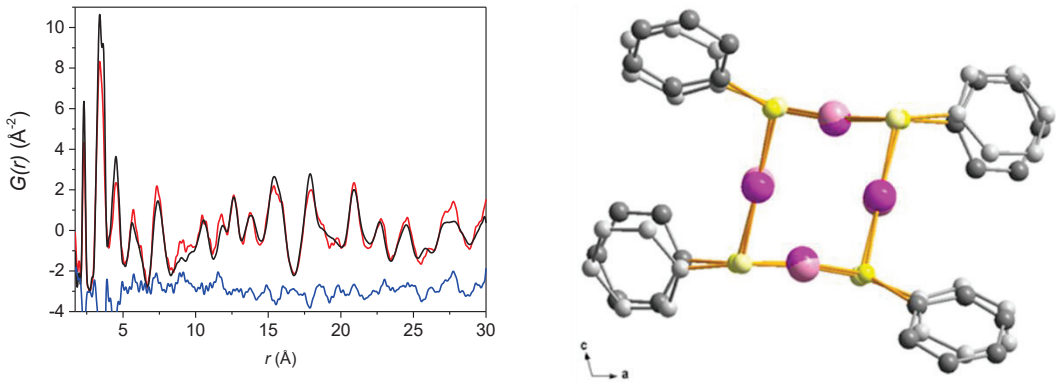

(a) (b)

Figure 5. 7 (a) Result of the PDF refinement using the MolPDF software for the crystalline phase of $[Au(SPh)]_n$: experimental data (red), calculation (black) and difference (blue). (b) Projection along *b* axis of the reported structure [2] of $[Au(SPh)]_n$ (light color atoms) and the one refined with MolPDF. Pink, Au; yellow, S; gray, C.

The refined by MolPDF structure of the crystalline phase of $[Au(SPh)]_n$ was used as a starting model for the refinement of the structural model of the amorphous phase. We kept the *C* 2/*c* monoclinic symmetry and applied the same type of structure constraints as we used

for the crystalline phase. The refinement was carried out between 1.7 Å and 12.0 Å, which mainly corresponds to the distances within a chain. At longer distances, roughly periodic oscillations with decreasing amplitude persist up to ~50 Å. The approximate period of ~11.5 Å is close to the interchain distance in the crystalline compound, which confirms that a global interchain positional correlation is still present in the amorphous phase. Results of the refinement are given in **Figure 5. 8** and **Table 5. 1**. The agreement is poorer than in the case of the crystalline sample, however, the fit reproduces well all the Au-S and Au-Au distance peaks up to ~9 Å. It indicates the preservation of the double helix chain coherence up to two unit cells along the *b* axis on average. It corresponds to six gold atoms along one helix (**Figure 5. 8** (a)). One can propose that the Au-S covalent bonds would tend to preserve the structural coherence along the chains. Disorder would be introduced through displacements/rotations between the molecules weakly linked through C-H···π interactions between phenyl rings. The largest local structure modification with respect to the crystalline phase is a displacement of ~0.3 Å of both Au atoms in the *(bc)* plane. The interchain Au-Au distances inside of one double helix are closer in amorphous phase (3.82 Å and 3.27 Å) than in crystalline phase (4.15 Å and 3.35 Å) (**Figure 5. 8** (b)).

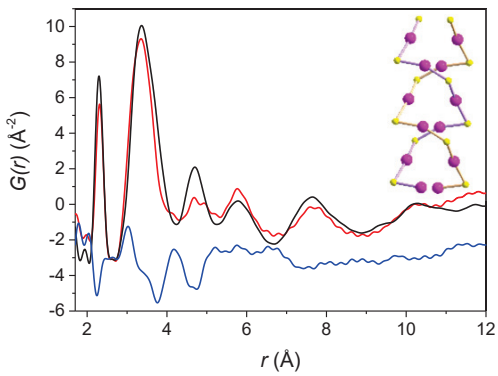

(a)

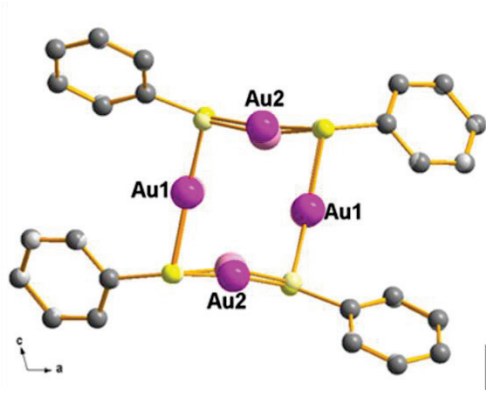

(b)

Figure 5. 8 (a) Result of the PDF refinement achieved with help of MolPDF software for the *a*[Au(SPh)]$_n$ using double-helix model (shown on inset; pink, Au; yellow, S; C and H are omitted). Experimental data (red), calculation (black), difference (blue). (b) Projection along *b* axis of the structures of [Au(SPh)]$_n$ and *a*[Au(SPh)]$_n$ (light color atoms) both refined with MolPDF. Pink, Au; yellow and orange, S; gray, C.

The PDF data of *a*[Au(SPh)]$_n$ were also refined using a model consisting of tetramer rings like it was performed in the publication of D. E. Cliffel.[1] It is also a common trend of gold

thiolates to form cyclic structures with bulky ligands.[6, 7] Moreover, several tetrameric oligomers, $[Au(SR)]_4$, have been reported as intermediates in the formation or fragmentation of gold thiolate clusters.[8, 9] The distorted eight-membered ring model was built based on the refined double-helix model of the crystalline phase. Refinement was achieved by displacement of half of the tiophenolate molecules by 0.5 f. u. along the *b* axis (see Experimental Part, **Figure 5. 15**). Given the preservation of the atomic positions of gold atoms, the main difference between the helix and tetrameric ring models are the more acute Au-S-Au angles, in the latter model of 159° and 170°, (vs. 104° and 140°, see Experimental Part, **Table 5. 3**). Despite the fact, that the nearest Au-S and Au-Au distances (which correspond to the contacts inside of the ring) are well described by this model, it fails to reproduce longer correlations at 4.5 Å and 7.7 Å (which correspond to Au-Au contacts between neighboring tetramers) (see Experimental Part, **Figure 5. 16** and **Figure 5. 17**). It results in worse agreement factors. The situation is opposite to the one described by D. E. Cliffel. In addition, the polymeric nature of $a[Au(SPh)]_n$ is in agreement with the insolubility of product, unlikely to the reported soluble tetrameric species.[10] Nevertheless, the presence of tetrameric motifs defects intercalated in a double helix could occur, what would reduce the coherence length.

5.4 Comparison of PDFs of $a[Au(SPh)]_n$, $a[Au(SMePh)]_n$ and $a[Au(SEtPh)]_n$

The three amorphous compounds $a[Au(SPh)]_n$, $a[Au(SMePh)]_n$ and $a[Au(SEtPh)]_n$ show PDFs with similar features (**Figure 5. 9** (a)). The peaks corresponding to the first Au-S and Au-Au are placed at 2.3 Å and 3.5 Å for all three materials. Thus, one can propose that all three amorphous phases are formed by disordered double-helix Au(I)-S core. At large *r*, only broad features are observed, which are damped out to disappear at around 50 Å (**Figure 5. 9** (b)). Similarly to $a[Au(SPh)]_n$, same interpretation holds for $a[Au(SMePh)]_n$ and $a[Au(SEtPh)]_n$ as due to the positional correlations between the double helices. Expectedly, the shift of these broad features to longer distances is related to the larger thiolate ligands in $a[Au(SMePh)]_n$ and $a[Au(SEtPh)]_n$.

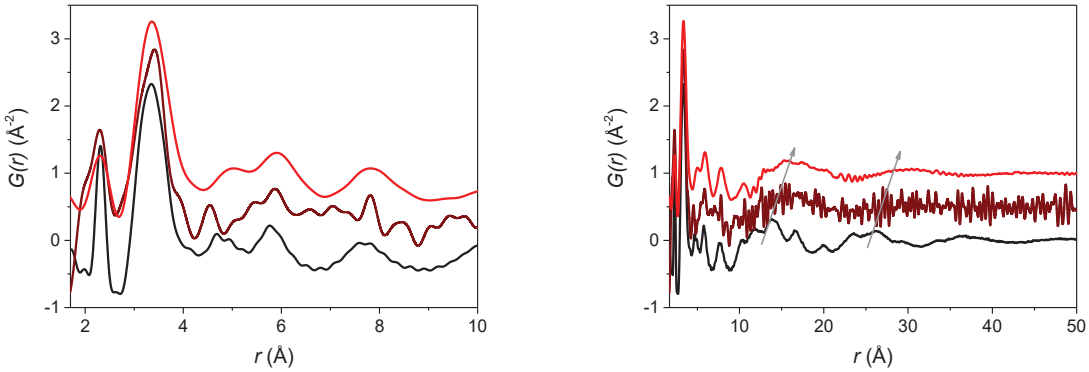

Figure 5. 9 Comparison of the pair distribution functions *G(r)* of samples (a) *a*[Au(SPh)]$_n$ (black), *a*[Au(SMePh)]$_n$ (dark red) and *a*[Au(SEtPh)]$_n$ (red); (b) the region of large *r* part of the PDFs up to 50 Å; arrows are indicating shift of the position of broad features corresponding to the correlations between the double helices. Apparent difference of profiles is caused by different instrument resolution.

5.5 Photophysical Properties

The three amorphous compounds exhibit allowed high-energy absorption between λ_{abs} = 200-400 nm (**Figure 5. 10**), which is assigned to a π–π* transition of the phenyl group.[11] It might originate from the metal-perturbed IL or LMCT transition.[12,13] Slight shift of the absorption band from *a*[Au(SPh)]$_n$ to *a*[Au(SEtPh)]$_n$ towards shorter wavelength is in agreement with the loss of the color after the addition of –CH_2– group.

Crystalline [Au(SPh)]$_n$ is luminescent at room temperature, while *a*[Au(SPh)]$_n$ is not. Photophysical studies at low temperature were performed (**Figure 5. 11** (a)). It was found to be emissive at low temperature from 250 K. The position of the emission maximum is slightly red shifted from 675 nm to 690 nm for the amorphous product (**Figure 5. 11** (b)). The width of the emission peak is bigger for the amorphous product (3340 cm^{-1}) than for the crystalline one (1380 cm^{-1}) (93 K). The Stokes shift is more significant for amorphous phase: 9780 cm^{-1} vs. 16435 cm^{-1} (**Table 5. 2**).

Less intense emission of *a*[Au(SPh)]$_n$ can be explained by the energy loss in the defects that are omnipresent in amorphous materials. The presence of defects could explain significant width of the peak.

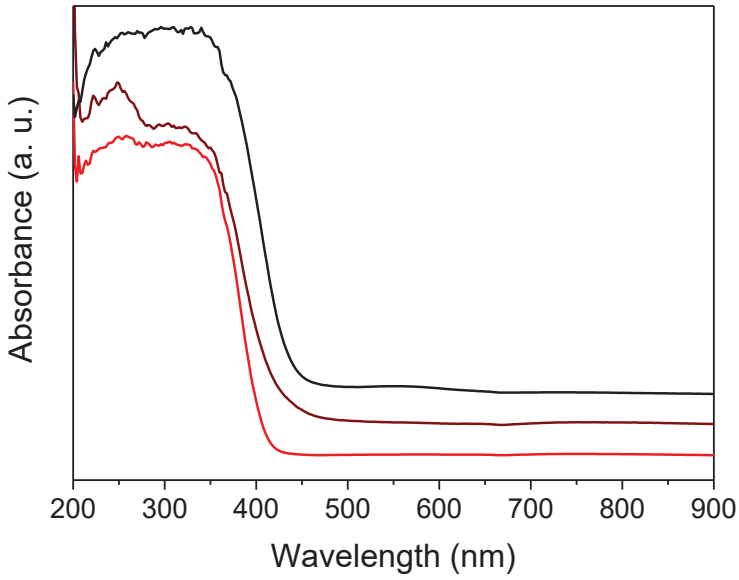

Figure 5. 10 UV-vis spectra of *a*[Au(SPh)]$_n$ (black), *a*[Au(SMePh)]$_n$ (dark red) and *a*[Au(SEtPh)]$_n$ (red) obtained in the solid state at the room temperature.

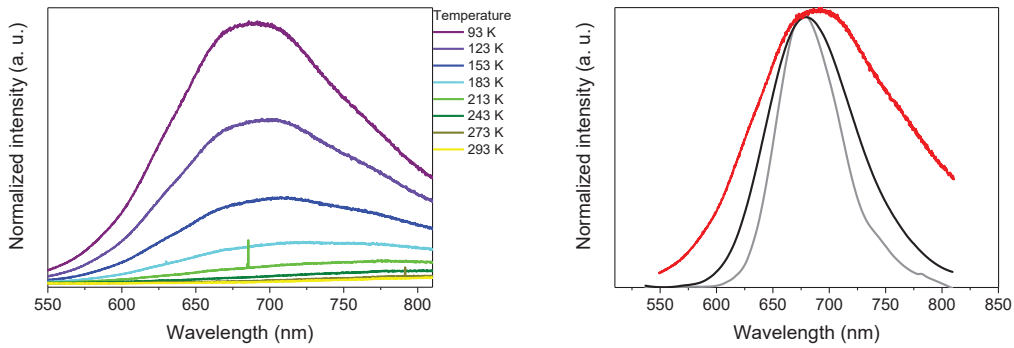

(a) (b)

Figure 5. 11 (a) Variation of emission spectra (λ_{exc} =412 nm) of *a*[Au(SPh)]$_n$ in the solid state with the temperature. (b) Comparison of emission spectra of the crystalline [Au(SPh)]$_n$ at 293 K (black) and at 93 K (grey) (λ_{exc} = 320 nm, λ_{em} = 675 nm) and *a*[Au(SPh)]$_n$ at 93 K (red) (λ_{exc} = 412 nm, λ_{em} = 690 nm) obtained in solid state.

Table 5. 2 Emission, excitation wavelengths and Stokes shift of the studied CPs (93 K).

Product	Excitation, nm	Emission, nm	Stokes shift, cm^{-1}
[Au(SPh)]$_n$ crystalline	320	675	16435
a[Au(SPh)]$_n$	412	690	9779
a[Au(SMePh)]$_n$	372	675	12067
a[Au(SEtPh)]$_n$	344	655	13803

Closely placed emission peaks of amorphous and crystalline phases suggest the same nature of LUMO states and eventually the same mechanism involved in the luminescence process – LMMCT. [2] Small red shift (320 cm^{-1}) of the *a*[Au(SPh)]$_n$ can be attributed to the slightly shorter (in average) Au-Au distances[14] of the amorphous phase.

a[Au(SPh)]$_n$ and *a*[Au(SEtPh)]$_n$ are not luminescent at room temperature, while *a*[Au(SMePh)]$_n$ is weakly emissive (**Figure 5. 12**). Three amorphous samples are quite similar in term of structural disorder. Therefore, an explanation for the presence of the emission of *a*[Au(SMePh)]$_n$ at room temperature could be related to some different electronic transitions induced by the ligand. At 93 K, *a*[Au(SMePh)]$_n$ and *a*[Au(SEtPh)]$_n$ emit similar red emission centered at 675 nm and significant Stokes shift > 12000 cm^{-1}, (**Figure 5. 13** and **Table 5. 2**) indicating phosphorescent mechanism.

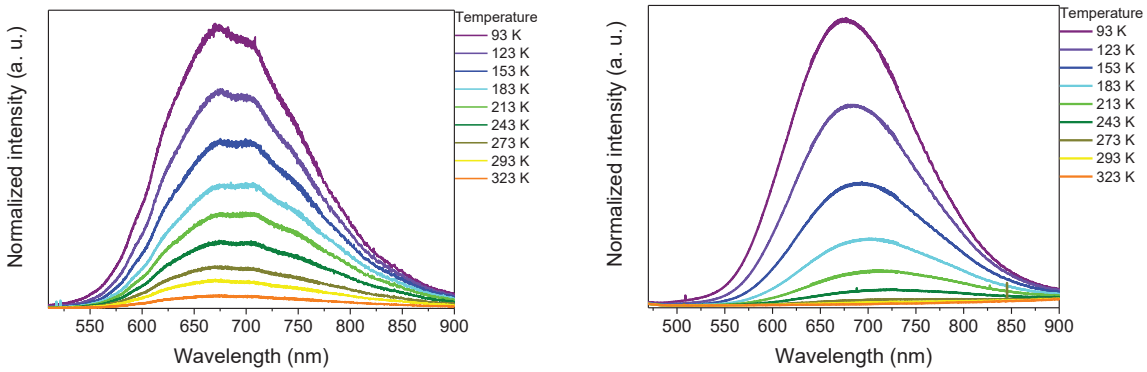

(a) (b)

Figure 5. 12 Variation of the emission spectra of *a*[Au(SMePh)]$_n$ (λ_{exc} = 372 nm) and *a*[Au(SEtPh)]$_n$ (λ_{exc} = 340 nm) in the solid state with the temperature change.

Close emission positions suggest that all three compounds have closely lying LUMOs, probably of a similar nature. Thus, we tentatively attribute the luminescent origin of all three compounds to LMMCT.

The shift of the positions of excitation peak centered at 412 nm, 372 nm and 340 nm for the three samples from *a*[Au(SPh)]$_n$ to *a*[Au(SEtPh)]$_n$ can be explained by the different distribution of the electronic density of the HOMO level on the different organic ligands.

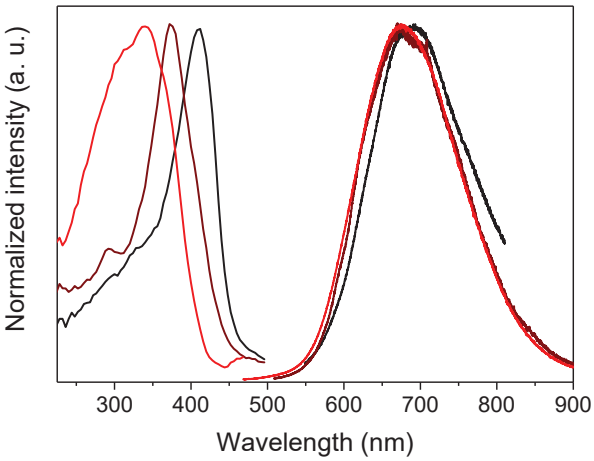

Figure 5. 13 Emission-excitation spectra of *a*[Au(SPh)]$_n$ (black, λ_{exc} = 412 nm, λ_{em} = 690 nm), *a*[Au(SMePh)]$_n$ (dark red, λ_{exc} = 372 nm, λ_{em} = 675 nm) and *a*[Au(SEtPh)]$_n$ (red, λ_{exc} = 340 nm, λ_{em} = 675 nm) obtained in solid state at 93 K.

The luminescence lifetimes are rather close for crystalline (9.5 µs) and amorphous (13.7 µs) phases of [Au(SPh)]$_n$, as well as the one of *a*[Au(SEtPh)]$_n$[a] (8.2 µs) (Appendix B). The micro-second range of the values confirms phosphorescent origin of the luminescence. The similarity of the values is another indication of the same mechanism which gives rise to the luminescence in the different phases.

[a] Data for *a*[Au(SMePh)]$_n$ was not collected.

5.6 Conclusions

We have seen that PDF is a powerful mean that can be used to confirm previously solved crystallographic structure, as it was in the case of crystalline $[Au(SPh)]_n$. Above all, it can give valuable structural information about the amorphous phases that is difficult to obtain by other means of analysis.

The comparison of the PDFs of crystalline $[Au(SPh)]_n$ and the three amorphous phases shows resemblance of their local structures. All of them are formed with the double helix chains. In the amorphous phases, the coherence is preserved only up to two unit cells along the chain.

Based on the structural similarity, we can attribute the same luminescence mechanism – LMMCT to all compounds in question. The proximity of the structures let us assign the modification of the excitation energy to the electronic effect of different ligands.

There is one interesting property that has not been discussed here, but is worth mentioning. These three products have shown an exceptional ability to form transparent glasses upon a soft mechanical pressurization. This opens a possibility to classify gold(I)-thiolate CPs as a new group capable of glass formation.

5.7 Experimental Part

5.7.1 Synthesis

Synthesis of *a*[Au(SPh)]$_n$: the same procedure as described previously was used.[5]

Synthesis of *a*[Au(SMePh)]$_n$: to a solution of $HAuCl_4 \cdot 3H_2O$ (100 mg, 0.253 mmol, 1 eq.) in methanol (10 mL) phenylmethanethiol (178 µL, 1.518 mmol, 6 eq.) was added, and stirred for 18 hours at 60°C. Pale yellow product was recovered by centrifugation (4000 rpm, 10 min), washed by methanol and collected via centrifugation again. The last step was repeated three times in order to completely remove the salts and the disulfide which is formed in the reaction. Yield: 75 % (70 mg). Chemical Formula: C_7H_7AuS. Molecular Weight: 320.16. Gold content from TGA (calc.) wt%: 60.7 (61.5).

Synthesis of *a*[Au(SEtPh)]$_n$: to a solution of $HAuCl_4 \cdot 3H_2O$ (200 mg, 0.508 mmol, 1 eq.) in methanol (10 mL) phenylethanethiol (408 µL, 3.047 mmol, 6 eq.) was added, and stirred for 1 hour at room temperature. White product was recovered by centrifugation (4000 rpm, 10 min), washed by ethanol and collected via centrifugation again. The last step was repeated three times in order to completely remove the salts and the disulfide which is formed in the reaction. Yield: 61 % (120 mg). Chemical Formula: C_8H_9AuS. Molecular Weight: 334.19. Gold content from TGA (calc.) wt%: 58.6 (58.9).

5.7.2 Total Scattering Measurements

Finely powdered samples were loaded into 0.7 mm diameter borosilicate glass capillaries. Room temperature X-ray diffraction patterns for crystalline and amorphous phase of [Au(SPh)]$_n$ were collected at the ID22 beamline of the ESRF, Grenoble, France, at a wavelength of λ = 0.206773 Å (60 keV). We used a Perkin-Elmer flat panel detector located at 38.5 cm from the sample (Q_{max} = 24 Å^{-1}). Diffraction images were corrected and transformed to 1D patterns using the PyFAI software. [16] For *a*[Au(SMePh)]$_n$ and *a*[Au(SEtPh)]$_n$ samples, the data were collected using a Bruker kappaCCD diffractometer equipped with Incoatec IµS microsource for AgKα radiation (λ = 0.5608 Å, 22.1 keV) and a CCD camera located at 10 cm from sample. It was rotated around its axis by 180° during the acquisition. 36 images were collected with step of 3° from 2θ = 0° to 105°. Images were then integrated and averaged to yield a 1D pattern up to Q_{max} = 17 Å^{-1}. In all cases, data from an empty capillary were also collected for background

subtraction and standard samples (LaB_6, CeO_2 and Ni) were used to characterize the instrumental resolution function. The reciprocal space data were converted to PDFs using the PDFgetX3 software. [17] For the laboratory data, a damping correction using the Lorch function was applied prior to Fourier transform.

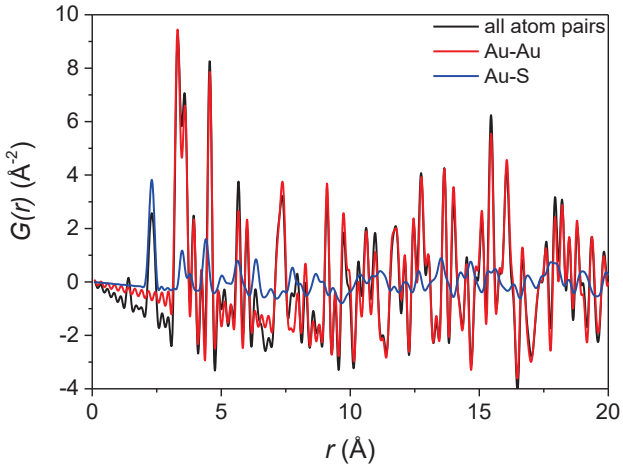

Figure 5. 14 Comparison of simulated PDF of $[Au(SPh)]_n$ using all atom pairs (black), Au-Au pairs only (red) and Au-S pairs only (blue).

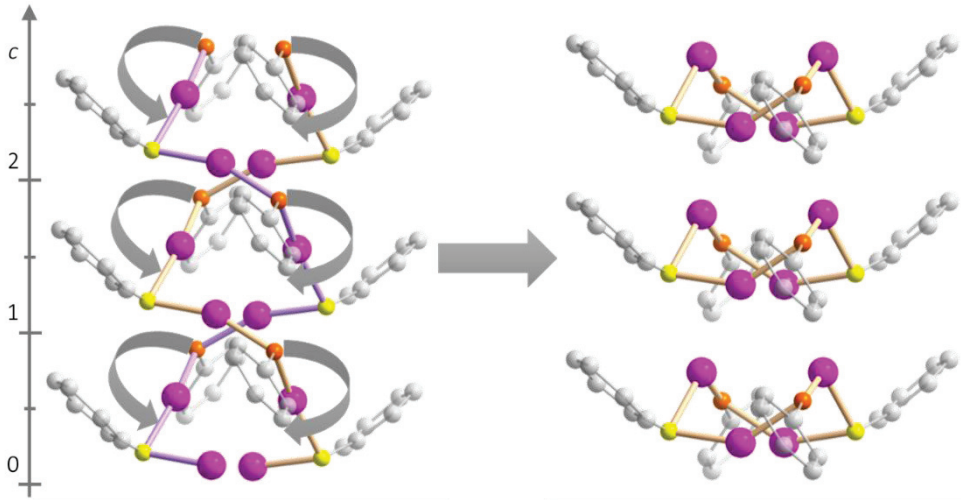

Figure 5. 15 Schematic representation of the tetramer ring model transformation from the double helix model of $[Au(SPh)]_n$. Pink, Au; yellow and orange, S; gray, C.

Table 5. 3 Bonds and angles observed for the double helix and tetramer ring models used for the PDF refinements.

	Double helix model	Tetramer ring model
Au-S, Å	2.28(4)	1.92(6)
	2.28(5)	2.31(5)
	2.32(5)	2.34(4)
	2.36(3)	2.36(3)
Au-S-Au, °	86(2)	86(2)
	108(2)	103(2)
S-Au-S, °	159(2)	104(2)
	166(2)	140(2)

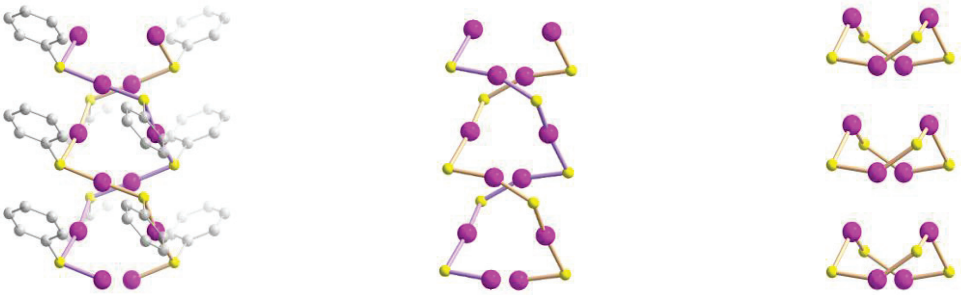

(a) (b) (c)

Figure 5. 16 Comparisons of the crystalline structure of $[Au(SPh)]_n$ (a) and the models obtained by PDF refinements with MolPDF software for *a*$[Au(SPh)]_n$ sample by using the double-helix (b) and the tetramer ring (c) models. Pink, Au; yellow, S; gray, C.

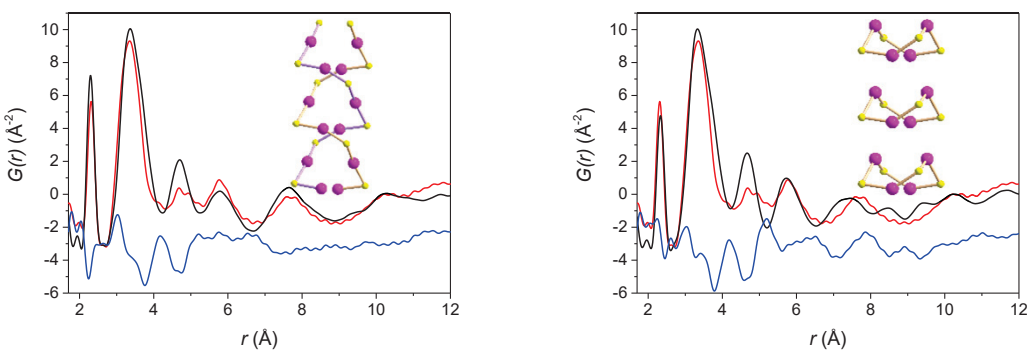

(a) (b)

Figure 5. 17 Results of the PDF refinement using the MolPDF software for the *a*$[Au(SPh)]_n$ sample using double-helix (a) and tetramer ring (b) models (models are shown on insets; pink, Au; yellow, S; C and H are omitted). Experiment (red), calculation (black), difference (blue).

5.8 References

1. C. A. Simpson, C. L. Farrow, P. Tian, S. J. L. Billinge, B. J. Huffman, K. M. Harkness and D. E. Cliffel, *Inorg. Chem.*, 2010, **49**, 10858-10866.
2. C. Lavenn, L. Okhrimenko, N. Guillou, M. Monge, G. Ledoux, C. Dujardin, R. Chiriac, A. Fateeva and A. Demessence, *J. Mater. Chem. C*, 2015, **3**, 4115-4125.
3. D. A. Keen, 2001, **34**, 172-177.
4. J. Rodriguez-Carvajal and A. Bytchkov, *Institut Laue-Langevin, Grenoble, France*, 2016.
5. C. Lavenn, L. Okhrimenko, N. Guillou, M. Monge, G. Ledoux, C. Dujardin, R. Chiriac, A. Fateeva and A. Demessence, *J. Mater Chem. C*, 2015, **3**, 4115-4125.
6. W. Wojnowski, B. Becker, J. Sassmannshausen, E.-M. Peters, K. Peters and H. G. von Schnering, *Z. Anorg. Allg. Chem.*, 1994, **620**, 1417.
7. P. J. Bonasia, D. E. Gindelberger and J. Arnold, *Inorg. Chem.*, 1993, **32**, 5126-5131.
8. K. M. Harkness, D. E. Cliffel and J. A. McLean, *Analyst*, 2010, **135**, 868-874.
9. A. Dass, A. Stevenson, G. R. Dubay, J. B. Tracy and R. W. Murray, *J. Am. Chem. Soc.*, 2008, **130**, 5940-5946.
10. C. A. Simpson, C. L. Farrow, P. Tian, S. J. L. Billinge, B. J. Huffman, K. M. Harkness and D. E. Cliffel, *Inorg. Chem.*, 2010, **49**, 10858-10866.
11. J. S. Lim, H. Choi, I. S. Lim, S. B. Park, Y. S. Lee and S. K. Kim, *J. Phys. Chem. A*, 2009, **113**, 10410-10416.
12. C.-H. Li, S. C. F. Kui, I. H. T. Sham, S. S.-Y. Chui and C.-M. Che, *Eur. J. Inorg. Chem.*, 2008, **2008**, 2421-2428.
13. R. Langer, M. Yadav, B. Weinert, D. Fenske and O. Fuhr, *Eur. J. Inorg. Chem.*, 2013, **2013**, 3623-3631.
14. J. M. Forward, D. Bohmann, J. P. Fackler and R. J. Staples, *Inorg. Chem.*, 1995, **34**, 6330-6336.
15. T. D. Bennett, Y. Yue, P. Li, A. Qiao, H. Tao, N. G. Greaves, T. Richards, G. I. Lampronti, S. A. T. Redfern, F. Blanc, O. K. Farha, J. T. Hupp, A. K. Cheetham and D. A. Keen, *J. Am. Chem. Soc.*, 2016, **138**, 3484-3492.
16. J. Kieffer and D. Karkoulis, *Journal of Physics: Conference Series*, 2013, **425**, 202012.
17. P. Juhas, T. Davis, C. L. Farrow and S. J. L. Billinge, *J. Appl. Crystallogr.*, 2013, **46**, 560-566.

Conclusions

This work was dedicated to the understanding of the correlation of structure and properties of new $[M(SR)]_n$ CPs. Use of solvothermal synthetic conditions and techniques such as PXRD and PDF let us shed a light on the structure of $[M(SR)]_n$ CPs.

The work illustrated an influence of different parameters on the structure formation (see Appendix A, **Table A.1**). A systematic study of the role of the position of substituent and comparison with unsubstituted phenylthiolated CPs showed following trends. The use of *para*-substituted ligands leads to a formation of 2D inorganic networks. They often exhibit double or even triple emission properties. The use of *meta*-substituted ligand also results in 2D networks. However, the steric hindrance (near the coordination site, in *ortho*-substituted ligand) leads to the decrease of dimensionality to 1D networks. 1D CPs exhibit a single emission peak of low energy. Use of various metals let to obtain an emission in the range from orange to NIR part of the spectrum.

Both groups of CPs, with $–CO_2H$ or $–CO_2Me$, form 2D networks. However, inside of the inorganic layer $[MS]_n$ the atoms form different patterns. This illustrates a non-negligible role of hydrogen bonds in structure formation.

The comparison of CPs based on copper, silver and gold show that the first two, copper- and silver-based CPs, have more in common. Both form resembling patterns – both predominantly form structures based on hexagonal tiles. On the other hand, gold-based CPs form different $[MS]_n$ arrays due to their common linear or angular geometry.

The use of ligands with flexible points has proven to be a good strategy towards formation of amorphous CPs. Therefore $[Au(SR)]_n$ CPs are a new class of *a*CP, which were previously represented mainly by imidazole- and triazole-based CPs.

It is often reasonable to assume that, two compounds which share similar structures exhibit similar properties. In this context, the case of $[Au(m\text{-}SPhCO_2H)]_n$ is worth mentioning. This CP has structure similar to its *para*-substituted counterpart. However, it shares its

properties with structurally different CP. This example points out a necessity to continue the study with the special attention to in-depth understanding of the origin of photophysical properties via TD-DFT calculi.

As perspectives, the conductivity measurements should be considered. Some of the reported $[Cu(SR)]_n$ CPs have already shown their interest for this kind of properties. Therefore, next natural step would be to study the correlation of structure and conductivity for these CPs in finer details.

Relatively to the properties discussed in this work, XANES S K-edge and Au L-edge measurements will be performed. It will give the information about the position of the electronic orbitals. This will help to rationalize the observed photophysical properties.

The synthesis of CPs with $–CO_2Me$ in *meta*- and *ortho*-positions and their comparison with CPs presented in this work will further illustrate the role of weak interactions and steric hindrance. The use of the ligands with substituents exhibiting similar electronic effect and of similar size (-COH, -COMe, etc.) will help to better pinpoint the correlation between the electronic effect of the ligand and photophysical properties. Finally, the use of more complicated ligands with more and different substituents, as well as multidentate thiolate ligands (in order to generate 3D networks) will further uncover the richness of the structural arrays and properties. Furthermore, it will probably expand the potential applications which now already list an illumination and optical thermometry.

Appendix A. Experimental Part

A.1 Experimental Part

Chemicals. Copper (II) chloride dihydrate ($CuCl_2 \cdot 2H_2O$, ≥ 99 %), thiophenol (HSPh, > 99 %), phenylethanethiol (HSEtPh, 98 %), THF, hydrochloric acid (HCl, 37 %, ACS reagent), nitric acid (HNO3, ≥ 65 %) and sulfuric acid (H_2SO_4, 95-97 %) were purchased from Sigma Aldrich. *para*-mercaptobenzoic acid (or *p*-$HSPhCO_2H$) (> 95.0 %), *meta*-mercaptobenzoic acid (or *m*-$HSPhCO_2H$) (> 97.0 %), *ortho*-mercaptobenzoic acid (or *o*-$HSPhCO_2H$) (> 90.0 %), phenylmethanethiol (HSMePh, 96 %) were purchased from TCI. Copper (II) oxide (Cu_2O, ≥ 99.9 % metal basis), silver (I) nitrate ($AgNO_3$, 99+ %), tetrachloroauric acid trihydrate ($HAuCl_4 \cdot 3H_2O$, ≥ 49 % Au basis) were purchased from Alfa Aesar. Copper (II) acetate monohydrate ($Cu(CH_3COO)_2 \cdot H_2O$, 98+ %) was purchased from Avocado. Methanol, ethanol, acetone and DMF were purchased from VWR Chemicals. All reagents and solvents were used without further purification.

para-methylmercaptobenzoate (*p*-$HSPhCO_2Me$) was obtained by reaction in MeOH at reflux in acidified medium (with H_2SO_4) overnight.

Routine PXRD. Routine powder X-ray diffraction was carried out by a Bruker D8 Advance A25 diffractometer using Cu Kα radiation equipped with a 1-dimensional position-sensitive detector (Bruker LynxEye). XR scattering was recorded between 4° and 90° (2θ) with 0.02° steps and 0.5 s per step (28 min for the scan). Divergence slit was fixed to 0.2° and the detector aperture to 192 channels (2.95°).

SEM. SEM images were obtained by FEI Quanta 250 FEG scanning electron microscope. Samples were mounted on stainless pads and sputtered with Au/Pd alloy to prevent charging during observation.

FTIR. The infrared spectra were obtained by a Bruker Vector 22 FT-IR spectrometer with KBr pellets at room temperature and registered from 4000 cm^{-1} to 400 cm^{-1}.

TGA. Thermo-gravimetric analysis was performed by a TGA/DSC 1 STARe System from Mettler Toledo. Around 5 mg of sample was heated at a rate of 40 °C.min^{-1}, in a 70 μL alumina crucible, under the air atmosphere (20 mL.min^{-1}).

UV-vis. UV-vis absorption spectra were obtained by a LAMBDA 365 UV/Vis Spectrophotometer from Perkin Elmer in solid state at room temperature.

Elemental analysis. Sulphur content is determined by full combustion at 1320-1360°C under O_2 stream and analysis of SO_2. It is titrated in a coulometric-acidimetric cell. Carbon and hydrogen percentages are determined by full combustion at 1030-1070°C under O_2 stream and transformed into CO_2 and H_2O. They are titrated on a coulometric detector. Analysis precision is 0.3% absolute for carbon, sulfur and hydrogen.

Photoluminescence excitation and emission spectra measurements. For those compounds which were used for photophysical studies, PXRD was always measured to exclude presence of impurities.

The photoluminescence measurements were performed on a homemade apparatus. The sample was deposited on a silicon substrate to form a small mound of 4 mm in diameter and of ∼1 mm in thickness. It was illuminated by an EQ99X laser driven light source filtered by a Jobin Yvon Gemini 180 monochromator. The exit slit from the monochromator was then reimaged on the sample by two 100m focal length, 2 inch diameter MgF_2 lenses. The whole apparatus has been calibrated by means of a Newport 918D low power calibrated photodiode sensor over the range 190-1000 nm. The resolution of the system is 4 nm. The emitted light from the sample is collected by an optical fiber connected to a Jobin-Yvon TRIAX320 monochromator equipped with a cooled CCD detector. At the entrance of the monochromator, various long pass filters can be chosen in order to eliminate the excitation light. A complete mapping of excitation and emission was then performed on the sample and corrected both by the excitation lamp power and wavelength dependence of the detection that was previously calibrated using a NIST calibrated QTH 45W lamp. Corrected excitation spectra integrating the entire emission wavelength were then extracted from this data. The resolution of the detection system is 2 nm.

Temperature control over the sample was regulated by a THMS-600 heating stage with T95-PE temperature controller made by Linkam Scientific Instruments.

Luminescence lifetime measurements. During the luminescence lifetime measurements compounds were excited by a diode pumped 50 Hz tunable OPO laser made by EKSPLA. The luminescence emitted by the sample was collected by an optical fiber and afterwards filtered by a long pass filter (by Thorlabs: FEL400, FEL450, FEL500, FEL550 or FEL600) and fed to a R2949 photomultiplier tube from Hamamatsu. Photon arrival times were categorized by the MCS6A multichannel scaler from Fast ComTec.

Lifetime measurements for $[Cu(p\text{-}SPhCO_2H)]_n$ and $[Au(p\text{-}SPhCO_2H)]_n$ (Chapter 2) were performed by an equipment different to the one which was used for the rest of the compounds. It was performed by a R2949 photomultiplier tube made by Hamamatsu. 379 nm picosecond (57 ps) laser with frequency controller by Hamamatsu was employed in the measurements. Photon arrival times were recorded by a MCS6A multichannel scaler by Fast ComTec.

I case of many samples, the measurements could not be fitted by a sum of simple exponential decays. For this reason, one (or more) stretched exponential decay is often used (Eq. 1):[1]

$$I = a_1 e^{-(x/t_1)^{\beta_1}} + a_2 e^{-(x/t_2)^{\beta_2}} + a_3 e^{-(x/t_3)^{\beta_3}} \quad \text{(Eq. 1)}$$

Here, a_i and t_i are an amplitude and lifetime of a given component *i* and β_i is enclosed between 0 and 1.

The β factor is introduced into the function in order to account for possibility of energy transfer towards a distribution of non-radiative centers by dipole-dipole/quadrupole-quadrupole/etc. interactions. Its value is given by the type of interactions and the dimensionality of the system.

The average lifetime of the stretched exponential decay $< \tau_i >$ is calculated using the Equation 2. The procedure used for the fitting is described in [2].

$$< \tau_i > = \tau_i \cdot \frac{1}{\beta_i} \cdot \Gamma\left(\frac{1}{\beta_i}\right) \quad \text{(Eq. 2)}$$

For a multiexponential decay, by variation of the lifetime one achieves compensation of the amplitude and vice versa. It is possible to obtain similar decay intensity with different values of a_i and t_i. In other words, a_i and t_i are correlated. The situation turns even more complicated, once β_i is different from 1. The unfortunate result is that the ability to determine

the precise values is greatly hindered by parameter correlation.[3] For this reason, some of the fit parameters should be considered carefully.

Quantum yield. Two different methods were used in this work. For the $[Au(p\text{-}SPhCO_2H)]_n$, discussed in the Chapter 2, comparison of the sample to a known standard was used.[4] For the $[Au(m\text{-}SPhCO_2H)]_n$ (in Chapter 3) and $[Cu(o\text{-}SPhCO_2H)]_n$, $[Ag(o\text{-}SPhCO_2H)]_n$ and $[Au(o\text{-}SPhCO_2H)]_n$ (in Chapter 4) an integrating sphere was used.

Determination of quantum yield with reference sample.[4]

As a reference sample of porous silicon with 80 % porosity was used. It has been thoroughly characterized in terms of quantum yield (3.2%) by two independent teams.[5, 6] Porous silicon has its maximum of absorption at 280 nm. For the investigated sample, the excitation spectra shows a maximum and a plateau around this wavelength. It is, therefore, reasonable to assume, that all samples absorb almost all incoming light at this wavelength. The signal obtained at this excitation wavelength can be taken as a reference for the comparative quantum yields of the samples. Additionally, as a cross reference of the validity of the measure, the number of counts on the detector as a function of incoming photons for a quantum yield of 100 % was checked to correspond within an error of 20 % to the inverse of the collection efficiency of the optical system.

Determination of the QY by a standard integrating sphere (IS) (shown schematically in **FIgure A. 1** (a)). To illuminate the sample, a stabilized Xenon lamp (Hamamatsu, L2273) coupled to a double-grating monochromator (Solar, MSA130) was used. The excitation beam was split by spectrally broad bifurcated fiber (Ocean Optics, BIF600-UV-VIS). One part of the beam was used to monitor the fluctuations of the excitation intensity using a power-meter (Ophir Photonics, PD300-UV). The other part was used to excite the sample. A collimator lens was used to reduce the spot-size at the sample position to enable direct excitation of the sample (F=1). The powder samples were placed in ethanol solution in quartz cuvette. They were suspended using an aluminium holder in the center of the IS with a diameter of 10 cm (internal walls were made of Spectralon® (PTFE), Newport, 70672). The use of such type of holder is verified by ray-tracing simulations. Light was detected using a second spectrally broad optical fiber (Ocean Optics, QP1000-2-VIS-BX), coupled to a spectrometer (Solar, M266) equipped by a CCD (Hamamatsu, S7031-1108S). Sample (powder) did not dissolve completely in the solvent

(ethanol), so the sample has been shaken before the measurement and then measured. This has been repeated several times to ensure reproducibility of the result. All measurements were corrected for the spectral response of the detection system. We determined it by illumination of the IS (via the excitation port) by a tungsten halogen calibration lamp (standard of spectral irradiance, Oriel, 63358) for the visible range, and a deuterium lamp (Oriel, 63945) for the UV range (< 400 nm). The measured calibration spectrum was corrected for the spectrometer's stray-light contribution. Re-absorption effects were accounted for by using the procedure described by *Ahn et al.*[7] We compared the measured PL spectrum with the one of the low concentration sample, for which re-absorption is negligible. Error estimates were obtained by the same method as presented in *Chung et al.*.[8] QY was evaluated by the Equation 3, where N_{em} and N_{abs} are numbers of emitted and absorbed photons, $N_S$and N_{Ref} are numbers of photons transmitted through sample (sample in solvent and cuvette) and reference (just cuvette with solvent) (asterisk denotes emission spectral range, no asterisk means excitation spectral range). I_S and I_{Ref} are emission intensities detected from the studied sample and from the reference (**FIgure A. 1** (b)), *C* is a correction factor for the spectral response of the detection system.

$$QY = \frac{N_{em}}{N_{abs}} = \frac{N_S^* - N_{Ref}^*}{N_{Ref} - N_S} = \frac{\int^{em}[I_S(\lambda) - I_{Ref}(\lambda)]C(\lambda)d\lambda}{\int^{exc}[I_{Ref}(\lambda) - I_S(\lambda)]C(\lambda)d\lambda} \quad \text{(Eq. 3)}$$

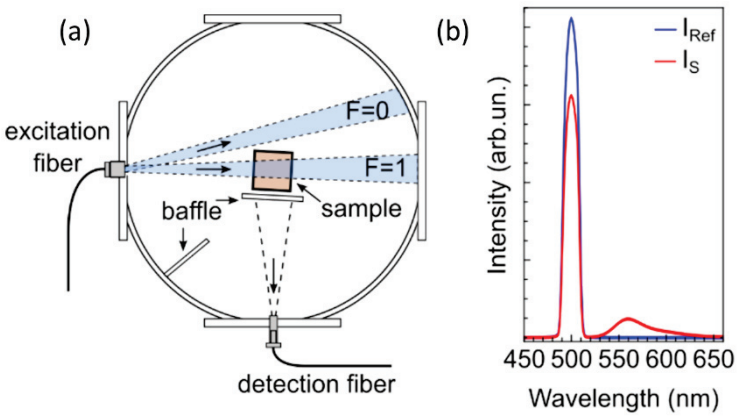

FIgure A. 1 A scheme of standard integrating sphere setup which was used in our study (a) a graphical representation of emission intensities detected from the studied sample and from the reference (b).

Table A. 1 Summary of structural parameters and properties of the CPs studied in the work.

CP	Dimensionality	Metal geometry and μ_n-S	M-S, Å	M-M, Å	S-M-S, °	M-S-M, °	π- π or hydrogen bonds	Decomposition temperature, °C	Band gap, eV	λ_{em} at RT, nm	λ_{em} at 93 K, nm	QY, %	Application
$[Cu(SPh)]_n$ **1**	1D	Trigonal, μ_3	2.270(2) 2.298(2) 2.303(2)	2.965(3)† 3.437(3)† 3.593(5) 3.268(3)†	112.9(1) 113.6(1) 133.5(1)	80.0(1) 97.6(1) 113.6(1)	π- π 3.827(2)	225	2.59	667, 850	669, 850	-	τ-thermometry
$[Ag(SPh)]_n$ **1**	2D	Trigonal, μ_3	2.963(4)† 2.981(4)† 3.687(5)† 3.712(5)†	2.454(3) 2.490(3) 2.566(3) 2.577(3) 2.599(4) 2.614(3)	94.9(1) 95.4(1) 119.8(2) 121.5(2) 130.9(2) 136.1(2)	71.5(1) 72.0(1) 92.8(1) 95.3(1) 122.7(1) 123.2(1)	-	235	2.7	-	810	-	
$[Ag(SPh)]_n$ **2**	2D	-	-	-	-	-	-	235	2.8	-	550, 750	-	-
$[Au(SPh)]_n$	1D	Linear, μ_2	2.289(2) 2.332(2) 2.313(2) 2.345(2)	3.323(3)† 3.331(3) 3.369(3) 3.603(3) 3.610(3)†	171.57(9) 175.23(8)	91.36(7) 102.32(7)	C-H- π bonds	200	2.8	680	676	5	τ-thermometry
$[Cu(p\text{-}SPhCO_2H)]_n$	2D	Trigonal, μ_3	2.243(3) 2.290(2) 2.302(3)	3.030(2)† 3.519(2)†	104.1(1) 126.0(1) 129.8(1)	83.6(1) 101.9(1) 116.4(1)	H-bonds	300	2.79		485, 530, 650	-	-
$[Cu(p\text{-}SPhCO_2Me)]_n$	2D	Trigonal, μ_3	2.244(3) 2.255(3) 2.282(4)	3.313(3)† 3.493(3)†	114.0(2) 122.2(2) 123.6(2)	93.8(2) 101.0(2) 123.6(2)	π- π 3.966(1)	270	2.68	460, 560, 740	460, 560, 740	-	RIM
$[Ag(p\text{-}SPhCO_2H)]_n$	2D	Trigonal, μ_3	2.456(4) 2.493(4) 2.623(4)	2.936(2)† 3.687(2)†	97.2(2) 126.4(2) 131.3(2)	70.5(1) 96.3(2) 118.2(2)	H-bonds	340	2.99	-	484, 528, 700	-	-
$[Ag(p\text{-}SPhCO_2Me)]_n$	2D	Trigonal, μ_3	2.437(5) 2.489(5) 2.627(5)	2.973(3)† 3.653(2)†	97.0(2) 124.4(2) 132.3(2)	71.8(2) 95.7(2) 120.2(2)	-	290	3.04	-	489, 526, 650	-	-
$[Au(p\text{-}SPhCO_2H)]_n$	2D	Angular, μ_2	2.272(1) 2.272(8) 2.342(5) 2.367(1)	3.355(4) 3.422(6) 3.591(3)† 3.732(3)†	77.5(1) 124.0(1)	99.4(1) 110.4(1)	H-bonds	330	3.05	665,	490, 620	<1	RIM
$[Au(p\text{-}SPhCO_2Me)]_n$	2D	Linear, μ_2	2.307(1) 2.375(1)	3.199(5) 3.509(5)†	177.5(1)	97.1(1)	-	260	2.84	645	488, 645	70	Illumination

$[Cu(m\text{-}SPhCO_2H)]_n$	2D	Trigonal, μ_3	2.242(2) 2.244(2) 2.294(2)	3.494(1) 3.599(2) 3.905(1)	116.3(1) 121.0(1) 121.1(1)	100.7(1) 105.0(1) 121.0(1)	π- π 3.905(1) + H-bonds	300	2.68	-	575	-	-
$[Ag(m\text{-}SPhCO_2H)]_n$	2D	-	-	-	-	-	H-bonds	320	3.1	460, 556	482	-	-
$[Au(m\text{-}SPhCO_2H)]_n$	2D	Angular, μ_2	2.251(8) 2.355(8) 2.365(8) 2.367(8)	3.20(2)† 3.28(2)† 3.39(2) 3.61(2)	89.6(3) 150.3(4)	85.1(4) 90.9(4)	H-bonds	300	2.9	475, 595	615	18.9	Illumination
$[Cu(o\text{-}SPhCO_2H)]_n$	1D	Trigonal, μ_3	2.261(5) 2.285(5) 2.400(5)	3.048(4)† 3.276(5) 3.962(3)†	117.4(2) 118.3(2) 121.3(2)	81.1(2) 81.6(2) 121.3(2)	π- π 3.96(2) + H-bonds	200	2.43	719	700	0.17	-
$[Ag(o\text{-}SPhCO_2H)]_n$	1D	Trigonal, μ_3	2.486(8) 2.561(8) 2.641(7)	3.296(4)† 3.442(5) 4.434(3)†	114.8(3) 117.4(3) 122.9(3)	78.5(3) 79.8(2) 122.9(3)	H-bonds	260	2.23	655	634	51.55	Illumination
$[Au(o\text{-}SPhCO_2H)]_n$	1D	Linear, μ_2	2.26(4) 2.31(4)	3.44(2) 3.64(1)	162(2)	98(2)	H-bonds	270	2.83	813	787	7.30	NIR emitter
$\alpha[Au(SPh)]_n$	1D	Linear, μ_2	2.28(4) 2.28(5) 2.32(5) 2.36(3)	3.19(3) † 3.27(3) 3.34(2) 3.55(3) 3.68(2)†	159(2) 166(2)	86(2) 108(2)	-	240	2.86	-	690	-	Glass formation-
$\alpha[Au(SMePh)]_n$	1D	-	-	-	-	-	-	184	2.93	-	675	-	Glass formation-
$\alpha[Au(SEtPh)]_n$	1D	-	-	-	-	-	-	225	3.04	-	655	-	Glass formation-

† bridged by sulfur atoms; τ-thermometry – Lifetime Luminescence Thermometry; RIM – Ratiometric Intensity Measurement Luminescence Thermometry.

A.2 References

1. J. Klafter and M. F. Shlesinger, *Proc. Natl. Acad. Sci. U.S.A.*, 1986, **83**, 848-851.
2. I. Mihalcescu, PhD, Université Joseph Fourier-Grenoble 1, 1994.
3. J. R. Lakowicz, *Principles of fluorescence spectroscopy*, Second edition. New York : Kluwer Academic/Plenum, [1999] ©1999, 1999.
4. S. Mishra, E. Jeanneau, G. Ledoux and S. Daniele, *Inorg. Chem.*, 2014, **53**, 11721-11731.
5. G. Ledoux, O. Guillois, F. Huisken, B. Kohn, D. Porterat and C. Reynaud, *Astron. Astrophys.*, 2001, **377**, 707-720.
6. J. C. Vial, R. Herino, S. Billat, A. Bsiesy, F. Gaspard, M. Ligeon, I. Mihalcescu, F. Muller and R. Romestain, *IEEE T. Nucl. Sci.*, 1992, **39**, 563-569.
7. T.-S. Ahn, R. O. Al-Kaysi, A. M. Müller, K. M. Wentz and C. J. Bardeen, *Rev. Sci. Instrum.*, 2007, **78**, 086105.
8. N. X. Chung, R. Limpens and T. Gregorkiewicz, *Investigating photoluminescence quantum yield of silicon nanocrystals formed in SiOx with different initial Si excess*, SPIE, 2015.

Appendix B. Photophysical Measurements

B.1 Photophysical Measurements

B.1.1 Chapter 1

Summary of conditions for luminescent measurements of all compounds discussed in the Chapter 1 can be found in the **Table B. 1**.

Table B. 1 Luminescent measurements conditions for compounds discussed in Chapter 1.

Compound	Temperature range, K	Long pass filter used	Wavelength range for 2D maps and emission-exciation spectra, nm		(λ_{exc}, λ_{em}) for lifetime measurements
			λ_{exc}	λ_{em}	
$[Cu(SPh)]_n$ **1**	93-293 K	FEL500	200-500	520-940	(432, 670) (432, 850)
$[Cu(SPh)]_n$ **2**	93-383 K	FEL500	200-500	520-780	(436, 667)-
$[Cu(SPh)]_n$ **3**	93-383 K	FEL500	200-500	520-780	(436, 662)
$[Cu(SPh)]_n$ **4**	93-383 K	FEL500	200-500	520-780	(436, 650)
$[Ag(SPh)]_n$ phase **1**	93 K	FEL450	340-436	470-940	(380, 830) (432, 810)
$[Ag(SPh)]_n$ phase **2**	93-273 K	FEL450	250-450	470-940	(408, 550) (408, 750)
$[Au(SPh)]_n$	93-413 K	FEL450	200-450	560-820	-
	93-383 K	FEL450	-	-	(332, 675)

Temperature-dependent luminescence decays of $[Cu(SPh)]_n$ were not presented in the main part of the chapter, they could be found on **Figure B. 1**.

For none of the compounds discussed in this chapter, it was not possible to fit lifetime decay measurements by a sum of simple exponential decays. For this reason, one or more stretched exponential decay curves were implemented. [1] Used equation are listed in the **Table B. 2** below.

Use of this equation led to the fits of sufficient quality (**Figure B. 2** - **Figure B. 8**) which yielded the individual luminescence lifetimes (**Table B. 3** - **Table B. 11**).

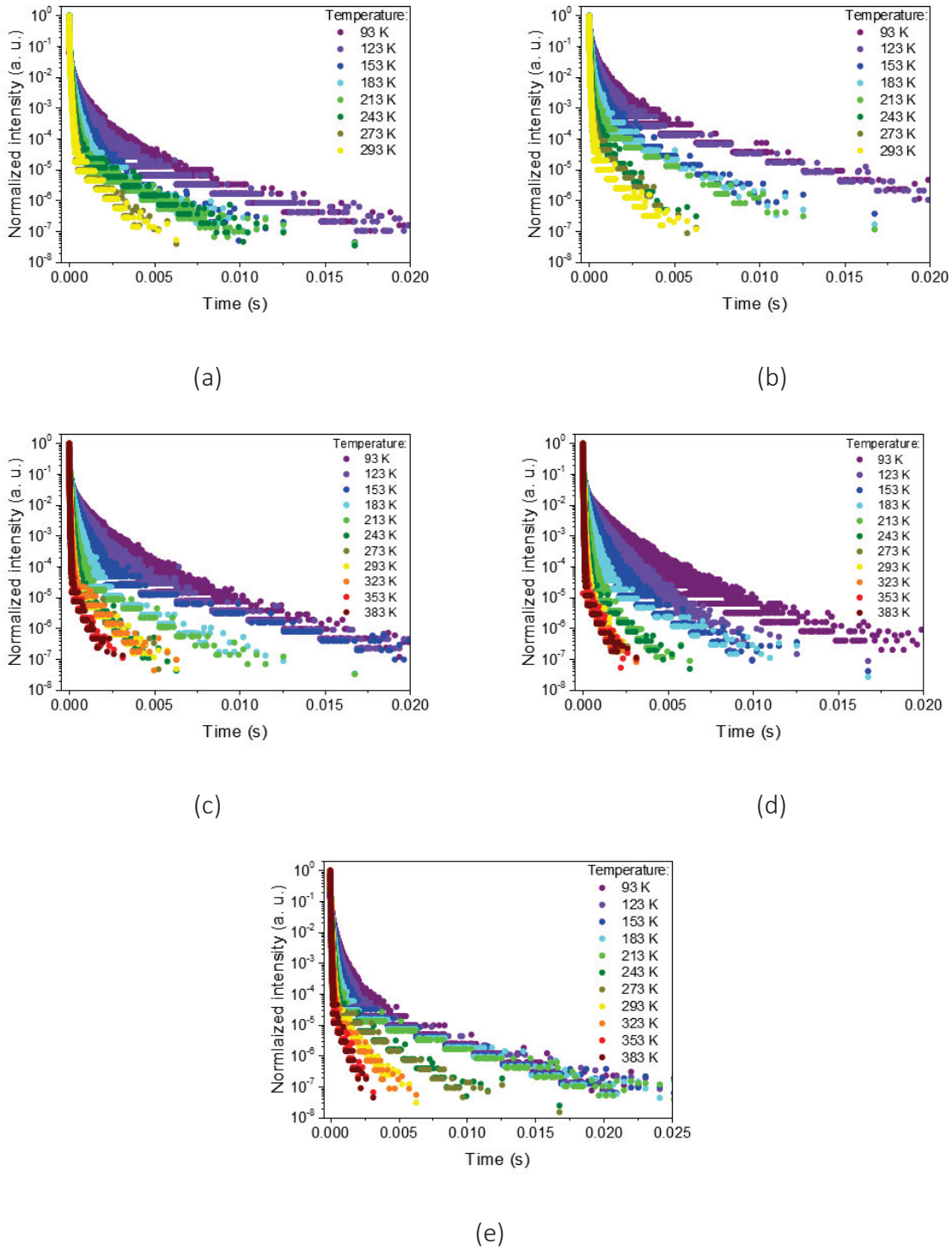

Figure B. 1 Temperature-dependent luminescence decays of $[Cu(SPh)]_n$ measured for the compound **1** at (a) λ_{em} = 670 nm and (b) λ_{em} = 850 nm, (c) compound **2**, (d) compound **3** and (e) compound **4**.

Table B. 2 Equations used to fit lifetime decay curves.

General form of the equation	$\boldsymbol{I = a_1 e^{-(x/t_1)^{\beta_1}} + a_2 e^{-(x/t_2)^{\beta_2}} + a_3 e^{-(x/t_3)^{\beta_3}}}$, with $\boldsymbol{\beta_i = (0, 1)}$
$[Cu(SPh)]_n$ **1**, λ_{em} = 670 and 850 nm	$I = a_1 e^{-(x/t_1)^{\beta_1}} + a_2 e^{-(x/t_2)^{\beta_2}}$
$[Cu(SPh)]_n$ **2**	$I = a_1 e^{-(x/t_1)^{\beta_1}} + a_2 e^{-(x/t_2)^{\beta_2}}$
$[Cu(SPh)]_n$ **3**	$I = a_1 e^{-(x/t_1)^{\beta_1}} + a_2 e^{-(x/t_2)^{\beta_2}}$
$[Cu(SPh)]_n$ **4**	$I = a_1 e^{-(x/t_1)^{\beta_1}} + a_2 e^{-(x/t_2)^{\beta_2}}$
$[Ag(SPh)]_n$ phase **1**	$I = a_1 e^{-(x/t_1)^{\beta_1}} + a_2 e^{-(x/t_2)^{\beta_2}}$
$[Ag(SPh)]_n$ phase **2**, λ_{em} = 550 nm	$I = a_1 e^{-(x/t_1)^{\beta_1}} + a_2 e^{-(x/t_2)^{\beta_2}}$
$[Ag(SPh)]_n$ phase **2**, λ_{em} = 750 nm	$I = a_1 e^{-(x/t_1)^{\beta_1}} + a_2 e^{-(x/t_2)^{\beta_2}} + a_3 e^{-(x/t_3)^{\beta_3}}$
$[Au(SPh)]_n$	$I = a_1 e^{-(x/t_1)^{\beta_1}} + a_2 e^{-(x/t_2)^{\beta_2}}$

It should be noted, that in some datasets for $[Cu(SPh)]_n$ products, further improvement of fit quality could be reached by introduction of third stretched component. However, the gain in its quality was not substantial. Thus, the same function with two components was used for all the products in whole temperature range. It makes the comparison of the fitted values easier and more direct.

In the case of fits for $[Ag(SPh)]_n$, the presence of two or even three stretched components with β of low values (~0.2) made fit convergence quite difficult. It contributes to high uncertainties. For this reason, some of the fit parameters should be understood as the approximations to the exact values.

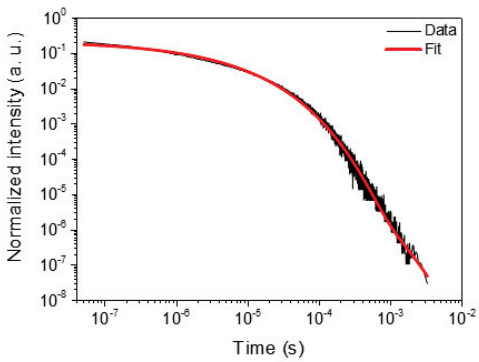

(a)

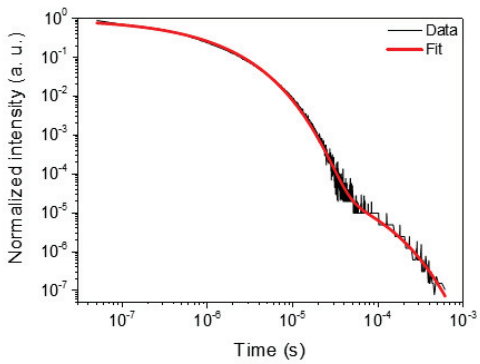

(b)

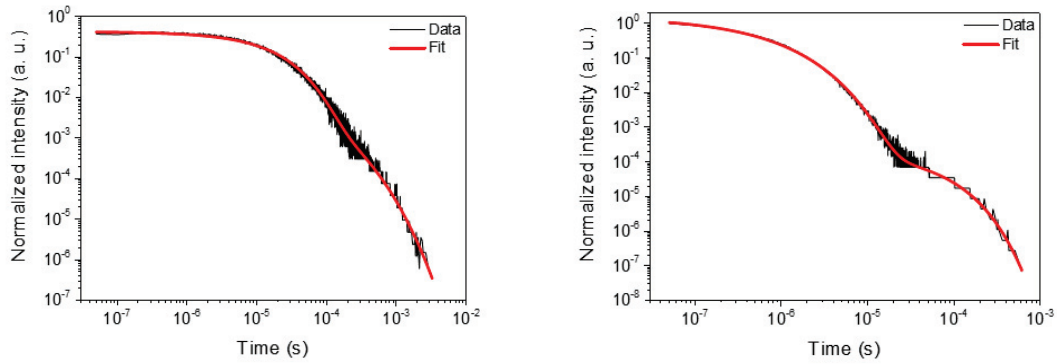

(c) (d)

Figure B. 2 Examples of lifetime decay fit of $[Cu(SPh)]_n$ **1** at λ_{em} = 670 nm at 93 K (a), 293 K (b) and at λ_{em} = 850 nm at 93 K (c), 293 K (d).

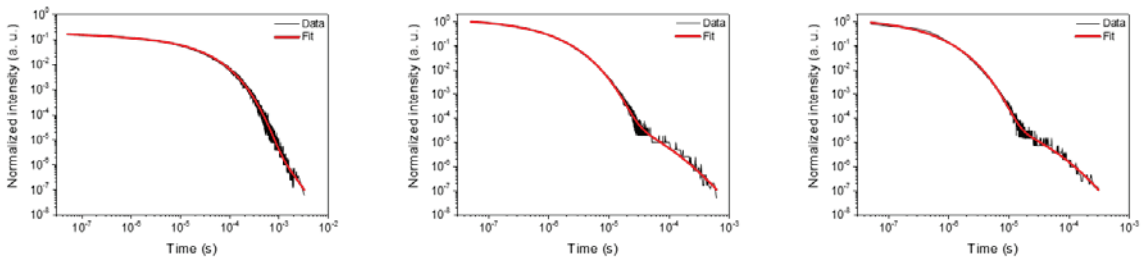

(a) (b) (c)

Figure B. 3 Examples of lifetime decay fit of $[Cu(SPh)]_n$ **2** at 93 K (a), 293 K (b) and 383 K (c).

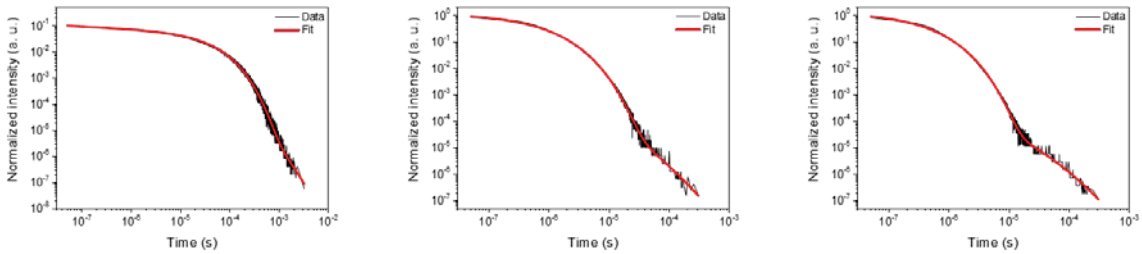

(a) (b) (c)

Figure B. 4 Examples of lifetime decay fit of $[Cu(SPh)]_n$ **3** at 93 K (a), 293 K (b) and 383 K (c).

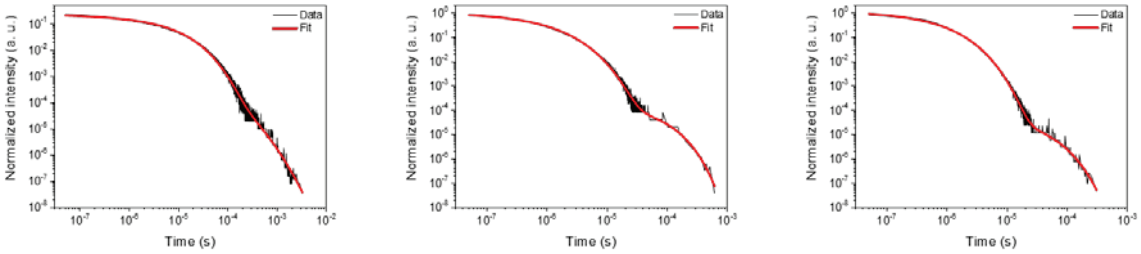

(a) (b) (c)

Figure B. 5 Examples of lifetime decay fit of $[Cu(SPh)]_n$ **4** at 93 K (a), 293 K (b) and 383 K (c).

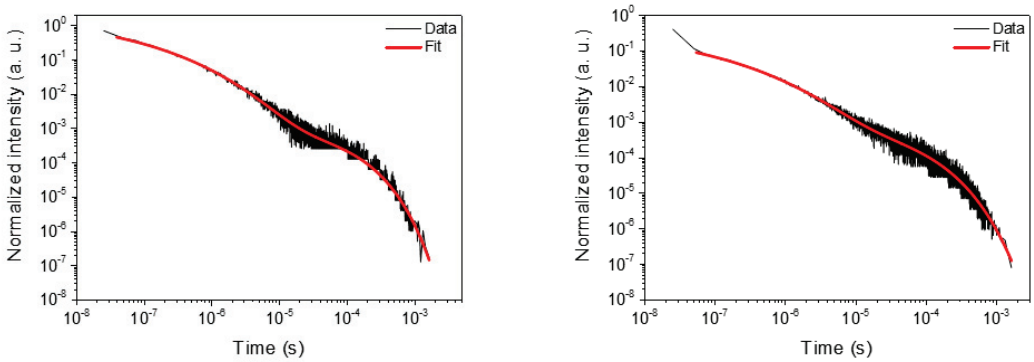

(a) (b)

Figure B. 6 Examples of lifetime decay fit of $[Ag(SPh)]_n$ phase **1** at 93 K at (380 nm, 830 nm) (a) and (432 nm, 810 nm) (b).

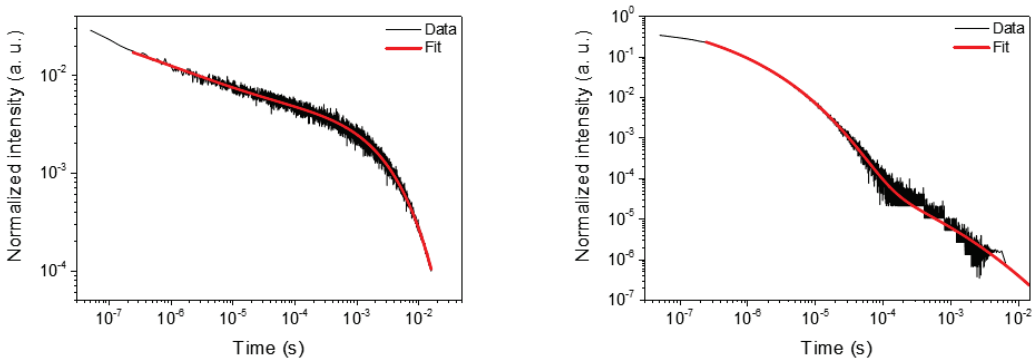

(a) (b)

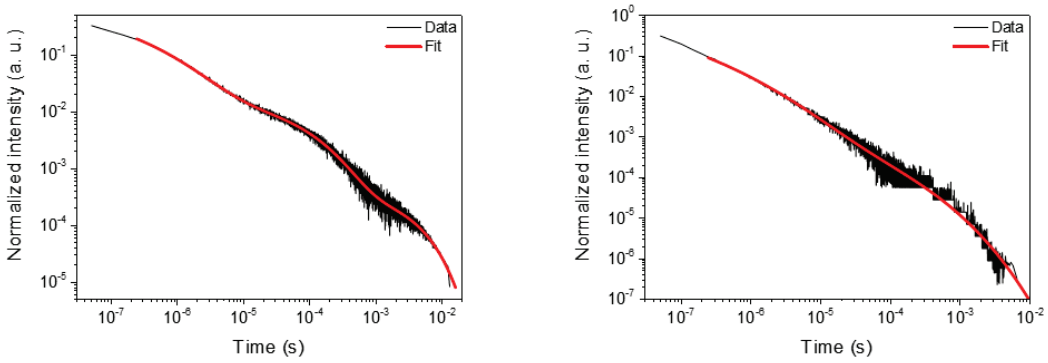

(c) (d)

Figure B. 7 Examples of lifetime decay fit of $[Ag(SPh)]_n$ phase **2** at 93 K at λ_{em} = 670 nm (a), 293 K (b) and at λ_{em} = 850 nm at 93 K (c), 273 K (d).

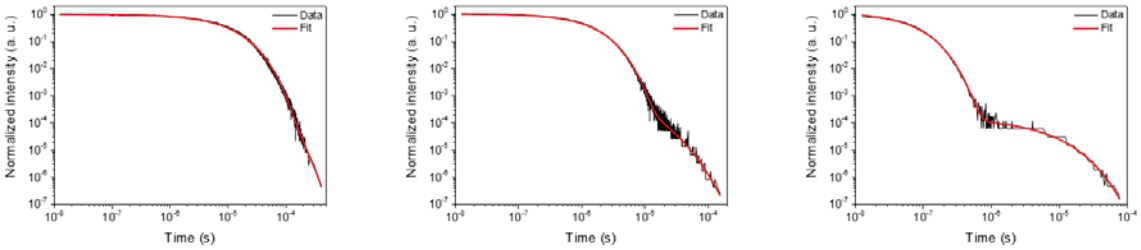

(a) (b) (c)

Figure B. 8 Examples of lifetime decay fit of $[Au(SPh)]_n$ at 93 K (a), 293 K (b) and 383 K (c).

Table B. 3 Luminescence lifetimes (τ_i), their pre-exponential factors (a_i), parameters β_i, average lifetimes ($<\tau_i>$) and contributions of $[Cu(SPh)]_n$ **1** for λ_{em} = 670 nm at 93 to 293 K temperature range.

Temperature, K	$a_1 \pm \sigma a_1$	$\tau_1 \pm \sigma\tau_1$, s	$\beta_1 \pm \sigma\beta_1$	$<\tau_1> \pm \sigma<\tau_1>$, s	Contribution of τ_1, %	$a_2 \pm \sigma a_2$	$\tau_2 \pm \sigma\tau_2$, s	$\beta_2 \pm \sigma\beta_2$	$<\tau_2> \pm \sigma<\tau_2>$, s	Contribution of τ_2, %	R^2
93	0.2196 ± 0.0018	1.89E-06 ± 3.54E-08	0.408 ± 0.002	5.96E-06 ± 1.20E-07	~ 100	4.87E-05 ± 4.44E-05	3.99E-05 ± 3.99E-05	0.437 ± 0.069	1.06E-04 ± 1.10E-04	< 1	0.99761
123	0.2366 ± 0.0022	2.38E-06 ± 4.39E-08	0.459 ± 0.002	5.64E-06 ± 1.11E-07	98	1.42E-03 ± 7.48E-04	3.43E-06 ± 2.02E-06	0.343 ± 0.022	1.86E-05 ± 1.15E-05	2	0.99753
153	0.3518 ± 0.0029	1.62E-06 ± 2.58E-08	0.474 ± 0.002	3.59E-06 ± 6.04E-08	99	4.38E-04 ± 3.11E-04	3.56E-06 ± 2.95E-06	0.357 ± 0.035	1.67E-05 ± 1.45E-05	1	0.99770
183	0.4459 ± 0.0036	1.41E-06 ± 2.16E-08	0.509 ± 0.002	2.72E-06 ± 4.37E-08	99	3.90E-04 ± 7.28E-05	8.03E-06 ± 1.66E-06	0.418 ± 0.013	2.37E-05 ± 5.06E-06	1	0.99790
213	0.6341 ± 0.0056	1.05E-06 ± 1.64E-08	0.529 ± 0.002	1.91E-06 ± 3.10E-08	~ 100	2.73E-04 ± 4.03E-05	5.77E-06 ± 1.10E-06	0.384 ± 0.010	2.15E-05 ± 4.28E-06	< 1	0.99785
243	0.8052 ± 0.0069	8.71E-07 ± 1.27E-08	0.550 ± 0.002	1.48E-06 ± 2.26E-08	99	1.46E-04 ± 7.88E-06	2.43E-05 ± 1.51E-06	0.511 ± 0.006	4.68E-05 ± 3.01E-06	1	0.99817
273	0.9094 ± 0.0073	6.89E-07 ± 8.90E-09	0.556 ± 0.002	1.15E-06 ± 1.55E-08	~ 100	6.29E-05 ± 4.56E-06	2.69E-05 ± 2.05E-06	0.610 ± 0.012	3.96E-05 ± 3.13E-06	< 1	0.99823
293	0.9606 ± 0.0077	6.06E-07 ± 7.69E-09	0.559 ± 0.002	1.00E-06 ± 1.32E-08	~ 100	9.75E-05 ± 7.42E-06	1.51E-05 ± 1.31E-06	0.531 ± 0.010	2.71E-05 ± 2.44E-06	< 1	0.99841

Table B. 4 Luminescence lifetimes (τ_i), their pre-exponential factors (a_i), parameters β_i, average lifetimes ($<\tau_i>$) and contributions of $[Cu(SPh)]_n$ **1** for λ_{em} = 850 nm at 93 to 293 K temperature range.

Temperature, K	$a_1 \pm \sigma a_1$	$\tau_1 \pm \sigma\tau_1$, s	$\beta_1 \pm \sigma\beta_1$	$<\tau_1> \pm \sigma<\tau_1>$, s	Contribution of τ_1, %	$a_2 \pm \sigma a_2$	$\tau_2 \pm \sigma\tau_2$, s	$\beta_2 \pm \sigma\beta_2$	$<\tau_2> \pm \sigma<\tau_2>$, s	Contribution of τ_2, %	R^2
93	0.3665 ± 0.0059	1.48E-05 ± 2.53E-07	0.750 ± 0.007	1.76E-05 ± 3.43E-07	86	0.0499 ± 0.0077	5.54E-06 ± 8.88E-07	0.387 ± 0.008	2.03E-05 ± 3.37E-06	14	0.99695
123	0.4894 ± 0.0027	1.11E-05 ± 1.12E-07	0.753 ± 0.004	1.32E-05 ± 1.50E-07	92	0.0125 ± 0.0010	1.64E-05 ± 1.40E-06	0.445 ± 0.006	4.18E-05 ± 3.68E-06	8	0.99753
153	0.6053 ± 0.0061	6.53E-06 ± 9.38E-08	0.784 ± 0.005	7.51E-06 ± 1.19E-07	92	0.0570 ± 0.0090	1.57E-06 ± 2.71E-07	0.357 ± 0.007	7.37E-06 ± 1.32E-06	8	0.99767
183	0.8211 ± 0.0042	4.19E-06 ± 3.84E-08	0.732 ± 0.003	5.09E-06 ± 5.09E-08	97	2.54E-03 ± 1.04E-04	3.04E-05 ± 1.21E-06	0.573 ± 0.005	4.87E-05 ± 1.99E-06	3	0.99824
213	0.9961 ± 0.0060	2.16E-06 ± 2.25E-08	0.689 ± 0.003	2.78E-06 ± 3.09E-08	98	1.20E-03 ± 3.41E-05	3.69E-05 ± 1.090E-06	0.596 ± 0.004	5.60E-05 ± 1.70E-06	2	0.99832
243	1.1841 ± 0.0097	1.02E-06 ± 1.41E-08	0.630 ± 0.003	1.44E-06 ± 2.11E-08	98	2.18E-03 ± 1.58E-04	7.09E-06 ± 5.50E-07	0.495 ± 0.007	1.44E-05 ± 1.15E-06	2	0.99771
273	1.3697 ± 0.0127	4.71E-07 ± 6.96E-09	0.563 ± 0.002	7.74E-07 ± 1.19E-08	99	2.74E-04 ± 7.00E-06	3.82E-05 ± 9.55E-07	0.742 ± 0.006	4.59E-05 ± 1.21E-06	1	0.99821
293	1.5066 ± 0.0144	3.19E-07 ± 4.83E-09	0.541 ± 0.002	5.57E-07 ± 8.79E-09	99	1.85E-04 ± 3.97E-06	3.88E-05 ± 8.45E-07	0.740 ± 0.005	4.67E-05 ± 1.07E-06	1	0.99847

Table B. 5 Luminescence lifetimes (τ_i), their pre-exponential factors (a_i), parameters β_i, average lifetimes ($<\tau_i>$) and contributions of $[Cu(SPh)]_n$ **2** for λ_{em} = 667 nm at 93 to 293 K temperature range.

Temperature, K	$a_1 \pm \sigma a_1$	$\tau_1 \pm \sigma\tau_1$, s	$\beta_1 \pm \sigma\beta_1$	$<\tau_1> \pm \sigma<\tau_1>$, s	Contribution of τ_1, %	$a_2 \pm \sigma a_2$	$\tau_2 \pm \sigma\tau_2$, s	$\beta_2 \pm \sigma\beta_2$	$<\tau_2> \pm \sigma<\tau_2>$, s	Contribution of τ_2, %	R^2
93	0.1297 ± 0.0013	1.41E-05 ± 2.08E-07	0.564 ± 0.002	2.31E-05 ± 3.55E-07	97	0.1913 ± 0.0155	3.71E-09 ± 6.15E-10	0.195 ± 0.002	5.54E-07 ± 1.03E-07	3	0.99796
123	0.1366 ± 0.0017	1.37E-05 ± 2.26E-07	0.633 ± 0.003	1.92E-05 ± 3.34E-07	91	0.1805 ± 0.0095	4.99E-08 ± 3.58E-09	0.243 ± 0.001	1.42E-06 ± 1.10E-07	9	0.99818
153	0.1906 ± 0.0027	9.98E-06 ± 1.81E-07	0.706 ± 0.005	1.25E-05 ± 2.42E-07	90	0.4792 ± 0.0297	9.27E-09 ± 8.10E-10	0.217 ± 0.001	5.80E-07 ± 5.52E-08	10	0.99784
183	0.2963 ± 0.0034	5.60E-06 ± 8.02E-08	0.691 ± 0.003	7.18E-06 ± 1.08E-07	92	0.5988 ± 0.0399	7.19E-09 ± 6.00E-10	0.227 ± 0.001	3.21E-07 ± 2.88E-08	8	0.99869
213	0.5240 ± 0.0081	2.43E-06 ± 4.68E-08	0.655 ± 0.004	3.29E-06 ± 6.66E-08	96	0.3643 ± 0.1143	2.24E-09 ± 9.76E-10	0.205 ± 0.005	2.17E-07 ± 1.03E-07	4	0.99804
243	0.7451 ± 0.0117	1.30E-06 ± 2.43E-08	0.628 ± 0.003	1.85E-06 ± 3.58E-08	95	2.8704 ± 0.7614	8.18E-11 ± 3.03E-11	0.180 ± 0.003	2.65E-08 ± 1.07E-08	5	0.99808
273	1.1583 ± 0.0126	6.64E-07 ± 1.09E-08	0.585 ± 0.003	1.03E-06 ± 1.77E-08	99	0.0708 ± 0.0417	2.68E-09 ± 2.40E-09	0.210 ± 0.012	2.15E-07 ± 2.12E-07	1	0.99759
293	1.3129 ± 0.0138	4.64E-07 ± 7.52E-09	0.569 ± 0.002	7.51E-07 ± 1.26E-08	99	0.0161 ± 0.0061	8.75E-09 ± 5.36E-09	0.222 ± 0.009	4.68E-07 ± 3.14E-07	1	0.99790
323	1.1805 ± 0.0163	4.24E-07 ± 8.82E-09	0.595 ± 0.003	6.45E-07 ± 1.40E-08	99	0.0343 ± 0.0141	2.31E-09 ± 1.66E-09	0.201 ± 0.009	2.62E-07 ± 2.09E-07	1	0.99666
353	1.3520 ± 0.0151	2.62E-07 ± 4.28E-09	0.558 ± 0.002	4.37E-07 ± 7.39E-09	99	0.0112 ± 0.0046	7.47E-09 ± 4.93E-09	0.228 ± 0.011	3.22E-07 ± 2.32E-07	1	0.99816
383	1.3835 ± 0.0162	2.30E-07 ± 3.81E-09	0.575 ± 0.002	3.67E-07 ± 6.30E-09	~ 100	0.0016 ± 0.0003	1.16E-07 ± 3.39E-08	0.286 ± 0.008	1.34E-06 ± 4.20E-07	< 1	0.99814

Table B. 6 Luminescence lifetimes (τ_i), their pre-exponential factors (a_i), parameters β_i, average lifetimes ($<\tau_i>$) and contributions of $[Cu(SPh)]_n$ **3** for λ_{em} = 662 nm at 93 to 293 K temperature range.

Temperature, K	$a_1 \pm \sigma a_1$	$\tau_1 \pm \sigma\tau_1$, s	$\beta_1 \pm \sigma\beta_1$	$<\tau_1> \pm \sigma<\tau_1>$, s	Contribution of τ_1, %	$a_2 \pm \sigma a_2$	$\tau_2 \pm \sigma\tau_2$, s	$\beta_2 \pm \sigma\beta_2$	$<\tau_2> \pm \sigma<\tau_2>$, s	Contribution of τ_2, %	R^2
93	0.0684 ± 0.0007	2.59E-05 ± 3.38E-07	0.645 ± 0.006	3.57E-05 ± 5.62E-07	95	0.1143 ± 0.0056	1.72E-08 ± 2.20E-09	0.217 ± 0.002	1.06E-06 ± 1.52E-07	5	0.99784
123	0.1039 ± 0.0012	1.69E-05 ± 2.31E-07	0.663 ± 0.003	2.26E-05 ± 3.23E-07	94	0.1787 ± 0.0076	3.13E-08 ± 3.82E-09	0.247 ± 0.003	8.11E-07 ± 1.09E-07	6	0.99786
153	0.1884 ± 0.0020	8.80E-06 ± 1.16E-07	0.640 ± 0.003	1.20E-05 ± 1.68E-07	96	0.3020 ± 0.0255	4.74E-09 ± 5.89E-10	0.214 ± 0.002	3.29E-07 ± 4.48E-08	4	0.99805
183	0.2773 ± 0.0034	4.99E-06 ± 7.92E-08	0.667 ± 0.003	6.63E-06 ± 1.10E-07	92	1.2966 ± 0.0994	7.36E-10 ± 8.34E-11	0.194 ± 0.001	1.17E-07 ± 1.46E-08	8	0.99823
213	0.4751 ± 0.0060	2.12E-06 ± 3.28E-08	0.634 ± 0.003	2.97E-06 ± 4.80E-08	93	2.8186 ± 0.2656	2.61E-10 ± 3.37E-11	0.194 ± 0.001	4.05E-08 ± 5.72E-09	7	0.99849
243	0.8771 ± 0.0116	9.27E-07 ± 1.46E-08	0.603 ± 0.003	1.39E-06 ± 2.27E-08	98	0.8302 ± 0.5322	1.02E-10 ± 9.90E-11	0.177 ± 0.008	3.86E-08 ± 4.17E-08	2	0.99819
273	1.2194 ± 0.0144	5.69E-07 ± 7.93E-09	0.577 ± 0.002	9.02E-07 ± 1.30E-08	98	1.0852 ± 0.7309	8.72E-11 ± 8.04E-11	0.184 ± 0.008	2.20E-08 ± 2.23E-08	2	0.99831
293	1.2072 ± 0.0108	4.65E-07 ± 6.23E-09	0.564 ± 0.002	7.63E-07 ± 1.06E-08	99	0.4464 ± 0.4182	3.34E-11 ± 4.96E-11	0.168 ± 0.012	2.15E-08 ± 3.64E-08	1	0.99822
323	1.2295 ± 0.0109	3.87E-07 ± 4.89E-09	0.582 ± 0.002	6.08E-07 ± 7.95E-09	~ 100	0.1450 ± 0.1188	2.19E-10 ± 2.81E-10	0.187 ± 0.013	4.74E-08 ± 6.82E-08	< 1	0.99955
353	1.5242 ± 0.0184	2.69E-07 ± 4.60E-09	0.569 ± 0.002	4.36E-07 ± 7.71E-09	99	0.0360 ± 0.0220	1.04E-09 ± 1.01E-09	0.203 ± 0.012	1.10E-07 ± 1.19E-07	1	0.99787
383	1.3782 ± 0.0152	2.37E-07 ± 3.61E-09	0.581 ± 0.002	3.73E-07 ± 5.88E-09	~ 100	0.0057 ± 0.0019	5.80E-09 ± 3.38E-09	0.219 ± 0.009	3.38E-07 ± 2.17E-07	< 1	0.99832

Table B. 7 Luminescence lifetimes (τ_i), their pre-exponential factors (a_i), parameters β_i, average lifetimes ($<\tau_i>$) and contributions of $[Cu(SPh)]_n$ **4** for λ_{em} = 662 nm at 93 to 293 K temperature range.

Temperature, K	$a_1 \pm \sigma a_1$	$\tau_1 \pm \sigma\tau_1$, s	$\beta_1 \pm \sigma\beta_1$	$<\tau_1> \pm \sigma<\tau_1>$, s	Contribution of τ_1, %	$a_2 \pm \sigma a_2$	$\tau_2 \pm \sigma\tau_2$, s	$\beta_2 \pm \sigma\beta_2$	$<\tau_2> \pm \sigma<\tau_2>$, s	Contribution of τ_2, %	R^2
93	0.1856 ± 0.0043	5.76E-06 ± 1.37E-07	0.592 ± 0.005	8.83E-06 ± 2.23E-07	91	8.02E-02 ± 1.60E-02	9.23E-08 ± 2.18E-08	0.255 ± 0.004	1.96E-06 ± 4.93E-07	9	0.99777
123	0.2678 ± 0.0018	4.14E-06 ± 5.40E-08	0.579 ± 0.002	6.52E-06 ± 8.97E-08	99	4.12E-04 ± 4.37E-05	2.51E-05 ± 2.87E-06	0.460 ± 0.009	5.92E-05 ± 6.98E-06	1	0.99771
153	0.3583 ± 0.0022	2.94E-06 ± 3.45E-08	0.587 ± 0.002	4.55E-06 ± 5.61E-08	99	2.03E-04 ± 1.02E-05	5.20E-05 ± 2.79E-06	0.534 ± 0.006	9.28E-05 ± 5.12E-06	1	0.99829
183	0.4904 ± 0.0035	2.03E-06 ± 2.57E-08	0.593 ± 0.002	3.10E-06 ± 4.10E-08	99	1.16E-04 ± 3.93E-06	8.44E-05 ± 3.17E-06	0.589 ± 0.005	1.30E-04 ± 5.04E-06	1	0.99813
213	0.6143 ± 0.0046	1.45E-06 ± 1.83E-08	0.593 ± 0.002	2.22E-06 ± 2.92E-08	99	6.56E-05 ± 1.42E-06	1.39E-04 ± 3.30E-06	0.679 ± 0.005	1.82E-04 ± 4.48E-06	1	0.99828
243	0.7838 ± 0.0067	1.06E-06 ± 1.49E-08	0.588 ± 0.002	1.64E-06 ± 2.41E-08	99	1.74E-04 ± 9.80E-06	1.97E-05 ± 1.31E-06	0.491 ± 0.006	4.07E-05 ± 2.79E-06	1	0.99800
273	0.9317 ± 0.0079	8.38E-07 ± 1.13E-08	0.590 ± 0.002	1.29E-06 ± 1.82E-08	~ 100	9.51E-05 ± 3.15E-06	4.00E-05 ± 1.49E-06	0.582 ± 0.005	6.27E-05 ± 2.40E-06	< 1	0.99827
293	1.0130 ± 0.0078	6.61E-07 ± 8.33E-09	0.578 ± 0.002	1.05E-06 ± 1.37E-08	99	1.70E-04 ± 4.69E-06	4.50E-05 ± 1.16E-06	0.776 ± 0.007	5.22E-05 ± 1.42E-06	1	0.99840
323	1.0451 ± 0.0073	6.89E-07 ± 7.31E-09	0.607 ± 0.002	1.02E-06 ± 1.13E-08	~ 100	8.22E-05 ± 3.41E-06	2.42E-05 ± 1.09E-06	0.615 ± 0.007	3.54E-05 ± 1.64E-06	< 1	0.99870
353	1.0958 ± 0.0081	5.99E-07 ± 6.53E-09	0.613 ± 0.002	1.05E-06 ± 1.18E-08	~ 100	6.02E-05 ± 3.44E-06	2.17E-05 ± 1.18E-06	0.708 ± 0.012	2.71E-05 ± 1.55E-06	< 1	0.99844
383	1.1494 ± 0.0095	4.86E-07 ± 5.70E-09	0.622 ± 0.002	6.99E-07 ± 8.52E-09	~ 100	6.60E-05 ± 3.17E-06	1.74E-05 ± 8.28E-07	0.681 ± 0.009	2.27E-05 ± 1.12E-06	< 1	0.99837

Table B. 8 Luminescence lifetimes (τ_i), their pre-exponential factors (a_i), parameters β_i, average lifetimes ($<\tau_i>$) and contributions of $[Ag(SPh)]_n$ phase **1** at 93 K.

(λ_{em}, λ_{exc}), nm	$a_1 \pm \sigma a_1$	$\tau_1 \pm \sigma\tau_1$, s	$\beta_1 \pm \sigma\beta_1$	$<\tau_1> \pm \sigma<\tau_1>$, s	Contribution of τ_1, %	$a_2 \pm \sigma a_2$	$\tau_2 \pm \sigma\tau_2$, s	$\beta_2 \pm \sigma\beta_2$	$<\tau_2> \pm \sigma<\tau_2>$, s	Contribution of τ_2, %	R^2
(380, 830)	2.3456 ± 0.2264	6.16E-09 ± 1.34E-09	0.266 ± 0.006	1.03E-07 ± 2.52E-08	77	1.00E-03 ± 3.62E-05	4.91E-05 ± 1.95E-06	0.618 ± 0.006	7.12E-05 ± 2.92E-06	23	0.99355
(432, 810)	0.4739 ± 0.0546	7.65E-09 ± 2.16E-09	0.264 ± 0.009	1.35E-07 ± 4.33E-08	61	8.74E-04 ± 4.52E-05	2.45E-05 ± 1.49E-06	0.516 ± 0.006	4.62E-05 ± 2.90E-06	39	0.99280

Table B. 9 Luminescence lifetimes (τ_i), their pre-exponential factors (a_i), parameters β_i, average lifetimes ($<\tau_i>$) and contributions of $[Ag(SPh)]_n$ phase **2** for λ_{em} = 550 nm at 93 to 273 K temperature range.

Temperature, K	$a_1 \pm \sigma a_1$	$\tau_1 \pm \sigma\tau_1$, s	$\beta_1 \pm \sigma\beta_1$	$<\tau_1> \pm \sigma<\tau_1>$, s	Contribution of τ_1, %	$a_2 \pm \sigma a_2$	$\tau_2 \pm \sigma\tau_2$, s	$\beta_2 \pm \sigma\beta_2$	$<\tau_2> \pm \sigma<\tau_2>$, s	Contribution of τ_2, %	R^2
93	0.1135 ± 0.0394	6.43E-10 ± 1.24E-09	0.134 ± 0.018	8.55E-06 ± 5.03E-05	6	4.64E-03 ± 1.89E-04	1.85E-03 ± 6.99E-05	0.621 ± 0.012	1.03E-03 ± 4.35E-05	94	0.99524
123	0.0876 ± 0.0166	4.83E-10 ± 4.62E-09	0.146 ± 0.014	1.83E-06 ± 1.78E-05	1	4.92E-03 ± 2.74E-04	1.52E-03 ± 7.52E-04	0.599 ± 0.015	8.22E-04 ± 4.07E-04	99	0.99641
153	0.0875 ± 0.0031	6.79E-07 ± 6.36E-08	0.217 ± 0.006	4.28E-05 ± 9.19E-06	28	5.87E-03 ± 6.10E-04	1.04E-03 ± 9.10E-05	0.583 ± 0.020	5.53E-04 ± 5.23E-05	72	0.99824
183	0.2006 ± 0.0019	1.20E-06 ± 4.50E-08	0.246 ± 0.001	3.21E-05 ± 1.57E-06	56	5.53E-03 ± 5.94E-04	5.24E-04 ± 5.27E-05	0.558 ± 0.016	2.81E-04 ± 2.88E-05	44	0.99897
213	0.4096 ± 0.0018	3.46E-07 ± 3.98E-09	0.238 ± 0.001	1.13E-05 ± 1.31E-07	100	-	-	-	-	-	0.99936
243	1.1569 ± 0.0328	4.28E-08 ± 3.06E-09	0.239 ± 0.002	1.38E-06 ± 1.12E-07	98	1.21E-05 ± 4.98E-05	1.82E-04 ± 3.29E-03	0.198 ± 0.037	9.19E-04 ± 1.68E-03	2	0.99691
273	1.5427 ± 0.0829	2.43E-08 ± 2.72E-09	0.279 ± 0.003	3.15E-07 ± 3.88E-08	92	3.80E-03 ± 2.32E-03	5.35E-09 ± 9.21E-09	0.153 ± 0.014	2.47E-07 ± 5.56E-07	8	0.99537

Table B. 10 Luminescence lifetimes (τ_i), their pre-exponential factors (a_i), parameters β_i, average lifetimes ($<\tau_i>$) and contributions of $[Ag(SPh)]_n$ phase **2** for λ_{em} = 750 nm at 93 to 243 K temperature range.

Temperature, K	$a_1 \pm \sigma a_1$	$\tau_1 \pm \sigma\tau_1$, s	$\beta_1 \pm \sigma\beta_1$	$<\tau_1> \pm \sigma<\tau_1>$, s	Contribution of τ_1, %	$a_2 \pm \sigma a_2$	$\tau_2 \pm \sigma\tau_2$, s	$\beta_2 \pm \sigma\beta_2$	$<\tau_2> \pm \sigma<\tau_2>$, s	Contribution of τ_2, %	$a_3 \pm \sigma a_3$	$\tau_3 \pm \sigma\tau_3$, s	$\beta_3 \pm \sigma\beta_3$	$<\tau_3> \pm \sigma<\tau_3>$, s	Contribution of τ_3, %	R^2
93	3.69E-04 ± 1.59E-05	3.00E-03 ± 1.56E-04	0.795 ± 0.021	3.42E-03 ± 2.01E-04	43	0.0163 ± 0.0007	5.06E-05 ± 3.30E-06	0.558 ± 0.012	8.43E-05 ± 8.16E-06	47	0.8711 ± 0.0894	5.79E-08 ± 1.38E-08	0.326 ± 0.013	4.02E-08 ± 1.26E-08	10	0.99730
123	3.02E-04 ± 1.80E-05	2.64E-03 ± 1.82E-04	0.769 ± 0.024	3.08E-03 ± 2.34E-04	41	0.0185 ± 0.0010	2.46E-05 ± 2.43E-06	0.459 ± 0.012	5.86E-05 ± 6.26E-06	48	0.8150 ± 0.0855	6.67E-08 ± 1.49E-08	0.352 ± 0.015	4.07E-08 ± 1.02E-08	11	0.99723
153	2.10E-04 ± 2.25E-05	1.63E-03 ± 1.98E-04	0.677 ± 0.028	2.13E-03 ± 3.56E-04	33	0.0193 ± 0.0019	1.05E-05 ± 2.02E-06	0.395 ± 0.016	3.62E-05 ± 7.57E-06	52	1.5166 ± 0.3352	1.66E-08 ± 8.16E-09	0.302 ± 0.021	1.36E-08 ± 7.57E-09	15	0.99644
183	4.71E-03 ± 2.74E-03	3.57E-06 ± 3.43E-06	0.263 ± 0.023	6.45E-05 ± 6.81E-05	41	0.0120 ± 0.0045	8.19E-06 ± 4.12E-06	0.432 ± 0.048	2.23E-05 ± 1.21E-05	36	6.6495 ± 7.5348	3.42E-10 ± 1.03E-09	0.207 ± 0.052	1.32E-09 ± 9.75E-09	23	0.99453
213	2.39E-01 ± 3.04E-01	1.36E-08 ± 4.10E-08	0.204 ± 0.055	1.39E-06 ± 1.49E-05	73	0.0008 ± 0.0259	2.73E-07 ± 1.32E-5	0.199 ± 0.726	3.43E-05 ± 1.66E-03	6	3.4358 ± 5.3944	1.55E-09 ± 5.26E-09	0.259 ± 0.097	2.02E-09 ± 3.25E-08	21	0.99456
243	-	-	-	-	-	0.0038 ± 0.0.0007	1.34E-06 ± 4.09E-07	0.256 ± 0.007	2.30E-05 ± 7.65E-06	35	3.9052 ± 1.2939	1.84E-10 ± 1.66E-10	0.186 ± 0.012	1.49E-09 ± 1.61E-09	65	0.99257

Table B. 11 Luminescence lifetimes (τ_i), their pre-exponential factors (a_i), contributions and the parameters β_i for compound $[Au(SPh)]_n$ λ_{em} = 675 nm at 93 to 383 K temperature range.

Temperature, K	$a_1 \pm \sigma a_1$	$\tau_1 \pm \sigma\tau_1$, s	$\beta_1 \pm \sigma\beta_1$	$\langle\tau_1\rangle \pm \sigma\langle\tau_1\rangle$, s	Contribution of $\langle\tau_1\rangle$, %	$a_2 \pm \sigma a_2$	$\tau_2 \pm \sigma\tau_2$, s	$\beta_2 \pm \sigma\beta_2$	$\langle\tau_2\rangle \pm \sigma\langle\tau_2\rangle$, s	Contribution of $\langle\tau_2\rangle$, %	R^2
93	0.9782 ± 0.0270	8.37E-06 ± 1.27E-07	0.783 ± 0.006	9.63E-06 ± 1.62E-07	98	0.0183 ± 0.0296	6.42E-06 ± 6.32E-06	0.564 ± 0.096	1.05E-05 ± 1.05E-05	2	0.99895
123	0.9606 ± 0.0036	9.35E-06 ± 6.70E-08	0.856 ± 0.003	1.01E-05 ± 8.38E-08	98	0.0026 ± 0.0001	6.05E-05 ± 1.99E-06	0.703 ± 0.006	7.62E-05 ± 2.59E-06	2	0.99805
153	0.9583 ± 0.0035	8.90E-06 ± 6.26E-08	0.856 ± 0.003	9.64E-06 ± 7.87E-08	97	0.0046 ± 0.0002	3.64E-06 ± 1.53E-06	0.612 ± 0.006	5.35E-05 ± 2.30E-06	3	0.99816
183	0.9656 ± 0.0221	7.71E-06 ± 1.14E-07	0.794 ± 0.005	8.79E-06 ± 1.41E-07	97	0.0375 ± 0.0259	4.04E-06 ± 1.64E-06	0.538 ± 0.034	7.13E-06 ± 2.93E-06	3	0.99879
213	0.9749 ± 0.0070	6.79E-06 ± 4.90E-08	0.788 ± 0.003	7.78E-06 ± 6.22E-08	99	0.0053 ± 0.0073	4.15E-06 ± 4.29E-06	0.497 ± 0.081	8.39E-06 ± 8.88E-06	1	0.99843
243	0.8978 ± 0.0087	5.66E-06 ± 4.62E-08	0.892 ± 0.003	5.98E-06 ± 5.42E-08	95	0.1245 ± 0.0128	9.59E-07 ± 5.70E-08	0.481 ± 0.004	2.07E-06 ± 1.33E-07	5	0.99866
273	0.9860 ± 0.0048	2.48E-06 ± 1.66E-08	0.897 ± 0.003	2.62E-06 ± 2.00E-08	99	0.0094 ± 0.0039	8.98E-07 ± 3.33E-07	0.450 ± 0.003	2.22E-06 ± 8.25E-07	1	0.99793
293	1.0357 ± 0.0047	1.23E-06 ± 8.46E-09	0.901 ± 0.003	1.30E-06 ± 1.02E-08	99	0.0067 ± 0.0009	6.83E-07 ± 9.83E-08	0.430 ± 0.009	1.88E-06 ± 2.80E-07	1	0.99823
323	1.0793 ± 0.0061	4.11E-07 ± 1.55E-09	0.911 ± 0.004	4.30E-07 ± 3.79E-09	99	0.0159 ± 0.0021	7.62E-08 ± 1.16E-08	0.350 ± 0.006	3.83E-07 ± 6.11E-08	1	0.99831
353	1.1546 ± 0.0104	1.42E-07 ± 1.55E-09	0.879 ± 0.004	1.51E-07 ± 1.84E-09	99	0.0011 ± 0.0001	3.07E-07 ± 2.67E-08	0.392 ± 0.005	1.08E-06 ± 9.68E-08	1	0.99761
383	1.1745 ± 0.0132	5.79E-08 ± 6.69E-10	0.900 ± 0.004	6.09E-08 ± 7.75E-10	99	0.0002 ± 0.0001	3.97E-06 ± 7.57E-08	0.646 ± 0.013	5.46E-05 ± 1.53E-07	1	0.99778

B.1.2 Chapter 2

Summary of conditions for luminescent measurements of all compounds discussed in the Chapter 2 can be found in the **Table B. 12**.

Table B. 12 Conditions of luminescent measurements for compounds discussed in Chapter 2.

Compound	Temperature range, K	Long pass filter used	Wavelength range for 2D maps and emission-exciation spectra, nm		(λ_{exc}, λ_{em}) for lifetime measurements, nm
			λ_{exc}	λ_{em}	
p-HSPhCO$_2$H	93-293 K	FEL450	200-425	460-720	-
p-HSPhCO$_2$Me	93-293 K	FEL450	200-425	450-710	-
[Cu(*p*-SPhCO$_2$H)]$_n$	93-293 K	FEL450	200-425	450-710	379
[Cu(*p*-SPhCO$_2$Me)]$_n$	93 K	FEL400	200-390	420-930	-
	92-503 K		380		
[Ag(*p*-SPhCO$_2$H)]$_n$	93-273 K	FEL450	200-425	450-710	-
	93 K	FEL400	-	-	(352, 528) (368, 700)
[Ag(*p*-SPhCO$_2$Me)]$_n$	93-243 K	FEL450	200-425	450-710	-
	93 K	FEL400	-	-	(364, 524) (364, 650)
[Au(*p*-SPhCO$_2$H)]$_n$	80-290 K	FEL450	200-425	450-710	379

Fit functions have a form of a sum of exponentials. They appear occasionally with one or more extra stretched exponential decay curves. [1] Their equations are given in the **Table B. 13**.

Table B. 13 Equations used for lifetime decay curves fit.

General form of the equation	$\boldsymbol{I = a_1 e^{-(x/t_1)^{\beta_1}} + a_2 e^{-(x/t_2)^{\beta_2}} + a_3 e^{-(x/t_3)^{\beta_3}} + a_4 e^{-(x/t_4)^{\beta_4}}}$, with $\boldsymbol{\beta_i = (0, 1)}$
[Cu(*p*-SPhCO$_2$H)]$_n$	$I = a_1 e^{-x/t_1} + a_2 e^{-x/t_2} + a_3 e^{-x/t_3} + a_3 e^{-x/t_4}$
[Ag(*p*-SPhCO$_2$H)]$_n$	$I = a_1 e^{-x/t_1} + a_2 e^{-(x/t_2)^{\beta}} + a_3 e^{-x/t_3}$
[Ag(*p*-SPhCO$_2$Me)]$_n$	$I = a_1 e^{-x/t_1} + a_2 e^{-(x/t_2)^{\beta}} + a_3 e^{-x/t_3}$
[Au(*p*-SPhCO$_2$H)]$_n$	$I = a_1 e^{-x/t_1} + a_2 e^{-x/t_2} + a_3 e^{-x/t_3}$
[Au(*p*-SPhCO$_2$Me)]$_n$	$I = a_1 e^{-(x/t_1)^{\beta_1}} + a_2 e^{-x/t_2} + a_3 e^{-x/t_3}$

In order to have access to various dynamics involved in the [Ag(*p*-SPhCO$_2$H)]$_n$ and [Ag(*p*-SPhCO$_2$Me)]$_n$ CPs, various measurements were performed with various optical densities at the detection side. Thanks to the combination of different measurements dynamics, over 7 orders of magnitude in time and intensities could have been covered. Based on the data, it is clear,

that the measurements cannot be fitted by a simple sum of exponential decay curves. The best fits are obtained by the sum of one fast exponential decay (in the sub μs range), a slow single exponential decay (a few ms) and a distribution of lifetimes in the intermediate region (μs range) well fitted by a stretched exponential.

In case of $[Au(p\text{-}SPhCO_2H)]_n$, collected data were fitted by a three-exponential function, which yields the individual luminescence lifetimes. The fastest lifetime (τ_3) was an unidentified component which was present in the measurement even without the sample (probably residual excitation pulse). The other two lifetimes were linked to their respective emission peaks (τ_2 – fast component – LE and τ_1 – slow component – HE peak) with the time resolved spectroscopy measurements, the τ_3 was omitted from discussion.

$[Au(p\text{-}SPhCO_2Me)]_n$[2] has been already reported by our team. Its characterization is completed by the temperature dependent studies of lifetime decay. The collected data were fitted by a three-exponential function, where one of the components was a stretched exponential (**Figure B. 9**, **Figure B. 10**).

Use of this equation led to the satisfactory quality fits which yields the individual luminescence lifetimes (**Table B. 14** -**Table B. 18**).

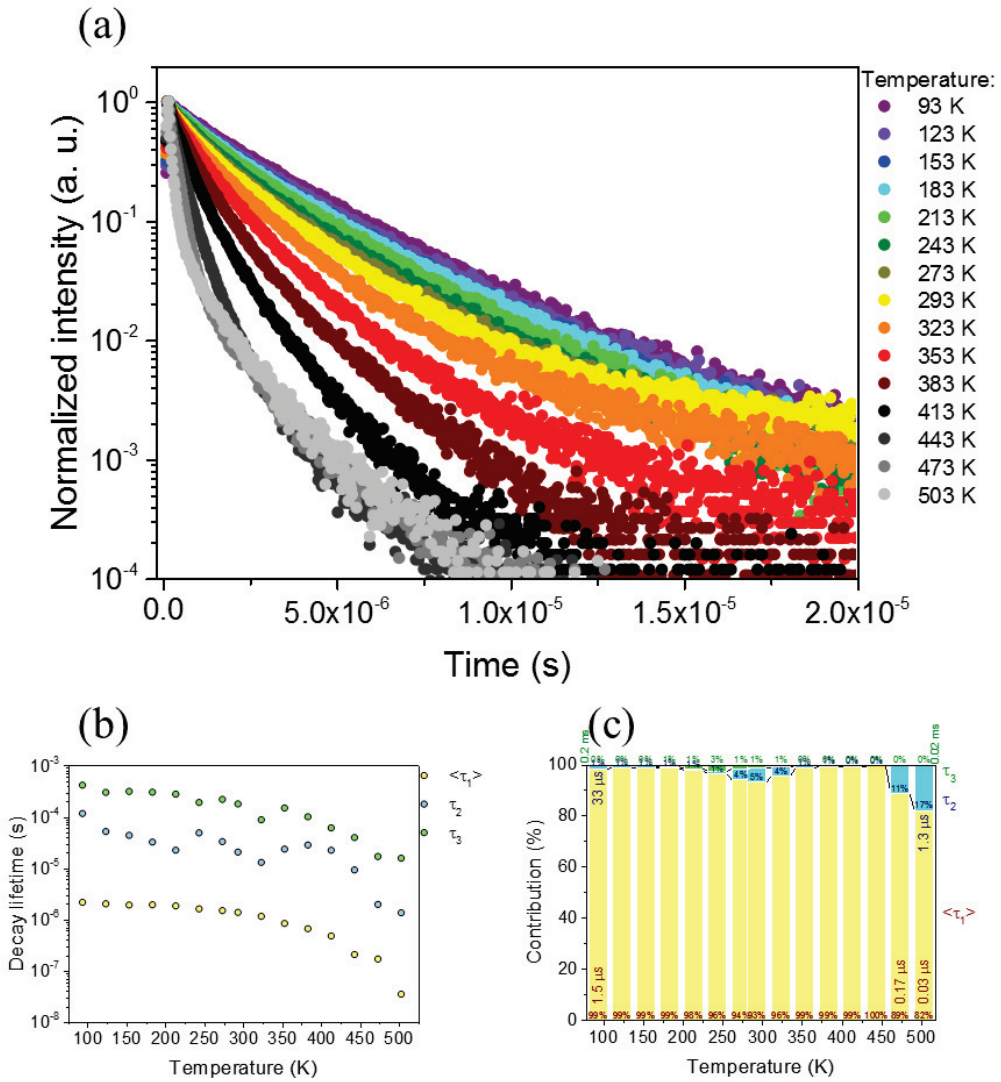

Figure B. 9 Temperature-dependent luminescence decays (λ_{exc} = 380 nm, λ_{em} = 640 nm) of [Au(*p*-SPhCO$_2$Me)]$_n$ (a). Values of the lifetime decays (b) and of contributions of different components (c) at various temperatures.

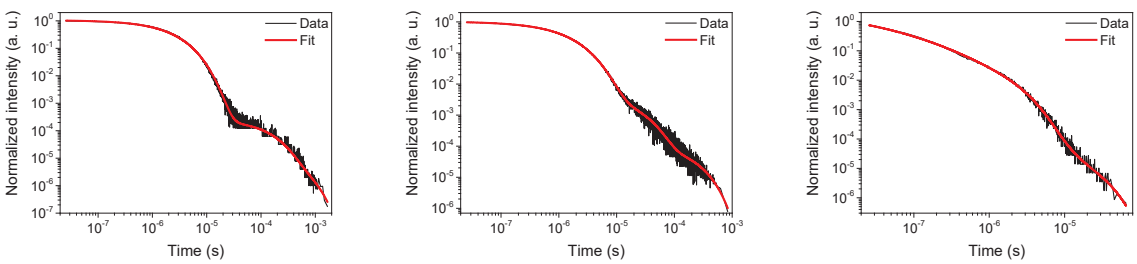

(a) (b) (c)

Figure B. 10 Examples of lifetime decay fit of [Au(*p*-SPhCO$_2$Me)]$_n$ at 93 K (a), 293 K (b) and 503 K (c).

Table B. 14 Luminescence lifetimes (τ_i) and their contributions of $[Cu(p\text{-}SPhCO_2H)]_n$ at 93 to 273 K temperature range.

Temperature, K	τ_1, s	Contribution of τ_1, %	τ_2, s	Contribution of τ_2, %	τ_3, s	Contribution of τ_3, %	τ_4, s	Contribution of τ_4, %	R^2
93	4.44E-06	5	4.41E-05	24	2.68E-04	42	9.20E-03	26	0.99518
153	1.28E-06	8	9.58E-06	22	5.53E-05	32	2.46E-03	36	0.99481
213	5.70E-07	10	3.11E-06	20	2.34E-05	29	2.84E-03	41	0.9957
273	1.40E-07	11	8.40E-07	23	8.40E-06	28	7.64E-04	42	0.99641

Table B. 15 Luminescence lifetimes (τ_i) and their contributions of $[Ag(p\text{-}SPhCO_2H)]_n$ at 93 K.

(λ_{exc}, λ_{em}), nm	τ_1, s	Contribution of τ_1, %	$<\tau_2>$, s	β	Contribution of τ_2, %	τ_3, s	Contribution of τ_3, %
(352, 528)	1.57E-08	4.5	1.82E-07	0.06216	83.5	2.5E-02	12
(368, 700)	2.2E-05	27.6	4.5E-09	0.06492	19.4	1.91E-04	53

Table B. 16 Luminescence lifetimes (τ_i) and their contributions of $[Ag(p\text{-}SPhCO_2Me)]_n$ at 93 K.

(λ_{exc}, λ_{em}), nm	τ_1, s	Contribution of τ_1, %	$<\tau_2>$, s	β	Contribution of τ_2, %	τ_3, s	Contribution of τ_3, %
(364, 524)	1.36E-06	3.5	4.756E-04	0.09786	94.4	1.17E-02	2.1
(364, 650)	1.53E-06	29.4	1.75E-04	0.36937	70.5	8E-03	0.5

Table B. 17 Luminescence lifetimes (τ_i) and their contributions of $[Au(p\text{-}SPhCO_2H)]_n$ at 93 to 293 K temperature range.

Temperature, K	τ_1, s	Contribution of τ_1, %	τ_2, s	Contribution of τ_2, %
93	9.94E-06	86	1.02E-06	14
153	9.23E-06	86	9.82E-07	14
213	6.85E-06	82	7.67E-07	18
273	5.82E-06	79	7.18E-07	21
293	4.62E-06	76	6.28E-07	24

Table B. 18 Luminescence lifetimes (τ_i), their pre-exponential factors (a_i), parameters β_1, average lifetimes ($<\tau_i>$) and contributions of [Au(*p*-SPhCO$_2$Me)]$_n$ at 93 to503 K temperature range.

Temperature, K	$a_1 \pm \sigma a_1$	$\tau_1 \pm \sigma\tau_1$, s	$\beta_1 \pm \sigma\beta_1$	$<\tau_1> \pm \sigma<\tau_1>$, s	Contribution of τ_1, %	$a_2 \pm \sigma a_2$	$\tau_2 \pm \sigma\tau_2$, s	Contribution of τ_2, %	$a_3 \pm \sigma a_3$	$\tau_3 \pm \sigma\tau_3$, s	Contribution of τ_3 %	R^2
93	1.0518 ± 0.0057	1.89E-06 ± 1.64E-08	0.796 ± 0.003	2.15E-06 ± 2.03E-08	98.6	2.32E-04 ± 2.20E-06	1.18E-04 ± 1.09E-06	1.2	1.34E-05 ± 5.69E-07	4.23E-04 ± 6.24E-06	0.2	0.99811
123	1.0435 ± 0.0060	1.75E-06 ± 1.62E-08	0.787 ± 0.003	2.01E-06 ± 2.03E-08	98.9	3.41E-04 ± 5.65E-06	5.23E-05 ± 6.26E-07	0.8	1.76E-05 ± 5.64E-07	3.05E-04 ± 5.26E-06	0.3	0.99769
153	1.0411 ± 0.0062	1.66E-06 ± 1.57E-08	0.784 ± 0.003	1.91E-06 ± 1.97E-08	99.0	3.00E-04 ± 6.56E-06	4.40E-05 ± 6.90E-07	0.7	2.35E-05 ± 5.65E-07	3.20E-04 ± 4.71E-06	0.4	0.99755
183	1.0232 ± 0.0060	1.69E-06 ± 1.61E-08	0.793 ± 0.003	1.92E-06 ± 2.01E-08	98.7	3.58E-04 ± 1.30E-05	3.25E-05 ± 7.77E-07	0.6	4.71E-05 ± 7.93E-07	3.07E-04 ± 3.40E-06	0.7	0.99741
213	1.0006 ± 0.0061	1.63E-06 ± 1.62E-08	0.810 ± 0.004	1.83E-06 ± 2.01E-08	98.1	4.46E-04 ± 3.05E-05	2.25E-05 ± 9.00E-07	0.5	9.17E-05 ± 1.19E-06	2.81E-04 ± 2.42E-06	1.4	0.99706
243	1.0243 ± 0.0056	1.38E-06 ± 1.24E-08	0.774 ± 0.003	1.60E-06 ± 1.58E-08	96.4	3.61E-04 ± 1.03E-05	4.91E-05 ± 1.89E-06	1.1	2.21E-04 ± 4.77E-06	1.94E-04 ± 1.53E-06	2.5	0.99767
273	1.0154 ± 0.0060	1.28E-06 ± 1.29E-08	0.776 ± 0.004	1.48E-06 ± 1.66E-08	94.2	2.13E-03 ± 2.90E-05	3.32E-05 ± 2.90E-07	4.5	9.76E-05 ± 1.61E-06	2.22E-04 ± 1.68E-06	1.4	0.99768
293	1.0210 ± 0.0069	1.17E-06 ± 1.38E-08	0.766 ± 0.004	1.37E-06 ± 1.80E-08	93.3	3.86E-03 ± 6.95E-05	2.07E-05 ± 1.83E-07	5.4	1.04E-04 ± 1.32E-06	1.81E-04 ± 9.64E-07	1.3	0.99746
323	1.0366 ± 0.0062	9.40E-07 ± 9.81E-09	0.732 ± 0.004	1.14E-06 ± 1.31E-08	95.6	3.36E-03 ± 8.95E-05	1.30E-05 ± 1.51E-07	3.6	1.20E-04 ± 2.03E-06	8.87E-05 ± 7.00E-07	0.9	0.99788
353	1.1775 ± 0.0107	6.26E-07 ± 8.69E-09	0.670 ± 0.003	8.28E-07 ± 1.22E-08	98.9	3.86E-04 ± 8.57E-06	2.36E-05 ± 3.22E-07	0.9	1.16E-05 ± 6.22E-07	1.51E-04 ± 5.25E-06	0.2	0.99674
383	1.1447 ± 0.0095	5.04E-07 ± 6.33E-09	0.683 ± 0.003	6.54E-07 ± 8.65E-09	99.4	1.43E-04 ± 2.17E-06	2.84E-05 ± 3.79E-07	0.5	5.90E-06 ± 5.32E-07	1.02E-04 ± 3.60E-06	0.1	0.99743
413	1.1529 ± 0.0100	3.62E-07 ± 4.56E-09	0.680 ± 0.003	4.72E-07 ± 6.25E-09	99.4	9.85E-05 ± 1.64E-06	2.24E-05 ± 3.97E-07	0.4	1.44E-05 ± 7.11E-07	6.17E-05 ± 8.03E-07	0.2	0.9978
443	1.6962 ± 0.0239	1.26E-07 ± 2.61E-09	0.569 ± 0.003	2.05E-07 ± 4.39E-09	99.6	1.29E-04 ± 3.75E-06	9.26E-06 ± 1.54E-07	0.4	7.44E-06 ± 2.87E-07	3.98E-05 ± 5.69E-07	0.1	0.99708
473	1.2268 ± 0.0215	1.22E-07 ± 3.31E-09	0.652 ± 0.007	1.66E-07 ± 4.84E-09	88.7	1.17E-02 ± 2.44E-04	1.95E-06 ± 1.15E-08	11.0	3.46E-05 ± 6.15E-07	1.70E-05 ± 1.33E-07	0.3	0.99712
503	4.0989 ± 0.1644	4.41E-09 ± 3.51E-10	0.313 ± 0.003	3.42E-08 ± 2.92E-09	82.2	1.84E-02 ± 5.92E-04	1.34E-06 ± 1.33E-08	17.4	3.34E-05 ± 8.56E-07	1.57E-05 ± 1.39E-07	0.3	0.99785

B.1.3 Chapter 3

Summary of conditions for luminescent measurements of all compounds discussed in the Chapter 3 can be found in the **Table B. 19**.

Table B. 19 Luminescent measurements conditions for compounds discussed in Chapter 3.

Compound	Temperature range, K	Long pass filter used	Wavelength range for 2D maps and emission-exciation spectra, nm		(λ_{exc}, λ_{em}) for lifetime measurements
			λ_{exc}	λ_{em}	
m-HSPhCO$_2$H	93-243 K	FEL400	200-450	420-680	-
[Cu(*m*-SPhCO$_2$H)]$_n$	93-323 K	FEL450	225-450	460-825	(412, 590)
[Ag(*m*-SPhCO$_2$H)]$_n$	93-323 K	FEL400	200-400	420-680	(352, 500) for 93-183 K (352, 550) for 213-323 K
[Au(*m*-SPhCO$_2$H)]$_n$	93-503 K	FEL450	200-450	470-730	(352, 610)
[Au(*p*-SPhCO$_2$Me)]$_n$	123-403 K†	FELH600	200-480	520-780	-
	93-503 K	FEL450	-	-	(380, 640)

† published prior to beginning of this PhD project in [2].

Note on *m*-HSPhCO$_2$H luminescence. In the discussion of photophysical properties of [Cu(*m*-SPhCO$_2$H)]$_n$ the emission-excitation spectra (λ_{em} = 384 nm, λ_{exc} = 447 nm) of *m*-HSPhCO$_2$H are given. It should be noted that its photophysical behavior is more complicated than that: it possesses yet another two emission peaks at higher excitation energy (at 280 and 332 nm) (**Figure B. 11**).

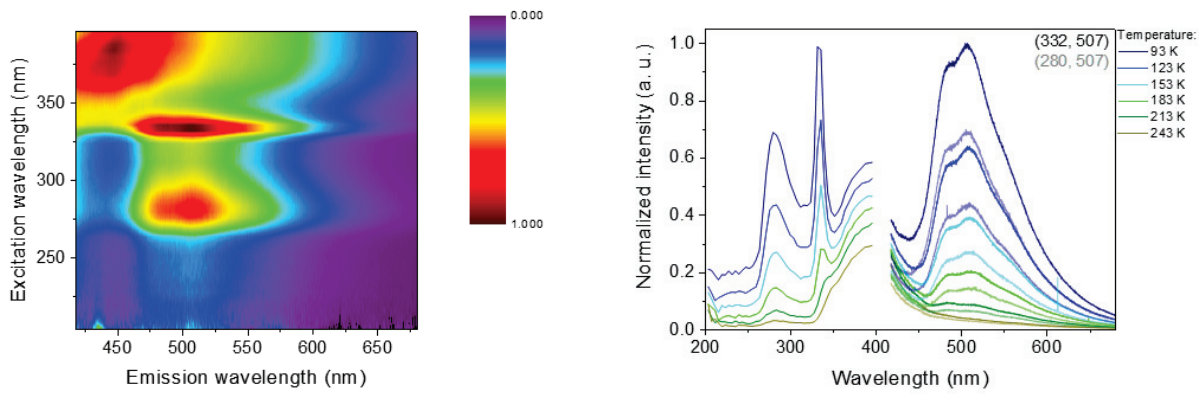

(a) (b)

Figure B. 11 Luminescent properties of *m*-HSPhCO$_2$H: (a) 2D map of the emission and excitation spectra obtained in the solid state at 93 K and (b) emission-excitation spectra (λ_{exc} = 332/280 nm, λ_{em} = 507 nm) obtained in the solid state at variable temperatures.

Lifetime decay curve of none of compounds (discussed in this chapter) could be fitted by a sum of simple exponential decays. For this reason, one or more stretched exponential decay curves were implemented. The forms of the fitting functions are given in the **Table B. 20** below.

Table B. 20 Equations used for lifetime decay curves fit.

General form of the equation	$\boldsymbol{I = a_1 e^{-(x/t_1)^{\beta_1}} + a_2 e^{-(x/t_2)^{\beta_2}} + a_3 e^{-(x/t_3)^{\beta_3}}}$, with $\boldsymbol{\beta_i = (0, 1)}$
[Cu(*m*-SPhCO$_2$H)]$_n$	$I = a_1 e^{-x/t_1} + a_2 e^{-(x/t_2)^{\beta_2}} + a_3 e^{-(x/t_3)^{\beta_3}}$
[Ag(*m*-SPhCO$_2$H)]$_n$	$I = a_1 e^{-(x/t_1)^{\beta_1}} + a_2 e^{-(x/t_2)^{\beta_2}}$
[Au(*m*-SPhCO$_2$H)]$_n$	$I = a_1 e^{-(x/t_1)^{\beta_1}} + a_2 e^{-x/t_2} + a_3 e^{-x/t_3}$

Use of this equation led to the satisfactory quality fits (**Figure B. 12** - **Figure B. 14**) yielding the individual luminescence (**Table B. 21** - **Table B. 23**).

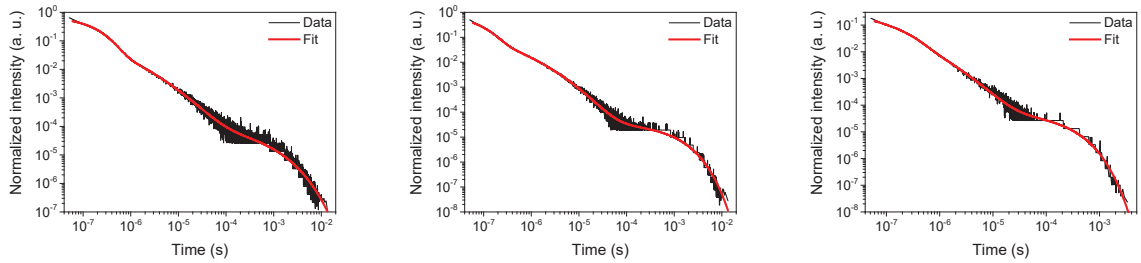

(a) (b) (c)

Figure B. 12 Examples of lifetime decay fit of [Cu(*m*-SPhCO$_2$H)]$_n$ at 93 K (a), 183 K (b) and 293 K (c).

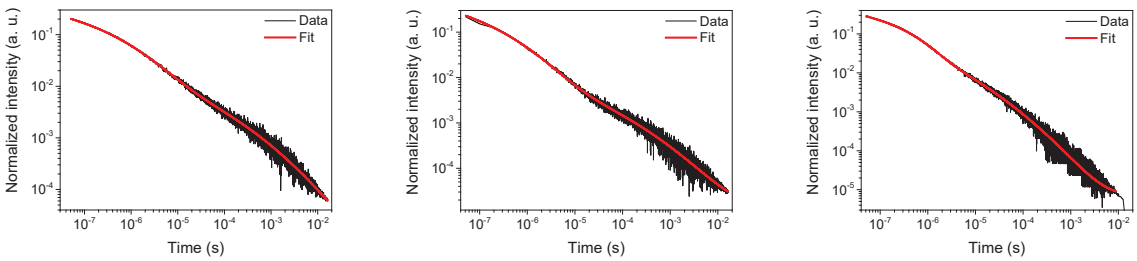

(a) (b) (c)

Figure B. 13 Examples of lifetime decay fit of [Ag(*m*-SPhCO$_2$H)]$_n$ at 93 K (a), 183 K (b) and 293 K (c).

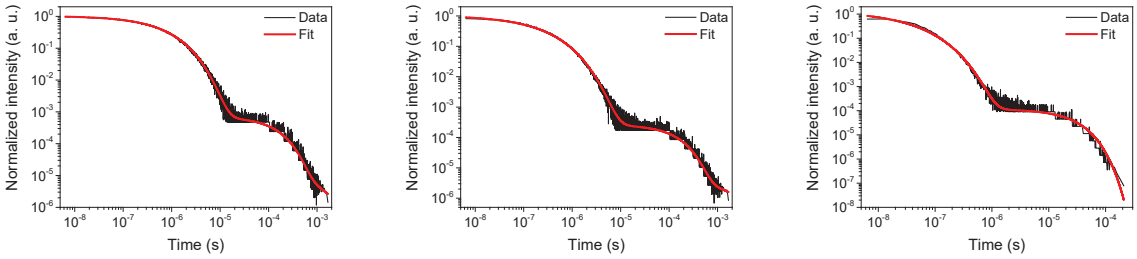

(a) (b) (c)

Figure B. 14 Examples of lifetime decay fit of [Au(*m*-SPhCO$_2$H)]$_n$ at 93 K (a), 293 K (b) and 503 K (c).

Table B. 21 Luminescence lifetimes (τ_i), their pre-exponential factors (a_i), parameters β_i, average lifetimes ($<\tau_i>$) and contributions of [Cu(*m*-SPhCO$_2$H)]$_n$ at 93 to323 K temperature range.

Temperature, K	$a_1 \pm \sigma a_1$	$\tau_1 \pm \sigma\tau_1$, s	Contribution of τ_1, %	$a_2 \pm \sigma a_2$	$\tau_2 \pm \sigma\tau_2$, s	$\beta_2 \pm \sigma\beta_2$	$<\tau_2> \pm \sigma<\tau_2>$, s	Contribution of τ_2, %	$a_3 \pm \sigma a_3$	$\tau_3 \pm \sigma\tau_3$, s	$\beta_3 \pm \sigma\beta_3$	$<\tau_3> \pm \sigma<\tau_3>$, s	Contribution of τ_3, %	R^2
93	0.5068 ± 0.0120	1.88E-07 ± 2.68E-09	34	1.5005 ± 0.5340	5.25E-10 ± 4.43E-10	0.194 ± 0.011	8.28E-08 ± 8.10E-08	45	1.07E-04 ± 4.06E-06	2.60E-04 ± 1.51E-05	0.491 ± 0.006	1.30E-04 ± 7.75E-06	21	0.99541
123	0.5742 ± 0.0095	1.62E-07 ± 2.13E-09	40	0.2332 ± 0.0339	2.35E-08 ± 7.11E-09	0.266 ± 0.008	3.95E-07 ± 1.32E-07	41	7.14E-05 ± 2.15E-06	3.25E-04 ± 1.38E-05	0.546 ± 0.006	1.67E-04 ± 7.33E-06	18	0.99578
153	0.5654 ± 0.0143	1.09E-07 ± 2.07E-09	35	0.8539 ± 0.1615	1.68E-09 ± 6.93E-10	0.218 ± 0.007	1.02E-07 ± 4.75E-08	52	3.24E-05 ± 8.35E-07	4.43E-04 ± 1.55E-05	0.597 ± 0.006	2.39E-04 ± 8.71E-06	13	0.99573
183	0.5843 ± 0.0222	7.73E-08 ± 2.11E-09	27	1.1203 ± 0.2134	1.40E-09 ± 5.70E-10	0.222 ± 0.007	7.31E-08 ± 3.33E-08	53	3.55E-05 ± 5.97E-07	6.81E-04 ± 1.52E-05	0.699 ± 0.005	4.22E-04 ± 9.91E-06	20	0.99517
213	0.5073 ± 0.0461	4.91E-08 ± 2.74E-09	18	1.5381 ± 0.2679	1.04E-09 ± 3.75E-10	0.226 ± 0.006	4.81E-08 ± 1.93E-08	60	2.80E-05 ± 4.11E-07	7.51E-04 ± 1.51E-05	0.723 ± 0.005	4.83E-04 ± 5.24E-05	22	0.99469
243	0.5368 ± 0.1914	2.70E-08 ± 3.95E-09	13	4.6454 ± 0.8584	1.30E-10 ± 5.18E-11	0.201 ± 0.005	1.52E-08 ± 6.86E-09	79	4.78E-05 ± 1.38E-06	8.81E-05 ± 3.29E-06	0.572 ± 0.005	4.63E-05 ± 1.79E-06	8	0.99598
273	0.0566 ± 0.0054	2.37E-07 ± 1.02E-08	16	3.2150 ± 0.8672	1.72E-10 ± 9.69E-11	0.203 ± 0.008	1.85E-08 ± 1.18E-08	70	5.35E-05 ± 1.09E-06	1.49E-04 ± 3.62E-06	0.677 ± 0.005	8.96E-05 ± 2.27E-06	13	0.99628
293	0.0664 ± 0.0056	1.93E-07 ± 7.11E-09	19	3.8261 ± 1.5360	5.70E-11 ± 4.98E-11	0.189 ± 0.010	1.13E-08 ± 1.14E-08	63	5.13E-05 ± 9.88E-07	1.72E-04 ± 3.80E-06	0.714 ± 0.005	1.09E-04 ± 2.53E-06	17	0.99579
323	0.0867 ± 0.0070	1.62E-07 ± 4.95E-09	24	2.9905 ± 1.6069	5.81E-11 ± 6.81E-11	0.188 ± 0.014	1.21E-08 ± 1.66E-08	59	4.31E-05 ± 9.43E-07	1.90E-04 ± 4.66E-06	0.734 ± 0.006	1.24E-04 ± 3.21E-06	18	0.99468

Table B. 22 Luminescence lifetimes (τ_i), their pre-exponential factors (a_i), parameters β_i, average lifetimes ($<\tau_i>$) and contributions of [Ag(*m*-SPhCO$_2$H)]$_n$ at 93 to323 K temperature range.

Temperature, K	$a_1 \pm \sigma a_1$	$\tau_1 \pm \sigma\tau_1$, s	$\beta_1 \pm \sigma\beta_1$	$<\tau_1> \pm \sigma<\tau_1>$, s	Contribution of τ_1, %	$a_2 \pm \sigma a_2$	$\tau_2 \pm \sigma\tau_2$, s	$\beta_2 \pm \sigma\beta_2$	$<\tau_2> \pm \sigma<\tau_2>$, s	Contribution of τ_2, %	R^2
93	0.4590 ± 0.0308	4.60E-08 ± 7.03E-09	0.285 ± 0.008	5.42E-07 ± 1.01E-07	4	0.1387 ± 0.0353	8.87E-09 ± 8.42E-09	0.143 ± 0.008	8.87E-07 ± 1.09E-06	96	0.99692
123	1.1900 ± 0.1280	7.79E-09 ± 2.56E-09	0.220 ± 0.008	4.33E-07 ± 1.72E-07	10	0.0110 ± 0.0017	1.74E-05 ± 7.89E-06	0.249 ± 0.014	2.67E-05 ± 1.46E-05	90	0.99958
153	1.1038 ± 0.1465	9.05E-09 ± 3.22E-09	0.244 ± 0.010	2.54E-07 ± 1.06E-07	9	0.0230 ± 0.0047	5.91E-07 ± 4.02E-07	0.188 ± 0.010	4.44E-06 ± 3.77E-06	91	0.99514
183	0.9506 ± 0.1704	1.05E-08 ± 4.65E-09	0.262 ± 0.014	1.91E-07 ± 9.80E-08	8	0.0770 ± 0.0155	8.82E-09 ± 6.02E-09	0.148 ± 0.006	5.91E-07 ± 4.96E-07	92	0.99385
213	0.5857 ± 0.0538	8.92E-08 ± 1.47E-08	0.332 ± 0.009	5.43E-07 ± 1.00E-07	13	1.7000 ± 1.8485	1.00E-13 ± 4.39E-13	0.095 ± 0.013	1.18E-08 ± 2.89E-07	87	0.99365
243	0.6356 ± 0.0492	5.44E-08 ± 8.64E-09	0.329 ± 0.009	3.44E-07 ± 9.27E-08	16	2.3039 ± 1.3291	1.01E-13 ± 2.21E-13	0.099 ± 0.068	4.93E-09 ± 1.20E-09	84	0.99373
273	0.9094 ± 0.1091	1.90E-08 ± 4.99E-09	0.296 ± 0.011	1.33E-07 ± 4.56E-08	17	3.2585 ± 1.6626	1.00E-13 ± 1.79E-13	0.101 ± 0.006	2.65E-09 ± 6.61E-09	83	0.99333
293	0.2294 ± 0.0304	2.20E-07 ± 3.65E-08	0.579 ± 0.037	3.47E-07 ± 6.25E-08	11	4.2438 ± 1.5153	1.49E-12 ± 1.66E-12	0.119 ± 0.005	2.09E-09 ± 2.92E-09	89	0.99439
323	3.3395 ± 6.7562	1.00E-09 ± 4.30E-09	0.250 ± 0.107	2.40E-08 ± 1.46E-06	14	6.9403 ± 4.3130	3.89E-13 ± 7.07E-13	0.115 ± 0.007	8.99E-10 ± 2.17E-09	86	0.99157

Table B. 23 Luminescence lifetimes (τ_i), their pre-exponential factors (a_i), parameters β_1, average lifetimes ($<\tau_i>$) and contributions of [Au(*m*-$SPhCO_2H$)]$_n$ at 93 to503 K temperature range.

Temperature, K	$a_1 \pm \sigma a_1$	$\tau_1 \pm \sigma\tau_1$, s	$\beta_1 \pm \sigma\beta_1$	$<\tau_1> \pm \sigma<\tau_1>$, s	Contribution of τ_1, %	$a_2 \pm \sigma a_2$	$\tau_2 \pm \sigma\tau_2$, s	Contribution of τ_2, %	$a_3 \pm \sigma a_3$	$\tau_3 \pm \sigma\tau_3$, s	Contribution of τ_3 %	R^2
93	1.0281 ± 0.0058	6.35E-07 ± 6.96E-09	0.649 ± 0.003	8.69E-07 ± 1.01E-08	89	6.84E-04 ± 4.39E-06	1.47E-04 ± 8.62E-07	10	8.93E-06 ± 5.37E-07	1.37E-03 ± 8.70E-05	1	0.99775
123	1.0663 ± 0.0070	3.67E-07 ± 4.80E-09	0.583 ± 0.002	5.74E-07 ± 7.92E-09	85	6.20E-04 ± 3.78E-06	1.49E-04 8.06E-07	13	5.95E-06 ± 3.90E-07	1.69E-03 ± 1.41E-04	1	0.99772
153	1.1449 ± 0.0093	2.26E-07 ± 3.65E-09	0.533 ± 0.002	4.05E-07 ± 6.86E-09	87	3.96E-04 ± 2.65E-06	1.49E-04 ± 9.46E-07	11	4.91E-06 ± 3.22E-07	1.77E-03 ± 1.57E-04	2	0.99741
183	1.1843 ± 0.0102	1.77E-07 ± 3.04E-09	0.516 ± 0.002	3.34E-07 ± 6.03E-09	84	4.32E-04 ± 2.72E-06	1.50E-04 ± 8.72E-07	14	4.42E-06 ± 3.10E-07	1.61E-03 ± 1.38E-04	2	0.99746
213	1.3044 ± 0.0128	1.33E-07 ± 2.59E-09	0.492 ± 0.002	2.74E-07 ± 5.63E-09	85	3.63E-04 ± 2.45E-06	1.44E-04 ± 9.28E-07	13	4.80E-06 ± 3.09E-07	1.43E-03 ± 1.03E-04	2	0.99724
243	1.3183 ± 0.0131	1.17E-07 ± 2.31E-09	0.484 ± 0.002	2.49E-07 ± 5.17E-09	86	3.09E-04 ± 2.08E-06	1.41E-04 ± 9.43E-07	12	5.05E-06 ± 2.98E-07	1.27E-03 ± 7.53E-05	2	0.99736
273	1.1665 ± 0.0105	1.57E-07 ± 2.75E-09	0.522 ± 0.002	2.91E-07 ± 5.33E-09	87	3.01E-04 ± 1.96E-06	1.43E-04 ± 9.05E-07	11	3.91E-06 ± 2.37E-07	1.76E-03 ± 1.47E-04	2	0.99738
293	1.0452 ± 0.0088	1.88E-07 ± 2.96E-09	0.556 ± 0.002	3.14E-07 ± 5.19E-09	88	2.57E-04 ± 1.65E-06	1.44E-04 ± 9.06E-07	10	3.30E-06 ± 1.93E-07	2.30E-03 ± 2.44E-04	2	0.99744
323	1.0032 ± 0.0074	2.02E-07 ± 2.68E-09	0.599 ± 0.002	3.04E-07 ± 4.23E-09	87	2.41E-04 ± 1.33E-06	1.49E-04 ± 8.01E-07	11	2.41E-06 ± 1.44E-07	2.95E-03 ± 4.02E-04	2	0.99787
353	0.9304 ± 0.0070	1.89E-07 ± 2.41E-09	0.644 ± 0.003	2.61E-07 ± 3.51E-09	83	2.71E-04 ± 1.37E-06	1.52E-04 ± 7.88E-07	15	2.53E-06 ± 1.79E-07	1.70E-03 ± 1.54E-04	3	0.99777
383	0.9701 ± 0.0085	1.30E-07 ± 1.84E-09	0.629 ± 0.003	1.85E-07 ± 2.74E-09	89	1.33E-04 ± 7.15E-07	1.47E-04 ± 8.76E-07	10	1.87E-06 ± 1.27E-07	1.14E-03 ± 6.76E-05	1	0.99766
413	1.0048 ± 0.0103	8.74E-08 ± 1.40E-09	0.629 ± 0.003	1.24E-07 ± 2.08E-09	92	1.32E-04 ± 7.97E-07	7.05E-05 ± 4.49E-07	7	2.03E-06 ± 1.43E-07	4.34E-04 ± 2.04E-05	1	0.9973
443	1.1003 ± 0.0218	5.47E-08 ± 1.63E-09	0.604 ± 0.005	8.16E-08 ± 2.54E-09	96	1.16E-04 ± 1.16E-06	3.06E-05 ± 1.32E-07	4				0.99124
473	1.1470 ± 0.0237	3.84E-08 ± 1.14E-09	0.612 ± 0.005	5.63E-08 ± 1.74E-09	94	1.37E-04 ± 1.16E-06	2.56E-05 ± 8.14E-08	6				0.99275
503	1.3674 ± 0.0333	2.26E-08 ± 7.77E-10	0.574 ± 0.005	3.61E-08 ± 1.29E-09	94	1.16E-04 ± 9.21E-07	2.42E-05 ± 6.98E-08	6				0.99328

B.1.4 Chapter 4

Summary of conditions for luminescent measurements of all compounds discussed in the Chapter 4 can be found in the **Table B. 25**.

Table B. 24 Luminescent measurements conditions for compounds discussed in Chapter 4.

Compound	Temperature range, K	Long pass filter used	Wavelength range for 2D maps and emission-exciation spectra, nm		(λ_{exc}, λ_{em}) for lifetime measurements
			λ_{exc}	λ_{em}	
o-HSPhCO$_2$H	93-383 K	FEL385	215-368	390-640	-
[Cu(*o*-SPhCO$_2$H)]$_n$	93-413 K	FEL550	220-524	580-840	(412, 715)
[Ag(*o*-SPhCO$_2$H)]$_n$	93-443 K	FEL550	220-492	530-790	(484, 650)
[Au(*o*-SPhCO$_2$H)]$_n$	93-473 K	FEL550	220-492	630-890	(376, 790)

Note on *o*-HSPhCO$_2$H luminescence. In the discussion the photophysical properties of *o*-HSPhCO$_2$H are not presented. Therefore, 2D emission-excitation map and temperature dependent emission-excitation spectra can be found in **Figure B. 15**.

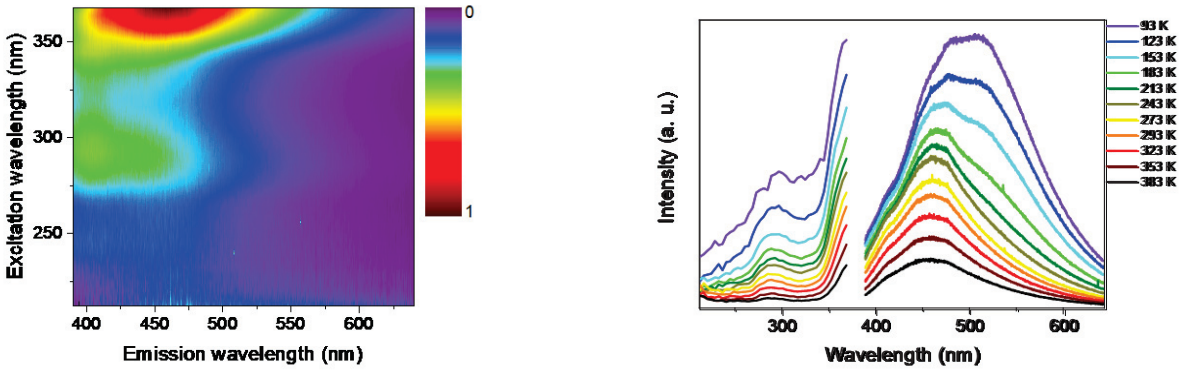

(a) (b)

Figure B. 15 Luminescent properties of *o*-HSPhCO$_2$H: (a) 2D map of the emission and excitation spectra obtained in the solid state at 93 K and (b) emission-excitation spectra (λ_{exc} = 368 nm, λ_{em} = 480 nm) obtained in the solid state at variable temperatures.

Lifetime decay curve of none of compounds (discussed in this chapter) could be fitted by a sum of simple exponential decays. For this reason, one or more stretched exponential decay curves were implemented. The forms of the fitting functions are given in the **Table B. 26** below.

Table B. 25 Equations used for lifetime decay curves fit.

General form of the equation	$\boldsymbol{I = a_1 e^{-(x/t_1)^{\beta_1}} + a_2 e^{-(x/t_2)^{\beta_2}} + a_3 e^{-(x/t_3)^{\beta_3}}}$, with $\boldsymbol{\beta_1 = (0, 1)}$
[Cu(*o*-SPhCO$_2$H)]$_n$	$I = a_1 e^{-x/t_1} + a_2 e^{-x/t_2}$
[Ag(*o*-SPhCO$_2$H)]$_n$	$I = a_1 e^{-(x/t_1)^{\beta_1}} + a_2 e^{-x/t_2}$
[Au(*o*-SPhCO$_2$H)]$_n$	$I = a_1 e^{-(x/t_1)^{\beta_1}} + a_2 e^{-x/t_2}$

Use of this equation led to the satisfactory quality fits (**Figure B. 16** - **Figure B. 18**) yielding the individual luminescence lifetimes (**Table B. 26** - **Table B. 28**).

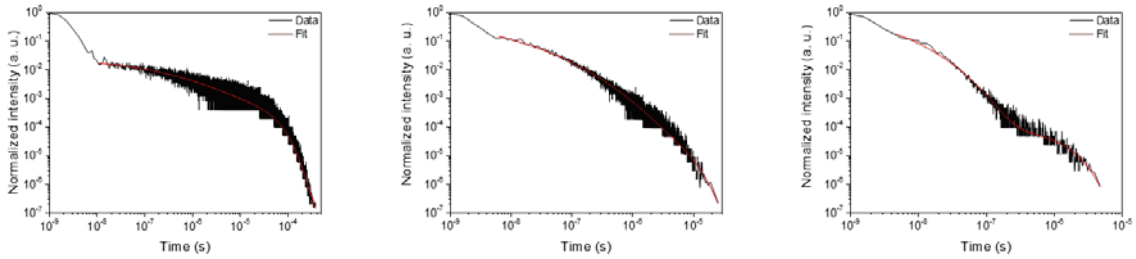

(a) (b) (c)

Figure B. 16 Examples of lifetime decay fit of [Cu(*o*-SPhCO$_2$H)]$_n$ at 93 K (a), 293 K (b) and 413 K (c).

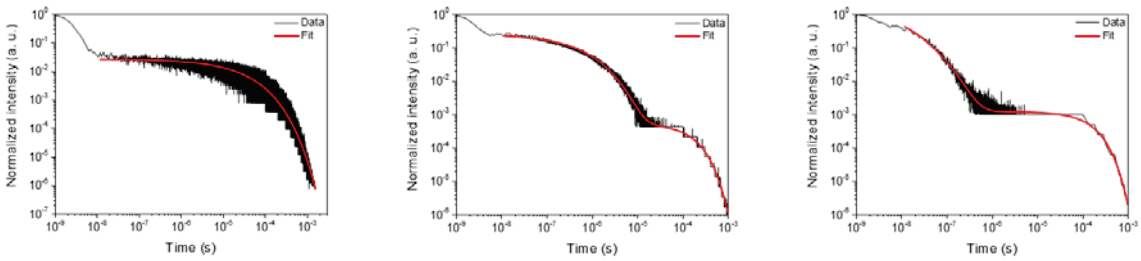

(a) (b) (c)

Figure B. 17 Examples of lifetime decay fit of [Ag(*o*-SPhCO$_2$H)]$_n$ at 93 K (a), 293 K (b) and 443 K (c).

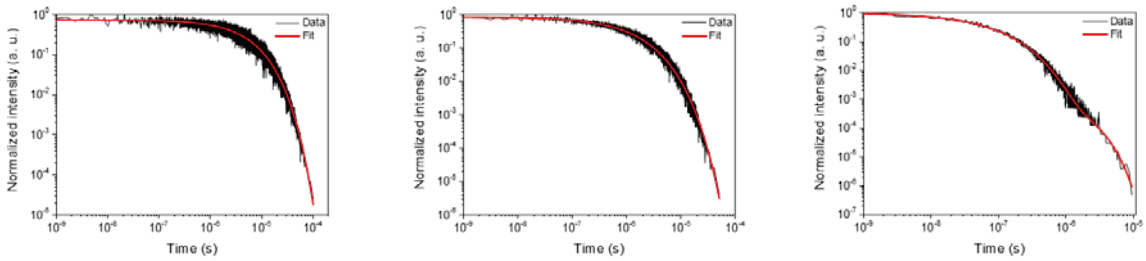

(a) (b) (c)

Figure B. 18 Examples of lifetime decay fit of $[Au(o\text{-}SPhCO_2H)]_n$ at 93 K (a), 293 K (b) and 503 K (c).

Table B. 26 Luminescence lifetimes (τ_i), their pre-exponential factors (a_i), parameter β_1, average lifetime ($<\tau_1>$) and contributions of [Cu(*o*-SPhCO$_2$H)]$_n$ at 93 to413 K temperature range.

Temperature, K	$a_1 \pm \sigma a_1$	$\tau_1 \pm \sigma\tau_1$, s	$\beta \pm \sigma\beta$	$<\tau_1> \pm \sigma<\tau_1>$, s	Contribution of $<\tau_1>$, %	$a_2 \pm \sigma a_2$	$\tau_2 \pm \sigma\tau_2$, s	Contribution of τ_2, %	R^2
93	0.0284 ± 0.0006	7.73E-08 ± 5.21E-09	0.294 ± 0.023	7.79E-07 ± 9.49E-07	46	7.19E-04 ± 1.24E-05	3.61E-05 ± 2.17E-07	54	0.9868
123	0.0477 ± 0.0010	3.80E-08 ± 2.20E-09	0.285 ± 0.002	4.51E-07 ± 7.12E-08	50	5.88E-04 ± 7.83E-06	3.62E-05 ± 1.70E-07	50	0.9908
153	0.1067 ± 0.0028	8.67E-09 ± 5.65E-10	0.263 ± 0.002	1.57E-07 ± 4.06E-08	64	5.33E-04 ± 9.40E-06	1.79E-05 ± 1.03E-07	36	0.9909
183	0.2694 ± 0.0082	1.97E-09 ± 1.40E-10	0.245 ± 0.001	5.39E-08 ± 2.32E-08	78	4.67E-04 ± 1.09E-05	8.85E-06 ± 6.86E-08	22	0.9919
213	0.2872 ± 0.0093	2.25E-09 ± 1.91E-10	0.261 ± 0.002	4.16E-08 ± 1.42E-08	90	1.99E-04 ± 7.64E-06	6.61E-06 ± 1.02E-07	10	0.9905
243	0.6456 ± 0.0216	5.96E-10 ± 4.44E-11	0.241 ± 0.002	1.80E-08 ± 9.33E-09	92	1.67E-04 ± 4.49E-06	5.81E-06 ± 5.38E-08	8	0.9938
273	0.9616 ± 0.0514	4.18E-10 ± 5.21E-11	0.249 ± 0.003	1.04E-08 ± 7.80E-09	97	7.90E-05 ± 3.15E-06	4.37E-06 ± 3.93E-08	3	0.9936
293	1.3886 ± 0.0893	2.12E-10 ± 3.08E-11	0.239 ± 0.003	6.76E-09 ± 7.45E-09	98	4.25E-05 ± 2.13E-06	4.35E-06 ± 4.88E-08	2	0.9926
323	2.8345 ± 0.2552	8.12E-11 ± 1.58E-11	0.234 ± 0.004	2.94E-09 ± 4.56E-09	97	9.44E-05 ± 1.81E-06	3.27E-06 ± 1.42E-08	3	0.9942
353	2.8720 ± 0.2309	1.39E-10 ± 2.18E-11	0.264 ± 0.004	2.45E-09 ± 1.47E-09	98	7.47E-05 ± 1.86E-06	1.92E-06 ± 1.55E-08	2	0.9930
383	1.6795 ± 0.1271	5.42E-10 ± 6.77E-11	0.339 ± 0.005	3.06E-09 ± 5.28E-10	97	1.23E-04 ± 1.44E-06	1.43E-06 ± 5.50E-09	3	0.9936
413	1.9195 ± 0.1780	4.52E-10 ± 6.12E-11	0.369 ± 0.007	1.91E-09 ± 3.05E-10	98	8.62E-05 ± 1.07E-06	1.02E-06 ± 6.13E-09	2	0.9908

Table B. 27 Luminescence lifetimes (τ_i), their pre-exponential factors (a_i), parameter β_1, average lifetime ($<\tau_1>$) and contributions of [Ag(*o*-SPhCO$_2$H)]$_n$ at 93 to443 K temperature range.

Temperature, K	$a_1 \pm \sigma a_1$	$\tau_1 \pm \sigma\tau_1$, s	$\beta \pm \sigma\beta$	$<\tau_1> \pm \sigma<\tau_1>$, s	Contribution of $<\tau_1>$, %	$a_2 \pm \sigma a_2$	$\tau_2 \pm \sigma\tau_2$, s	Contribution of τ_2, %	R^2
93	0.0263 ± 0.0002	2.09E-05 ± 2.80E-07	0.539 ± 0.002	3.67E-05 ± 5.12E-07	100	-	-	-	0.9847
123	0.0488 ± 0.0003	9.11E-06 ± 1.05E-07	0.494 ± 0.001	1.86E-05 ± 2.24E-07	100	-	-	-	0.9926
153	0.0713 ± 0.0005	4.71E-06 ± 9.90E-08	0.481 ± 0.003	1.01E-05 ± 2.35E-07	93	2.74E-04 ± 1.07E-05	1.93E-04 ± 1.19E-06	7	0.9942
183	0.0919 ± 0.0008	3.26E-06 ± 7.06E-08	0.499 ± 0.003	6.53E-06 ± 1.53E-07	91	3.32E-04 ± 6.35E-06	1.89E-04 ± 7.92E-07	9	0.9941
213	0.1199 ± 0.0011	2.17E-06 ± 4.88E-08	0.508 ± 0.004	4.22E-06 ± 1.02E-07	89	3.30E-04 ± 4.64E-06	1.89E-04 ± 6.72E-07	11	0.9941
243	0.1700 ± 0.0017	1.19E-06 ± 2.76E-08	0.515 ± 0.004	2.25E-06 ± 5.58E-08	83	4.48E-04 ± 4.53E-06	1.75E-04 ± 4.72E-07	17	0.9948
273	0.2202 ± 0.0022	6.86E-07 ± 1.52E-08	0.538 ± 0.004	1.21E-06 ± 2.85E-08	74	5.50E-04 ± 4.16E-06	1.69E-04 ± 3.69E-07	26	0.9957
293	0.2599 ± 0.0026	4.42E-07 ± 9.47E-09	0.546 ± 0.004	7.62E-07 ± 1.73E-08	70	5.29E-04 ± 3.36E-06	1.63E-04 ± 3.06E-07	30	0.9964
323	0.3232 ± 0.0036	2.20E-07 ± 4.70E-09	0.558 ± 0.004	3.67E-07 ± 8.27E-09	53	6.53E-04 ± 3.22E-06	1.58E-04 ± 2.43E-07	47	0.9970
353	0.4074 ± 0.0055	1.10E-07 ± 2.61E-09	0.561 ± 0.004	1.82E-07 ± 4.53E-09	48	5.06E-04 ± 2.30E-06	1.58E-04 ± 2.38E-07	52	0.9970
383	0.5993 ± 0.0118	4.04E-08 ± 1.35E-09	0.500 ± 0.004	8.07E-08 ± 2.81E-09	46	3.54E-04 ±1.59E-06	1.59E-04 ± 2.44E-07	54	0.9969
413	0.8855 ± 0.0303	1.80E-08 ± 9.61E-10	0.517 ± 0.007	3.40E-08 ± 1.89E-09	12	1.37E-03 ± 5.66E-06	1.57E-04 ±2.40E-07	88	0.9951
443	3.3138 ± 0.3025	1.67E-09 ± 2.49E-10	0.366 ± 0.008	7.20E-09 ± 1.31E-09	11	1.22E-03 ± 5.03E-06	1.56E-04 ± 2.40E-07	89	0.9946

Table B. 28 Luminescence lifetimes (τ_i), their pre-exponential factors (a_i), parameter β_1, average lifetime ($<\tau_1>$) and contributions of [Au(*o*-SPhCO$_2$H)]$_n$ at 93 to473 K temperature range.

Temperature, K	$a_1 \pm \sigma a_1$	$\tau_1 \pm \sigma\tau_1$, s	$\beta \pm \sigma\beta$	$<\tau_1> \pm \sigma<\tau_1>$, s	Contribution of $<\tau_1>$, %	$a_2 \pm \sigma a_2$	$\tau_2 \pm \sigma\tau_2$, s	Contribution of τ_2, %	R^2
93	0.7375 ± 0.0018	4.71E-06 ± 2.16E-08	0.763 ± 0.001	5.53E-06 ± 2.71E-08	100	-	-	-	0.9947
123	0.6864 ± 0.0018	4.18E-06 ± 1.95E-08	0.767 ± 0.013	4.88E-06 ± 8.42E-08	100	-	-	-	0.9950
153	0.6866 ± 0.0015	4.71E-06 ± 2.04E-08	0.866 ± 0.002	5.06E-06 ± 2.44E-08	100	-	-	-	0.9919
183	0.6789 ± 0.0017	3.84E-06 ± 1.82E-08	0.835 ± 0.002	4.23E-06 ± 2.19E-08	100	-	-	-	0.9919
213	0.7156 ± 0.0017	2.95E-06 ± 1.37E-08	0.784 ± 0.001	3.39E-06 ± 1.70E-08	100	-	-	-	0.9937
243	0.7477 ± 0.0016	2.22E-06 ± 8.82E-09	0.741 ± 0.002	2.67E-06 ± 1.19E-08	100	-	-	-	0.9963
273	0.7803 ± 0.0019	1.53E-06 ± 6.81E-09	0.695 ± 0.001	1.95E-06 ± 9.10E-09	100	-	-	-	0.9965
293	0.8455 ± 0.0024	9.76E-07 ± 4.94E-09	0.635 ± 0.001	1.37E-06 ± 7.20E-09	100	-	-	-	0.9966
323	0.7922 ± 0.0014	7.32E-07 ± 2.47E-09	0.666 ± 0.000	9.75E-07 ± 3.30E-09	100	-	-	-	0.9981
353	0.9222 ± 0.0021	3.90E-07 ± 1.54E-09	0.615 ± 0.001	5.69E-07 ± 2.32E-09	100	-	-	-	0.9983
383	0.9468 ± 0.0042	2.62E-07 ± 2.51E-09	0.626 ± 0.002	3.74E-07 ± 3.80E-09	98	1.17E-03 ± 1.73E-05	5.78E-06 ± 1.69E-08	2	0.9975
413	0.9765 ± 0.0044	1.38E-07 ± 1.26E-09	0.584 ± 0.002	2.16E-07 ± 2.07E-09	99	3.86E-04 ± 1.02E-05	3.45E-06 ± 1.78E-08	1	0.9978
443	0.9764 ± 0.0049	8.87E-08 ± 8.95E-10	0.614 ± 0.002	1.30E-07 ± 1.39E-09	99	1.21E-03 ± 5.06E-05	1.36E-06 ± 1.05E-08	1	0.9969
473	0.9880 ± 0.0056	5.92E-08 ± 5.92E-10	0.632 ± 0.002	8.35E-08 ± 8.92E-10	98	8.63E-04 ± 1.33E-05	1.41E-06 ± 5.60E-09	2	0.9970

B.1.5 Chapter 5

Summary of conditions for luminescent measurements of all compounds discussed in the Chapter 5 can be found in the **Table B. 29**.

Table B. 29 Luminescent measurements conditions for compounds discussed in Chapter 5.

Compound	Temperature range, K	Long pass filter used	Wavelength range for 2D maps and emission-exciation spectra, nm		(λ_{exc}, λ_{em}) for lifetime measurements
			λ_{exc}	λ_{em}	
a[Au(SPh)]$_n$	93-293 K	FEL500	200-500	550-810	-
	93		-	-	(412, 690)
a[Au(SMePh)]$_n$	93-443 K	FEL500	200-500	510-900	-
a[Au(SEtPh)]$_n$	93-473 K	FEL500	200-500	510-900	-
	93		-	-	(344, 655)

Lifetime decay curve of none of compounds (discussed in this chapter) could be fitted by a sum of simple exponential decays. For this reason, one or more stretched exponential decay curves were implemented. The forms of the fitting functions are given in the **Table B. 30** below.

Table B. 30 Equations used for lifetime decay curves fit.

General form of the equation	$\boldsymbol{I = a_1 e^{-(x/t_1)^{\beta_1}} + a_2 e^{-(x/t_2)^{\beta_2}} + a_3 e^{-(x/t_3)^{\beta_3}}}$, with $\boldsymbol{\beta_1 = [0, 1]}$.
[Au(SPh)]$_n$	$I = a_1 e^{-(x/t_1)^{\beta_1}} + a_2 e^{-(x/t_2)^{\beta_2}}$
a[Au(SPh)]$_n$	$I = a_1 e^{-(x/t_1)^{\beta_1}} + a_2 e^{-(x/t_2)^{\beta_2}}$
a[Au(SEtPh)]$_n$	$I = a_1 e^{-(x/t_1)^{\beta_1}} + a_2 e^{-(x/t_2)^{\beta_2}}$

Use of this equation led to the satisfactory quality fits (**Figure B. 19**) yielding the individual luminescence lifetimes (**Table B. 31**).

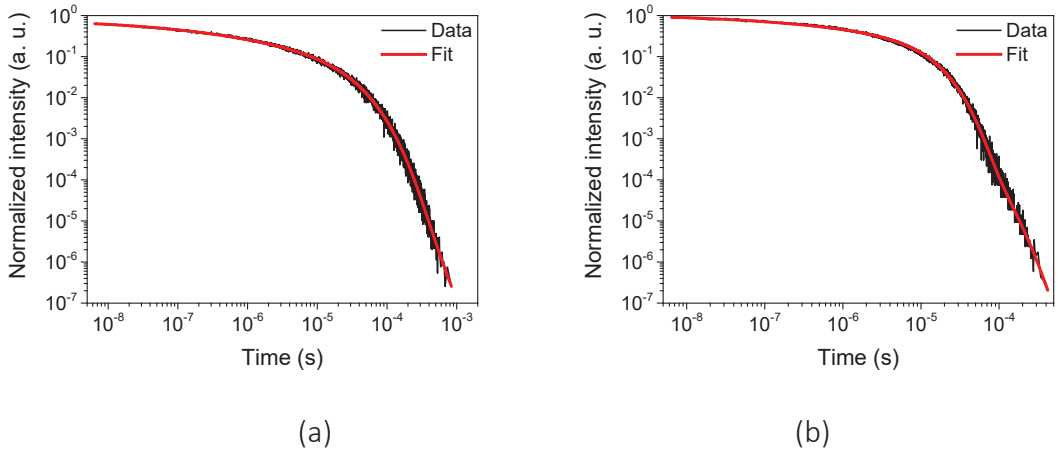

Figure B. 19 Lifetime decay fit of (a) *α*[Au(SPh)]$_n$ and (b) *α*[Au(SEtPh)]$_n$ at 93 K.

Table B. 31 Luminescence lifetimes (τ_i), their pre-exponential factors (a_i), contributions and the parameters β_i for compound $[Au(SPh)]_n$, *a*$[Au(SPh)]_n$ and *a*$[Au(SEtPh)]_n$ at 93 K.

Compound	$a_1 \pm \sigma a_1$	$\tau_1 \pm \sigma\tau_1$, s	$\beta_1 \pm \sigma\beta_1$	$<\tau_1> \pm \sigma<\tau_1>$, s	Contribution of $<\tau_1>$, %	$a_2 \pm \sigma a_2$	$\tau_2 \pm \sigma\tau_2$, s	$\beta_2 \pm \sigma\beta_2$	$<\tau_2> \pm \sigma<\tau_2>$, s	Contribution of $<\tau_2>$, %	R^2
$[Au(SPh)]_n$	0.9782 ± 0.0270	8.37E-06 ± 1.27E-07	0.783 ± 0.006	9.63E-06 ± 1.62E-07	98	0.0183 ± 0.0296	6.42E-06 ± 6.32E-06	0.564 ± 0.096	1.05E-05 ± 1.05E-05	2	0.99895
a$[Au(SPh)]_n$	0.1961 ± 0.0074	9.86E-06 ± 3.44E-07	0.642 ± 0.007	1.37E-05 ± 4.97E-07	71	0.6468 ± 0.0095	1.38E-07 ± 1.65E-08	0.309 ± 0.004	1.12E-06 ± 1.44E-07	29	0.99756
a$[Au(SEtPh)]_n$	0.3873 ± 0.0050	7.72E-06 ± 1.01E-06	0.879 ± 0.005	8.23E-06 ± 1.20E-07	82	0.6923 ± 0.0108	2.24E-07 ± 6.27E-09	0.360 ± 0.001	1.03E-06 ± 3.04E-08	18	0.99813

B.2. References

1. J. Klafter and M. F. Shlesinger, *Proc. Natl. Acad. Sci. U.S.A.*, 1986, **83**, 848-851.
2. C. Lavenn, N. Guillou, M. Monge, D. Podbevšek, G. Ledoux, A. Fateeva and A. Demessence, *ChemComm*, 2016, **52**, 9063-9066.

Abstract

The coordination polymers (CPs) based on thiolates of coinage metals are well known for their luminescence properties. However, their structures stayed underexplored.

In the thesis we present a pioneering study targeting the understanding of the structure formation and the 'structure-properties' correlation for neutral homoleptic CPs, $[M(SR)]_n$, M = Cu(I), Ag(I), Au(I). The compounds with thiophenolate derivatives studied in the work, illustrate how the use of some functionalized organic ligands leads to the formation of extended 2D networks or 1D columns by addition of some steric hindrance. The first comparative structural study of amorphous thiolated CPs was performed by PDF analysis.

The photophysical studies showed the diversity of luminescent properties of the CPs based on thiolates of coinage metals. Double or multiple emission peaks, high quantum yield of orange-to-infrared emitters, significant lifetime variation with temperature… all of these intrinsic properties reveal the high potential of these compounds for diverse optical applications.

Keywords: thiolate coordination polymer, coinage metals, 1D / 2D extended network, luminescence, double emitters, NIR emitters, luminescence thermometry.

Résume

Les polymères de coordination (PCs) à base de thiolates de métaux monétaires sont bien connus pour leurs propriétés luminescentes. Cependant, leurs structures sont sous-explorées.

Dans cette thèse, nous présentons une étude pionnière visant la compréhension de la formation de la structure et de la corrélation 'structure-propriétés' des PCs homoleptiques neutres, $[M(SR)]_n$, M = Cu(I), Ag(I), Au(I). Les composés avec les dérivés du thiophénolate étudiés dans ce travail, illustrent comment l'utilisation de certains ligands organiques fonctionnalisés conduit à la formation de réseaux 2D étendus ou de colonnes 1D par l'addition d'un encombrement stérique. De plus,la première étude structurelle comparative des PC thiolées amorphes a été réalisée par analyse PDF.

Les études photophysiques ont montré la diversité des propriétés luminescentes des PCs à base de thiolates de métaux monétaires. Des pics d'émission doubles ou multiples, un rendement quantique élevé, des émetteurs orange à proche infrarouge, des variations significatives de durée de vie en fonction de la température... toutes ces propriétés intrinsèques révèlent le potentiel élevé de ces composés pour diverses applications optiques.

Mots clés : polymère de coordination thiolaté, métaux monétaires, réseau étendu 1D / 2D, luminescence, émetteurs doubles, émetteurs proche IR, thermométrie par luminescence.